ANTIBACTERIAL POLYMER SURFACES INSPIRED BY CICADA WING NANOTOPOGRAPHY

Thomas Elliot Catley

A thesis submitted for the degree of Doctor of Philosophy

Department of Physics and Astronomy
University of Sheffield
October, 2022



The University Of Sheffield.

Acknowledgements

Firstly, I would like to thank my supervisors Andy Parnell and Rebecca Corrigan for offering me this amazing opportunity and providing endless support along the way. I couldn't have asked for better supervisors, the guidance and inspiration you have given me has been invaluable.

Thanks to the members of the polymer physics group for all of their help and discussions over the years, especially to Rachel Kilbride, Thomas Sexton, and Stephanie Burg who helped me to feel part of the group when I first started, and to the numerous recent additions to the group, who have made it such a rewarding environment to work in. Thanks, also, to the members of the Corrigan Lab who were also incredibly welcoming and have put up with a physicist running amok for the last few years. I am also very grateful to Raveen Tank, whose enthusiasm and expertise helped to push this project in a really interesting direction.

Thank you to my family for always supporting me and helping me get where I am today. Finally, to Mary, who has been my rock throughout, thank you for listening to me endlessly rant about bacteria, lifting me during tough times, and always being there to celebrate the good times.

Abstract

Bacterial colonisation of surfaces presents a substantial problem in medical environments. Without disruption of the early attachment of bacteria, this can lead to many different infections, that often lead to poor patient outcomes. The rising issue of antimicrobial resistance means that chemical routes to preventing bacterial biofilm formation are increasingly detrimental. Therefore, it is important to develop new, "drug-free", antibacterial surface technologies.

The work contained in this thesis describes the development of antibacterial surfaces, inspired by the nanotopography of the cicada wing. The wing of the cicada *Megapomponia intermedia* has been fully characterised to understand the nanostructures which confer bactericidal properties. Then, a simple process of solution casting into a mould allowed the formation of nanostructures on a variety of polymers. This was utilised to test the effect of nanopillar stiffness on bactericidal efficiency against *Escherichia coli*, by creating a range of nanostructured surfaces with different stiffnesses. The stiffest nanostructures were found to kill the highest proportion of bacteria. This was attributed to the bending of the nanopillars causing shear forces to be exerted on the bacterial envelope. It was postulated that the degree of killing on elastic nanostructured surfaces depends on a combination of the pillar stiffness and spacing. Additionally, it was shown that defects in the cell wall of gram-positive *Staphylococcus aureus* do not make them more susceptible to killing by certain nanostructured surfaces. It was also shown that the killing effect is not influenced by the growth dynamics of the cell. Finally, progress was made towards a method to allow the imaging of the bacteria-nanopillars interaction, through doping of the nanostructures with quantum dots to allow them to be localised. These are key findings in gaining more understanding the bactericidal process of nanostructured surfaces and therefore increasing their effectiveness against a range of pathogens.

Publicly Presented Work

- Florey Institute Postgraduate Symposium, Sheffield, **June 2019**, *"Antibacterial Surfaces Inspired By Cicada Wing Nanotopography"* (Poster).
- Physics of Life Summer School, Durham, **July 2019**, *"Antibacterial Surfaces Inspired By Cicada Wing Nanotopography"* (Poster).
- IOP Physics Meets Biology Conference, Oxford, **September 2019**, *"Antibacterial Surfaces Inspired By Cicada Wing Nanotopography"* (Poster).
- Material and Biological Physics Group Away Day, Sheffield, **January 2020**, *"Antibacterial Surfaces Inspired By Cicada Wing Nanotopography"* (Poster).
- IOP Physics Meets Biology Conference, Online, **July 2021**, *Understanding the bactericidal mechanism of nanostructured surfaces* (Poster).

Contents

Acknowledgements iii
Abstract v
Publicly Presented Work vii
List of Figures xviii
List of Tables xix
List of Equations xxi
List of Abbreviations xxiii

Introduction **1**
0.1 Overview 1
0.2 Aims and Objectives 4
0.3 Thesis Outline 4

1 Background and Literature **7**
1.1 Overview 7
1.2 Bacterial Cell Envelope 7
1.3 Bacterial Biofilms 9
1.4 Nanostructured Antibacterial Surfaces in Nature 10
1.4.1 Anti-biofouling Surfaces 11
1.4.2 Bactericidal Surfaces 13
1.5 Synthetic Nanostructured Antibacterial Surfaces 16
1.5.1 Inorganic Materials 16
1.5.2 Organic Materials 21
1.5.3 Summary 24
1.6 Bactericidal Mechanism of Nanostructured Surfaces 24
1.6.1 "Stretching" Mechanism 25
1.6.2 Alternative Mechanisms 26
1.7 Factors Influencing Bactericidal Efficiency 27

1.7.1 Nanostructured Surface Characteristics . . . 27
1.7.2 Bacterial Characteristics . . . 31
1.8 Summary . . . 33

2 Experimental Techniques **35**
2.1 Atomic Force Microscopy . . . 35
2.1.1 Contact Mode AFM . . . 36
2.1.2 Tapping Mode AFM . . . 37
2.1.3 PeakForce Tapping Mode . . . 38
2.2 Scanning Electron Microscopy . . . 40
2.3 LIVE/DEAD Staining . . . 42
2.3.1 Staining and Microscopy . . . 43
2.3.2 Image Analysis . . . 43
2.4 Bacterial Strains . . . 45

3 Characterisation of the *Megapomponia intermedia* Wing **47**
3.1 Introduction . . . 47
3.2 Methods . . . 48
3.2.1 Topographical and Mechanical Properties . . . 48
3.2.2 Surface Chemistry . . . 49
3.2.3 Bactericidal Properties . . . 49
3.3 Topographical Characterisation . . . 50
3.4 Mechanical Characterisation . . . 55
3.4.1 Quantitative Mechanical AFM . . . 56
3.5 Chemical Characterisation . . . 58
3.5.1 Contact Angle Measurements . . . 58
3.5.2 Surface Chemistry Analysis . . . 59
3.6 Bactericidal Testing . . . 61
3.7 Summary of Findings and Conclusions . . . 64

4 Fabricating Synthetic Nanostructured Surfaces **67**
4.1 Introduction . . . 67
4.2 Solution Casting and Moulding . . . 69
4.2.1 The LightSmyth (LS) “mould” . . . 71
4.2.2 Casting Glassy Polymers . . . 72
4.2.3 Casting Elastomeric Polymers . . . 76
4.2.4 LS Casting Summary . . . 84

4.2.5 The Cicada Replica "mould" . . . 85
4.3 Nanosphere/Colloid Lithography . . . 92
4.3.1 Nanosphere Synthesis . . . 93
4.3.2 Nanosphere Deposition . . . 94
4.3.3 Etching . . . 104
4.4 Summary of Findings and Conclusions . . . 109

5 Effect of Nanopillar Stiffness on Bactericidal Efficiency 113
5.1 Introduction . . . 113
5.2 Experimental Methods . . . 115
5.2.1 Materials . . . 115
5.2.2 Polymer Mechanical Characterisation . . . 115
5.2.3 Fabrication of Polymer NSS . . . 117
5.2.4 Polymer NSS Characterisation . . . 118
5.2.5 Bacterial Culture . . . 118
5.2.6 Bacterial Viability Assay . . . 118
5.2.7 Visualising Bacterial Interaction with Nanostructures . . . 119
5.3 Fabrication of Polymer NSS with Varied Stiffness . . . 119
5.3.1 Selection of Polymer Materials . . . 119
5.3.2 Mechanical Characterisation of Polymers . . . 120
5.3.3 Optimisation of Procedure to Produce NSS . . . 122
5.4 Effect of NSS Stiffness on Bactericidal Efficiency . . . 127
5.5 Bacterial Interaction with NSS . . . 130
5.5.1 Cell Length and Orientation . . . 133
5.5.2 Nanopillar Bending and Forces . . . 137
5.6 Summary of Findings and Conclusions . . . 148
S5 Supplementary Figures . . . 150

6 Elucidating the Bactericidal Mechanism of Nanostructured Surfaces 155
6.1 Introduction . . . 155
6.2 Susceptibility of Different Bacterial Strains to NSS . . . 156
6.2.1 Introduction . . . 156
6.2.2 g.moth^{TM} Surfaces . . . 157
6.2.3 Bacterial Strains . . . 158

6.2.4 Developing High-Throughput Testing Procedure 160
6.2.5 Assessing Viability of Bacterial Strains with a Microplate Reader 165
6.2.6 Assessing Viability of Bacterial Strains with Fluorescence Microscopy 168
6.2.7 SEM Imaging of Bacteria on g.moth 170
6.2.8 Summary of Findings and Conclusions 175
6.3 Effect of Bacterial Growth Cycle on Susceptibility to NSS 177
6.3.1 Introduction 177
6.3.2 Methods 178
6.3.3 Results and Discussion 179
6.3.4 Summary of Findings and Conclusions 186
6.4 Towards Imaging the Bacteria-Nanopillar Interaction 187
6.4.1 Introduction 187
6.4.2 Fluorescently Labelled NSS 188
6.4.3 Visualising the Bacterial Cell Wall 190
6.4.4 Preliminary Microscopy 193
6.4.5 Summary of Findings and Conclusions 197
6.5 Overall Conclusions 198

7 Concluding Remarks and Future Work **201**
7.1 Plans for Future Work 203

Bibliography **206**

List of Figures

0.1.1 : Global annual deaths attributable to AMR and compared to other causes. 1
0.1.2 : Global annual deaths associated with various antimicrobial resistant bacteria in 2019. 2

1.2.1 : Structure of the cell envelope of gram-positive and gram-negative bacteria. 8
1.3.1 : Stages of biofilm formation 9
1.4.1 : Mechanisms of structured antibacterial surfaces to prevent bacterial proliferation 11
1.4.2 : Self-cleaning effect of micro-structured surfaces due to superhydrophobicity 13
1.5.1 : Process of hot embossing/nanoimprint lithography to create structure polymers. 22
1.5.2 : Process of using Nanosphere Lithography to make polymer NSS 23
1.5.3 : Literature Survey of Synthetic NSS Killing Efficiency per Year 24
1.6.1 : "Stretching" Theory of Bacterial Killing on NSS 26
1.7.1 : Data obtained from a literature survey of the factors that influence the bactericidal efficiency of NSS 32

2.1.1 : Schematic diagram of Atomic Force Microscopy operation 36
2.1.2 : Grain analysis in Gwyddion to determine average feature height 38
2.1.3 : Fit to PFT force curve data to determine the Young's modulus 39
2.2.1 : Schematic diagram of Scanning Electron Microscopy 41
2.3.1 : Illustration of the mechanism of LIVE/DEAD stain dyes 42
2.3.2 : Data analysis process for counting the number of live and dead bacteria from the microscopy images using FIJI. 44

3.1.1 : Image of the cicada, *Megapomponia intermedia* 48
3.3.1 : The nano-topography of the wing of the cicada, *M. intermedia* 51
3.3.2 : Distribution of measurements of the nanopillars parameters from three individual *M. intermedia* wings 53
3.3.3 : Variation in height of nanopillars across the *M. intermedia* cicada wing . 55

3.4.1 : Histogram of Young's Modulus measurements taken for the *M. intermedia* wing using AFM 56
3.4.2 : Comparing the topography of the *M. intermedia* wing with air vs liquid AFM 58
3.5.1 : Water contact angle of the *M. intermedia* wing. 59
3.5.2 : FTIR spectra of the *M. intermedia* wing, with comparison to spectrum of pure chitin. 60
3.6.1 : Bactericidal Efficiency of *M. intermedia* wing against exponential phase *Escherichia coli* 61
3.6.2 : SEM images of *E. coli* on *M. intermedia* wing 63

4.2.1 : Illustration of the method used to create NSS by moulding with a master template 69
4.2.2 : Cleaning and treatment of the nanostructured mould changes it hydrophobicity and aids the release of the polymer. 70
4.2.3 : LightSmyth master template mould used to make NSS 71
4.2.4 : Representative AFM scans of PS and PMMA NSS from the LS mould . . 73
4.2.5 : SEM of a NSS made from 30 wt% PS, showing stretching of the nanopillars. 74
4.2.6 : Nanopillar height on polystyrene NSS decreases with the wt% of the polymer solution 75
4.2.7 : PS NSS produced with vacuum curing step. 76
4.2.8 : The structure of styrene–ethylene–butylene–styrene block copolymers . . 77
4.2.9 : Phase separation of the styrene and ethylene-butylene blocks of Kraton G1657 and FG1901 77
4.2.10: NSS made from 15 wt% Kraton G1657 using the LS mould 78
4.2.11: Nanopillar height on Kraton G1657 NSS increases with the decreasing wt% of the polymer solution 80
4.2.12: Bactericidal Efficiency of the G1657 NSS against *E. coli* determined with Live/Dead staining 81
4.2.13: NSS made from 10 wt% Kraton FG1901 using the LS mould 82
4.2.14: Bactericidal Efficiency of the FG1901 NSS against *E. coli* determined with Live/Dead staining 83
4.2.15: SEM and AFM images of the Cicada Replica master template mould used to make NSS 86
4.2.16: G1657 NSS made with the CR mould using different solution concentrations 87

4.2.17: Nanopillar height for the G1657 NSS made with different concentration G1657 solutions 88
4.2.18: Polystyrene NSS made using the CR mould 89
4.2.19: Distribution of pillar heights on the PS NSS made from the CR mould . 90
4.3.1 : Process of using NSL to make polymer NSS 92
4.3.2 : AFM and DLS measurement to determine the size of colloids produced through emulsion polymerisation. 94
4.3.3 : Process of depositing a monolayer of PS beads with spin coating 95
4.3.4 : First trial of spin coating 500 nm PS beads onto glass substrate. 96
4.3.5 : 3-step spin coating process for depositing PS colloids onto glass substrate. 98
4.3.6 : AFM data showing the well ordered structure of the colloid monolayer, spin coated (3-step) from 5 wt% PS in 50/50 H_2O/EtOH solution 99
4.3.7 : Process of depositing a monolayer of PS beads with interface coating . . 101
4.3.8 : Iridescence pattern caused by the diffraction of light from the well ordered colloids on the water surface. 102
4.3.9 : Monolayer of 500 nm PS colloids deposited onto a thin PS film with interface coating. 103
4.3.10: PS Colloid Etching under O_2 plasma for different times. 105
4.3.11: Etching rates of HMW PS, LMW PS, and PMMA under O_2 plasma, measured by ellipsometry. 106
4.3.12: Etching a PMMA film using O_2 plasma, using a monolayer of 300 nm HCP colloids as a mask. 107

5.2.1 : Capillary wrinkling of PS thin film due to a droplet of water. 116
5.3.1 : Results of the capillary wrinkling method to determine the Young's modulus for PS. 120
5.3.2 : Stress-Strain curves from the mechanical testing of the Kraton polymers used in this study. 121
5.3.3 : Young's modulus values for the polymer used to form NSS in this study. 121
5.3.4 : Optimisation of solution concentration for each polymer in order to make consistent NSS. 123
5.3.5 : Average feature height for the surfaces made from the 5 different stiffness polymers. 125
5.3.6 : AFM images of the NSS made from the various polymer tested in this study. 126

5.4.1 : Killing Efficiency of the Nanostructured Surfaces made from Different Stiffness Polymers. 128
5.4.2 : Killing Efficiency of the Nanostructured Surfaces vs. the Young's Modulus. 129
5.4.3 : Killing Efficiency vs. Nanopillar Height for the polymer NSS 130
5.5.1 : SEM of *E. coli* incubated on different stiffness NSS (PS, A1536 + FG1901) 131
5.5.2 : SEM of *E. coli* incubated on different stiffness NSS (A1535 + G1657) . . 132
5.5.3 : Average length of the cells on the NSS compared to the flat surfaces . . . 133
5.5.4 : Distribution of length of the cells on the NSS compared to the flat surfaces 134
5.5.5 : Orientation of the cells on the NSS 136
5.5.6 : Illustration of the number of contact points between the LS nanopillars and the bacteria for different orientation angles. 136
5.5.7 : Magnitude of the length of nanopillar bending on different polymer NSS. 137
5.5.8 : Illustration of Euler-Bernoulli Beam Theory 138
5.5.9 : Magnitude of the length of pillar force on different polymer NSS. 140
5.5.10: Magnitude of the stored elastic energy of the pillars on different polymer NSS. 141
5.5.11: Illustration of the shear stress imparted on the bacterial membrane as a result of the release of potential energy in the bent nanopillar. 142
5.5.12: Approximate shear force acting on bacterial envelope as a result of nanopillar bending. 143
5.5.13: Average shear stress per nanopillar imparted by the NSS compared to the bactericidal efficiency. 144
5.5.14: Illustration of the number of contact points between the nanopillars and the bacteria. 145
5.5.15: "Total" shear stress imparted by all nanopillars in contact with bacterial membrane. 146
S5.1 : Counts of the number of surfaces whose average pillar height fell within ± 55 nm of a certain height. 150
S5.2 : Total number of attached cells found on each of the different polymer nanostructured and control surfaces. 150
S5.3 : SEM of *E. coli* on different stiffness flat surfaces 151
S5.4 : Change in cell length of *E. coli* incubated on NSS compared to flat surfaces 152
S5.5 : *E. coli* on FG1901 NSS imaged with environmental SEM. 153

6.2.1 : Characterisation of the g.moth surfaces with AFM and SEM. 158

6.2.2 : Method 1 for the high-throughput assay to test the viability of bacteria on NSS. 161
6.2.3 : Fluorescence intensity of the SYTO9 and PI signals from *E. coli* MG1655 cells changes linearly with the proportion of dead cells in the suspension. . 162
6.2.4 : Combined SYTO9 and PI signal intensity for the g.moth and control surfaces, along with the "blank" background, for method 1 (OD_{600} = 1 suspension, 24 h incubation). 163
6.2.5 : "Improved" Method 2 for the high-throughput assay to test the viability of bacteria on NSS. 164
6.2.6 : Combined SYTO9 and PI signal intensity for the g.moth and control surfaces, along with the "blank" background, for method 2 (OD = 1 suspension, 24 h incubation). 165
6.2.7 : Fold enhancement in the percentage of dead *E. coli* and MSSA *S. aureus* on the g.moth surface compared to a control. 166
6.2.8 : Fold enhancement in the % of dead MRSA *S. aureus* and cell wall mutant strains on the g.moth surface compared to a control. 167
6.2.9 : Bacterial Viability of bacterial strains on g.moth, assessed with fluorescent microscopy. 169
6.2.10: Morphology of the MG1655, UPEC and RN4220 strains assessed with SEM. 172
6.2.11: Morphology of the Je2, Je2 Δ*pbp3* and Je2 Δ*pbp4* strains assessed with SEM. 173
6.2.12: Morphology of the Je2 Δ*sagB*, Je2 Δ*atl* and Je2 ppGpp^o strains assessed with SEM. 174
6.3.1 : Growth Curve for the GFP-expressing *E. coli* strain. 180
6.3.2 : Percentage of GFP *E. coli*, taken from different points on the growth curve, killed on the cicada wing surface. 181
6.3.3 : Growth of *E. coli* cells is arrested by 100 μg/ml cam added after 4 h. . . 182
6.3.4 : Percentage of GFP *E. coli*, taken from different points on the growth curve, killed on the cicada wing surface. 183
6.3.5 : Fold Increase in the percentage of dead bacteria for the *E. coli* at different points in the growth curve. 184
6.4.1 : Excitation spectra of ZnCdSe/ZnS quantum dots used to dope the NSS. 189
6.4.2 : Characterisation of quantum-dot doped PS NSS. 190
6.4.3 : Visualising the outer bacterial membrane of *E. coli* with respect to the main body of the cell. 191

6.4.4 : Joint staining of *E. coli* cells with GFP and FM4-64 membrane stain. . . 192
6.4.5 : Illustration of the principal of Total Internal Reflection Microscopy. . . . 194
6.4.6 : Epifluorescence image of SYTO9-labelled *E. coli* on QD-labelled NSS. . . 196

List of Tables

1.4.1 Summary of bactericidal surfaces found in nature 14
1.4.2 Feature parameters and bactericidal efficiency of three cicada species studied by Kelleher *et al.* 15
1.5.3 Summary of synthetic bactericidal surfaces developed and tested over the last decade 17
1.5.4 Summary of synthetic bactericidal surfaces developed and tested over the last decade (continued) 18
1.5.5 Summary of synthetic bactericidal surfaces developed and tested over the last decade (continued) 19
1.5.6 Summary of synthetic bactericidal surfaces developed and tested over the last decade (continued) 20
1.7.7 Summary of results testing the spacing against killing efficiency by Linklater *et al.*. 29

2.4.1 Bacterial strains used throughout the work presented in this thesis. 45

3.3.1 Summary of geometry of structures on 3 *M. intermedia* wings 51
3.4.2 Typical Young's modulus values for materials commonly used to fabricate NSS, compared to the measured value for the cicada wing. 57
3.5.3 Surface composition of the *M. intermedia* wings, determined by XPS . . . 60

4.2.1 Summary of the manufacturer values for the LS mould parameters. 72
4.2.2 Summary of the manufacturer values for the CR mould parameters. 85
4.3.3 3-step spin coating parameters for applying monolayer of PS colloids . . . 97

5.3.1 Summary of Young's modulus values for 5 different stiffness polymers. . . . 122
5.3.2 Summary of geometry of NSS made from 5 different stiffness polymers. . . 126

6.3.1 Growth phase of the sample time points taken from the growth curve of the GFP-expressing *E. coli*, along with the calculated doubling time. . . . 181

List of Equations

1.1 : Young equation for contact angle on flat surfaces 11
1.2 : Cassie-Baxter equation for contact angle on rough surfaces 12
1.3 : Solid fraction of surface in liquid contact for Cassie-Baxter model 12
1.4 : Wenzel equation for contact angle on rough surfaces 12
1.5 : Wenzel roughness factor for textured surfaces 12
1.6 : Aspect ratio of nanopillars 14
1.7 : Spatial density of nanopillars 14
2.1 : Diffraction limit of conventional optical microscopy 35
2.2 : Hertz model fit to calculate the elastic modulus from force-curve AFM data, assuming a parabolic tip geometry. 39
2.3 : de Broglie wavelength for the electron. 40
2.4 : Calculation of % dead bacteria from Live/Dead stain counts 44
3.1 : Conversion of k-space to real-space for the PSDF 57
3.2 : Euler–Bernoulli equation for the force required to bend a beam with a fixed end. 57
4.1 : Young-Laplace equation for the pressure difference across a capillary interface. 91
5.1 : Relation between wrinkle length and film properties. 115
5.2 : Mechanical Strain. 117
5.3 : Mechanical Stress. 117
5.4 : Calculation of Young's modulus from mechanical stress and strain. 117
5.5 : Euler–Bernoulli equation for the force required to bend a beam with a fixed end. 138
5.6 : Elastic constant of a beam with a fixed end. 139
5.7 : Area moment of inertia for a circular rod. 139
5.8 : Reduced elastic constant of a beam with a fixed end. 139
5.9 : Tilting coefficient of beam with on an elastic substrate. 139
5.10 Reduced force required to displace a cantilever with a fixed end. 140
5.11 Elastic potential energy stored in bending rod. 141
5.12 Shear stress exerted by pillar on bacterial membrane. 142
6.1 : Calculating % of dead cells from fluorescence signal intensities. 163
6.2 : Calculation of doubling time for the growth of bacteria. 179

6.3 : Calculation of fold increase in killing on NSS. 183
6.4 : Critical angle condition for total internal reflection. 193

List of Abbreviations

B. subtilis *Bacillus subtilis.*

E. coli *Escherichia coli.*

E. faecalis *Enterococcus faecalis.*

K. pneumoniae *Klebsiella pneumoniae.*

M. intermedia *Megapomponia intermedia.*

M. smegmatis *Mycobacterium smegmatis.*

P. aeruginosa *Pseudomonas aeruginosa.*

P. fluorescens *Pseudomonas fluorescens.*

R. capsulatus *Rhodobacter capsulatus.*

S. aureus *Staphylococcus aureus.*

S. cerevisiae *Saccharomyces cerevisiae.*

S. epidermidis *Staphylococcus epidermidis.*

S. mutans *Streptococcus mutans.*

S. pneumoniae *Streptococcus pneumoniae.*

AFM Atomic Force Microscopy.

AMR Antimicrobial Resistance.

BE Bactericidal Efficiency.

bSi Black Silicon.

cam Chloramphenicol.

CFU Colony Forming Unit.

DI Deionised.

DLS Dynamic Light Scattering.

EPS Extracellular polymeric substances.

erm Erythromycin.

FFT Fast Fourier Transform.

FIB Focussed Ion Beam.

FOTS 1H,1H,2H,2H-Perfluorooctyltriethoxysilane.

FTIR Fourier Transform Infrared Spectroscopy.

GFP Green Fluorescent Protein.

HCAIs Healthcare Associated Infections.

HCP Hexagonally Closed Packed.

HIM Helium Ion Microscopy.

kan Kanamycin.

LB Luria Broth.

LS LightSmyth.

$\mathbf{M_w}$ Molecular Weight.

MRSA Methicillin-Resistant *Staphylococcus aureus*.

MSSA Methicillin-Susceptible *Staphylococcus aureus*.

NIL Nanoimprint Lithography.

NSL Nanosphere Lithography.

NSS Nanostructured Surface(s).

OD_{600} Optical Density @ 600 nm.

pbp Penicillin Binding Protein(s).

PBS Phosphate-Buffered Saline.

PDMS Polydimethylsiloxane.

PEDOT:PSS poly(3,4-ethylenedioxythiophene) polystyrene sulfonate.

PEEK polyetheretherketone.

PET Polyethylene terephthalate.

PFA Paraformaldehyde.

PFT PeakForce Tapping Mode.

PG Peptidoglycan.

PI Propidium Iodide.

PMMA Poly(methyl methacrylate).

PP Polypropylene.

PS Polystyrene.

PSDF Power Spectral Density Function.

QD Quantum Dot.

RIE Reactive Ion Etching.

ROS Reactive Oxygen Species.

RT Room Temperature.

SDS Sodium Dodecyl Sulfate.

SEBS styrene–ethylene–butylene–styrene.

SEM Scanning Electron Microscopy.

SIM Structured Illumination Microscopy.

T_g Glass Transition Temperature.

TEM Transmission Electron Microscopy.

TiO_2 Titanium Dioxide.

TIRFM Total Internal Reflection Microscopy.

TSB Tryptic Soy Broth.

UPEC UroPathogenic *Escherichia coli*.

UTI Urinary Tract Infections.

WCA Water Contact Angle.

wt% Percentage by Weight/Mass Fraction.

XPS X-Ray Photoelectron Spectroscopy.

YM Young's Modulus.

ZnO Zinc Oxide.

Introduction

0.1. Overview

The 2016 Review on Antimicrobial Resistance (AMR), funded by the UK government and chaired by Jim O'Neill, suggested that AMR infections could become a leading cause of mortality worldwide. The report estimated that these infections could kill up to 10 million people a year by 2050 (Figure 0.1.1) [1]. Whilst some have claimed that this is an overestimate [2], it is clear that AMR is a global issue and one that requires urgent action. A recent study in *The Lancet* reports that nearly 5 million deaths worldwide were associated with AMR bacteria in 2019, with 1.27 million deaths directly attributable to bacterial AMR infection [3]. The burden of AMR infection is at least as large, if not worse, than HIV or malaria and so must be considered as a huge threat to global health. This new data shows that we may be on track to reach these 2016 estimates, highlighting the need to act quickly to combat this issue.

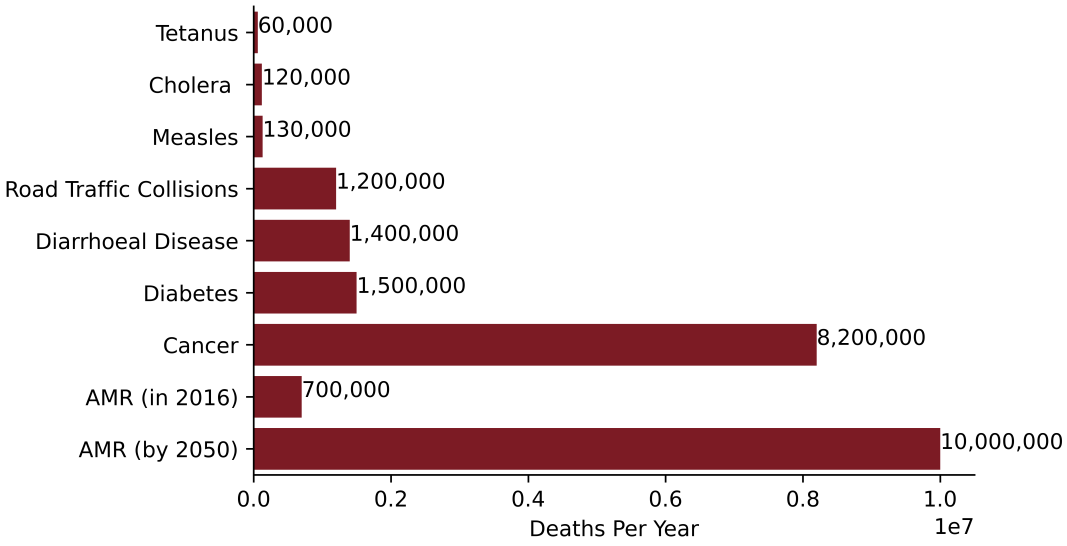


Figure 0.1.1: Global annual deaths attributable to AMR and compared to other causes. Adapted from data in the 2016 Review on Antimicrobial Resistance (AMR) chaired by Jim O'Neill [1]

The overuse and misuse of current antibiotic treatments is one of the leading reasons that AMR is such a large issue today, however, infection control in hospital settings is also a big contributor. Treating persistent infections, and infections in immunocompromised patients in hospitals has led to the emergence and spread of many antibiotic-resistant bacteria [4]. Due to their ability to cling to surfaces, bacterial biofilms often colonise medical devices such as urinary catheters, shunts, ventilator tubing and central venous catheters. Colonisation on such devices can lead to infections such as urinary tract infections (UTIs), lower respiratory tract infections or bloodstream infections - all of which may lead to negative patient outcomes. The typical bacteria which cause these issues are *Escherichia coli*, *Staphylococcus aureus*, *Klebsiella pneumoniae*, and *Streptococcus pneumoniae*. All of the these bacteria were accountable with the highest number of AMR associated deaths in 2019 (see Figure 0.1.2) [3]. These type of infections, known as Healthcare Associated Infections (HCAIs), can lead to intense additional pain for the patient and often require the device to be removed or replaced. Treating these infections (which can often become chronic) extends hospital stays and generally is a huge burden on healthcare. For example in 2016/17, HCAIs resulted in an extra 5.5 million hospital bed days and an additional £2 billion of cost to the NHS [5].

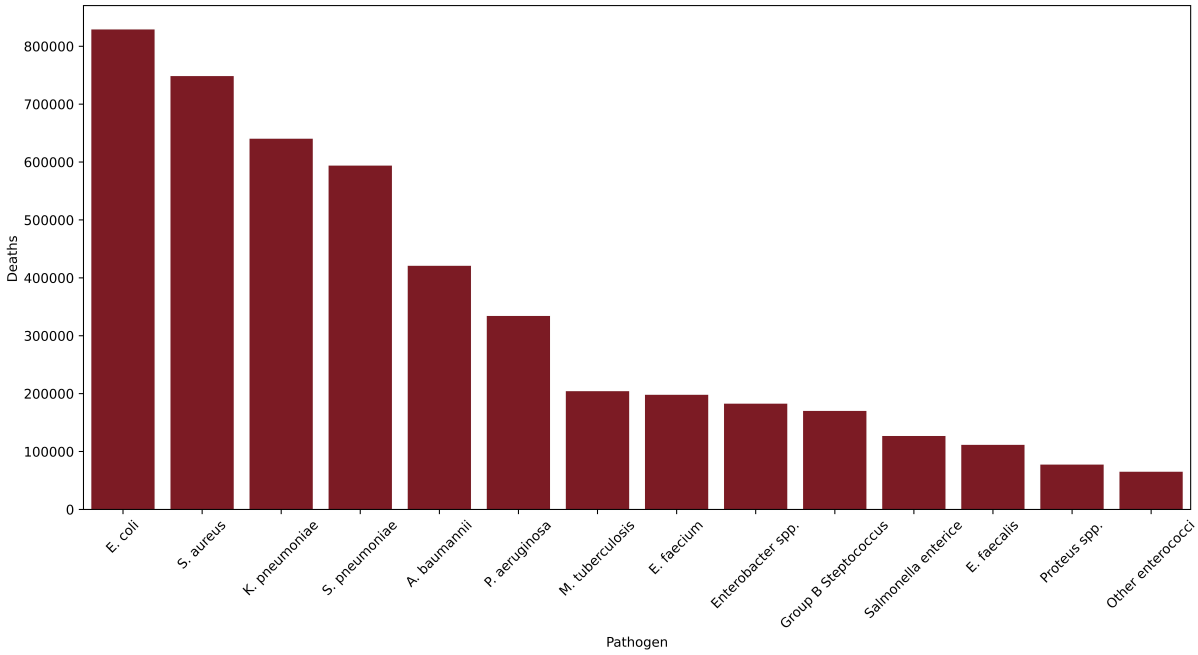


Figure 0.1.2: Global annual deaths associated with various antimicrobial resistant bacteria in 2019. Adapted from the data in the Lancet report [3].

Given that many of our current antibiotic treatments are failing, it is of upmost importance that we begin to look for other routes to prevent the early colonisation of bacteria on medical surfaces, helping to prevent the formation of the mature biofilms which lead to infection. These technologies could potentially dramatically increase patient outcomes and save billions in costs. The best way to prevent the formation of a mature biofilm is to stop the initial colonisation of bacteria. The current methods for this typically involve a chemical or small-molecule being impregnated or grafted onto a surface which is then slowly released into the surroundings. The antimicrobial action of these chemical agents then kill any bacteria near the surface, preventing them from attaching. These agents can come in the form of metal nanoparticles (such as sliver and copper) [6], antibiotic coatings [7, 8], silver ions [9] and quaternary ammonium compounds [10], which are all highly effective at killing bacteria. However, these "chemical" antibacterial surfaces do have some drawbacks. Due to the finite amount of active material, these surface generally have a limited lifetime, after which the concentration of the chemical they release is not sufficient to continue killing bacteria. The continual release of chemical compounds into the surroundings of these surfaces could also leads to toxic accumulation, especially when considering the use of metal nanoparticles. Finally, as previously mentioned, the use of chemical-based strategies has been heavily linked to the continued development of AMR bacteria.

The negative implications of current antibacterial surface technologies requires a shift in focus towards surfaces which acquire their bacteria-combatting properties through non-chemical routes. The last decade has seen a rise in the development of antibacterial surfaces that take their properties from biological structures such as lotus leaves, shark skin and cicada wings [11]. The micro-scale structures which are present on the lotus leaf and the shark skin create a superhydrophobic surface that displays good anti-fouling properties - stopping bacteria sticking to their surface [12, 13]. However, the nano-scale structures on the wings of the cicada are able to kill bacteria upon contact [11, 14]. It was proposed that this killing process took place purely as a result of the mechanical interaction between the bacteria and the surface nanopillars. Therefore, taking inspiration from these biological structures could pave the way for a new generation of antibacterial surface technology which act through a physical mechanism, negating our reliance on chemicals or drugs.

0.2. Aims and Objectives

The overall aim of this research was to develop antibacterial polymer surfaces inspired by the topography of the cicada wing, and use them to understand more about the antibacterial mechanism of nanostructured surfaces (NSS). This process had the following objectives:

1. Carry out full characterisation of the topographical, chemical, mechanical and bactericidal properties of a cicada wing. This will provide the basis for the design of any polymer nanostructured surfaces.

2. Develop techniques that would allow the low-cost fabrication of nanostructured surfaces which mimic the cicada wing using a range of polymer materials. The technique would also need to allow the creation of surfaces with different feature sizes.

3. Test the effects of changing the nanopillar stiffness on the bactericidal efficiency of these NSS by fabricating with a range of polymers with different Young's modulus.

4. Develop methods to allow the imaging of the bacteria-nanopillar interactions, with the aim of gaining more knowledge about the bactericidal mechanism.

0.3. Thesis Outline

- **Chapter 1** provides a presentation of the background literature related to natural and synthetic nanostructured antibacterial surfaces. A discussion of the proposed bactericidal mechanism is given, along with an overview of the factors that have been reported to influence the rate of killing.

- **Chapter 2** describes the experimental technique most commonly used in this study. These include the surface characterisation techniques Atomic Force Microscopy (AFM) and Scanning Electron Microscopy (SEM), along with a discussion of the Live/Dead stain used to bacterial viability. Additional techniques used are presented with each chapter.

- **Chapter 3** gives the results from the characterisation of the cicada (*Megapomponia intermedia*) wing. This included topographical characterisation with AFM and SEM, mechanical characterisation to find the Young's modulus of the wing, and

chemical characterisation to analyse the composition of the wing. Additionally, the bactericidal efficiency of the wing against the bacterium *E. coli* was assessed using the Live/Dead stain assay.

- **Chapter 4** explores the different methods tested for fabricating the bio-inspired nanostructured surfaces using a variety of polymer materials. A simple but successful solution casting process was developed and tested for a range of polymers, both glassy and rubbery. A further method of colloidal lithography was also tested with the aim of mimicking the cicada wing surface, but with more control over the size and spacing of the nanopillars. The chapter includes the methodology for the techniques and the results of the characterisation of the subsequent surfaces.

- **Chapter 5** presents the results of a study into the effect of nanopillar stiffness on the bactericidal efficiency of nanostructured surfaces. Using the solution casting method from Chapter 4, a range of surfaces with different Young's Modulus are fabricated. These surfaces are characterised mechanically and topographically, before their bactericidal efficiency is tested against *E. coli*. Finally, the interaction of the nanopillars with the bacteria is assessed and the effect of the elastic forces on the killing of the bacteria is evaluated.

- **Chapter 6** details the efforts made to elucidate the bactericidal mechanism of the nanostructured surfaces with a variety of experiments. The susceptibility of several different bacterial strains, some of which had defect in their cell wall, to a nanostructured surface was tested. The effect of the growth cycle of *E. coli* on its susceptibility to killing by the cicada wing was also investigated. Finally, procedures were developed for the high-resolution imaging of the bacteria-nanopillar interaction with fluorescence microscopy. Preliminary results of this imaging are presented.

- **Chapter 7** provides conclusions of the work overall and recommendations for future work.

Chapter 1

Background and Literature

1.1. Overview

This chapter will discuss the current research on nanostructured antibacterial technology, including antibiofouling and bactericidal surfaces. Firstly an overview of the structure of the bacterial cell envelope and the formation of bacterial biofilms is given. Next, examples of both types of nanostructured antibacterial surface in nature will be presented, followed by the previous work done in creating synthetic replicas of the bactericidal surfaces. The current theories regarding the bactericidal mechanism of these surfaces will be discussed, and finally, the main factors which have been attributed to increased killing by nanostructured surfaces will also be presented.

1.2. Bacterial Cell Envelope

Gram-positive and gram-negative bacteria can be differentiated by the structure of their cell envelope (cross-sections of each are illustrated in Figure 1.2). The gram-negative cell envelope consists of three layers - the inner membrane, the peptidoglycan layer and the outer membrane. *E. coli* and *P. aeruginosa* are two common examples of gram-negative bacteria. In contrast, the gram-positive cell envelope only consists of a plasma membrane, surrounded by a thick (many layers) peptidoglycan mesh [15]. *S. aureus* and *B. subtilis* are common examples of gram-positive bacteria. In both groups of bacteria it is the peptidoglycan layer, which is unique to prokaryotic cells, that provides the strength and structure to the cell as a whole, and therefore is a common target for many classes of antibiotics (e.g. β-lactams). It has been shown that preventing new synthesis or damaging the peptidoglycan layer ultimately leads to the death of the cell [15, 16]. In gram-negative

bacteria this peptidoglycan layer has been measured at 2-6 nm thick using cryo-electron microscopy [15, 17]. For gram-positive bacteria, the peptidoglcan layer thickness has been measured at anywhere between 30 and 100 nm thick, with both cryo-electron microscopy and atomic force microscopy measurements [15, 18, 19]. Given that the bactericidal mechanism of the nanostructured surfaces presented in this work is thought to be a mechanical rupturing process, the structure and strength of each type of bacterial cell envelope is of key importance.

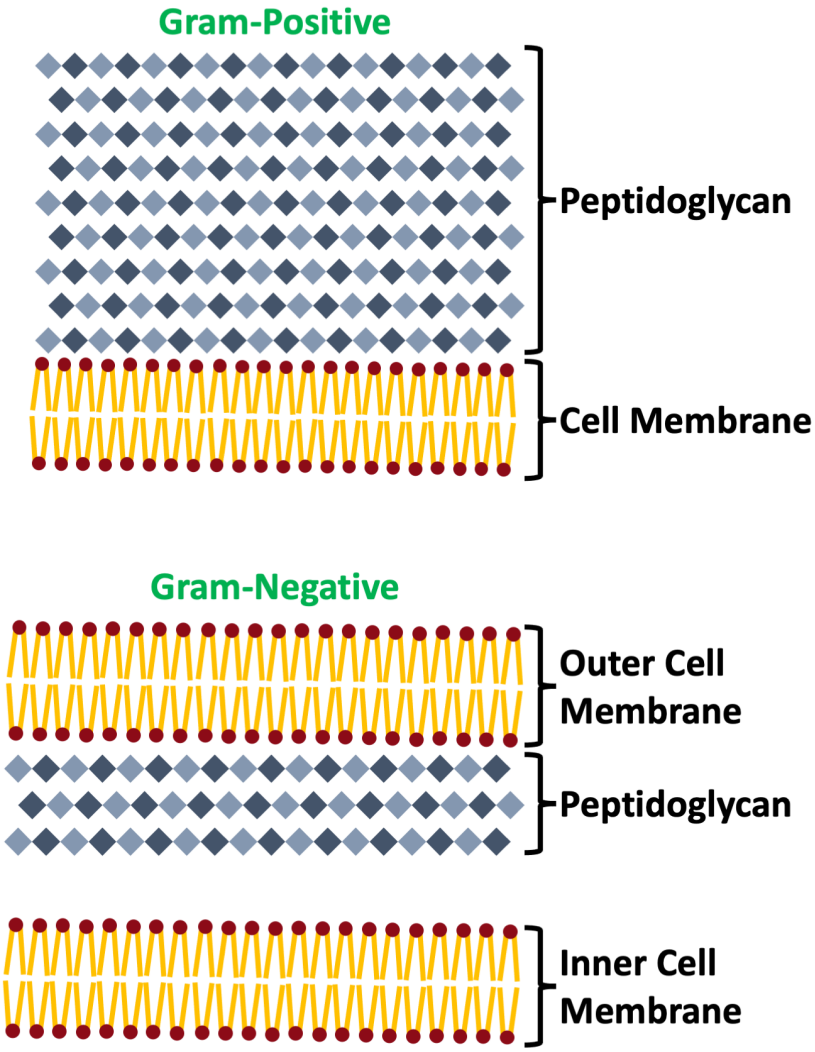


Figure 1.2.1: Structure of the cell envelope of gram-positive and gram-negative bacteria. Gram-positive bacteria have an inner cell membrane surrounded by a thick mesh of peptidoglycan, whereas gram-negative bacteria have a thin layer of peptidoglycan which is sandwiched between two plasma membranes. (Illustration inspired by [15])

1.3. Bacterial Biofilms

Biofilms form when bacteria settle on a surface and begin to proliferate. Once they have attached to the surface, through electrostatic interactions, the bacteria start to secrete extracellular polymeric substances (EPS), which form a matrix that encases the cell. EPS are formed of an array of proteins, lipids, sugars and extracellular-DNA, and act to anchor the bacteria to the surface and provide it with protection from the external environment [20, 21]. Once several clusters of the bacteria become irreversibly attached to the surface by the EPS, the number of cells in the biofilm rapidly increases, which provides more structural integrity as it reaches maturation. Eventually the mature biofilm breaks apart and re-disperses the bacteria to colonise other areas of the surface.

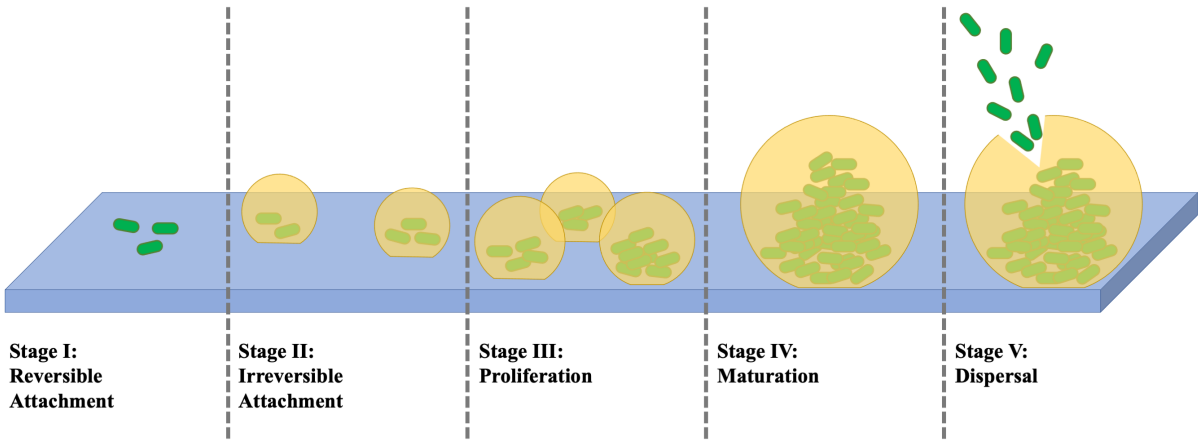


Figure 1.3.1: Stages of biofilm formation. 1) Planktonic bacteria attach to a surface through electrostatic interactions. 2) These bacteria start to secrete EPS which irreversibly sticks them to the surface. 3) The number of bacteria begin to increase rapidly. 4) 3D growth of the biofilm which forms the mature biofilm. 5) Biofilm breaks and bacteria are scattered to attach to other surfaces. (Adapted from [22, 23])

Many species of both gram-positive and gram-negative bacteria have the ability to form strong biofilms, with *S. aureus*, *P. aeruginosa* and *Staphylococcus epidermidis* commonly attributed as some of the strongest biofilm-formers [24]. Many studies have investigated the optimal environment for biofilm formation, with temperature [25], pH [26] and availability of nutrients [27] all key factors in the quality and strength of the biofilm. The protective nature of the EPS has been shown to make bacteria within a biofilm up to 1000-fold less susceptible to antibiotic treatment than (free-floating) planktonic bacteria. It is thought that this could be due to the physical barrier of the EPS layer preventing the penetration of the antimicrobial agent into the deepest parts of the biofilm [22]. It has also been proposed that the cells within a biofilm have a significantly reduced growth rate

which makes them less susceptible to the mechanism of action of some antibiotics [22, 28]. The result of this decreased susceptibility to antibiotic treatment is that some bacteria can remain alive within a biofilm even after treatment, and these cells can ultimately act as the starting point for further spread of the pathogen. Therefore, preventing the formation of the mature biofilm by hindering the early-attachment or proliferation of the bacteria on the surface is key. The rest of this chapter will discuss nanostructured surfaces which have been found to have antibacterial properties, either through attachment prevention or bactericidal abilities.

1.4. Nanostructured Antibacterial Surfaces in Nature

Antibacterial surfaces can broadly be categorised into one of two groups, antibiofouling or bactericidal, depending on how they prevent the proliferation of bacteria. Antibiofouling surfaces work by preventing the initial attachment of planktonic bacteria, thus preventing the synthesis of EPS and the irreversible attachment of the biofilm (illustrated in Figure 1.4.1a) [29]. Bactericidal surfaces are able to prevent the early biofilm formation by directly killing any bacteria that attach to the surface [10], also preventing proliferation and the subsequent excretion of the EPS (illustrated in Figure 1.4.1b). There are numerous examples of both of these types of antibacterial surfaces in nature, which have arisen due to the need for organisms to protect themselves against contamination from their environment [10]. These properties are often conferred by physical structures on their surfaces, making them ideal candidates when developing antibacterial surfaces which do not rely on chemicals or drugs.

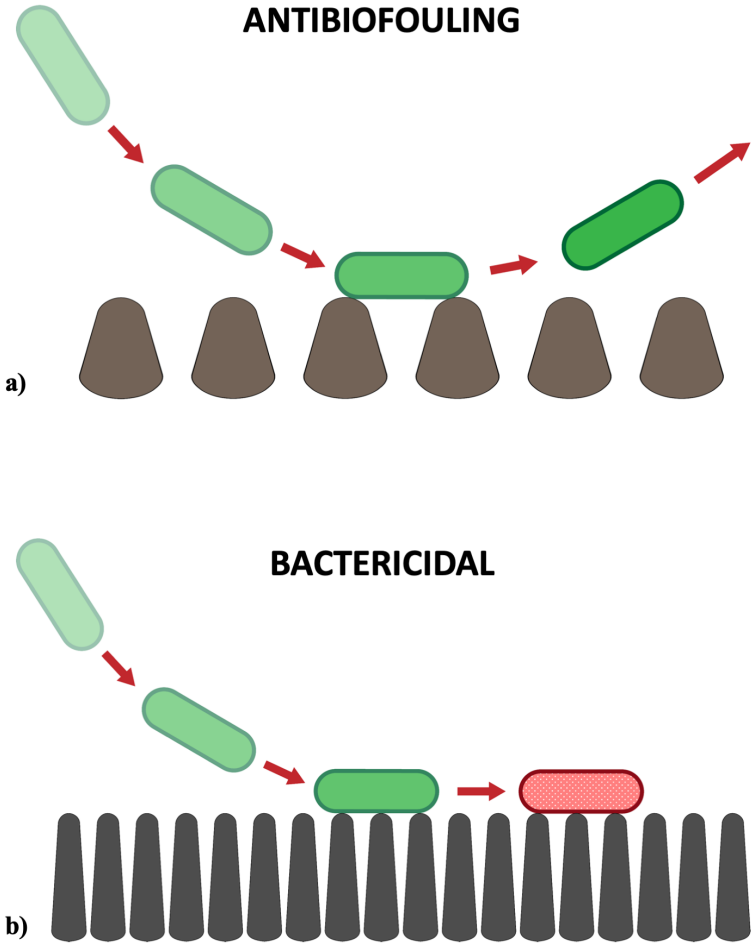


Figure 1.4.1: Structured antibacterial surfaces prevent the proliferation of bacteria through one of two routes. a) Anti-biofouling surfaces prevent the initial attachment of bacteria whereas b) Bactericidal surfaces kill bacteria on contact.

1.4.1. Anti-biofouling Surfaces

Anti-biofouling surfaces found in nature typically obtain their properties due to the presence of micron-scale structures, which create a superhydrophobic surface by increasing the Water Contact Angle (WCA). The contact angle, θ_C, of a planar surface is described by equation 1.1, where γ is the surface energy between any two of the **S**olid, **L**iquid, or **G**as phases [30].

$$\gamma_{SG} - \gamma_{SL} - \gamma_{LG}\, cos(\theta_C) = 0 \tag{1.1}$$

Even for surfaces that have been chemically modified to reduce their surface energy,

the WCA does not typically reach the superhydrophobic (θ_C >140°) region [31]. Two models were proposed that demonstrated how porous/structured surfaces can have a dramatically increased WCA over planar surfaces. The Cassie-Baxter model describes how air becomes trapped at the liquid-solid interface, between the surface structures, enhancing the contact angle [32]. This is described by the Cassie-Baxter equation (1.2), where θ_{CB} is the apparent contact angle on the rough surface, θ_C is the contact angle on the equivalent planar surface, and ϕ is the solid fraction of surface (with features of diameter, D and spacing/pitch, P) that is in contact with the liquid drop.

$$cos(\theta_{CB}) = \phi(1 + cos(\theta_C)) - 1 \tag{1.2}$$

$$\phi = \frac{D^2}{(D+P)^2} \tag{1.3}$$

Wenzel described an alternative situation whereby the water sinks down, in between the features, and the resulting increase in solid-liquid contact area increases the apparent contact angle. This "Wenzel" contact angle, θ_{W}, is described by 1.4 where r is the roughness parameter of the surface with features of diameter, D, spacing, P and height, H. Generally, surfaces with higher roughness (higher aspect ratio features) experience the Cassie-Baxter regime but then transition to the Wenzel regime after overcoming the energy barrier that allows the water to fill between the features [33, 34].

$$cos(\theta_W) = r\, cos(\theta_C) \tag{1.4}$$

$$r = \frac{(D+P)^2 + 4DH}{(D+P)^2} \tag{1.5}$$

The structures on anti-biofouling surfaces trap air and therefore dramatically increase the liquid-air interface (as illustrated in Figure 1.4.2a) which, as per the Cassie-Baxter model (equation 1.2), increases the apparent contact angle to values which would be considered superhydrophobic. The most well-known example of a superhydrophobic surface in nature is the lotus leaf (*Nelumbo nucifera*). Often considered a symbol of purity due to their ability to "self-clean", the lotus leaf surface is covered in $\sim 5\,\mu$m tall structures which trap air and give them a WCA > 140°, allowing water to roll straight off, picking

up and removing contaminants (such as bacteria) with it [35]. The taro leaf (*Colocasia esculenta*) surface also possesses micro-structures, 15 - 30 µm in diameter, which have been demonstrated to reduce the attachment of both polymer colloids and *P. aeruginosa* due to the highly hydrophobic nature of the leaf [36]. Whilst anti-biofouling surfaces do show the potential to resist bacterial attachment, and therefore biofilm accumulation, surfaces structures which kill bacteria have gathered much more research interest, as they often possess both superhydrophobic and bactericidal properties.

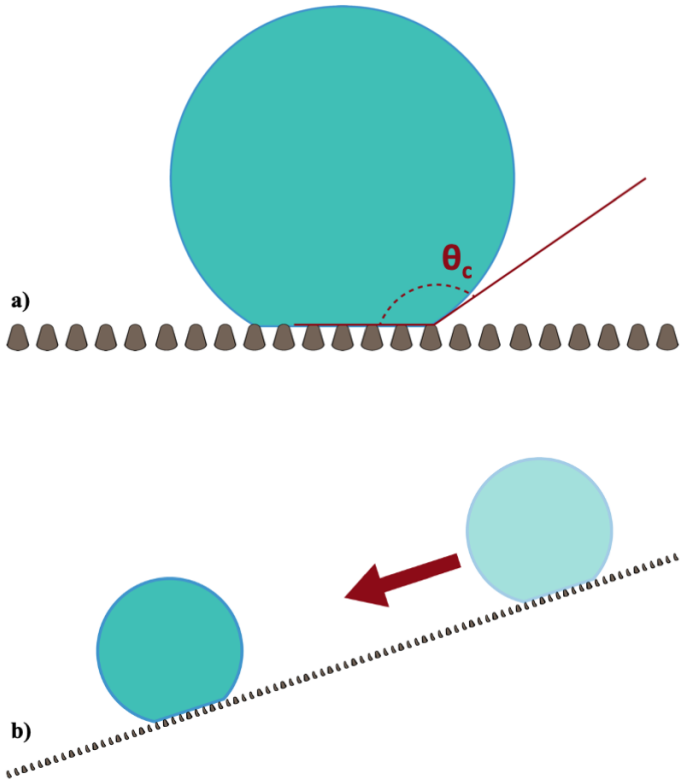


Figure 1.4.2: Self-cleaning effect of micro-structured surfaces due to superhydrophobicity. a) Natural anti-biofouling surfaces have a high Water Contact Angle (> 140°) due to their structured surfaces [32]. Air gaps form between the solid-liquid interface, as per the Cassie-Baxter model. b) The highly hydrophobic nature of these surfaces allows water to roll off the surface easily, collecting contaminants along the way (reproduced from [31]).

1.4.2. Bactericidal Surfaces

There are, perhaps surprisingly, several examples of surfaces in nature which have been found to be bactericidal due to nanostructures on their surfaces. The key studies are summarised Table 1.4.1. The features on these nanostructured surfaces are generally

>100 nm tall and <250 nm apart, giving them a higher aspect ratio (defined by eq. 1.6) and spatial density (defined by eq. 1.7) than the features on anti-biofouling surfaces.

$$\text{Aspect Ratio} = \frac{H}{D} \tag{1.6}$$

$$\text{Spatial Density} = \frac{\text{Number of Features}}{\text{Area}} \tag{1.7}$$

The bactericidal ability of these surfaces is generally quoted in the literature in terms of either a killing "rate" or "efficiency". The killing rate is usually determined by taking Colony Forming Unit (CFU) counts of a bacterial culture before and after it comes into contact with the NSS. The rate is then reported as the reduction in the CFU per cm^2 of the test material, per minute of the incubation time, which allows for normalisation to different sized surfaces and incubation conditions. The killing efficiency, which is typically determined using a LIVE/DEAD stain, reports what percentage of the bacteria which remain on the surface after incubation have been killed and is defined by equation 2.4 on page 43. This normalises to the amount of cells on the surfaces, and therefore the concentration of the initial culture.

Table 1.4.1: Summary of bactericidal surfaces found in nature.

Type	**Feature Dimensions**				**Bactericidal Ability**		**Ref.**
	Height (nm)	**Diameter (nm)**	**Aspect Ratio**	**Pitch (nm)**	**Microorganism Tested**	**Reported Rate/Efficiency**	
Cicada	200	100	2	170	*P. aeruginosa* (-)	$2.1 \times 10^{5\dagger}$	[11, 37]
Cicada	241	156	1.55	165	*P. fluorescens* (-)	22%	[38]
Cicada	182	159	1.15	187	*P. fluorescens* (-)	12%	[38]
Cicada	182	207	0.88	251	*P. fluorescens* (-)	7%	[38]
Cicada	84	167	0.5	252	*S. cerevisiae* (y)	8%	[39]
Cicada	183	104	1.8	175	*S. cerevisiae* (y)	84%	[39]
Damselfly	433	48	9	116	*S. aureus* (+)	87%	[40]
					P. aeruginosa (-)	97%	
Dragonfly	240	90	2.7	*	*P. aeruginosa* (-)	$3 \times 10^{5\dagger}$	[14]
					S. aureus (+)	$4.6 \times 10^{5\dagger}$	
Dragonfly	311	57	5.5	*	*E. coli* (-)	$2.3 \times 10^{5\dagger}$	[41]

† cfu/cm^2/min, * no value given, (-) Gram-negative bacterium, (+) Gram-positive bacterium, (y) Yeast

Cicada Wing

The first surface from nature which was reported to possess bactericidal properties was the wings of the cicada *Psaltoda claripennis*, which are covered in a hexagonally-packed array of conical pillars 200 nm tall, 60 nm in diameter at the cap, with a centre to centre separation of 170 nm [11]. The wings themselves were found to mainly comprise of the biopolymer chitin, covered in a waxy lipid layer [42]. The combination of these waxes and the nanostructures give the cicada wing a superhydrophobic nature, similar to that of the lotus leaf. It is thought that this highly ordered array of features could have evolved as an anti-reflective mechanism to prevent the cicada being easily spotted by predators [43]. However, Ivanova *et al.* also discovered that the Gram-negative bacterium *Pseudomonas aeruginosa* was killed "within 3 minutes" of contact with the wing surface [11]. The bactericidal effect of the wings was shown to be conserved even after the surface chemistry was altered by applying a 10 nm thick gold coating. This thin coating creates an inert layer on top of the cicada wing, preventing the chemistry of the wing from playing a role in the killing processes, whilst preserving the topography of the surface. This finding resulted in the theory that the bacteria were being killed through a purely physical process, as a result of the interaction with the surface nanostructures. Kelleher *et al.* later studied the wings of three cicada species, *Megapomponia intermedia* (ME), *Ayuthia spectabile* (AY), and *Cryptotympana aguila* (CA), each with a different topography (summarised in Table 1.4.2) and assessed the killing ability against the bacteria *Pseudomonas fluorescens* [38]. They found that the wing which had the highest aspect ratio features with the closest spacing resulted in the greatest percentage of dead bacteria. It was postulated that this was due to the greater number of interactions between the pillars and the bacteria causing more stress on the bacterial cell wall.

Table 1.4.2: Feature parameters and bactericidal efficiency of three cicada species [38].

Cicada	Height (nm)	Pitch (nm)	Diameter (nm)	Aspect Ratio	Bactericidal Efficiency (%)
ME	241	165 ± 8	156 ± 29	1.55	22.2
CA	182	187 ± 13	159 ± 47	1.15	12.3
AY	182	251 ± 31	207 ± 62	0.88	6.7

Dragonfly Wing

In contrast to the ordered features on the cicada wing, the nanopillars on the wing of the dragonfly form random clusters, which are also generally narrower and therefore have a higher aspect ratio. Ivanova *et al.* reported that the wing of the dragonfly, *Diplacodes bipunctata*, are covered in features 240 nm tall and 30-90 nm in diameter [14]. Just like

the cicada wing, the dragonfly wing is mainly comprised of chitin and lipids, conferring superhydrophobicity along with the topography. The killing effect of a dragonfly wing was first demonstrated against *P. aeruginosa*, *S. aureus* and the spores of *B. subtilis* [14]. The structures on the dragonfly wing were found to kill bacteria with at a higher rate/efficiency than the wings of the cicada, with nearly double the amount of *P. aeruginosa* bacteria killed (see Table 1.4.1). Additionally the dragonfly wing was found to be able to kill some gram-positive bacterial species which cicada wings were not able to [37]. The bacterial cell wall of gram-positive bacteria is much thicker than gram negative (see section 1.2), and so it would be expected that they are more resilient to mechanical breaking. It is generally accepted that the dragonfly wing is able to kill gram-positive bacteria because of the higher density of features compared to the cicada, which results in more contact points between the NSS and the bacteria, thus exerting a higher stress on the cell membrane (to be discussed in more detail in section 1.7.1).

1.5. Synthetic Nanostructured Antibacterial Surfaces

The fact that the bactericidal properties of these natural surfaces arise from their topography, rather than any surface chemistry, makes them a rich source of inspiration when looking to develop antibacterial surfaces that don't rely on a chemical or drug release. Consequently, there has been much work over the last 10 years to develop surfaces that mimic these nanostructures using synthetic materials, with some of these efforts summarised in Table 1.5.

1.5.1. Inorganic Materials

Using the naturally-occurring nanostructured surfaces for inspiration, the first "synthetic" NSS that was fabricated and demonstrated to have antibacterial effects was Black Silicon (bSi). Ivanova *et al.* reported how the bSi surfaces were fabricated from silicon wafers by Reactive Ion Etching (RIE) with sulphur hexafluoride (SF_6) and O_2 plasma to leave them covered in a random array of tall, spike-like features, very similar to those on the dragonfly wing [14]. They found that both the Gram-negative bacterium *P. aeruginosa* and the Gram-positive bacterium *S. aureus* were killed at $\sim$4.3 x 10^5 cfu/cm^2/min after 3 hr of incubation on the bSi surfaces. This was over twice as effective against the *P. aeruginosa* than the cicada wing that had previously been tested. Additionally, the bSi killed Gram-positive bacteria, which the cicada wing was unable to achieve. Several studies have reported the bactericidal ability of synthetic NSS against a range of different

bacteria since the first report by Ivanova *et al.*, which are summarised in Table 1.5.3.

Table 1.5.3: Summary of Synthetic Bactericidal Surfaces developed and tested over the last decade.

Material	Feature Dimensions			Bactericidal Ability		Year	Ref.
	Height (nm)	Diameter (nm)	Pitch (nm)	Microorganism Tested	Reported Rate/ Efficiency		
Black Silicon	500	50	*	*P. aeruginosa* (-)	$4.3 \times 10^{5\dagger}$	2013	[14]
				S. aureus (+)	$4.5 \times 10^{5\dagger}$	2013	
				B. subtilis (+)	$1.4 \times 10^{5\dagger}$	2013	
TiO2 Nanowires	3000	100	*	*P. aeruginosa* (-)	50%	2014	[44]
				S. aureus (+)	5%	2014	
				E. coli (-)	90%	2014	
				B. subtilis (+)	60%	2014	
				K. pneumoniae (-)	10%	2014	
Titanium	478	*	158	*E. coli* (-)	60%	2014	[45]
PMMA	210	70	100	*E. coli* (-)	22%	2015	[46]
	300	190	130	*E. coli* (-)	20%	2015	
	300	215	380	*E. coli* (-)	12%	2015	
Silicon	4000	20	*	*E. coli* (-)	83%	2015	[47]
				S. aureus (+)	86%	2015	
Titanium	40	*	*	*S. aureus* (+)	20%	2015	[48]
				P. aeruginosa (-)	47%	2015	
Diamond	1650	25	*	*P. aeruginosa* (-)	9%	2016	[49]
	4000	25	*	*P. aeruginosa* (-)	17%	2016	
Diamond Coated BSi	1000	*	*	*P. aeruginosa* (-)	13%	2016	[50]
TiO2 Nanowires	1000	25	*	*P. aeruginosa* (-)	30%	2016	[51]
Black Silicon	279	63	62	*P. aeruginosa* (-)	89%	2017	[52]
	279	63	62	*S. aureus* (+)	85%	2017	
	432	80	100	*P. aeruginosa* (-)	70%	2017	
	432	80	100	*S. aureus* (+)	65%	2017	
	612	93	140	*P. aeruginosa* (-)	82%	2017	
	612	93	140	*S. aureus* (+)	74%	2017	
Copper coated Silicon	8000	70	*	*E. coli* (-)	97%	2017	[53]
Titanium	1000	80	*	*E. coli* (-)	95%	2017	[54]
				P. aeruginosa (-)	98%	2017	
				S. aureus (+)	22%	2017	
				M. smegmatis (+)	92%	2017	
Black Diamond	1000	75	*	*E. coli* (-)	28%	2018	[55]
	3000	350	*	*E. coli* (-)	32%	2018	
	20000	350	*	*E. coli* (-)	23%	2018	
Carbon Nanotubes	1000	*	75	*P. aeruginosa* (-)	99%	2018	[56]
	32000	*	75	*P. aeruginosa* (-)	75%	2018	
	1000	*	75	*S. aureus* (+)	67%	2018	
	32000	*	75	*S. aureus* (+)	17%	2018	

† cfu/cm^2/min, * no value given, (-) Gram-negative bacterium, (+) Gram-positive bacterium

Table 1.5.4: Summary of Synthetic Bactericidal Surfaces developed and tested over the last decade. (continued from above)

Material	Feature Dimensions			Bactericidal Ability		Year	Ref.
	Height (nm)	Diameter (nm)	Pitch (nm)	Microorganism Tested	Reported Rate/Efficiency		
Black Silicon	400	50	130	*E. coli* (-)	10%	2018	[57]
				R. capsulatus (-)	81%	2018	
	700	70	180	*E. coli* (-)	59%	2018	
				R. capsulatus (-)	82%	2018	
	1200	100	280	*E. coli* (-)	42%	2018	
				R. capsulatus (-)	82%	2018	
	3600	220	380	*E. coli* (-)	58%	2018	
				R. capsulatus (-)	83%	2018	
	2500	170	400	*E. coli* (-)	42%	2018	
				R. capsulatus (-)	84%	2018	
	4800	320	490	*E. coli* (-)	59%	2018	
				R. capsulatus (-)	82%	2018	
	6700	490	600	*E. coli* (-)	57%	2018	
				R. capsulatus (-)	80%	2018	
Ormostamp Polymer	250	80	130	*S. aureus* (+)	31%	2018	[58]
	200	80	130	*S. aureus* (+)	23%	2018	
	400	80	170	*S. aureus* (+)	100%	2018	
	200	80	170	*S. aureus* (+)	98%	2018	
	300	80	300	*S. aureus* (+)	26%	2018	
	150	80	300	*S. aureus* (+)	31%	2018	
PET	419	304	*	*K. pneumoniae* (-)	11%	2018	[59]
	456	280	*	*K. pneumoniae* (-)	15%	2018	
	529	193	*	*K. pneumoniae* (-)	14%	2018	
	419	304	*	*E. coli* (-)	10%	2018	
	456	280	*	*E. coli* (-)	11%	2018	
	529	193	*	*E. coli* (-)	16%	2018	
	352	54	*	*K. pneumoniae* (-)	18%	2018	
	388	33	*	*K. pneumoniae* (-)	27%	2018	
	498	22	*	*K. pneumoniae* (-)	30%	2018	
	352	54	*	*E. coli* (-)	22%	2018	
	388	33	*	*E. coli* (-)	24%	2018	
	498	22	*	*E. coli* (-)	28%	2018	
Black Silicon	500	30	*	*E. coli* (-)	20%	2018	[55]
	2500	100	*	*E. coli* (-)	25%	2018	
	20000	50	*	*E. coli* (-)	15%	2018	
PMMA	310	90	250	*S. aureus* (+)	52%	2018	[60]
				E. coli (-)	44%	2018	
				P. aeruginosa (-)	28%	2018	

* no value given, (-) Gram-negative bacterium, (+) Gram-positive bacterium

Table 1.5.5: Summary of Synthetic Bactericidal Surfaces developed and tested over the last decade. (continued from above)

Material	Feature Dimensions			Bactericidal Ability		Year	Ref.
	Height (nm)	Diameter (nm)	Pitch (nm)	Microorganism Tested	Reported Rate/Efficiency		
TiO2-PMMA	310	90	250	*S. aureus* (+)	87%	2018	
				E. coli (-)	87%	2018	
				P. aeruginosa (-)	89%	2018	
ZnO-PMMA	310	90	250	*S. aureus* (+)	90%	2018	
				E. coli (-)	80%	2018	
				P. aeruginosa (-)	54%	2018	
Silicon	8000	350	*	*E. coli* (-)	97%	2018	[61]
				S. aureus (+)	52%	2018	
Titanium	1800	70	*	*S. epidermidis* (+)	40%	2018	[62]
Aluminium	200	15	*	*E. coli* (-)	67%	2019	[63]
Copper	1000	15	*	*E. coli* (-)	28%	2019	
Black Diamond (F-terminated)	3000	300	*	*E. coli* (-)	50%	2019	[64]
Cellulose Acetate	300	50	500	*E. coli* (-)	70%	2019	[65]
				B. subtilis (+)	65%	2019	
Gold	103	45	120	*P. aeruginosa* (-)	53%	2019	[66]
	302	60	211	*P. aeruginosa* (-)	88%	2019	
	416	94	312	*P. aeruginosa* (-)	76%	2019	
	555	103	355	*P. aeruginosa* (-)	78%	2019	
PEEK	350	130	200	*E. coli* (-)	80%	2019	[67]
	330	50	260	*E. coli* (-)	78%	2019	
Titanium	1510	93	503	*S. aureus* (+)	12%	2019	[68]
	1510	93	503	*P. aeruginosa* (-)	32%	2019	
	1990	103	*	*S. aureus* (+)	36%	2019	
	2120	114	*	*S. aureus* (+)	4%	2019	
	2350	135	*	*S. aureus* (+)	12%	2019	
	3510	158	*	*S. aureus* (+)	68%	2019	
	1990	103	*	*P. aeruginosa* (-)	68%	2019	
	2120	114	*	*P. aeruginosa* (-)	68%	2019	
	2350	135	*	*P. aeruginosa* (-)	88%	2019	
	3510	158	*	*P. aeruginosa* (-)	76%	2019	
PMMA	1000	1000	500	*S. mutans* (+)	45%	2020	[69]
				E. faecalis (+)	20%	2020	
	1400	1000	500	*S. mutans* (+)	55%	2020	
				E. faecalis (+)	15%	2020	
	2200	1000	500	*S. mutans* (+)	55%	2020	
				E. faecalis (+)	15%	2020	
PDMS	214	270	486	*E. coli* (-)	23%	2020	[70]
				S. aureus (+)	10%	2020	
	803	378	1087	*E. coli* (-)	6%	2020	
poly(ethylene glycol diacrylate)	437	188	277	*E. coli* (-)	25%	2020	[71]
	478	186	358	*E. coli* (-)	79%	2020	
	429	199	525	*E. coli* (-)	60%	2020	

* no value given, (-) Gram-negative bacterium, (+) Gram-positive bacterium

Table 1.5.6: Summary of Synthetic Bactericidal Surfaces developed and tested over the last decade. (continued from above)

Material	Feature Dimensions			Bactericidal Ability		Year	Ref.
	Height (nm)	Diameter (nm)	Pitch (nm)	Microorganism Tested	Reported Rate/Efficiency		
Polycarbonate	227	60	169	*E. coli* (-)	93%	2020	[72]
	307	45	170	*E. coli* (-)	98%	2020	
	149	56	175	*E. coli* (-)	3%	2020	
	422	50	176	*E. coli* (-)	97%	2020	
ZnO	717	20	118	*E. coli* (-)	95%	2020	[73]
				MRSA	69%	2020	
Acrylic	60	35	60	*S. aureus* (+)	50%	2021	[74]
	60	30	60	*S. aureus* (+)	75%	2021	
	60	35	60	*P. aeruginosa* (-)	80%	2021	
	60	30	60	*P. aeruginosa* (-)	80%	2021	
Nylon	80	40	60	*S. aureus* (+)	75%	2021	
				P. aeruginosa (-)	65%	2021	
PET	60	40	60	*S. aureus* (+)	18%	2021	
				P. aeruginosa (-)	15%	2021	
PP				*S. aureus* (+)	28%	2021	
				P. aeruginosa (-)	80%	2021	

* no value given, (-) Gram-negative bacterium, (+) Gram-positive bacterium

Titanium-based nanostructures are also commonly reported in the literature and can be split into two categories - pure titanium surfaces [48, 54, 68] and titanium dioxide (TiO_2) surfaces [44, 51, 75]. Pure titanium nanostructures are fabricated in a similar way to bSi, using RIE with a chlorine plasma to create the surface structures. In contrast, TiO_2 nanostructures are formed on the surface of titanium using a thermal oxidation process, whereby titanium discs are heated to very high temperatures ($\sim$850^{o}C) before passing an acetone vapour over them. Both types of titanium NSS have features which are similar to the bSi, in that they are high aspect ratio (>10) and are formed in random arrays. Hasan *et al.* produced titanium nanostructures that were $\sim$1 µm tall and only 80 nm in diameter, giving an extremely high aspect ratio [54]. After 4 hr of incubation on the nanostructured titanium surfaces they found that 95% of *E. coli*, 98% of *P. aeruginosa* and 22% of *S. aureus* cells had been killed. Additionally, materials which are already known to possess antibacterial properties, such as copper, have been used to create nanostructured surfaces. Reed *et al.* showed that by nano-texturing copper, the bactericidal properties against *E. coli* were slightly enhanced compared to bare copper [63].

1.5.2. Organic Materials

The majority of NSS reported in the literature are made from inorganic materials. Some of these materials, most notably TiO_2, have been shown to have photoactive properties, whereby Reactive Oxygen Species (ROS) are produced by photolysis [76]. The chemical effects of these ROS could possibly enhance the bactericidal properties of these surface, meaning that they are no longer purely mechanical killing systems. Additionally, the production methods and mechanical properties of these inorganic NSS make them hard to scale up and difficult to incorporate in existing medical devices where softness of the material is a key requirement. Pure polymer systems, on the other hand, are generally more chemically inert and can be mechanically tuned to fit the requirements of the antibacterial surface. There are some reports of NSS made from organic materials such as PMMA [46], PET [59], polycarbonate [72] and cellulose acetate [65]. The main methods currently described to make these surfaces will be presented here.

Nanoimprint Lithography/Hot Embossing

The primary method of producing NSS from polymer material in the literature is through a process of nanoimprint lithography (NIL)/hot embossing. This technique imprints a polymer with nanostructures under pressure and temperature using a master template (illustrated in Figure 1.5.1). Firstly, a polymer film is cast onto a substrate (typically with spin-coating), with a thickness >> the depth of the holes on the template. Then, the polymer film is heated well above its glass transition temperature (T_g), in order to give it free flowing, rubbery properties, before the master mould/template is pressed upon it at high pressure ($\sim 5\,\mathrm{MPa}$). The polymer is then cooled back below its T_g to put it back into a glassy state before the mould is removed, leaving behind nanopillars in the shape of the holes on the mould.

Dickson *et al.* demonstrated this technique using a series of moulds to imprint nanopillars in the surface of PMMA [46]. Three different moulds were used for this - a commercial silicon stamp, a commercial nickel stamp and a PDMS stamp taken from an imprint of the cicada wing. They found that good replication of all of the stamps were achieved, with the nanopillars on the PMMA surface closely matching the dimensions of the holes on the stamps. Testing the PMMA NSS against *E. coli* showed 22% of cells killed by the surface based on the cicada wing features. More recently this technique was used to great effect by Linklater *et al.* who imprinted several polymer films (PET, PP, nylon) with 60 nm tall nanostructures using an alumina template [74]. They found that these surfaces

were able to kill up to 80% of *P. aeruginosa* and *S. aureus* cells after 18 hr of incubation.

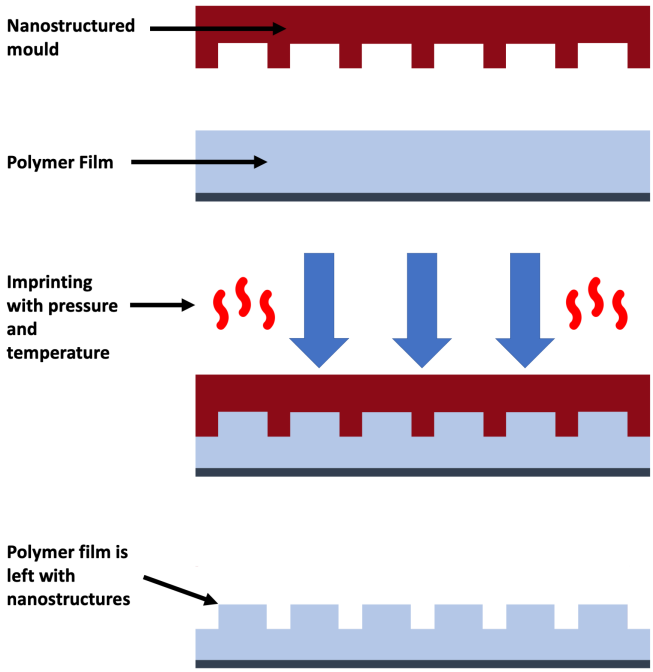


Figure 1.5.1: Process of hot embossing/nanoimprint lithography to create structure polymers. A structured mould/template is pressed into a polymer film with pressure and temperature. Once the film is cooled and the mould removed, the polymer is left with nanostructures.

Overall, NIL is a simple technique that allows for high resolution fabrication of nanostructured polymer surfaces. It is compatible with an array of thermoplastic polymers, meaning that a wide range of surfaces with different properties can be formed. There is also the opportunity with NIL to use roll-to-roll processing to create very large area patterned surfaces, which makes it highly attractive when considering how to scale NSS for use in medical devices.

Colloidal Lithography/Nanosphere Lithography

Colloidal Lithography or Nanosphere Lithography (NSL) is a technique by which nanospheres (typically made from polystyrene (PS)) are applied in a monolayer to a polymer film, and then used as a mask to etch (with a plasma) pillars in that film [77] (illustrated in Figure 4.3.1). Nowlin and LeJeunesse described how this technique could be used to create nanostructures on the surface of PET films, by coating them with a layer of polystyrene colloids before etching with RIE [77]. The colloids, when deposited in a good monolayer, pack in a hexagonal order which gives the resulting nanopillars in the film the same pattern (which is similar to the features on the cicada wing). NSL allows for

the tuning of nanopillar height and spacing without the need for several master moulds, although large area patterning is difficult.

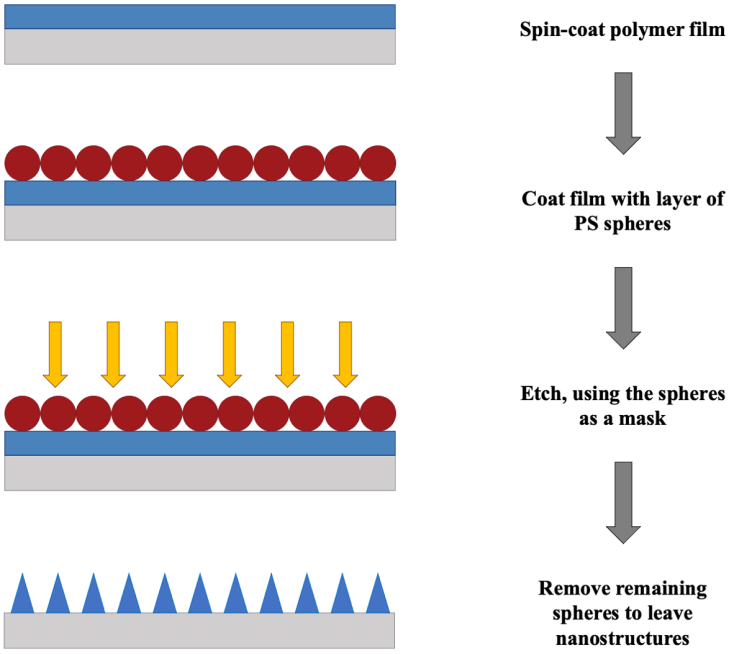


Figure 1.5.2: Process of using Nanosphere Lithography to make polymer NSS, highlighting the deposition of the nanosphere monolayer to be used as a mask for etching nanostructures into the base polymer. Adapted from [78].

Hazell *et al.* used this NSL technique to create nanopillars, ranging from 350-530 nm in height, in the surface of a PET film [59]. They reported that changing etching time with O_2 RIE decreased the width of the features and increased their height. By using colloids of two sizes (500 nm and 200 nm) they were able to create NSS with two different spacings (corresponding to the colloid diameter). Testing the surfaces against *E. coli* revealed that the denser nanopillars (200 nm spacing) and those with the highest aspect ratio (longer etch time) were able to kill the higher percentage of bacteria. Mo *et al.* recently showed how NSL could be used with argon and oxygen plasma to produce nanopillar and nanocone shaped features in polyetheretherketone (PEEK), a material commonly used to make catheter tubing. It was shown that both these polymer NSS morphologies were capable of killing *E. coli* with up to 80% efficiency after 3 h of incubation, with the nanocones achieving up to 90% killing after 24 h [79].

NSL is a good technique for producing nanostructured polymers and is able to alter the feature size easily, through either changing the size of the colloid or changing the etch

time. This makes it a useful technique for testing which parameters have the greatest impact on bactericidal efficiency, although the difficulty in coating large areas with the colloids would prevent it from being used at scale.

1.5.3. Summary

The bactericidal efficiencies achieved by the synthetic NSS often far exceed those of the natural NSS, such as the cicada wing. This is an indication that the natural surfaces do not have the optimal parameters for killing and that, by engineering NSS to have different feature parameters, it is possible to push this efficiency to a range where it would become useful as an antibacterial product. However, as Figure 1.5.3 shows, the overall efficiency of the synthetic NSS produced in the literature has not significantly increased year-on-year. This shows that there is still a lack of total understanding of the factors that influence the bactericidal efficiency, along with how the bacteria are inactivated by the NSS. By fully understanding this process, it may be possible to create antibacterial NSS which rival the killing ability of chemical antibacterials for a wide range of clinically-relevant micro-organisms.

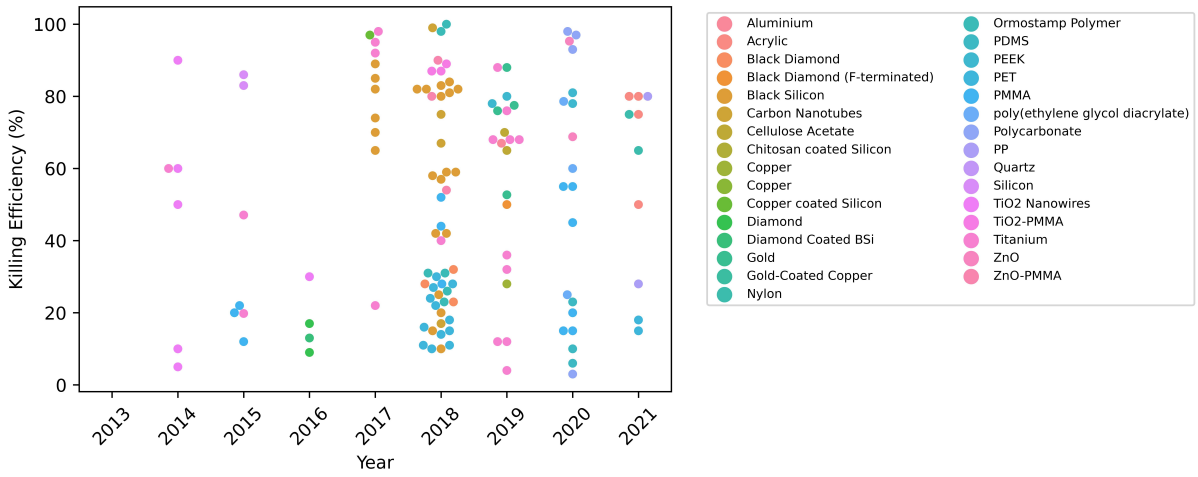


Figure 1.5.3: Literature Survey of Synthetic NSS Killing Efficiency per Year

1.6. Bactericidal Mechanism of Nanostructured Surfaces

Whilst there has been a number of studies demonstrating the antibacterial properties of various NSS, the underlying mechanism which causes the inactivation of the bacteria

has remained somewhat elusive. In the work that first demonstrated the antibacterial effects of the cicada wing, Ivanova *et al.* suggested that the bacteria *P. aeruginosa* were mechanically inactivated due to direct penetration by the surface nanopillars [11]. Whilst the piercing of the bacterial membrane by nanopillars has been seen in several studies, it is now believed that the bactericidal mechanism is more subtle than this. Several alternative theories have since been presented which propose different mechanisms by which the NSS kill bacteria, which will be discussed in this section.

1.6.1. "Stretching" Mechanism

One of the first theories for the bactericidal mechanism of NSS used a theoretical, biophysical approach to explain the interactions between the bacterial cell wall and the nanostructures. The model by Pogodin *et al.* describes the cell envelope as a thin elastic sheet, which experiences an increase in surface area as it comes into contact with the surface nanostructures [80]. In this case, the forces causing the attraction between the bacteria and the surface are kept generic. Once the bacterium has adsorbed to the nanopillars, there is an increase in the total area of the bacterial membrane and therefore an associated stretching degree, α. If α exceeds a critical value, which is set by elasticity of the membrane and the density of contact points of the nanopillars, then the membrane will rupture, resulting in a loss of turgor pressure and the death of the bacterium. It was also predicted through this model that the bacterial membrane would rupture in the areas *between* the pillars first, rather than directly at the nanopillar adsorption sites (shown in Figure 1.6.1), which defines this as cell membrane stretching rather than puncture. Later studies by Xue *et al.* [81] and Li [82] provided further additions to the theoretical "stretching" model, and described how changing the parameters of the nanopillars could alter the stretching degree of the membrane. Again, these models are based on the change in free energy of the membrane after adsorption onto the nanopillars. Overall, the stretching theory makes some predictions about the optimal conditions for bacteria to be killed on NSS. Firstly, because the degree of stretching is dependant on the membrane stiffness (with stiffer membranes experiencing less stretching) it is predicted that gram-positive bacteria (whose cell wall is thicker and therefore stronger) would be less likely to be ruptured and killed on NSS. This prediction is borne out in the data taken by Pogodin *et al.* and in subsequent studies, which finds that gram-positive bacteria are killed less effectively than gram-negative bacteria by the same surface [14, 37, 80].

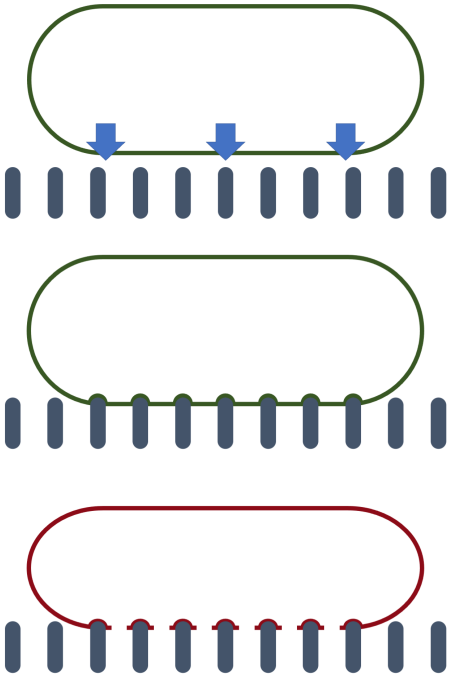


Figure 1.6.1: "Stretching" Theory of Bacterial Killing on NSS [80]. Bacteria adsorbs to the nanopillars and consequently experiences an increase in its surface area, which causes critical stretching of the membrane.

1.6.2. Alternative Mechanisms

Another of the early theories as to the mechanism of death on NSS came from Bandara *et al.*, who used their experimental findings from a study of *E. coli* death on dragonfly wings [41]. They used Helium Ion Microscopy (HIM), which has been shown to be a useful technique for imaging biological samples at high resolution without the need for a conductive coating [83], to image the interaction between the *E. coli* cells and the nanopillars on the dragonfly wing. It was reported that the bacteria strongly adhered to the nanopillars with a combination of EPS and "finger-like extensions" from the bacterium itself. It was then suggested that if these adhered bacteria face "non-favourable conditions at the interface between the membrane and the nanopillars", they may try to move away from the surface and in doing so, create large shear forces which results in membrane damage and cell death. This theory was disputed by Linklater *et al.*, who claimed that the bacteria would be killed far too quickly on the NSS for them to be able to produce EPS [84]. They also used Focussed Ion Beam (FIB) milling to make cross-sections of the bacteria interacting with the nanopillars and imaged with SEM, claiming to show the bacterial membrane stretching over the nanopillars. Several subsequent studies (both theoretical and experimental) have added to the theory that once the bacteria have bound to the

nanopillars, it is critical stretching of their membrane that causes bacterial death [85–89].

However there is also increasing evidence that other factors may be involved in the killing process. Köller *et al.* reported that *E. coli* cells whose growth had been halted were less susceptible to killing by titanium NSS, leading to the conclusion that the growth cycle of the cells plays a role in the bactericidal mechanism [90]. Jenkins *et al.* and Sorzabal-Bellido *et al.* also found evidence through SEM that bacterial growth can become impeded due the presence of the nanostructures [75, 91]. Additionally, Jenkins *et al.* reported that, whilst deformation of the *E. coli* membrane was seen on TiO_2 NSS, no mechanical rupture or lysis was found. They also carried out proteomic analysis of the bacteria after incubation on the NSS and found that there was a significant up-shift in expression of proteins related to oxidative stress. It was proposed that the bacteria produce Reactive Oxygen Species (ROS) (such as H_2O_2) in response to the stress associated with the NSS, which could contribute to the cell death [75].

Whilst it may be the rupturing of the bacterial envelope that ultimately leads to cell death on NSS, it is increasingly clear that other factors may be involved that enhance the killing. Several studies have noted the possibility of multiple mechanisms [57, 75, 85, 92], with the route to bacterial death dependent on the type and parameters of the surface. For example, Michalska *et al.* suggested that blunt-ended nanopillars may kill bacteria via a different route to sharp-ended pillars [57]. Therefore, understanding the role that each of these parameters plays in the bactericidal efficiency of NSS could provide great insight into how bacteria are killed.

1.7. Factors Influencing Bactericidal Efficiency

There have been many systematic studies carried out with the aim of finding which factors have the greatest influence on the bactericidal efficiency of NSS. Broadly these can be split into investigations into the parameters of the NSS and investigations into the bacterial characteristics. Examples of both are discussed below.

1.7.1. Nanostructured Surface Characteristics

Predictions about which surface parameters would create the highest degree of killing for NSS first came from Xue *et al.* and Li, with their theoretical models of the "stretching" theory [81, 82]. Xue *et al.* predicted that narrower and more widely spread nanopillars

would cause the greatest degree of membrane stretching, and therefore cell death. The model by Li predicts that the largest amount of membrane stretching comes when:

- The density of nanopillars increases - the effect of this increase is small for densities exceeding 40 pillars/μm^2.
- The height of the nanopillars increases - the effect of this increase is small for heights above $\sim$ 200 nm.
- The radius of the nanopillars increases - the effect of this increase is small for radii above $\sim$ 20 nm.
- The adhesion energy between the surface and the bacteria is increased (i.e. stronger adsorption onto the pillars)

Recent modelling by Maleki *et al.* determined that reducing the spacing of the nanopillars had the greatest impact on killing of gram-positive bacteria, and increasing the aspect ratio of the nanopillars contributed to more death of gram-negative bacteria. Experimentally, there have also been several studies which vary the parameters of the nanostructured surfaces (height, diameter, spacing of pillars) to investigate the effect on bactericidal efficiency.

Nanopillar Spacing/Density

Dickson *et al.* fabricated PMMA NSS using NIL with feature spacings of 100, 130 and 380 nm. They found that the percentage of *E. coli* killed on the surfaces increased with decreasing feature spacing (higher spatial density), with 22% killed on the 100 nm spacing and only 12% killed on the 380 nm spacing [46]. Similarly, Hazell *et al.* found that decreasing the spacing of PET nanocones from 500 nm to 200 nm increased their ability to kill *E. coli*, with up to 16% and 30% killed on the different spacings. However, Michalska *et al.* showed that the mostly densely-packed surfaces displayed the lowest levels of killing [57]. They created micron-length bSi features using RIE, and changed the etch time to give a range of surface topographies. For example, a 1.5 min etch gave a feature density of 26 μm^{-2} whereas a 30 min etch gave a density of 2 μm^{-2}. They found that for pillars <3 μm in height, the highest density of features (26 μm^{-2}) actually killed the lowest percentage of *E. coli* cells. However, the changing density also changed the height of the nanopillars which may also effect the killing efficiency. Later, Wu *et al.* found that the optimum density of polymer nanopillars for killing *S. aureus* was $\sim$40 features/μm^2 (98-100% killing) and that there was a significant reduction in killing ability

for < 20 features/μm^2 (26-31%) and > 60 features/μm^2 (23-31%) [58]. Again, the feature height was not kept constant, but in this case there was no correlation found between the height and the bactericidal efficiency. Recently, Linklater *et al.* carried out a study on the killing effect of NSS made from various polymers using NIL. They produced nylon NSS of a fixed aspect ratio, with spacings of 60, 100 and 200 nm, and tested the killing ability against both *P. aeruginosa* and *S. aureus* after 18 h of incubation. It was found that against the *P. aeruginosa*, the killing efficiency increased with decreasing spacing, whereas for the *S. aureus*, the killing efficiency was the highest for the smallest and largest spacing (summarised in Table 1.7.7) [74]. The key basis for the link between the pillar spacing and the bactericidal ability is the number of contact points between the surface and the bacteria. As the feature density increases, the number of pillars in contact with the bacterial envelope increases, therefore exerting more stress. However, as this density reaches very high values this stress actually reduces, as neighbouring pillars begin to take the load - much like how a bed of nails works.

Table 1.7.7: Summary of results testing the spacing against killing efficiency by Linklater et al. [74].

Spacing (nm)	Bactericidal Efficiency (%)	
	P. aeruginosa	*S. aureus*
60	90	40
100	60	20
200	35	40

Nanopillar Height

The height of the nanopillars has also been linked to the bactericidal efficiency, with Cui *et al.* finding an enhanced bactericidal efficiency of polycarbonate nanopillars with increasing height [72]. They created the NSS using NIL to have feature spacing of 170 nm heights of 150, 200, 300, and 400 nm. Only the NSS with feature heights >150 nm were able to kill more *E. coli* than the control surface, with 3% killed on the 150 nm and ∼90% killed on the rest of the surfaces. This indicates that there may be some minimum height of nanopillar required in order to create enough stress on the bacteria in order to kill it. This has also been proposed previously through theoretical models by Watson *et al.* [85]. Hazell *et al.* created a series of bSi and black diamond surfaces with short (0.5 - 1 μm), medium (2.5 - 3 μm) and tall (18 - 20 μm) features. The killing efficiency of both materials against *E. coli* was the highest for the medium length pillars, with the long pillars having the lowest levels of killing [55]. More recently, Linklater *et al.* incubated *S.*

aureus and *P. aeruginosa* on nylon NSS with a range of pillar heights and then did SEM analysis to look at the interaction [74]. They saw minimal cell envelope disturbance for both bacteria on the surfaces with 30 nm tall nanopillars. However, for the 120 nm pillars there was evidence of significant disturbance to the bacteria, which was further enhanced on the 220 nm pillars. This indicates that taller nanopillars are capable of inflicting more damage to the bacterial envelope.

Nanopillar Diameter

Investigating the effect of the nanopillar diameter on bactericidal efficiency, Hazell *et al.* found that PET nanocones with narrower tips killed a greater proportion of *E. coli*. Nanocones with a tip diameter of ∼300 nm killed ∼10% of *E. coli*, whereas those with a tip diameter of ∼20 nm killed > 20%. The study by Dickson *et al.* on PMMA NSS also found that reducing the width of the features from 215 nm to 70 nm gave an increase in killing of *E. coli* from 12% to 22%. Kelleher *et al.* investigated the killing effects of three different cicada species with different surface topographies (given in Table 1.4.2). Of the three species, the one with the narrowest features had the greatest bactericidal efficiency against *P. fluorescens* [38]. Overall, the literature generally suggests that nanopillars with a smaller diameter lead to higher killing efficiencies for NSS as they can provide a higher degree of curvature to the bacterial envelope, therefore imparting more stress.

Summary

It is obvious throughout the literature that is no overall consensus on the optimal feature parameters for antibacterial NSS, and there are many contradictions across the different studies. When looking at the results from the literature as a whole, the picture becomes even less clear. Figure 1.7.1 shows the reported bactericidal efficiency for a range of surfaces with different heights, diameters, and spacings (pitch). There is no clear relationship to the killing efficiency for any of these parameters, with only the pitch showing a slight trend (in that closer spaced/more densely packed pillars generally kill more bacteria). The key reason for this is that, for most of the studies, more than one parameter of the surfaces is varied at once making it difficult to dissect the effects of each. An additional complication is the lack of standardised testing for antibacterial NSS. Most of the experimental studies in the literature incubated the bacteria on the NSS in differing conditions (e.g. different buffers or media, different temperature etc.) and for different lengths of time. These factors could greatly impact the reported bactericidal efficiency of these surface and make it hard to compare the results of different studies.

There is also no standard bacterial strain chosen to test these surfaces which also makes the comparisons difficult, as it is possible that different strains are killed with various efficiencies. These differences in optimal parameters for different surface materials could also be more evidence that there are multiple mechanisms of killing by NSS - if there are different bactericidal mechanisms then it is likely that the "optimal" parameters are different for each process.

1.7.2. Bacterial Characteristics

Whilst there has been much work focussed on the optimal parameters for the NSS, relatively little work has been carried out into which bacterial characteristics make them the most susceptible to killing. Early work by Hasan *et al.* established that, unlike gram-negative bacteria, gram-positive cells were not killed by the structures on the cicada wing. This was attributed to the increase in thickness and stiffness of the gram-positive cell wall [37]. In this study it was also noted that the shape of the bacteria (rod vs. cocci) had no effect on how easily they were killed. The effect of the growth phase of bacteria on the amount of bacteria killed by NSS was carried out by Truong *et al.*, who grew both *S. aureus* and *P. aeruginosa* to different points in their growth curve before assessing how well they were killed by a nanostructured damselfly wing. They found that both strains were killed in the highest amounts in the early stages of their development (1 hr of growth) and late into stationary phase (24 hr of growth). The least killing was found in the intermediate stages of growth (6-18 hr). This was attributed to the differences in cell wall structure at each growth stage, with the cell wall in the early stages of growth undergoing lots of remodelling, making it more susceptible to the NSS [40]. Köller *et al.* made the link between the growth rate of *E. coli* and how well they were killed on nanostructured titanium, finding that if the growth was arrested, the percentage of dead cells on the surfaces decreased [90]. The adhesion and motility of micro-organisms on NSS has also been attributed to increasing bactericidal efficiency. Nowlin *et al.* showed that yeast cells (*S. cerevisiae*) that had stronger adhesion to surfaces were killed in greater amounts by NSS [39]. Additionally, Jindai *et al.* found that *E. coli* strains with higher motility were killed faster by silicon nanospikes [93]. Whilst these results are presented in the context of the "stretching" theory of bacterial death, the influence of factors such as motility and growth indicate that stretching may not be the full story.

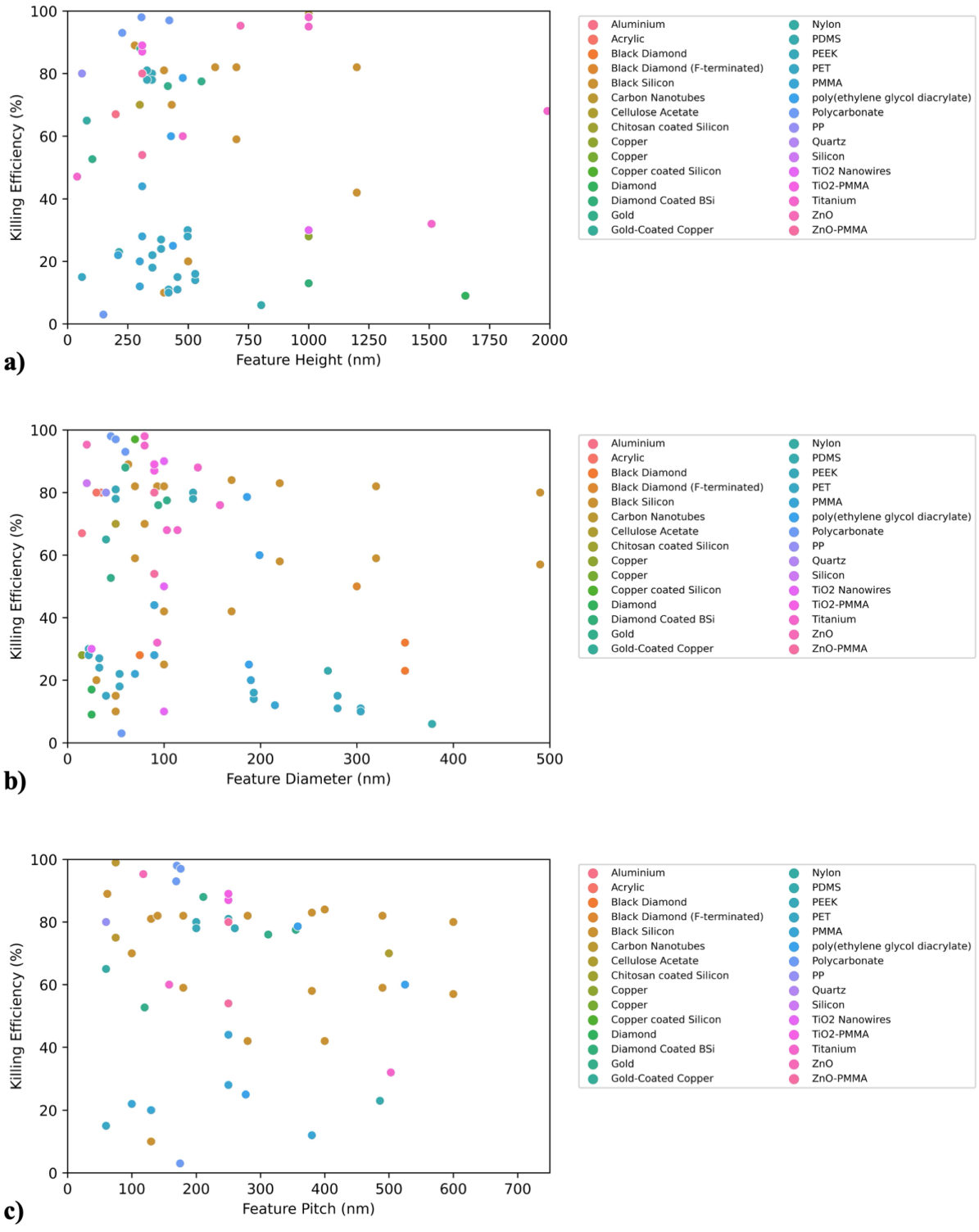


Figure 1.7.1: Data obtained from a literature survey to find the factors that influence the bactericidal efficiency of NSS. The nanopillar dimensions that were investigated were a) their height, b) their diameter, and c) their pitch. Data used is also summarised in Tables 1.5.3-1.5.6.

1.8. Summary

Overall, there has been many investigations into the antibacterial effects of NSS and they have been successfully fabricated from a range of synthetic materials. However, currently these materials are mainly inorganic, hard materials and there is lack of research into organic, polymer materials whose properties may be more appropriate when considering the potential use of these surface in medical devices. Additionally, pure polymer materials have no known "chemical" antibacterial effects and so provide a much cleaner system in which to investigate the bactericidal mechanism of NSS. There have also been numerous investigations into the factors which affect the bactericidal efficiency of NSS, especially regarding the topography of the surfaces. However, the lack of standardised testing procedures and the fact that multiple feature parameters are often changed at once, makes drawing meaningful conclusions from these studies difficult. Whilst the "stretching" theory of bacterial death on NSS remains dominant, recently there have been studies which have suggested that other factors may be at play in the bactericidal mechanism. However, without real-time imaging of the bacteria-nanopillar interaction, it is difficult to truly understand this mechanism. The remainder of this thesis will focus on the experimental work carried out during this project.

Chapter 2

Experimental Techniques

In this chapter, the experimental techniques that were used to characterise the NSS and subsequently test their bactericidal efficiency are discussed. Due to the nano-scale dimensions of the features, techniques such as AFM and SEM are vital as they can achieve the resolution required to visualise the surfaces. Live/Dead stain assessment of bacterial viability is also a key tool in determining the ability of the NSS to kill bacteria.

2.1. Atomic Force Microscopy

Atomic Force Microscopy (AFM) is a scanning probe microscopy technique invented by Gerd Binnig and Heinrich Rohrer in 1985 [94], who both won the Nobel Prize in 1986 for his work. AFM is an invaluable technique when studying samples or surfaces with nanoscale features and requires relatively little sample preparation to achieve high resolution images. Conventional light microscopy is limited in resolution by the diffraction of light, according to equation 2.1, where λ is the wavelength of light and NA is the numerical aperture of the objective lens. Thus, the resolution improves with decreasing illumination wavelength, but is typically no better than $\approx 200\,\text{nm}$.

$$d = \frac{\lambda}{2\ \text{NA}} \tag{2.1}$$

Rather than using light, AFM images samples by "feeling" their surface with an sharp probe on a flexible cantilever. This allows resolutions far better than the optical diffraction limit to be achieved, with atomic-resolution imaging of graphite and silicon previously demonstrated [95, 96].

2.1.1. Contact Mode AFM

In the most basic mode of operation (contact or constant-force mode), the flexible cantilever probe is moved down into contact with the surface, where it bends in response to the repulsive van der Waals forces between the tip and the surface. This bending is detected by a laser which reflects off the back surface of the cantilever and onto a split photo-detector (illustrated by Figure 2.1.1). As the cantilever moves across the surface, a piezoelectric motor driven by a feedback loop ensures that the deflection of the cantilever remains at a set value by making fine adjustments in its height in response to the topography. The position of the z-piezo during scanning is used to build up the height profile across an area [97]. In ambient conditions a thin layer of water condensation often builds up on the sample surface which creates a capillary force with the AFM tip as it is brought into contact. This water capillary layer increases the forces that are imparted on both the cantilever and the sample. Due to the constant contact between the AFM tip and the surface, this can result in high forces being applied to the sample resulting in artefacts and damage to soft or delicate samples.

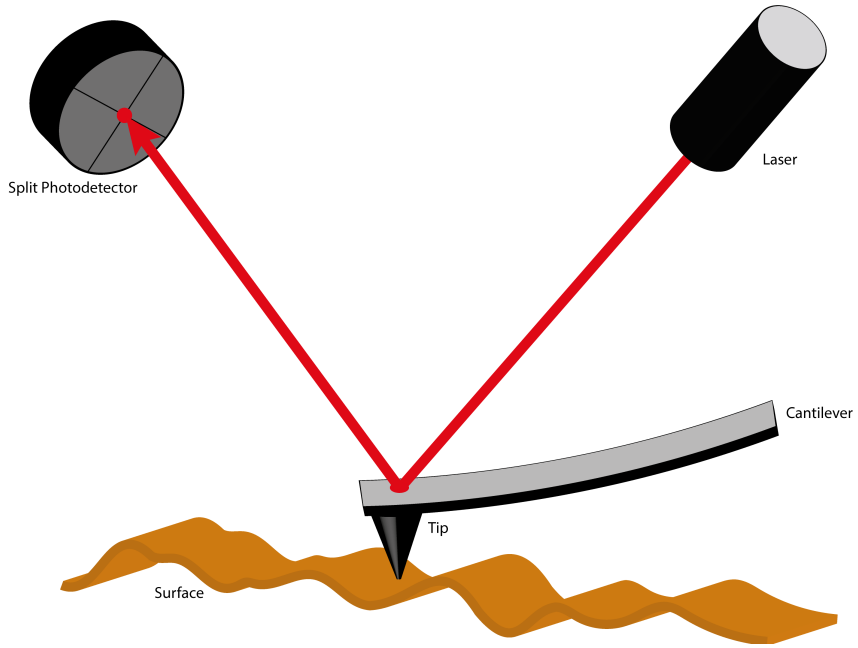


Figure 2.1.1: Schematic overview of the basic principal of AFM operation. Deflection of a flexible cantilever is detected by reflecting a laser onto a split photodiode. Adapted from [97, 98]

2.1.2. Tapping Mode AFM

Therefore, the most commonly used AFM mode when imaging soft samples is intermittent-contact or Tapping Mode, in which cantilever is driven to oscillate at near-resonance as it moves over the surface. Due to this oscillation, the cantilever is only briefly in contact with the surface before it moves away again, with the lateral movement of the cantilever across the sample taking place whilst it is not in contact. This greatly reduces the forces that are applied to the sample overall and makes it ideal for imaging soft samples which may be easily deformed or damaged. The topography map of the surface is acquired in Tapping Mode from the feedback loop which is maintaining the amplitude of oscillation at a constant value. As the cantilever approaches the sample the force from the interaction with the surface reduces the amplitude of the oscillation. The feedback loop associated with the z-piezo then alters the height of the cantilever in order to keep the oscillation amplitude at a pre-determined constant value. Again, it is the signal from this feedback loop which creates the height profile of the sample. The main advantage of Tapping Mode AFM is that the lateral forces applied to the sample are significantly reduced compared with contact mode, which results in less overall damage to the sample and better resolution for soft samples.

In this work, the samples are generally either biological, or soft organic polymers, so Tapping Mode AFM was the ideal choice to characterise their surfaces. A Veeco Dimension 3100 AFM in Tapping Mode equipped with either a NuNano Scout 350 cantilever (spring constant = $42\,\mathrm{N\,m^{-1}}$, resonant frequency = $350\,\mathrm{kHz}$), or TESPA-V2 cantilever (spring constant = $37\,\mathrm{N\,m^{-1}}$, resonant frequency = $320\,\mathrm{kHz}$) was used throughout for topographical characterisation of surfaces. Data analysis was carried out in the open-source SPM software Gwyddion [99]. When assessing the height of features on the NSS, the grain threshold feature of the software was utilised to select any part of the scan with a height greater than a set value (shown in Figure 2.1.2). Once this threshold was applied, the maximum height of each of the grains was found, which gave a measurement of the maximum height of the features on the NSS. The data for this height distribution was then exported for further analysis and visualisation in Python.

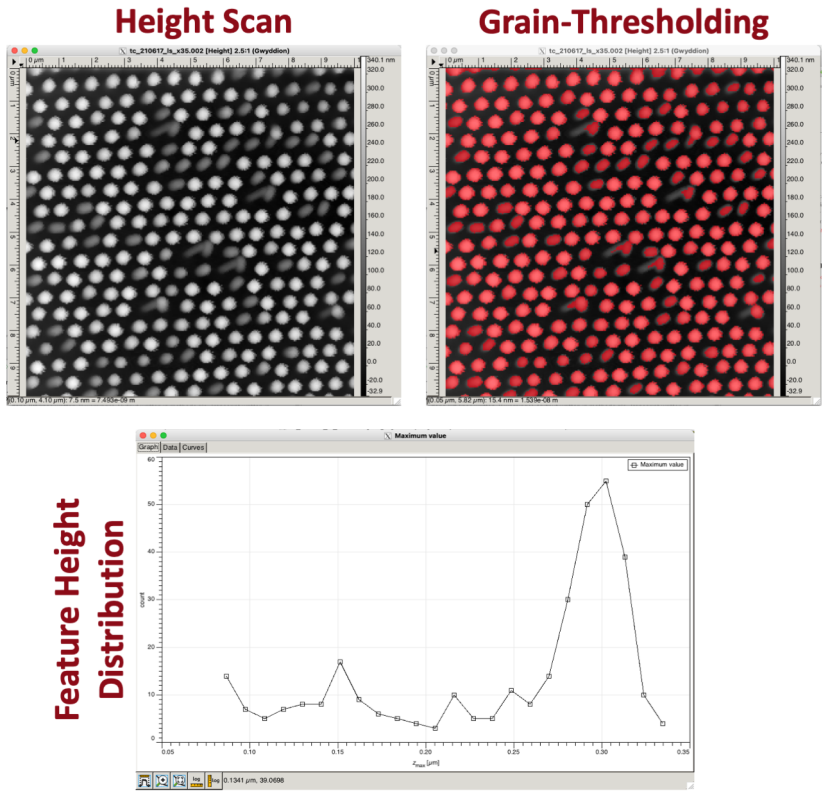


Figure 2.1.2: Grain analysis in Gwyddion to determine average feature height

2.1.3. PeakForce Tapping Mode

A relatively new development in AFM imaging has been PeakForce Tapping Mode (PFT). Simply, in PFT the cantilever is oscillated at well below its resonant frequency and brought close to the sample surface (which is immersed in liquid to reduce capillary forces). Once a set repulsive force is achieved the tip is moved away from the surface and onto the next point, with the feedback loop maintaining this set force. Each time the cantilever approaches the surface and then moves away, a force-distance curve is recorded, which occurs at a frequency of several every millisecond [100]. Therefore PFT is capable of producing high resolution imaging and force-volume mapping of the surface concurrently.

In this study PFT was used on a JPK Nanowizard III Bio AFM equipped with a FastScanD cantilever (nominal spring constant $0.25\,\mathrm{N\,m^{-1}}$, resonant frequency 110 kHz). The force curves were analysed using the JPK SPM analysis software [101]. Firstly a cantilever calibration was carried out which inputs the spring constant and sensitivity of the cantilever to convert the units of the force curve from volts into Newtons and metres. Next, the data is smoothed using the Gaussian method which removes the high-frequency

noise. Then a baseline subtraction is performed which removes any offset in the vertical deflection. This is achieved by averaging the deflection for the approach well above the sample and removing that value from all the data. The software then calculated the tip contact point and the tip-sample separation from this force curve. This pipeline is used to batch-process the (many) force curves which are produced in one scan and results in a final force curve which can be fit to find the Young's modulus (example shown in Figure. 2.1.3).

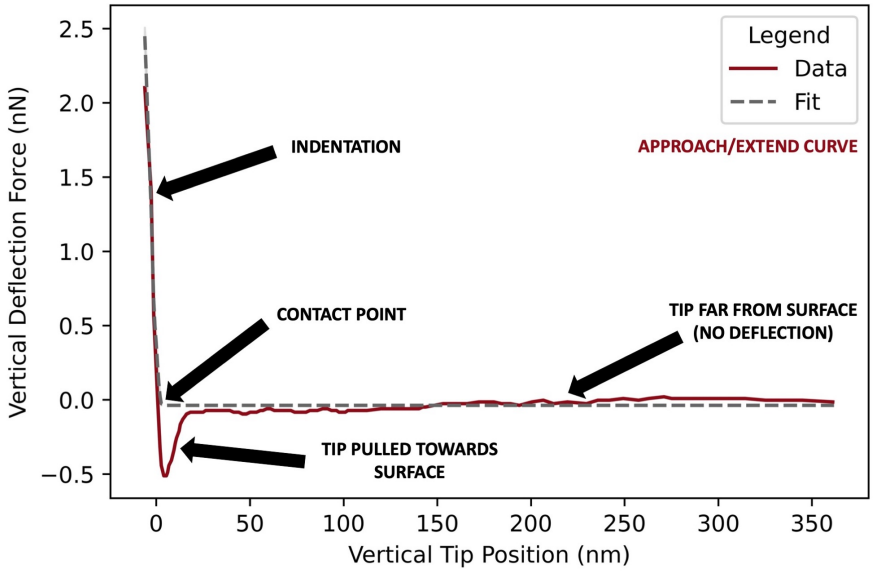


Figure 2.1.3: Force curve data (on approach) from a PFT measurement. An elasticity fit (Hertz model) has been applied to determine the Young's modulus from the slope of the indentation part of the curve.

In order to do this a elasticity fit was used which is based on a Hertz model. This model assumes that the sample is infinitely thick, homogeneous and elastic [101]. It also requires knowledge of the tip geometry and the shape and radius are required for the fit. The Hertz model for a parabolic tip is given by equation 2.2, where F is force, E is the Young's modulus, ν is the Poisson's ratio of the cantilever (typically 0.5), δ is the tip-sample separation and R_c is the radius of tip curvature.

$$F = \frac{E}{1-\nu^2}\frac{4\sqrt{R_c}}{3}\delta^{3/2} \tag{2.2}$$

This is fit to the indentation part of the curve and yields the Young's modulus. This is batch-processed to find the Young's modulus for each of the force curves taken across the sample.

2.2. Scanning Electron Microscopy

Scanning Electron Microscopy (SEM) is a type of electron microscopy technique often used in the analysis of surfaces. As with light microscopy, the resolution of SEM is limited by the diffraction equation (eq. 2.1), with the wavelength here given by the de Broglie wavelength (eq. 2.3), where h is Planck's constant, m is the electron mass, e is the electron charge and V is the accelerating voltage. Therefore, by using higher voltage electrons, it is possible to achieve better resolution, with a voltage of 10 keV resulting in a resolution of ~ 0.5 nm.

$$\lambda = \frac{h}{mv} = \frac{h}{\sqrt{2meV}} \tag{2.3}$$

In the most basic setup of SEM (illustrated in Figure 2.2.1), a very high current is passed through a filament (usually tungsten), providing a source of electrons. These electrons are directed at the sample by a grounded anode. As the electrons travel down the SEM chamber they pass through a series of "lenses", which in the case of electron microscopy are electromagnets, that collimate the beam and focus it onto the surface. The whole SEM chamber is kept under vacuum to aid the passage of the beam. Once the electrons impinge on the surface they undergo one of two interactions. Either they undergo elastic scattering from the sample and bounce back from the surface with little loss of energy, these are known as backscattered electrons and are picked up by a detector near to the source. The backscattered electrons do not provide great resolution, however they can be used to provide some chemical contrast, as the proportion of electrons which get backscattered depends on the atomic number of the elements in the sample [102]. A more useful interaction, in terms of resolution, is the secondary electrons. These are formed when the electron beam ionises the atoms on the sample surface. These are released with low energy and as such only travel a short distance ($\sim$ few nm) from the surface before they are collected by the secondary electron detector using an applied bias. Because of the low energy of the secondary electrons, not all of them reach the detector which creates contrast in the image with brighter areas due to high detection of electrons and darker areas fewer. This means that the secondary electron signal provides the most information about the topography and roughness of the samples [102].

Charge effects are one of the biggest factors effecting the image quality with SEM.

These occur when there is a build up of charge on the surface which creates artefacts such as increased brightness. For non-conductive samples this is prevented by first coating the sample in a conductive metal, typically gold, which helps the passage of electrons away from the surface and down the sample mount. Whilst increasing the accelerating voltage can improve the resolution, it can also lead to increased charge build up meaning there is a balance to be struck in order to achieve the best image quality. In this work a JEOL InTouchScope SEM was used throughout, and samples were prepared by sticking to conductive metal stubs with either carbon tape or silver paint and then coating with a thin layer of gold. Data analysis of images was carried out in the open source software FIJI [103].

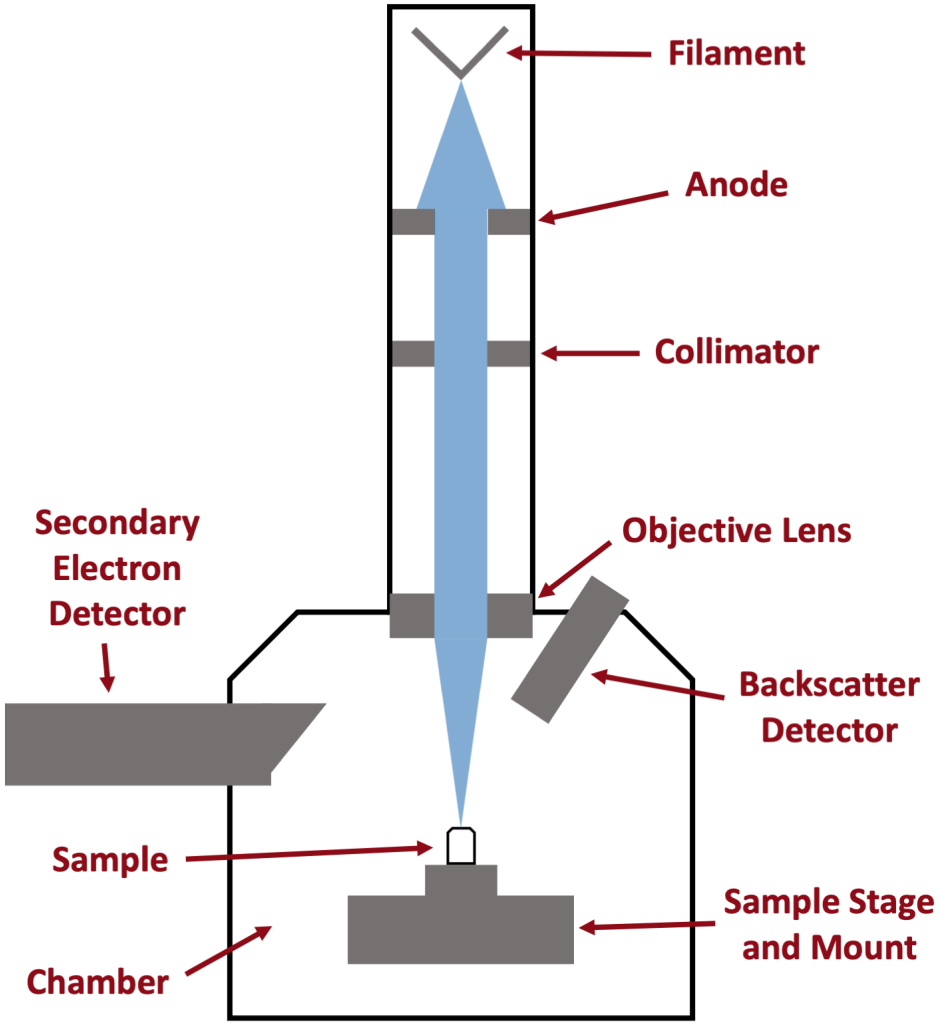


Figure 2.2.1: Schematic diagram of SEM. A tungsten filament is used to generate electrons which are collimated and focussed by a series of magnetic fields onto the sample. The electrons which return from the sample are detected by either the secondary electron or backscatter detector. Adapted from [102]

2.3. LIVE/DEAD Staining

In this work, the primary method of assessing the bactericidal efficiency of the nanostructured surfaces was using a Live/Dead stain combined with fluorescence microscopy. Live/Dead stains are a useful tool for assessing bacterial viability on NSS as they as indicate the proportion of the population of bacteria which adhere to the surface and are subsequently killed. This has the advantage over culture-based techniques such as Colony Forming Unit (CFU) counts which may be insensitive to surface killing, as the dead bacteria often remain adhered. Live/Dead stains can be assessed with fluorescence microscopy, flow cytometry, or fluorescence spectroscopy and is therefore used in a variety of assays. Throughout this work, the LIVE/DEAD BacLight Bacterial Viability Kit (L7012) was used in conjunction with a Nikon Widefield Microscope at the Wolfson Light Microscopy Facility. The BacLight LIVE/DEAD stain contains two components - SYTO 9 and Propidium Iodide (PI). SYTO 9 is a cell-permeant stain which can pass through the membrane of living cells and bind to nucleic acids. On the other hand, PI is cell-impermeant and can only bind to the nucleic acids of cell whose membrane is compromised. Once PI enters the cell it displaces the bound SYTO 9, significantly reducing the SYTO9 signal. Therefore, all of the live cells in the population are stained with the SYTO 9, and the dead cells (with compromised membranes) are stained with the PI (shown in Figure 2.3.1) [104].

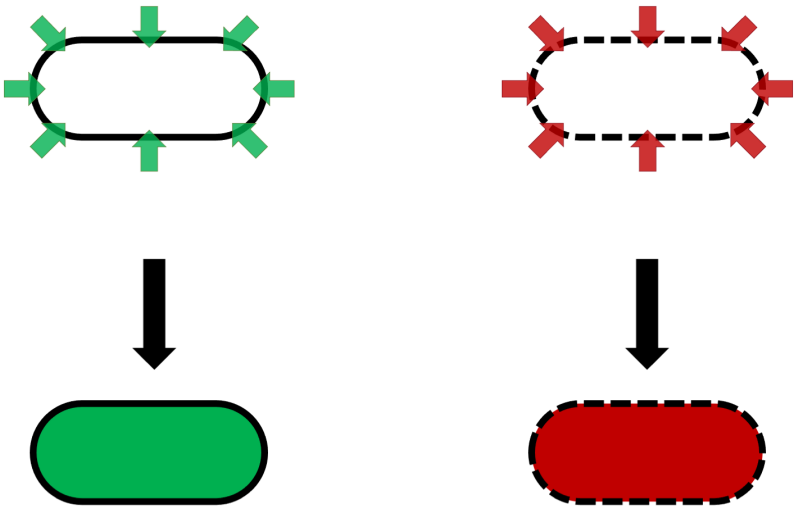


Figure 2.3.1: Illustration of the mechanism of LIVE/DEAD stain dyes. SYTO 9 (green) enters cells with intact membranes, whereas PI (red) only enters cells with compromised membranes.

2.3.1. Staining and Microscopy

In order to stain bacteria with the LIVE/DEAD kit a solution was prepared which was incubated on the test surfaces. The solution consisted of 1.5 µl SYTO 9 (3.34 mM) and 1.5 µl PI (20 mM) per 1 ml of buffer. 0.9% NaCl was used for the buffer as Phosphate-Buffered Saline (PBS) was found to interfere with the binding of the dye. The solution was then added to the test surfaces (NSS and controls) for 30 min in the dark. The PI stain enters the cells almost immediately, however the SYTO 9 takes longer to bind as it has to pass across the intact membranes. After this time the surfaces were rinsed to remove any unbound dye and then mounted on slides for imaging. A Nikon Ti Eclipse Widefield Fluorescence Microscope was used to image the surfaces and capture the emission of both stains. A FITC filter cube ($\lambda_{ex.}$ = 467 - 498 nm, $\lambda_{em.}$ = 513 - 556 nm) was used to capture the SYTO 9 and a TexasRed filter ($\lambda_{ex.}$ = 542 - 582 nm, $\lambda_{em.}$ = 604 - 644 nm) was used for the PI.

2.3.2. Image Analysis

Once a representative set of images were taken for the surfaces, the data was analysed with the open-source software FIJI [103] to determine the amount of cells stained with each dye. A summary of the image analysis process is shown in Figure 2.3.2. Each image is brought into the software and split into the separate SYTO 9 and PI channels. Any continuous background signal is removed with the "Subtract Background" feature, which improves the signal-to-noise ratio of the bacteria. The image is then converted to a binary (black and white) image, which normalises the intensity of the signal from the cells and improves their detection. The "Analyse Particles" tool is then used, which allows the counting of objects within a binary image. Firstly a filter is applied which excluded any objects which are either too big or small to be bacteria (these are usually dust or dirt that the stain has bound to) and then a separate filter excludes object based on the their "circularity". This allows any long streaks (which are usually scratches in the coverslip/NSS) to be excluded. Finally, a count of the number of objects remaining in each image is taken. The bacteria counted in the PI channel are considered to be the dead cells and the bacteria counted in the SYTO 9 channel and the live cells. Therefore the bactericidal efficiency can be calculated with eq. 2.4.

$$\%\ \text{Dead Bacteria} = \frac{\text{Dead Bacteria on Surface}}{\text{Total Bacteria on Surface}} = \frac{\text{PI Count}}{\text{SYTO 9 Count} + \text{PI Count}} \tag{2.4}$$

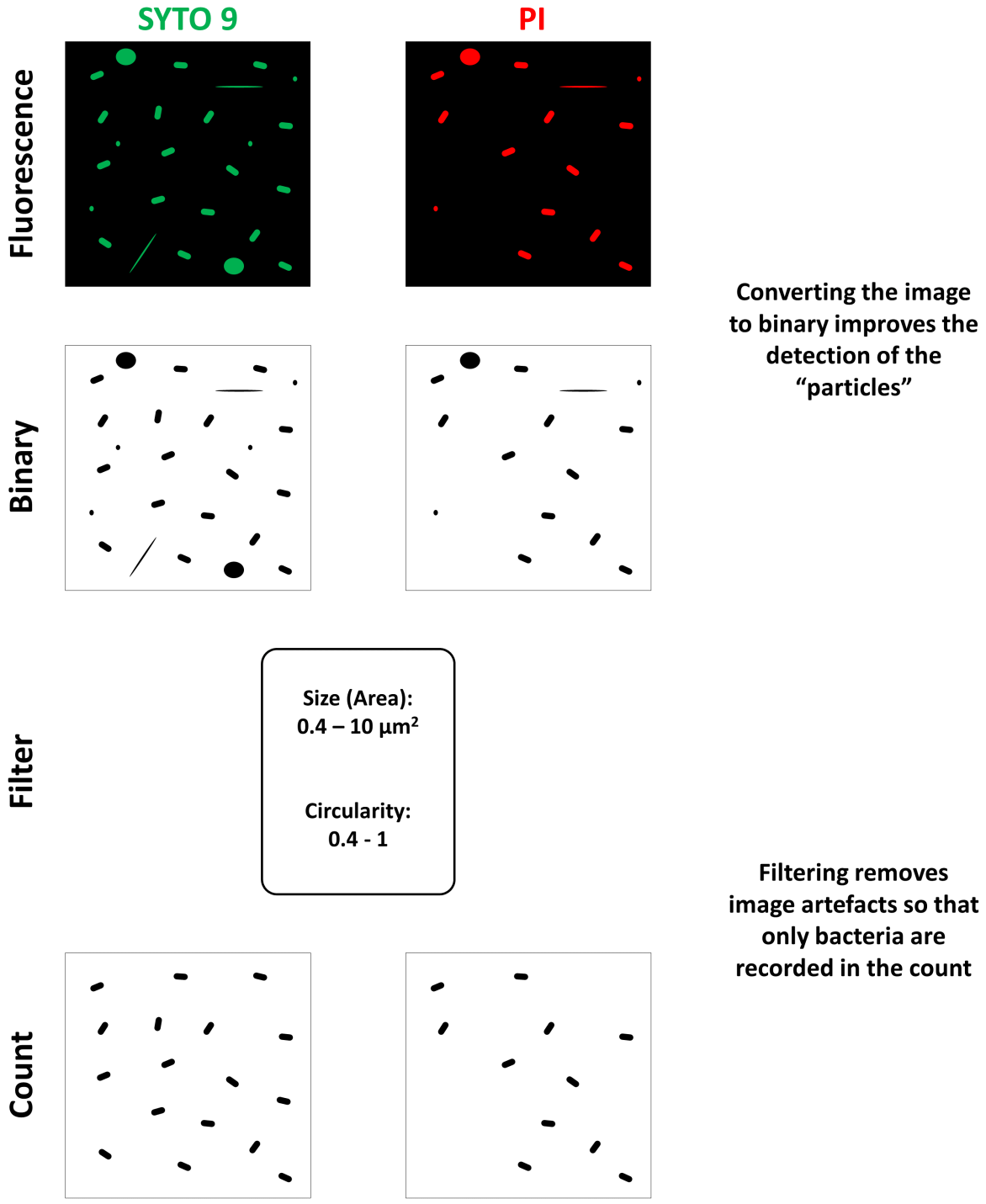


Figure 2.3.2: Illustration of the data analysis process for counting the number of live and dead bacteria from the microscopy images using FIJI. Fluorescent micrographs are converted to a binary image to help with the particle detection, before a filter is applied which removes the image artefacts, and ensures that only bacteria in the image are counted.

2.4. Bacterial Strains

The bacterial strains used throughout the work presented in this thesis are given in Table 2.4.1.

Table 2.4.1: Bacterial strains used throughout the work presented in this thesis.

Strain	**Bacteria**	**Type**	**Description**	**Ref.**
MG1655	*E. coli*	Gram -ve	Wild Type/Laboratory Strain	[105]
UPEC	*E. coli*	Gram -ve	Stronger adhesion and biofilm formation	[106]
RN4220	*S. aureus*	Gram +ve	Laboratory (MSSA) Strain	[107]
Je2	*S. aureus*	Gram +ve	Methicillin-resistant (MRSA) strain	[107]
Je2 Δ*pbp3*	*S. aureus*	Gram +ve	Reduced insertion of sidewall peptidoglycan, few morphological changes	[107]
Je2 Δ*pbp4*	*S. aureus*	Gram +ve	Cross-linking of peptidoglycan reduced, few morphological changes	[107]
Je2 Δ*sagB*	*S. aureus*	Gram +ve	Longer glycan strands, stiffer cell walls with irregular morphology	[107]
Je2 Δ*atl*	*S. aureus*	Gram +ve	Effects daughter cell separation, cells tend to form clusters	[107]
Je2 ppGpp^{o}	*S. aureus*	Gram +ve	Cannot initiate stringent response, few morphological changes	[107]

Chapter 3

Characterisation of the *Megapomponia intermedia* Wing

3.1. Introduction

Megapomponia intermedia (pictured in Figure 3.1.1) is a species of cicada, first documented by W. L. Distant in 1905 [108], native to many Southeast Asian countries such as Vietnam, Thailand and Burma. The nanofeatures present on the cicada wing surface were first described by Yoshida *et al.* [43] in 1996, who noted their similarity to the structures previously found on the corneas of insect eyes [109]. Ivanova *et al.* first demonstrated the antibacterial effect of the cicada wing (*Psaltoda claripennis*) in 2012, by showing killing of the gram-negative bacterium *Pseudomonas aeruginosa* [11]. The nanopillars on the cicada wing are likely to have evolved as a way of conferring superhydrophobicity to the wing, thus giving it self-cleaning properties [31], or as an anti-reflective device [43] for aiding in the evasion of predators. Therefore, they are likely not optimised for the killing of microorganisms, but do provide a useful starting point for this work.

This chapter presents the experimental results of topographical, chemical and mechanical characterisation of the structures present on the *M. intermedia* wing. The topography of the wing was analysed using Atomic Force Microscopy (AFM) and Scanning Electron Microscopy (SEM). PeakForce Tapping Mode (PFT) AFM was used to determine the mechanical properties of the wing, and chemical characterisation was undertaken using Fourier Transform Infrared Spectroscopy (FTIR), X-Ray Photoelectron Spectroscopy (XPS) and contact angle measurements. Finally, the effectiveness of the cicada wing in killing the gram negative bacterium *Escherichia coli* was quantified using a LIVE/DEAD

fluorescent stain assay.



Figure 3.1.1: Example specimen of the cicada M. intermedia

3.2. Methods

Specimens of the cicada, *M. intermedia*, were purchased from Taxentomo (taxentomo.com) who sourced them from Thailand. The wings were carefully removed from the body of the specimen and prior to all measurements, each wing was washed by gently sonicating in deionised (DI) water for 10 minutes, before drying with a stream of nitrogen gas.

3.2.1. Topographical and Mechanical Properties

AFM and SEM were used to determine the height (H), diameter (D), and centre-to-centre spacing/pitch (P) of the nanostructures on the surface, for three individual MI specimens. For the AFM measurements, sections of the wing were glued to glass microscope slides to ensure that they remained flat for imaging. A Bruker Veeco Dimension 3100 AFM was used with a TESPA-V2 cantilever (nominal spring constant $37\,\mathrm{N\,m^{-1}}$, resonant frequency 320 kHz) in tapping mode to image each sample. For each individual, 10 different $10\,\mu\mathrm{m} \times 10\,\mu\mathrm{m}$ scans were taken across the wing in random areas to avoid any bias. For the comparative analysis of the different cells of the wing, 10 scans were taken for each cell. The data was analysed using software Gwyddion [99], using the grain threshold feature to find the heights of the individual pillars (more details are given in section 2.1), and line profiles to find the average roughness, R_a. The SEM measurements were carried out using a JEOL InTouchScope Scanning Electron Microscope. The wings were washed as before and then mounted onto SEM stubs using conductive carbon tape.

These samples were then sputter coated with $\approx 30\,\text{nm}$ of gold to ensure good conductivity across the sample. For each individual, 10 scans (accelerating voltage = 17 kV) were taken and analysed using FIJI [103] with the analyse particles feature, to find the diameter and pitch of the nanopillars.

The mechanical properties of the cicada wing were assessed using PeakForce Tapping Mode AFM, in collaboration with Dr. Raveen K. Tank. Data was collected in quantitative imaging mode using a JPK Nanowizard III Bio AFM equipped with a FastScanD cantilever (nominal spring constant $0.25\,\text{N}\,\text{m}^{-1}$, resonant frequency 110 kHz). This imaging mode allows force curves to be taken at every pixel of the image with the same speed as regular imaging [110]. Images were taken with the cicada wing immersed in HPLC-grade water, which helps reduce the forces from the capillary water layer that act on the AFM tip when imaging in ambient conditions [97]. The force curves were analysed using the JPK SPM analysis software in order to find the Young's Modulus of the wing. More details of the model used are given in section 2.1.

3.2.2. Surface Chemistry

The surface chemistry of the *M. intermedia* wing was determined using contact angle tensiometry, FTIR spectroscopy, and XPS. The water contact angle (WCA) of the cicada wing sections (used for the AFM measurements) were measured with an optical tensiometer (Attension Theta - Biolin Scientific). The static contact angle was found across 10 repeat measurements using 20 µl droplets of DI water. The FTIR measurements were made in transmission mode (Thermo Scientific Nicolet iS10), with each spectra comprised of 128 scans. 5 spectra averaged from random areas across each wing. XPS measurements were performed by Debbie Hammond at the Sheffield Surface Analysis Centre. XPS data was collected with a Kratos Supra, with 3 areas of 700 µm × 300 µm analysed per wing. Survey scans were carried out with two 300 s sweeps at a 160 eV pass energy, between 0 and 1200 eV at an interval of 1 eV. High resolution scans were collected over the elements of interest at 20 eV pass energy, with a 0.1 eV interval and one 300 s sweep for O 1s, F 1s, N 1s and Si 2p spectra and two sweeps of 300 s for C 1s.

3.2.3. Bactericidal Properties

The bactericidal efficiency (BE) of the cicada wing was evaluated using a Live/Dead stain assay and fluorescence microscopy. *E. coli* (MG1655) colonies were used to inoculate Luria Broth (Miller) (LB) and then incubated at 37°C, shaking at 200 rpm, for 18 h.

These overnight cultures were then diluted to $OD_{600} = 0.05$ in fresh LB media and grown to mid-exponential phase (OD_{600} = 0.4-0.5). This culture was centrifuged to pellet the bacteria, after which the LB media was removed and replaced with a 0.9% NaCl buffer. The final suspension was adjusted to $OD_{600} = 0.1$. The bacterial suspension was statically incubated on the cicada wing surface for 20 h at 37°C, after which time it was removed and the surfaces gently washed with fresh buffer solution. Next, the bacteria on the wing were stained using the LIVE/DEAD BacLight Bacterial Viability Kit (details given previously in section 2.3) for 30 min in the dark. The dye was aspirated and any excess removed by gentle washing with buffer. The number of cells stained with either SYTO9 (Live) or Propidium Iodide (Dead) were assessed by imaging across 10 random areas with a Nikon Eclipse Ti Widefield microscope and counted with the image analysis software FIJI. The percentage of dead bacteria was determined using equation 2.4. Unstructured glass coverslips were tested in the same way and used as controls in this experiment. Any differences between the amount of bacteria that may attach on the respective surfaces due to differences in their surface chemistry will be accounted for in the calculation of the killing efficiency, as equation 2.4 normalises to the number of bacteria attached to the surface after incubation. For SEM measurements, instead of staining the bacteria after incubation, they were fixed with 4% Paraformaldehyde (PFA) for 30 min. After this the bacteria were dehydrated using a series of ethanol solutions (0, 20, 40, 60, 80, 100%), incubating in each for 10 min to slowly replace all of the water in the cells. The samples were left to air dry before coating them with gold and subsequently imaging, as per section 3.2.1.

3.3. Topographical Characterisation

The analysis of the AFM and SEM scans of the *M. intermedia* wing revealed a hexagonally-packed array of nanopillars present on both the front and back of the wing (shown in Figure 3.3.1). The SEM images and line profiles taken through the AFM scans showed that the pillars are conical in shape and taper in towards the top, capped by a round tip. Whilst some of this taper in the line profile is due to a convolution with the shape of the AFM tip, the SEM images show that the pillars do narrow towards their tip.

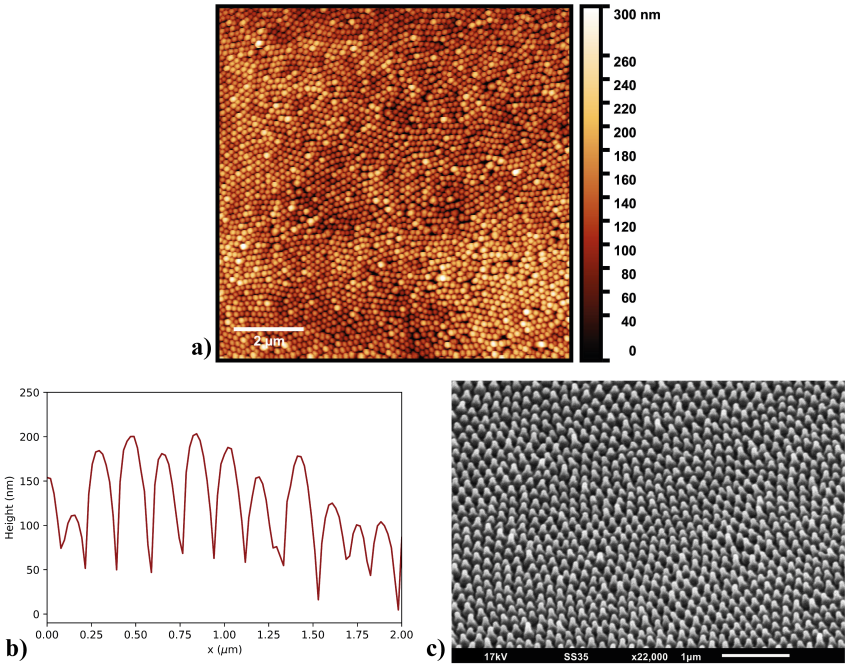


Figure 3.3.1: The nano-topography of the wing of the cicada, M. intermedia. a) Representative AFM scan of the cicada wing surface, showing the hexagonal packing of the nanostructures. b) Line profile taken across the AFM scan. c) SEM image of the cicada wing (taken at 25 ° tilt) showing the tapered shape of the nanopillars.

A summary of the average height, diameter and pitch measurements, as well as the average roughness R_a and spatial density of the nanostructures across all of the samples is given in Table 3.3.1. Two additional parameters which are useful when comparing different NSS are the aspect ratio (calculated with equation 1.6) and the Wenzel roughness factor, r (calculated with equation 1.5).

Table 3.3.1: Average measurements for various topographical parameters, across all the surface features for the three M. intermedia individuals. AFM was used to measure the height and the roughness R_a, and SEM used for the diameter and pitch.

Parameter	**Individual 1**	**Individual 2**	**Individual 3**	**Average**
Height (nm), H	209 ± 43	200 ± 56	219 ± 45	208 ± 50
Base Diameter (nm), D	135 ± 14	147 ± 32	134 ± 24	138 ± 24
Pitch (nm), P	162 ± 13	165 ± 15	151 ± 11	158 ± 14
Aspect Ratio	1.5 ± 0.4	1.4 ± 0.5	1.6 ± 0.4	1.5 ± 0.4
Wenzel Roughness Factor, r	5.3 ± 1.4	5.3 ± 2.0	6.2 ± 1.7	5.6 ± 1.8
Average Roughness, R_a (nm)	21 ± 4	23 ± 6	20 ± 4	21 ± 5
Feature Density (/µm^2)	35 ± 1	28 ± 4	39 ± 4	34 ± 6

The AFM and SEM measurements gave average values for the height (AFM), diameter and pitch (SEM) of 208 ± 50 nm, 138 ± 24 nm, and 158 ± 14 nm respectively. These values are in good agreement with previously reported values for *M. intermedia*, of 241 nm, 165 ± 8 nm, and 156 ± 29 nm [38]. These values are also typical for other cicada species examined in the literature, with pillar height generally in the 150 - 250 nm range [11, 37–39, 111]. These height values are also comparable to species of dragonfly which were found to have ≈ 200 nm nanostructures on their wings [14, 41, 112]. The pitch of the *M. intermedia* nanopillars is also very similar to other cicada species, whose nanopillars are also arranged in a hexagonally-packed array [11, 38]. In contrast, the pillars on the dragonfly wings are randomly packed and therefore have a much higher density than the cicada wing features [14, 41, 112]. There was no significant difference found between the height, diameter and pitch of the features across the three different cicada individuals, indicating that all *M. intermedia* cicada would have the same (taking into account some natural variation) features on their wings.

The AFM and SEM analysis of the wing features permitted measurements to be taken for each individual pillar as well as finding the total average. Therefore the distribution of these values could be found across the three *M. intermedia* individuals (shown in Figure 3.3.2). Both the diameter and pitch (b) and c)) of the pillars followed a typical normal distribution, which would be expected for this type of population. However, the height of the pillars (Figure 3.3.2a) was found to follow a bimodal distribution, indicating that there is two different height populations. Fitting a Gaussian function to the two peaks in this distribution finds populations with average heights of 132 ± 24 nm and 206 ± 38 nm. It is not clear how these two populations are distributed across the wing, but this effect could be in part due to the variation in height found across the different cells (Figure 3.3.3). This dual-height population has been previously reported for dragonfly wings [41], where it was suggested that it contributes to the mechanism of cell death by increasing the surface area of the wing, creating high adhesive forces between the nanopillars and the bacterium (discussed in more detail in section 1.6). Wu *et al.* also found that an inhomogeneity in the pillar height on synthetic "Ormostamp' NSS led to a higher killing degree of *S. aureus*, which was proposed to be due to an increased degree of stretching of the bacterial cell membrane [58].

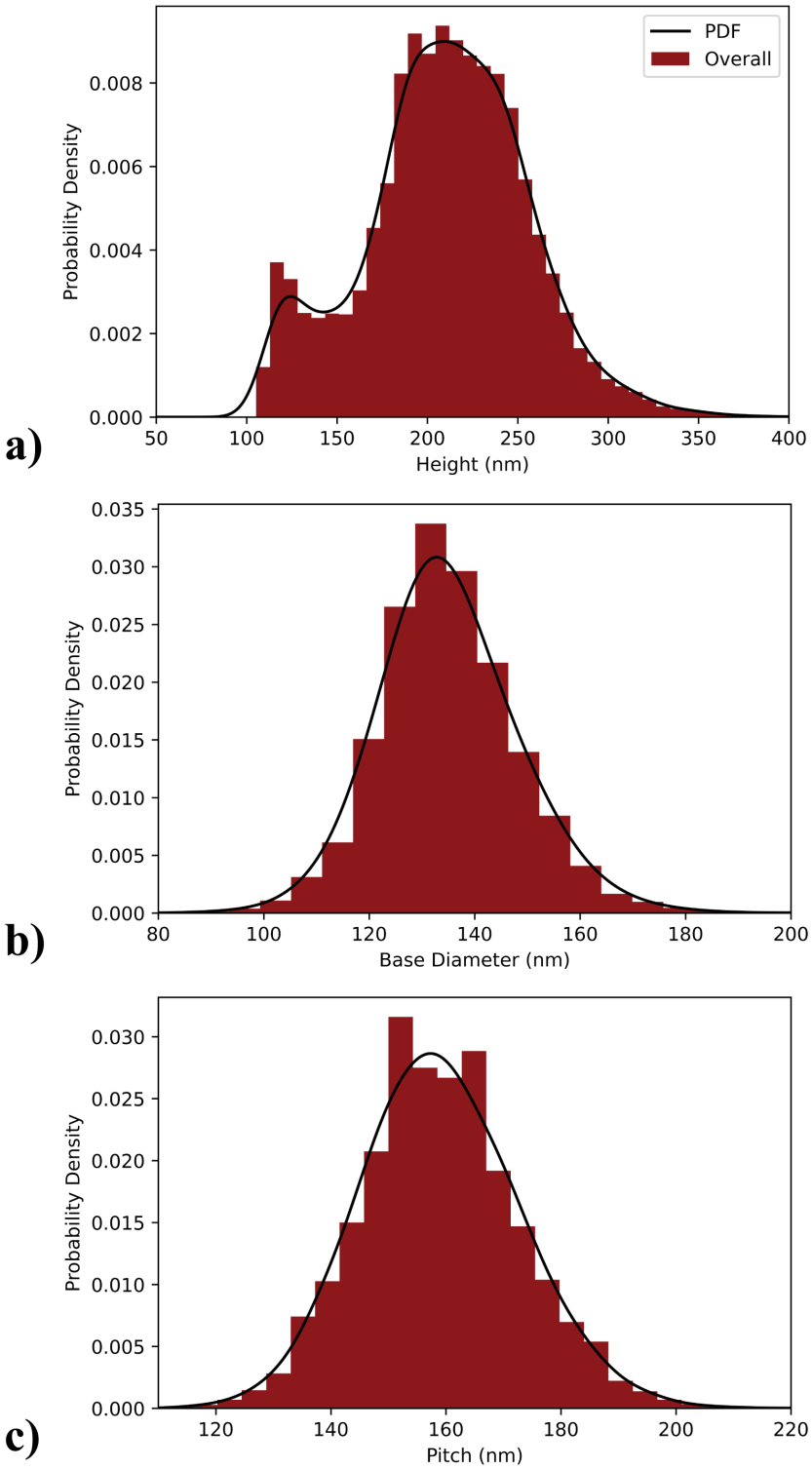


Figure 3.3.2: Distribution of measurements of the a) height, b) diameter, and c) pitch of the nanopillars over three individual M. intermedia wings.

By breaking down the cicada wing along the veins into its individual cells, it became possible to explore how the height of the nanopillars varied across each wing. Figure 3.3.3a shows a heat map of the average feature height across each cell on the wing. Generally, the regions with taller nanopillars were found near the inside edge of the wing, closest to the body, with the features becoming shorter towards the outer edge. This effect may be explained in the context of the self-cleaning properties of the cicada wing. As discussed by Murakami *et al.*, textured surfaces tend to be in the Wenzel state when the features have a high aspect ratio (¿1) [34], as is the case here. In the Wenzel [113] model of wettability, the static water contact angle increases with increasing surface roughness (as per eq. 1.4 and eq. 1.5). This "Wenzel" roughness is proportional to the height of the features, and therefore taller surface structures increase the water contact angle and decrease the wettability of the surface. It has previously been shown that a gradient in surface wettability can cause a water droplet to move towards the regions of high wettability (low WCA) due to the imbalanced force that is placed on the drop [114–116]. The edge of the water that is in the region of higher wettability will experience a higher surface tension force, dragging it along the surface. It is possible that a similar effect is happening here, due to the increasing wettability from the inside (near the cicada body) to the outside of the wing, which will pull the water away and off the wing (see illustration in Figure 3.3.3c). It is important to note that the height of the nanopillars does not vary greatly (by more than 100 nm) across the wing, especially in closely neighbouring areas. Therefore, there is no requirement to be selective when sampling areas of the wing for killing efficiency tests, as any height variation should not be significant enough to lead to a difference in the killing ability.

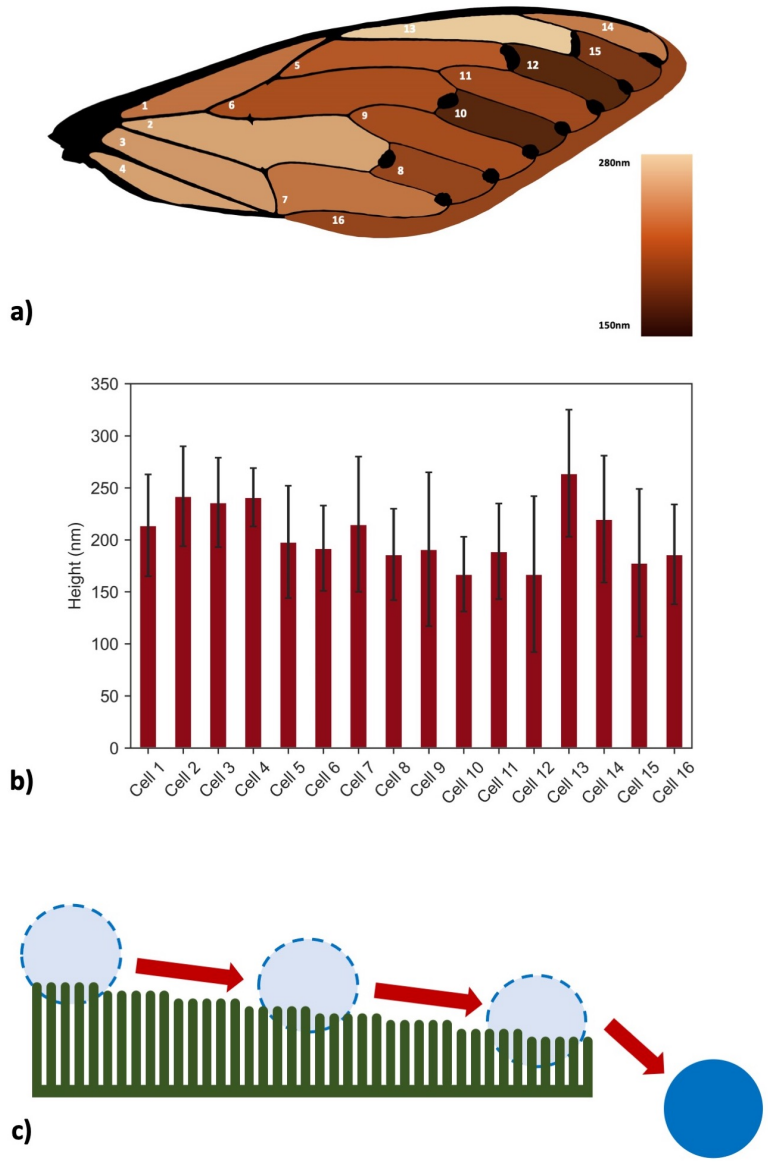


Figure 3.3.3: Variation in height of nanopillars across the cicada wing surface. a) Heat map of the heights of the nanopillars in each "cell" on the M. intermedia wing. b) Bar chart of the height values showing that, whilst there is some height variation, the difference between the cells is not large. c) Model of how the variation in nanopillar height across the wing could aid in the self-cleaning effect.

3.4. Mechanical Characterisation

When characterising NSS the mechanical properties are an important, and often overlooked, parameter to determine. Here, the Young's Modulus (E) of the *M. intermedia* wing was found using quantitative imaging mode on a JPK NanoWizard III AFM, with more discussion on the model used given in section 2.1.

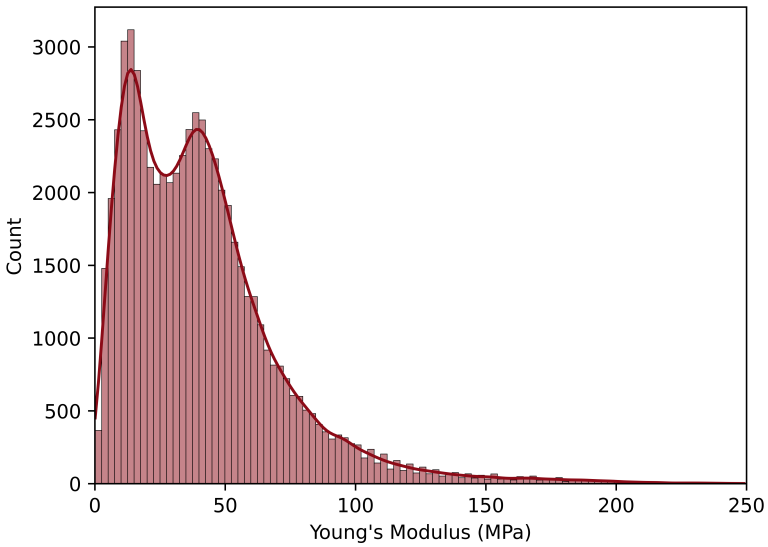


Figure 3.4.1: Histogram of Young's Modulus measurements taken for the M. intermedia wing using AFM in quantitative imaging mode.

3.4.1. Quantitative Mechanical AFM

Analysis of the AFM force curves for one 256 x 256 pixel scan yielded 65,536 data points for the Young's Modulus (YM), which are visualised in the histogram in Figure 3.4.1. The average YM across the wing was found to be 41 ± 31 MPa, although there are two peaks in the population distribution, one centred at ∼ 14 MPa and another at ∼ 40 MPa. These values are consistent with Young's modulus measurements by both Bandara *et al.*, who found nanopillars on the dragonfly wing to have a modulus of 38 ± 4 MPa [41], and Shahali, who measured 3 cicada wings and found that they had a Young's modulus between 35-45 MPa [117]. The large standard deviation of the results here may be explained by the topography of the wing, in that the high aspect ratio of the pillars could lead to poor contact between the tip and the surface (especially if it touches the side of a pillar). This could induce an error in the force measurements. It would be possible to account for this by using a cantilever loaded with a colloid, rather than a sharp probe, which would come into contact with many nanopillars at once and allowing an "average" force to be measured (reducing the overall error) [118].

All these results indicate that the cicada wing is much softer than the materials that have typically been used to make NSS in the past, with some examples given in Table 3.4.2. Glassy polymers such as Poly(methyl methacrylate) (PMMA) and Polystyrene (PS) both have YM values nearly 100x higher than the cicada wing, and inorganic surfaces such

as silicon and titanium are up to 4500x stiffer.

Table 3.4.2: Typical Young's modulus values for materials commonly used to fabricate NSS, compared to the measured value for the cicada wing.

Material	**Typical Young's Modulus**
Cicada Wing	41 ± 31 MPa (measured)
PMMA	3 GPa [119]
PS	3.5 GPa [120]
Silicon	130 - 188 GPa* [121]
Titanium	100 GPa [122]

*value depends on the crystal orientation

Another indication that the cicada wing nanopillars are relatively soft comes from comparing the topography of the surface in two different scans, one in air and one in liquid (Figure 3.4.2). The organisation of the nanopillars on the wing appears markedly different when imaged in liquid (Fig. 3.4.2a) compared to air (Fig. 3.4.2b), with the pillars seeming to shift and bend. By taking the Power Spectral Density Function (PSDF) of the AFM data (Figure 3.4.2c) it is possible to identify periodic features on the surface. The PSDF plot for the wing in air shows a strong peak at around $k = 0.04\,\mathrm{nm}^{-1}$ which, as per eq. 3.1, corresponds to a periodic length scale at 157 nm. This is the same value found from the SEM measurements (Table 3.3.1) for the spacing of the nanopillars (158 nm), confirming that this peak is due to the periodic packing on the nanopillars.

$$k = \frac{2\pi}{L} \tag{3.1}$$

However, for the scan of the cicada wing taken in liquid conditions the strength of this same peak in the PSDF decreases, showing that the periodicity at this length scale decreases. It is possible to roughly calculate the strength of the force required for this by using the Euler-Bernoulli theory equation for a beam with a fixed end, given by eq. 3.2, where F is the force required to bend a beam of length L, Young's Modulus E, and radius r, by an amount Δx [123, 124].

$$F = \frac{3}{4}\pi E \frac{r^4}{L^3}\Delta x \tag{3.2}$$

Using this, the predicted force required to bend the cicada nanopillars by a distance

equal to their radius is ≈ 20 nN. This is a relatively low force, for example, it is a similar magnitude to the force that would act on the pillar due to the surface tension of water (0.074 N m^{-1} over the 200 nm length of the pillar) is approximately 15-20 nN.

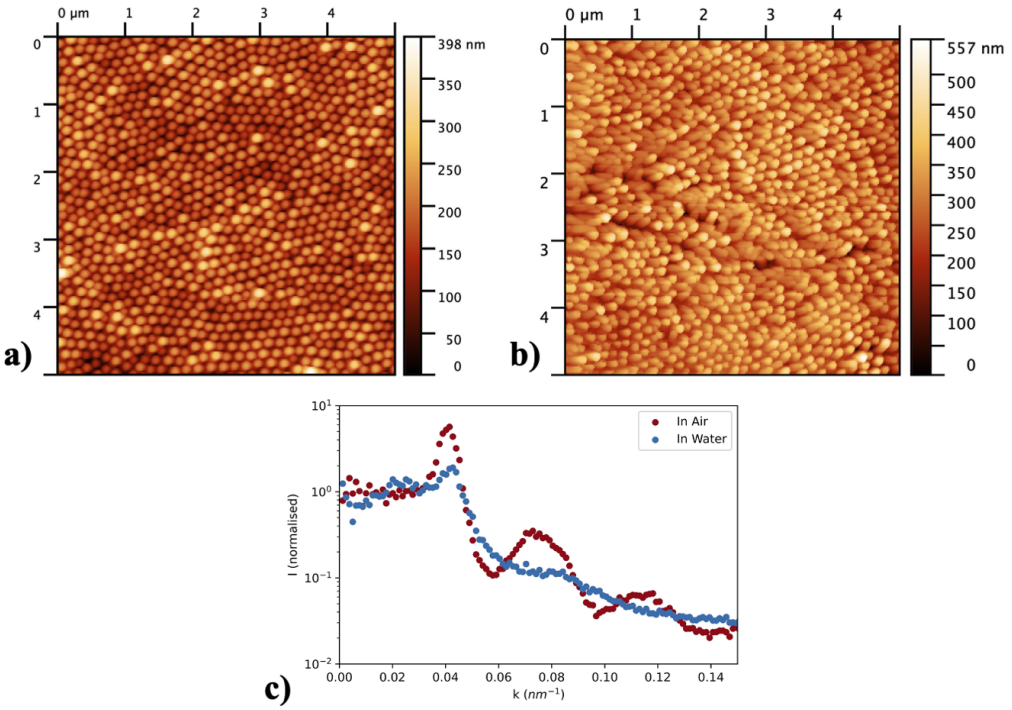


Figure 3.4.2: Comparing the topography of the M. intermedia wing with air vs liquid AFM. a) Cicada wing imaged in air. b) Cicada wing imaged immersed in liquid. c) Radial PSDF of the two datasets, showing a decrease in the order of the nanostructured pillars in water.

3.5. Chemical Characterisation

Next, the chemical composition of the *M. intermedia* wing was analysed in order to verify whether the bactericidal effect of cicada wings is a purely mechanical process. A combination of contact angle tensiometry, FTIR spectoscopy, and XPS was used for this assessment.

3.5.1. Contact Angle Measurements

Static water contact angle (WCA) measurements of the cicada wing revealed that the surface is highly hydrophobic (shown in Figure 3.5.1), with an average WCA over the 3 wings of 110 ± 20°. This is in line with previous experimental observations on the

hydrophobic nature of the cicada wing [125]. As previously discussed in section 1.4.1, the wetting of textured surfaces is predicted by the Wenzel [113] and Cassie-Baxter [32] models. In both cases, it is a high surface roughness that leads to an enhanced contact angle and therefore superhydrophobicity. It can be concluded that the nanopillars on the cicada wing create a nano-rough surface (average Wenzel Roughness Factor = 5.6 ± 1.8) and confer a high hydrophobicity.

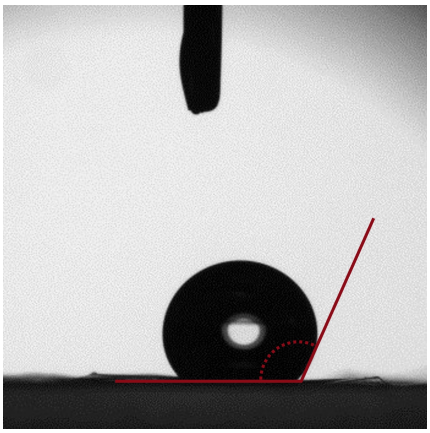


Figure 3.5.1: Representative water droplet on the surface of the M. intermedia wing. The water contact angle exceeds 100° showing its highly hydrophobic nature.

3.5.2. Surface Chemistry Analysis

Surface chemistry analysis using FTIR spectroscopy showed, as expected, that the cicada wings are dominated by organic compounds. The spectrum shown in Figure 3.5.2 is the average from 3 individual cicada wing specimens and shows the key features which have previously been identified in the literature [42, 126, 127]. The key features are as follows -

- **Amide I (1600-1650 $\mathbf{cm^{-1}}$):** Mainly due to stretching of the carbonyl (C=O) groups.
- **Amide II (1480-1570 $\mathbf{cm^{-1}}$):** Due to C-N and N-H vibrations.
- **$\mathbf{CH/CH_2/CH_3}$ (2800-3000 $\mathbf{cm^{-1}}$):** Due to C-H stretching.
- **OH Region (3200-3500 $\mathbf{cm^{-1}}$):** Due to OH stretching, likely from carboxylic acid groups. This could also be from ambient water contamination on the sample surface.

The peaks in the 1500-1700 m^{-1} region indicate that there are large amounts of α-chitin present in the wing [126]. This also becomes obvious when the cicada spectrum is compared to the IR-spectrum of pure chitin in Figure 3.5.2, which shows the presence of many of the same functional groups. The peaks in the 2800-3000 cm^{-1} region of the spectrum are indicative of the hydrocarbon waxes which are often present on the cuticle of insect wings [126, 128]. These results are consistent with other studies of the chemical composition of insect wings [40, 42, 126, 129].

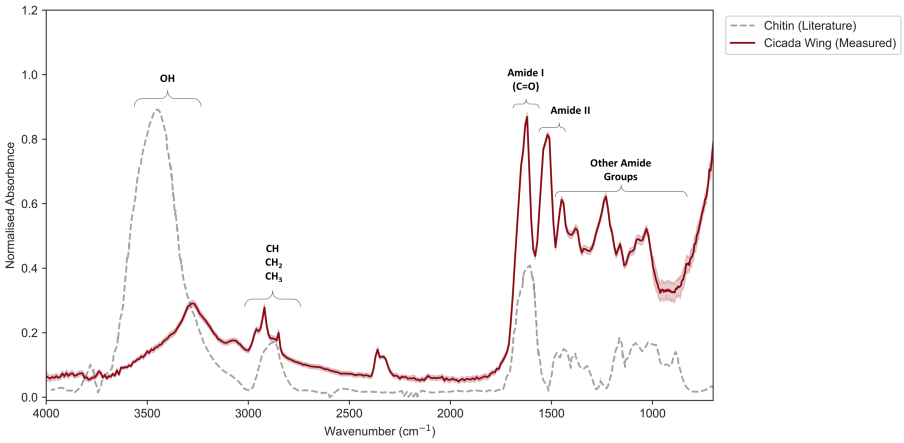


Figure 3.5.2: FTIR spectra averaged from 3 M. intermedia wings (error bands show the standard deviation of the mean) compared to the FTIR spectrum of pure chitin (adapted from [130]).

The results of the XPS survey scans (summarised in Table 3.5.3), largely confirm the FTIR results. Approximately 90% of the elements detected on the wing were found to be carbon, with $\approx$ 7% comprised of oxygen (XPS is not able to detect hydrogen). This is consistent with the cicada wing being comprised of both chitin and waxy hydrocarbon substances. Both Si and F were found to be present on the wing surface in low concentrations (generally <1%), this is likely due to contamination from external sources - some of the wing samples were stored with others that had been previously cast with PDMS in order to create a mould, with a fluoride-based polymer used to create an anti-adhesion layer (see Section 4.2). Fluorine is also a common contaminant in XPS chambers.

Table 3.5.3: Surface elemental composition (at%) of the three cicada wing samples, determined by XPS.

Sample	**F**	**O**	**N**	**C**	**S**	**Si**	**P**
Wing 1	0.2 ± 0.1	7.5 ± 0.4	3.5 ± 0.4	87.7 ± 0.6	0.2 ± 0.0	0.8 ± 0.4	<0.1
Wing 2	0.2 ± 0.1	4.0 ± 1.4	1.2 ± 0.6	93.2 ± 2.9	0.2 ± 0.1	1.2 ± 0.9	<0.1
Wing 3	0.3 ± 0.1	7.5 ± 3.4	2.5 ± 1.0	89.0 ± 4.5	0.2 ± 0.1	0.5 ± 0.1	<0.1

The combined results of the FTIR and XPS surveys of the cicada wing confirm that they are largely comprised of the bio-polymer chitin and some epicuticular waxes. Chitin is a polymer of N-Acetylglucosamine [131], which itself is one of the building blocks of the peptidoglycan layer which forms the cell wall of bacteria. Thus, it is very unlikely that the chemical composition of the cicada wing has any impact on the bactericidal ability. This is a result that has previously been experimentally demonstrated by Ivanova *et al.* who showed an equivalent killing effect of the *Psaltoda claripennis* wing before and after coating it with a layer of gold to render the surface chemically inert [11].

3.6. Bactericidal Testing

The antibacterial ability of the cicada wing was tested against the gram-negative bacterium *E. coli* and compared to an unstructured glass surface. An excess of exponential-phase *E. coli* MG1655 solution was incubated on the cicada wing for 20 hours at 37°C before being stained with the LIVE/DEAD stain and imaged with a wide-field microscope. The results of 4 repeats of this are shown in Figure 3.6.1.

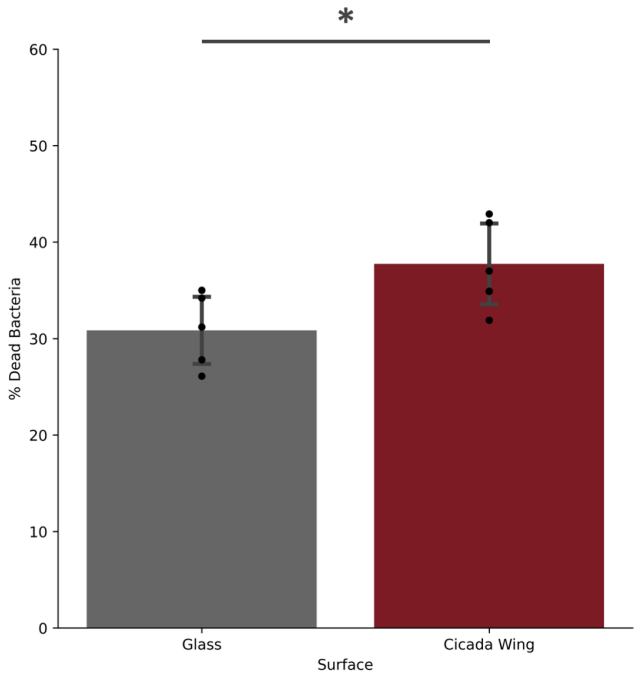


Figure 3.6.1: Bactericidal Efficiency of M. intermedia wing against exponential phase E. coli. Statistical significance tests were performed using Welch's t-test.

After 20 hours of incubation of bacteria on the cicada wing, it was found to have killed significantly more *E. coli* than the flat glass control surface ($p = 0.036$), with 37.7

± 4.7% of the bacteria killed on the cicada wing surface, compared to 30.9 ± 3.9% on the glass surface. This is a 20% increase in the percentage of dead bacteria and confirms the antibacterial effect of the cicada wing which has been previously reported [11, 37, 38], with Kelleher *et al.* reporting a Bactericidal Efficiency (BE) of 22% for the *M. intermedia* wing against *E. coli*, after 30 min of incubation.

SEM analysis of the *E. coli* that were incubated on the cicada wings for 20 h showed significant changes in morphology as a result of interactions with the nanopillars. There also appear to be changes in the wing surface as a result of the interaction with the bacteria. As seen when the cicada wings were imaged in liquid with AFM (Figure 3.4.2b), the nanopillars appear to bend into contact with the *E. coli* (shown by the purple arrows in Figure 3.6.2a and c), seemingly pinning them in place. It is not clear what force has caused the pillars to be pulled into contact with the bacteria, but previously both long range van der Waals force and shorter distance hydrophobic interactions have been attributed to the adhesion between a hydrophobic surface (like the cicada wing) and bacteria [132, 133], so these forces may also be at play here.

Figure 3.6.2a-d shows changes in the shape of the outer membrane of the cells, compared to the normal rod-shape of *E. coli* (shown in Figure 3.6.2e), as their membranes are deformed by the pillars. Some of the bacteria also appeared to be "deflated", highlighted by the red arrow in Figure 3.6.2b, indicating a potential loss of their turgor pressure due to a reduction in the cell wall integrity. There is also evidence of some bacteria whose cell wall has been completely torn open or ripped apart, which is highlighted by the blue arrows in Figure 3.6.2d. The *E. coli* incubated on a flat PS surface (Figure 3.6.2e) showed no cell wall related damage. This nanopillar-related bacterial deformation is consistent with previous studies on the bactericidal effect of cicada wings [11, 38]. The white arrows in Figure 3.6.2a and c show the nanopillars on the cicada wing conforming to the shape of the bacteria which sits upon them, seemingly bending into contact with the cell wall. This is a common phenomenon seen in this work and in the wider literature [46].

Whilst these images reveal that membrane damage is involved in bacterial death, the nature of SEM as an end-point imaging technique means that it cannot determine at what point during cell death this damage occurs. Is the damage and resulting cell death directly caused by the interaction with the nanopillars, or is the damage a consequence of the loss of viability/turgor pressure by some other pathway? Alternative techniques for elucidating the bacterial mechanism of NSS will be explored in section 6.

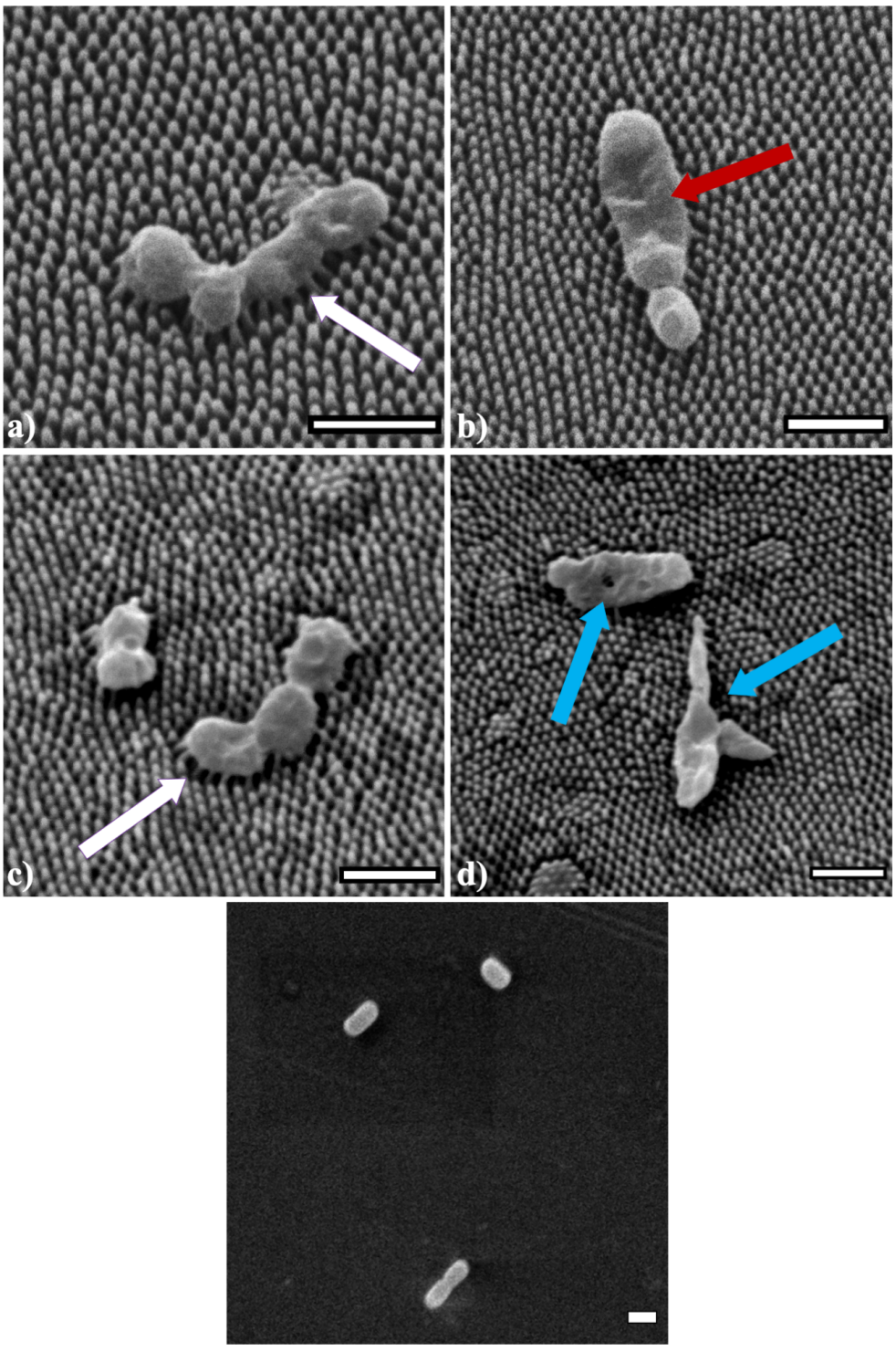


Figure 3.6.2: SEM images of E. coli on M. intermedia wing (a-d) and on flat polystyrene control surface (e). Significant disruption of the bacterial morphology can be seen for the cells on the cicada wing, with an indication that a loss of membrane integrity (blue arrows) and turgor pressure (red arrow) could have occured. The white arrows highlight that the nanopillars seem to conform to the outer membrane of the E. coli. The cells on the flat polystyrene display typical E. coli morphology. All scale bars = 1 µm

3.7. Summary of Findings and Conclusions

In this chapter a thorough characterisation of the wing of the cicada *M. intermedia* has been carried out. The nanotopography and mechanical properties were determined using SEM and AFM, the surface chemistry was analysed with contact angle measurement, FTIR and XPS. Finally, the bactericidal ability of the wing against *E. coli* was determined using LIVE/DEAD staining and the interaction of the bacteria with the nanopillars was visualised with SEM. The key conclusions are as follows -

- As expected, the *M. intermedia* wings were found to be covered in a hexagonal array of conical nanopillars, $\approx 200\,\text{nm}$ tall, $\approx 140\,\text{nm}$ wide and with a separation of $\approx 160\,\text{nm}$.

- From the SEM measurements both the diameter and the spacing of the nanopillars follow a normal distribution.

- From the AFM measurements the height of the nanopillars follows a bimodal distribution, indicating two height populations on the surface. It is possible that the inhomogeneous height distribution may enhance bactericidal efficiency.

- No significant variation was found between individual cicada wings, but some variation was found in areas across a single wing. It is possible that the gradient of nanopillar height is useful in removing water and surface contaminants from the wing surface, thus helping to avoid any damage.

- Quantitative AFM measurements revealed that the cicada wing has a Young's Modulus of $41 \pm 31\,\text{MPa}$. This is much softer than materials typically used to make NSS.

- The static water contact angle of the *M. intermedia* wing was measured to be $110 \pm 20°$, confirming its hydrophobic nature.

- FTIR analysis showed that the wing had a strong presence of Amide I and II groups as well as $CH/CH_2/CH_3$, which strongly indicates that it is primarily composed of chitin and hydrocarbon waxes.

- XPS analysis confirms this, finding that the dominant elements present are carbon, nitrogen and oxygen.

- The *M. intermedia* wing was shown to kill significantly more MG1655 (WT) *E. coli* than a flat glass control, after 20 h of incubation. 37.7 ± 4.7% of exponential phase *E. coli* were killed on the cicada wing surface ($p = 0.036$).
- SEM of *E. coli* incubated on the cicada wing surface showed significant changes in morphology compared to *E. coli* incubated on a flat surface. Loss of turgor pressure was evident in some cases, as was direct damage to the cell wall.
- The wing nanopillars were found to bend and conform to the shape of the bacteria, seemingly pinning them in place. This process may be implicated in the mechanism of cell death.
- As an end-point imaging technique, SEM (and other similar methods) are not suitable to determine the bactericidal mechanism of NSS, so other avenues require exploration.

The cicada wing provides excellent inspiration for other bactericidal NSS. The next chapter will explore the methods used to design and create polymer NSS, inspired by the topography and bactericidal abilities of the cicada wing.

Chapter 4

Fabricating Synthetic Nanostructured Surfaces

4.1. Introduction

For nanostructured surfaces to be considered as viable antibacterial surfaces, they need to be able to be produced on a large scale, with high quality, but also at relatively low cost. Creating synthetic replicas of the nanostructures seen on the cicada wing is also important when trying to investigate their bactericidal mechanisms, as the parameters of these natural surfaces (the pillar height, spacing etc.) are fixed, making it difficult to carry out systematic studies investigating their role on bactericidal efficiency.

Within a year of the first report of the antibacterial ability of cicada wings, Ivanova *et al.* reported that a synthetic nanostructured surface, Black Silicon (bSi), was effective in killing *P. aeruginosa*, *S. aureus*, and *B. subtilis* spores at a rate similar or higher than a dragonfly wing [14]. As Table 1.5.3 in section 1.5 shows, various different synthetic NSS have been developed from numerous materials using many different techniques. The majority of these synthetic NSS reported in the literature are made from inorganic materials. However, there are some reports of NSS made from organic materials such as PMMA [46], PET [59] and cellulose acetate [65]. The inorganic materials used have greatly different properties to the natural NSS (cicada and dragonfly wings) and to the polymeric materials. They are typically much stiffer and, importantly, can have photoactive properties which affect their chemistry. For example, it was shown in the 1970's that TiO_2 can produce Reactive Oxygen Species (ROS), such as hydrogen peroxide (H_2O_2), through photolysis [76]. H_2O_2, and other ROS, are well known to have antimicrobial properties

(and are consequently often used in cleaning products) [134–136]. Therefore, using purely polymeric materials allows the investigation of the bactericidal mechanism of NSS in a much "cleaner" system, without the involvement of any potential chemical effects that may alter the killing process. Using polymeric materials also offers the opportunity to tune the mechanical properties of the NSS (through the use of materials such as thermoplastic elastomers) which is hard to achieve with inorganic materials such as silicon or titanium. This may reveal more about the bactericidal mechanism of these structures and could also be very important when considering the potential applications of these materials. Indwelling medical devices such as catheters tubes or central lines need to be made from flexible materials to ease their insertion into the body, and the use of the common inorganic NSS would be impractical compared to more flexible polymer systems which these types of devices are currently made from.

This chapter will detail the investigation into different methods of producing NSS from a range of polymers. The aim was develop a technique that would allow the testing of the different parameters of NSS on their bactericidal efficiency, with a view to learning more about the killing mechanism and, ultimately, optimising their efficacy. Therefore, the production method would need to be able compatible with making NSS with different topographies (i.e. varying pillar heights and spacings) and also be suitable for use with different polymers (to probe the effect of changing mechanical properties), whilst maintaining a high replication quality. Firstly, a simple drop-casting and moulding process is described whereby polymers are imprinted using a master mould to give them surface nanostructures. To try and gain more control over the dimensions of the nanopillars, a nanosphere lithography method was also trialled in which O_2 plasma was used to etch a polymer film, with polystyrene spheres used as a mask to create the nanopillars. Details of the development of both techniques are given. The NSS were characterised with a combination of AFM and SEM to verify the quality and consistency of the nanostructures. Once a suitable set of NSS was formed, their bactericidal ability was tested using the LIVE/DEAD bacterial viability assay.

4.2. Solution Casting and Moulding

The first method used to try and produce synthetic NSS was based around casting polymer solutions into a master mould. This process is illustrated in Figure 4.2.1. Firstly, a "negative" silicon mould, which has been etched to possess an array of nano-holes, was cleaned with oxygen plasma treatment. The moulds were placed in an O_2 plasma cleaner (Henniker HP-200 Runcorn UK) on high power for 10 min. The oxygen species generated in the plasma react with organic contamination on the surface and convert them to water and CO_2 which is pumped away by the vacuum. These oxygen radicals also bind to the surface and increase the wettability, rendering it hydrophilic [137, 138]. Figure 4.2.2 shows the reduction in the WCA of a flat silicon wafer (used here as an analogue for the silicon mould), before and after cleaning with the O_2 plasma.

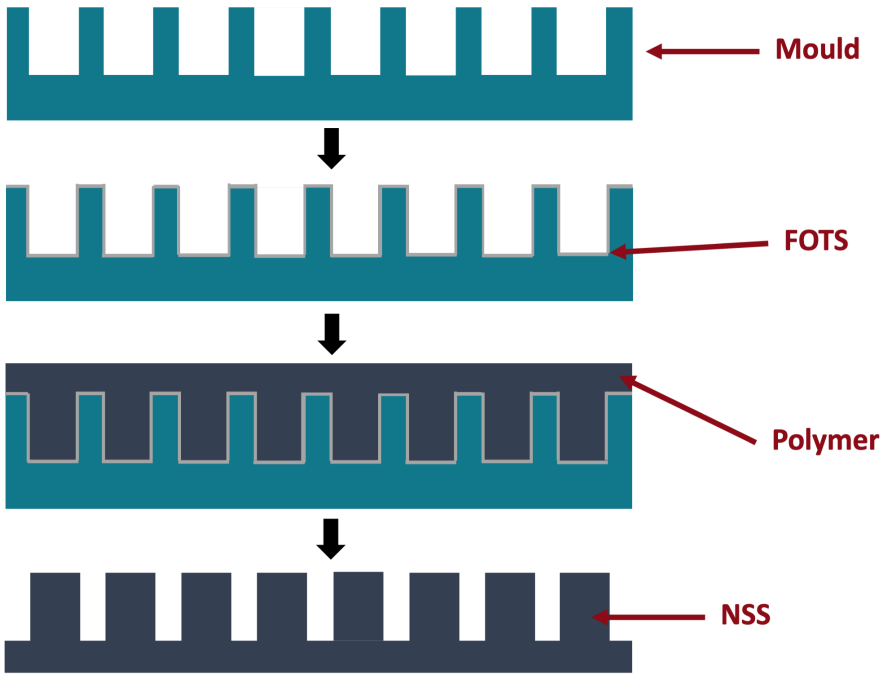


Figure 4.2.1: Illustration of the method used to create NSS by moulding with a master template. The mould is first cleaned with O_2 plasma, and then coated with FOTS to render it "non-stick". A polymer solution is then cast onto the mould, left to cure and then released, leaving a polymer surface covered with nanopillars.

Next, the mould was coated with 1H,1H,2H,2H-Perfluorooctyltriethoxysilane (FOTS), which has a low surface energy, that renders the surface hydrophobic [139]. The purpose of this "non-stick" layer is to ensure a clean release of the polymer from the mould af-

ter it has cured, allowing all of the individual nanostructures to be freed from the holes without breaking. This coating was applied via vapour deposition by placing the moulds into a vacuum desiccator (Bel-Art) with ∼100 µl of the FOTS solution (Sigma-Aldrich). The desiccator was then placed under vacuum and left for 24 h until a layer of the FOTS coated the mould. Figure 4.2.2 shows that after the coating, the flat silicon wafer has a higher WCA, indicating that a good layer has been applied and the surface has been functionalised.

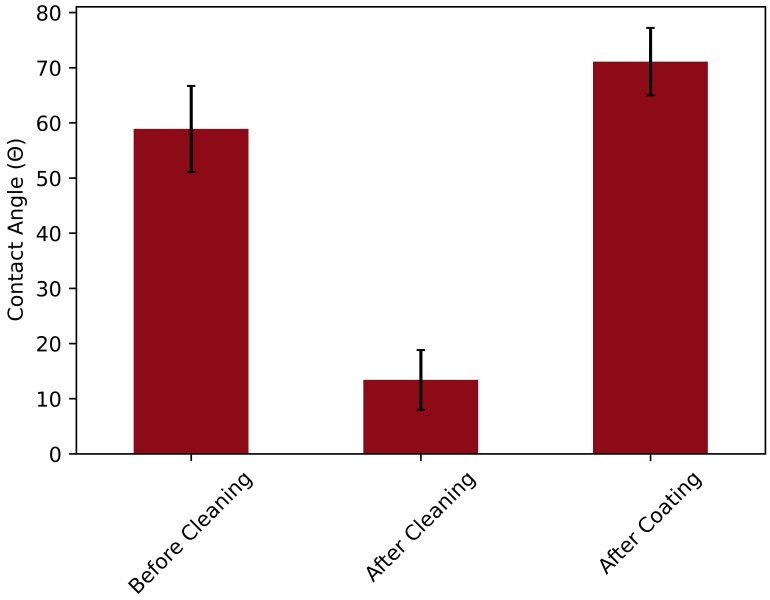


Figure 4.2.2: Cleaning and treatment of a flat silicon wafer (used as an analogue for the mould) changes it hydrophobicity. After cleaning with O_2 plasma the silicon becomes more hydrophilic, and then after coating with FOTS it regains its hydrophobicity.

Once the mould had been prepared, a polymer solution was then drop cast and left to cure at 40°C for 24 h. The polymer solutions were made in toluene, with the concentration adjusted depending on the polymer used. This is because the viscosity of a solution at a certain concentration (defined here as percentage by weight (wt%)) increases with the molecular weight (M_w) of the polymer. After curing, the polymer was released from the mould and is left with a surface uniformly covered in nanopillars. One of the key benefits to using this method is that, once a set of moulds are produced, no specialist equipment is required to make the NSS. Therefore this can be considered as a relatively inexpensive way of producing NSS quickly with different surface parameters and using a variety of polymers. The remainder of this section will discuss the results obtained from making NSS using this casting and moulding method with different polymers and master moulds.

4.2.1. The LightSmyth (LS) "mould"

One of the master moulds used when testing this method was a commercially available silicon stamp from LightSmyth. The holes on the stamp are arranged in a hexagonal array (illustrated by Figure 4.2.3a) with dimensions given in Table 4.2.1. Measurements of the mould made with AFM are consistent with the manufacturers values (Figure 4.2.3b).

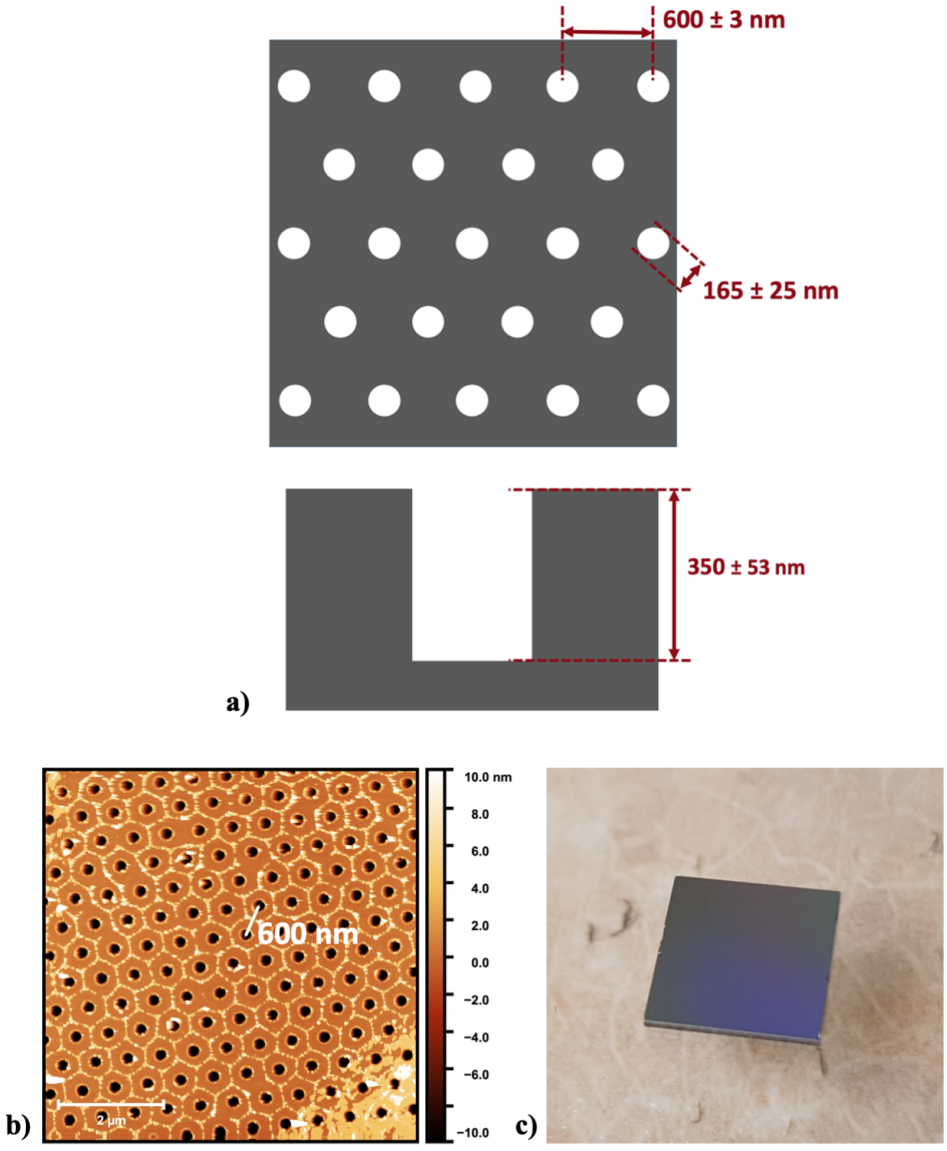


Figure 4.2.3: LightSmyth (LS) master template mould used to make NSS. a) Schematic of the mould with dimensions from the manufacturer, b) AFM of the mould with measurement of the hole to hole spacing, c) Image of the 8 x 8.3 mm LS mould.

Table 4.2.1: Summary of the manufacturer values for the LS mould parameters.

Parameter	**LS Manufacturer Value**	**Cicada Nanopillars**
Depth/Height (nm)	350 ± 53	210 ± 50
Diameter (nm)	165 ± 25	140 ± 20
Pitch (nm)	600 ± 3	160 ± 10
Aspect Ratio	2.1	1.5

Compared to the features on the cicada wing measured in section 3.3, the LS mould has holes which are similar in diameter, but 40% shorter and 275% further apart. The LS mould would also theoretically produce higher aspect ratio features than those on the cicada wing, at 2.1 and 1.5 respectively. Given that it is generally accepted that the pitch of the nanopillars has the biggest impact on bactericidal ability and closer spaced nanopillars lead to higher killing efficiencies [38, 46, 55], it would be expected that any NSS produced from the LS mould would have a lower bactericidal efficiency than the cicada wing. The holes on this mould are also straight-edged and so would not produce pillars that taper in towards the tip in the same way that those on the cicada wing do. However, it would not be expected that this would have any effect on the bactericidal efficiency. As previously mentioned, to verify that this technique is valid for producing viable antibacterial surfaces, it would need to be tested with a range of polymers. Here, both glassy and elastomeric polymers are tested for their replication quality.

4.2.2. Casting Glassy Polymers

The first polymers tested on the LS mould were PS and PMMA. Initially, both the PS (M_w = 350k) and the PMMA (M_w = 120k) were dissolved in toluene to 30 wt%. The viscosity of both the polymer solutions was quite high, however, the PS solution was considerably more viscous than the PMMA, owing to its higher molecular weight [140]. These solutions were drop-cast onto the prepared LS mould, and left for 24 h at 40°C to cure. Figure 4.2.4 shows representative AFM images of the NSS produced from both of the PS and PMMA (a + b, respectively), along with the average height of the nanopillars (c).

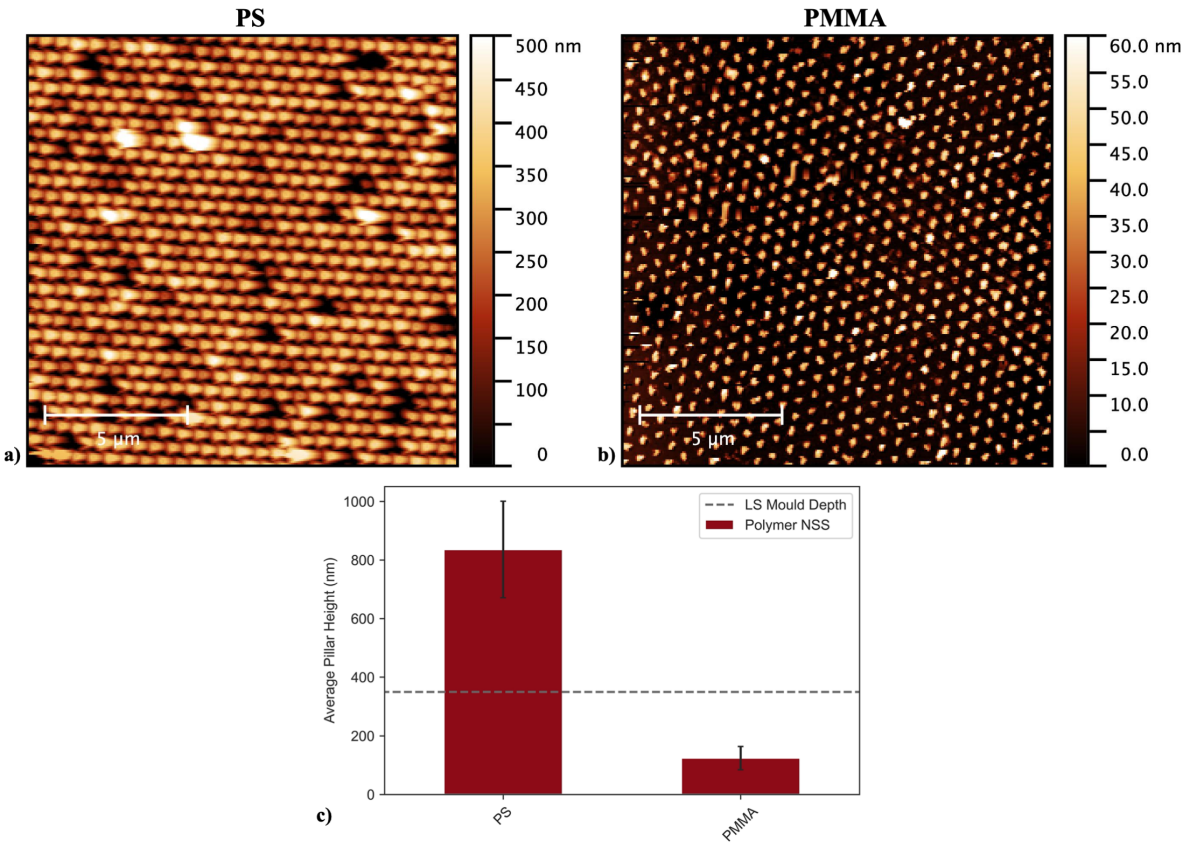


Figure 4.2.4: Representative AFM scans of PS (a) and PMMA (b) NSS from the LS mould, and average nanopillar height for each polymer(c). Dashed line represents the depth of the holes in the mould.

For the NSS made using PMMA, the feature height is much shorter (120 nm) than the maximum possible (350 nm). Initially, it could be concluded that the was because the polymer solution did not fill down to the full depth of the mould, resulting in shorter features. However, the PMMA surface was found to be very brittle and often cracked as it was released from the mould. Therefore, it is more likely that the nanopillars also cracked/snapped as they were being released and left shorter features behind. Using a higher molecular weight PMMA which would be more resilient to cracking, might have prevented this happening. However, this was not tested as PS was chosen as an ideal test polymer.

In contrast to the PMMA surfaces, the nanopillars made from PS were over double the height (840 $\pm$ 165 nm) than the depth of the LS mould should have allowed. This implies that the pillars are somehow stretched as the surface is released from the mould. This is confirmed when looking at the PS surfaces with SEM (example image shown in Figure 4.2.5).

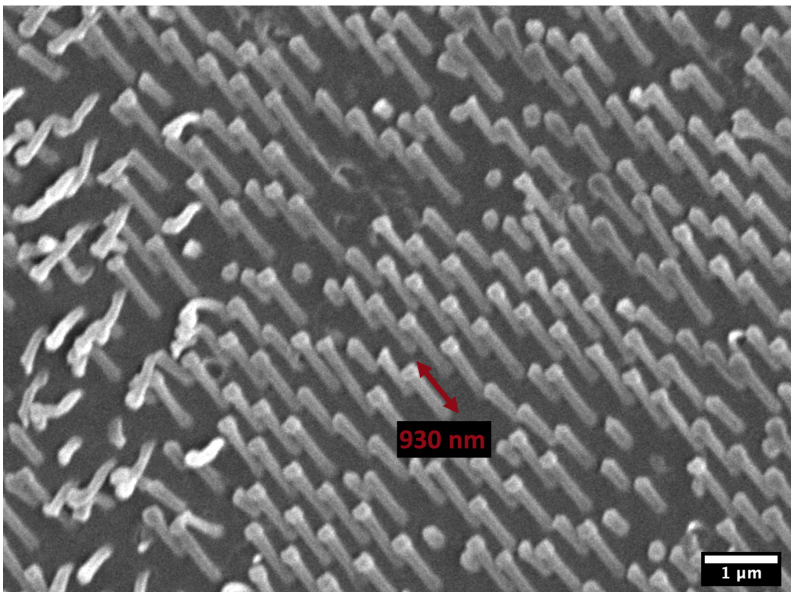


Figure 4.2.5: SEM of a NSS made from 30 wt% PS, showing stretching of the nanopillars to a height beyond the depth of the holes on the mould.

The nanopillars on the PS surface are clearly elongated, with some being measured at up to 1 µm in height. As PS is a glassy polymer, and therefore very stiff, it would not be expected to stretch far before fracturing (as seen with the PMMA). However, these pillars stretch to over double their standard length without breaking. A likely explanation for this effect is that some of the solvent from the solution had remained trapped in the polymer network (i.e it was not fully cured before it was released from the mould). Residual solvent can reduce the glass transition temperature of the polymer (T_g - the temperature at which the polymer moves from a hard, "glassy" state to a rubbery state) [141], and therefore could explain why the nanopillars were able to stretch so far without breaking.

PS Solution Concentration Series

To attempt to improve the replication quality of the PS NSS, the wt% of the solution was decreased. PS solutions at 10, 5, and 3 wt% were cast onto the LS mould, and the resulting NSS were measured with AFM. Figure 4.2.6 shows that the mean pillar height on the PS NSS decreases with the decreasing solution concentration, with the nanopillars formed from the 3 wt% solution being a similar height to the depth of the holes on the mould. As the same volume of each solution is deposited onto the moulds, the higher wt% solutions result in a thicker final surface due to the higher polymer content. For these thicker surfaces, a "skin" formed on the top of the solution during the early stages

of drying as the solvent quickly evaporated. It is possible that this "skin" layer slowed the evaporation of the solvent through the polymer network, especially towards the base (near the nanopillars), causing some to be trapped. This could then cause the pillar stretching observed in Fig. 4.2.5. For the lower wt% solutions the resulting surface was thinner and this skin layer did not form as quickly, allowing a more thorough evaporation of the solvent.

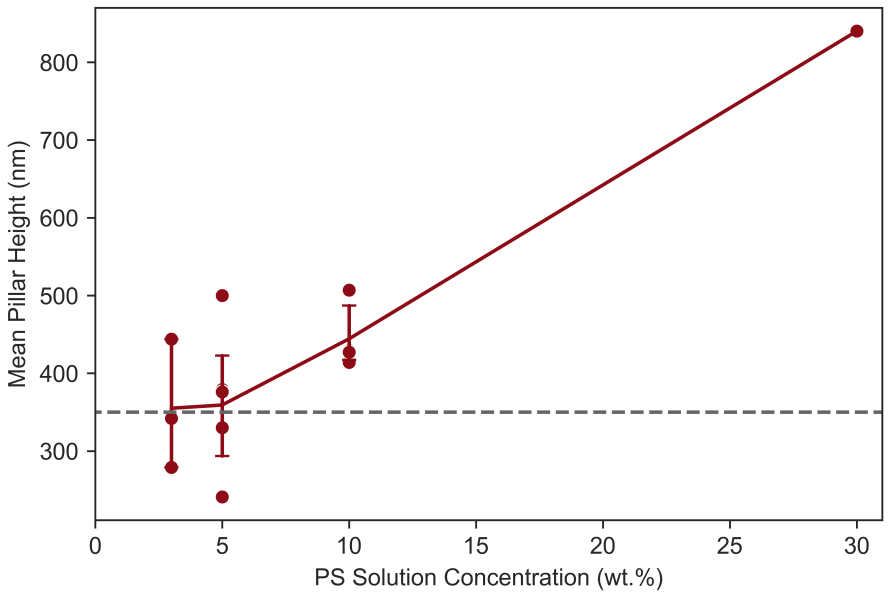


Figure 4.2.6: Mean height of nanopillars on polystyrene NSS cast from different concentration (wt%) solutions, measured with AFM. Dashed line represents the depth of the holes in the mould.

Vacuum-aided Curing

To further improve the replication quality of the polystyrene NSS, an additional step was added into the production process. After casting the solution on the mould, it was placed in a vacuum oven at 200 mBar for 20 min at room temperature to aid the solvent evaporation and to ensure that the mould is fully filled by drawing the solution into the holes. After the pre-cure in the vacuum oven, the surfaces were then cured at 40°C for 24 h, as before, before being peeled from the moulds. SEM evaluation of an NSS fabricated in this way from a 10 wt% PS solution is shown in Figure 4.2.7. The nanopillars are noticeably less stretched than those shown in Figure 4.2.5, and appear to be shorter compared to the 10 wt% surfaces in Figure 4.2.6. Measurements of the vacuumed surface with AFM revealed that the mean pillar height was 360 ± 60 nm, in comparison to 440 ± 40 nm using the previous method. There is still some stretching after using the vacuum technique, as evidenced by the thinning of the nanopillar towards its tip (inset of fig.

4.2.7). The "lollipop-like" morphology of the pillars may also be evidence that some solvent remained trapped even after the additional processing, as it appears that the tops of the pillars may have sunk/collapsed slightly onto themselves - giving a rounded end. However, given that the feature height is inline with the depth of the holes on the mould, even for a higher wt% PS solution, the additional vacuum processing step clearly leads to better replication quality for the casting and moulding fabrication method.

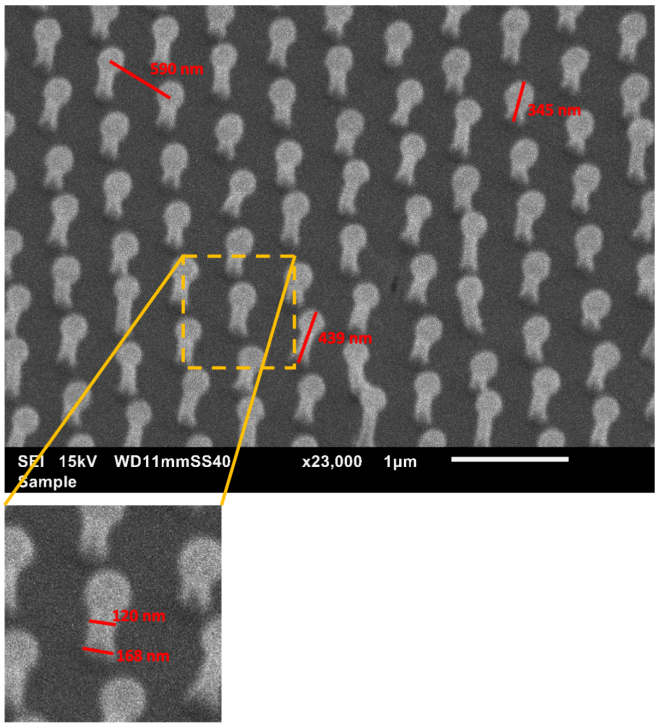


Figure 4.2.7: NSS produced from 10 wt% PS using an additional vacuum curing step to aid the evaporation of the solvent, evaluated with SEM

4.2.3. Casting Elastomeric Polymers

Polystyrene is a typical example of a glassy, stiff polymer (its Young's modulus is $\sim 3\,\text{GPa}$ [142]). For this moulding technique to be considered as a success, it needs to be capable of producing NSS from a range of polymers with different properties. To test the full ability of this procedure, elastomeric polymers were also tested for moulding into NSS. These materials are based on block copolymers, consisting of two or more individual polymer "blocks" covalently bonded together, which undergo micro/nanoscale phase-separation into distinct regions [143]. For this study Kraton polymers were selected, which are a range of thermoplastic elastomers based on styrene–ethylene–butylene–styrene (SEBS) block copolymers. SEBS block copolymers are formed from a rubbery block

(ethylene–butylene) which is bound on each side by a glassy block (styrene) (illustrated in Figure 4.2.8).

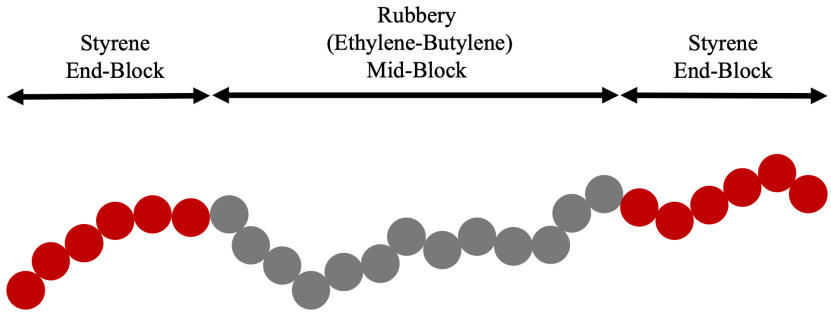


Figure 4.2.8: The structure of SEBS block copolymers. Glassy polystyrene blocks surround a rubbery mid-block. Tuning the ratio of the blocks can tune the bulk stiffness of the polymer. Adapted from [144].

Adjusting the ratio of the rubbery to the glassy block gives varying stiffness of the polymer. The two elastomers tested here were Kraton G1657, which has a PS content of 13%, and Kraton FG1901, which has a PS content of 30%. The low proportion of PS results in polymers which are much softer and more flexible than pure polystyrene. AFM measurements of a flat film of both the polymer shows the phase separation of the styrene and ethylene-butylene blocks (seen in Figure 4.2.9), with the individual domains very clear for both.

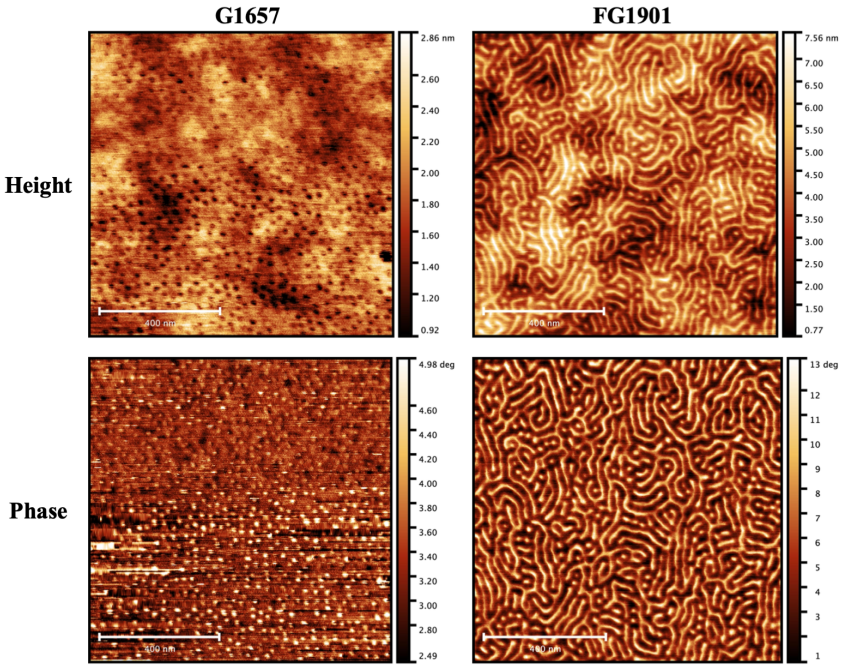


Figure 4.2.9: Phase separation of the styrene and ethylene-butylene blocks of Kraton G1657 and FG1901 films, imaged with AFM in height and phase mode.

Casting Kraton G1657

The first of the Kraton polymers tested was G1657 (13% PS), which was initially dissolved in toluene to 15 wt% and cast onto the moulds and cured, as before. The softness and flexibility of this polymer allowed for a much better release from the mould than the PS, and this is borne out in the replication quality of the nanopillars. Characterisation of these G1657 NSS is shown in Figure 4.2.10.

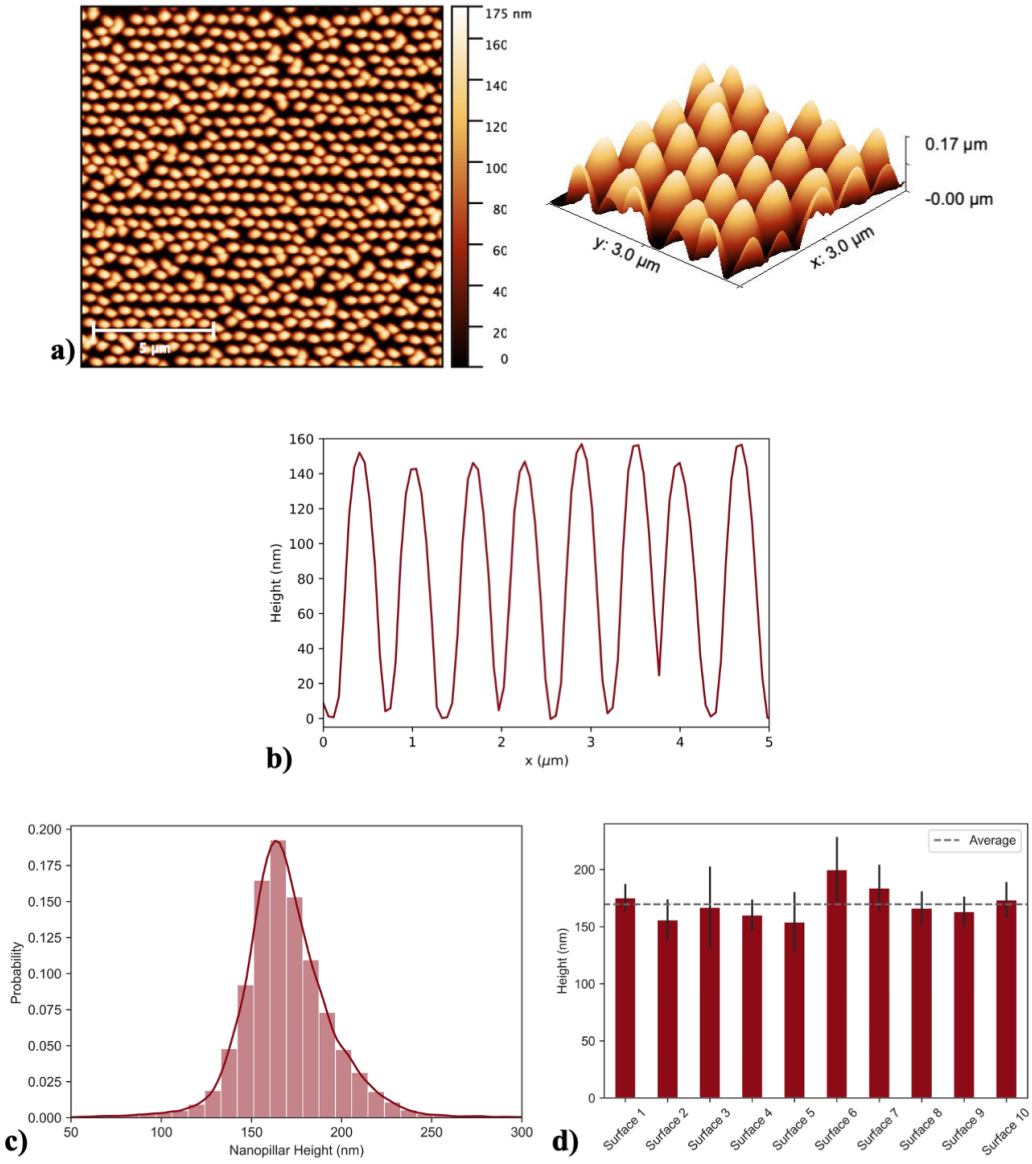


Figure 4.2.10: NSS made from 15 wt% Kraton G1657 using the LS mould. a) Representative AFM of the NSS, b) Height replication remains consistent over 10 replications of the NSS. c) Distribution of the heights of the nanopillars over the 10 NSS. d) Line profile taken across the AFM scan.

Figure 4.2.10a shows a representative AFM scan of the nanopillars on the G1657 NSS made with the LS mould. Compared to the PS NSS in Figure 4.2.4a, the nanopillars on the G1657 have much better height replication, with no signs of the pillars being stretched. There is however, some clustering of the pillars evident on the G1657 surface as the tips of the pillars bend to contact each other. This explains why the nanopillars on this surface also appear less ordered in their hexagonal pattern than the PS NSS. Figure 4.2.10b shows a line profile taken through one of the AFM scans of the G1657 NSS. It shows that the nanopillars have a similar morphology to what was seen on the *M. intermedia* surface, as they taper in towards a narrow tip.

The process of moulding the G1657 polymer was repeated 10 times consecutively, without cleaning or re-coating the master mould. AFM measurements of the NSS produced from this found that the average height of the nanopillars was 170 ± 14 nm, with only a 12% difference between the highest and lower values (Figure 4.2.10d). This highlights the consistency of the moulding and casting method for making NSS and shows that the FOTS coating is durable enough to last at least 10 rounds of polymer moulding before being replaced.

Despite the height of the pillars being just over half the depth of the mould, this is much more desirable result than stretching of the pillars as it is much more controllable and therefore gives more consistent results (as shown by Fig. 4.2.10d). For example, for the PS NSS produced using a vacuum the pillar height varied by 17% around the mean of 360 nm, whereas the G1657 only vary by 8% around the mean of 170 nm. Figure 4.2.10c shows that the nanopillars heights on the G1657 NSS follow a normal distribution with a narrow spread (in contrast to the cicada wing nanostructures which had a bimodal height distribution). This would be expected given that the depths of the holes on the mould should be uniform, but it is more confirmation that the moulding process produces consistent nanopillars.

G1657 Solution Concentration Series

As with the PS, the replication ability of the G1657 polymer at a range of solution concentrations was tested. AFM was used to assess the average nanopillar height with the results given in Figure 4.2.11. This shows that the nanopillar height on the G1657 surfaces increases with decreasing solution concentration, which is counter to the results seen for the PS solution concentration series. It is likely that this is due to a combina-

tion of the decreased viscosity of the solution allowing better filling of the holes and the rubbery qualities of the G1657 helping to prevent the plastic deformation/stretching of the pillars seen in the high wt% PS solutions. It is also likely that the block copolymer architecture enables more efficient and faster solvent removal via the rubbery network, than would be possible through a continuous glassy film.

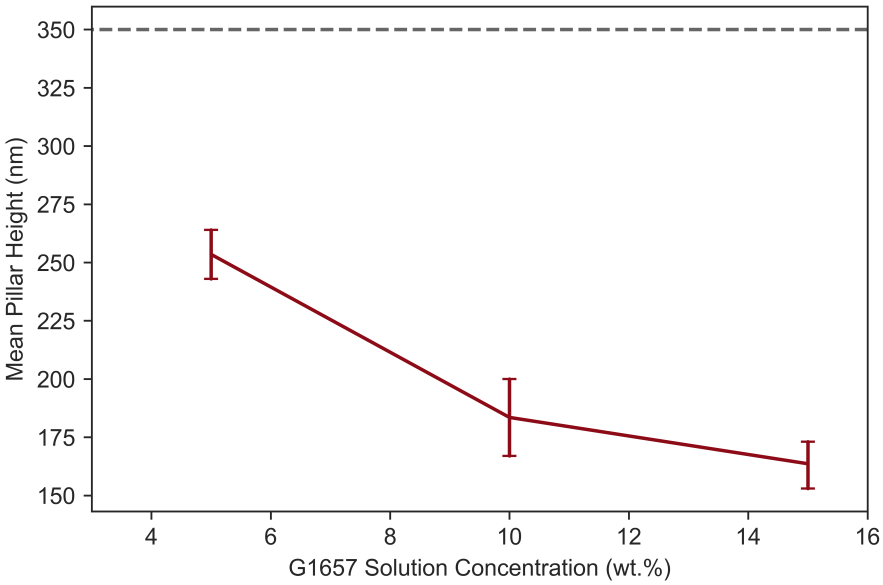


Figure 4.2.11: Average nanopillar height, measured with AFM, on Kraton G1657 NSS increases with the decreasing wt% of the polymer solution. Dashed line represents the depth of the holes in the mould.

Testing Bactericidal Properties of G1657 NSS

To assess whether the NSS produced from the G1657 had been conferred with bactericidal properties, an assay similar to that used in section 3.2.3 was used. Briefly, *E. coli* (MG1655) was grown from overnight culture to exponential phase (OD_{600} = 0.4 - 0.5) in LB media, before being centrifuged to pellet the bacteria. The media was then replaced with 0.9% NaCl buffer. This suspension was then incubated on the G1657 NSS, a flat G1657 control and a glass control for 2 h before rinsing and staining the adhered cells with the LIVE/DEAD BacLight Bacterial Viability Kit for 30 min (details given previously in section 2.3) and then imaging with a Nikon Wide-field microscope.

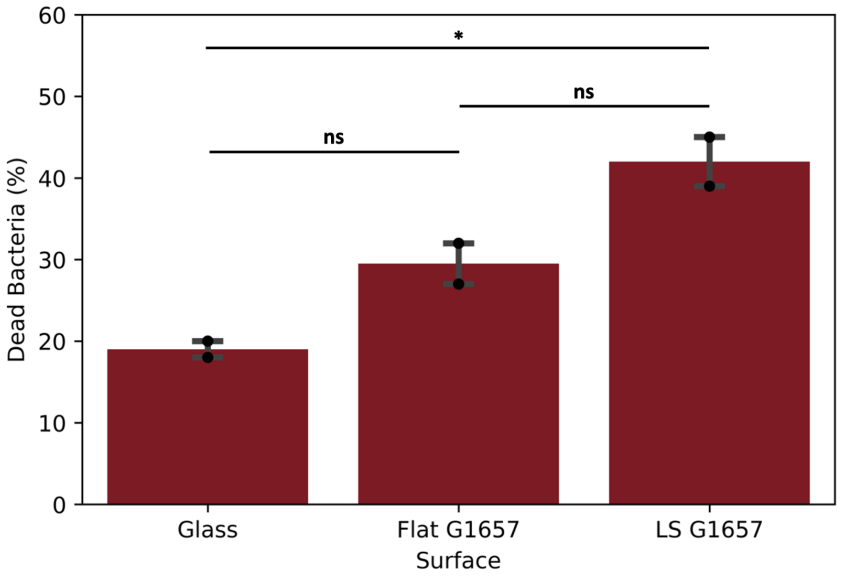


*Figure 4.2.12: Bactericidal Efficiency of the G1657 NSS against E. coli after 2 h of incubation determined with Live/Dead staining. Significance test carried out with one-way ANOVA. * - p = 0.012, (n=2).*

The results of 2 repeats of the Live/Dead assay on the G1657 surfaces is given in Figure 4.2.12. The NSS G1657 killed 42 ± 4% of the *E. coli* found on their surface, which is a 121% increase in the percentage of dead *E. coli* over the glass control surface and a 40% increase over the flat G1657 control. Therefore, the nanostructured G1657 surface did show an enhancement in the percentage of dead *E. coli* on its surface after 2 hours of incubation, indicating that it had been endowed with some bactericidal ability. However, there was only a significant increase in killing over the glass control surface, not over the flat G1657. Only 2 repeats of this experiment were carried out so any conclusions about the significance of the results are less meaningful, but the nano-patterning of the G1657 polymer did appear to successfully create an antibacterial surface.

Casting Kraton FG1901

Casting Kraton G1657 onto the LS mould did seem to confer it with some antibacterial effect, albeit not at a significant level over both controls. Therefore, another Kraton polymer (FG1901, 30% PS) was tested to verify if the technique could be used on other elastomers with higher PS content to enhance the antibacterial effect. The FG1901 was dissolved in toluene to 10 wt% and cast onto the LS mould before curing for 24 h. At this point it should be noted that during the course of testing different polymers to make NSS, the LS mould became contaminated with residual polymer and therefore the holes

were not as deep as before (even cleaning with piranha solution, which is a mixture of sulphuric acid and hydrogen peroxide, could not restore the mould to its original parameters). Results of this moulding process with the FG1901 polymer are shown in Figure 4.2.13.

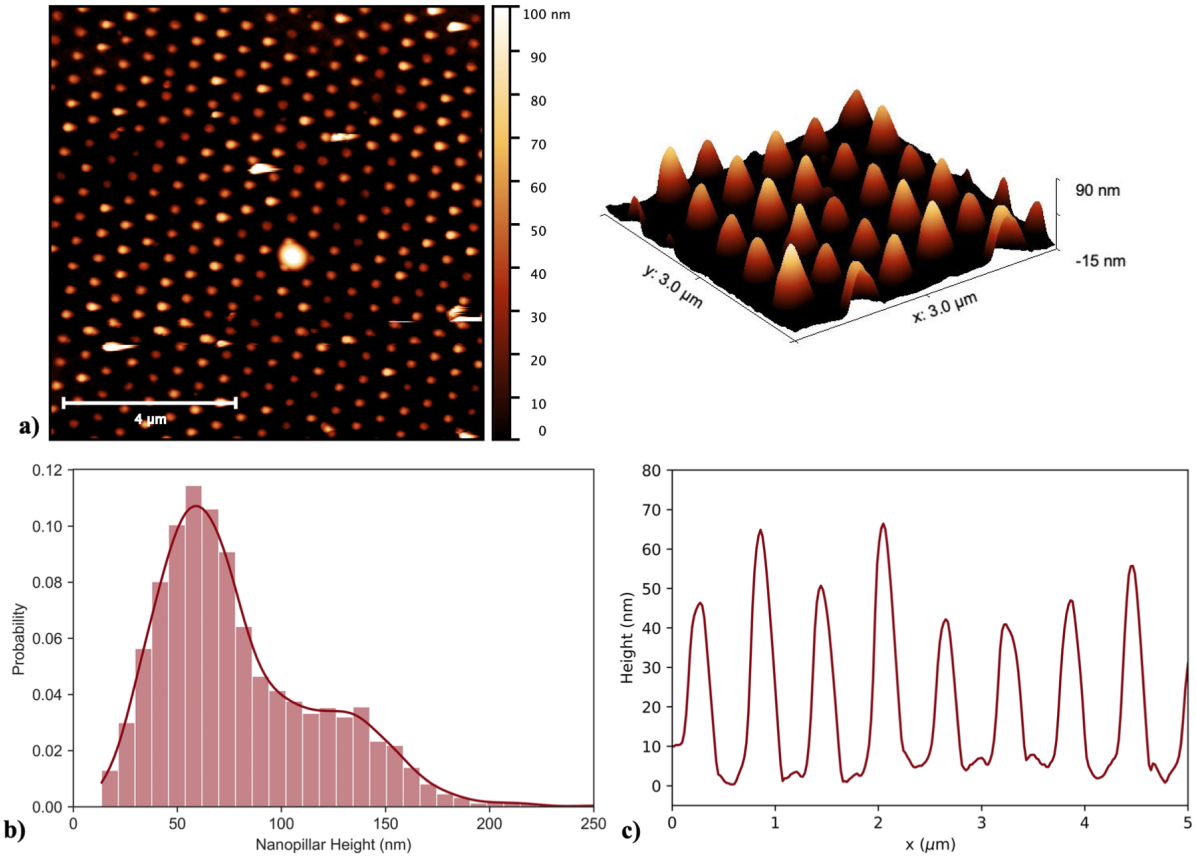


Figure 4.2.13: NSS made from 10 wt% Kraton FG1901 using the LS mould. a) Representative AFM of the nanostructures. b) Distribution of the heights of the nanopillars over the NSS. c) Line profile taken across the AFM scan.

The AFM images of the nanostructures (Fig. 4.2.13a) highlight the fact that they are noticeably shorter than the features on the G1657 NSS. As mentioned, this was due to contamination of the mould reducing the depth of the holes. Analysis of the AFM data revealed the distribution of heights of the nanopillars (Fig. 4.2.13b) and found the average pillar height for 8 FG1901 NSS to be 80 ± 40 nm. This distribution of heights is broader than for the pillars on the G1657 surface, but was due to the mould no longer being homogeneous. However, this still confirms that the moulding and casting method is an effective way of fabricating NSS for multiple different polymer materials.

Testing Bactericidal Properties of FG1901 NSS

The bactericidal ability of the nanostructured FG1901 surfaces was assessed against exponential phase *E. coli*, suspended in 0.9% NaCl buffer. The bacterial suspension was incubated on the NSS FG1901, and glass and flat FG1901 control surfaces for 24 h before staining with the BacLight LIVE/DEAD kit for 30 mins. The results of 5 repeats of this assay is shown in Figure 4.2.14.

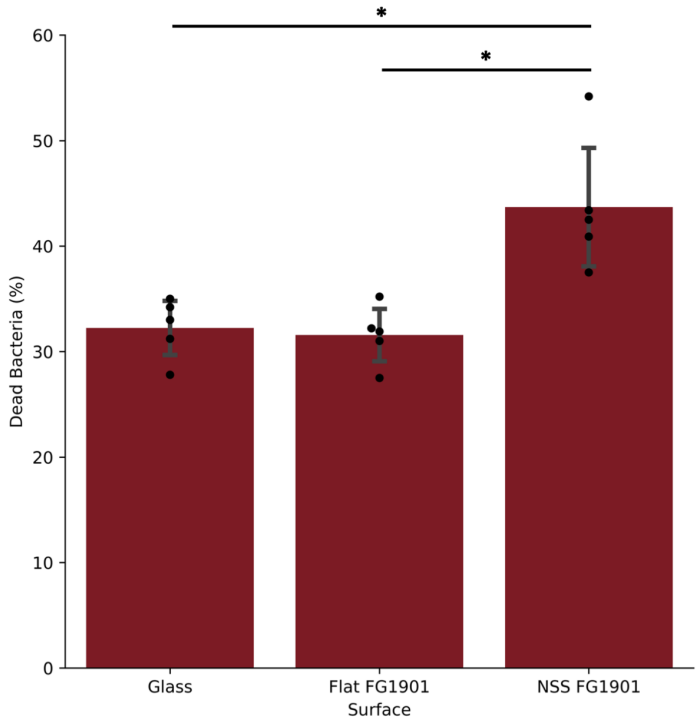


*Figure 4.2.14: Bactericidal Efficiency of the FG1901 NSS against E. coli determined with Live/Dead staining. (n=5) Significance test carried out with one-way ANOVA. * - $p \leq 0.05$. (n=5)*

An average of 44 ± 6% of *E. coli* were killed on the structured FG1901 surface after 24 h of incubation. This is a 38% increase in the percentage of dead *E. coli* over the glass surface and a 36% increase over the flat FG1901 surface. This killing enhancement for the NSS FG1901 was significant over both the glass and flat FG1901 surfaces. There was no significant difference found between the percentage of dead *E. coli* on the glass and flat FG1901 control surfaces, which shows that any killing enhancement of the NSS is not due to chemical effects from the surface. The absolute bactericidal efficiency of the FG1901 was found to be similar to that of the G1657 NSS, albeit over a longer incubation time.

4.2.4. LS Casting Summary

The moulding and casting with the LightSmyth master has therefore been shown to be an effective method for producing antibacterial NSS from a range of polymer materials. Thermoplastic elastomers have not previously been investigated as candidate materials for antibacterial NSS, but two such elastomers (with different PS content, and therefore mechanical properties) have been validated here. The bactericidal efficiencies of both the G1657 and FG1901 NSS exceed 40% against exponential-phase *E. coli*, although the fold-increase over the control surfaces was higher for the G1657 surfaces. This is most likely due to the increase in nanopillar height for these surfaces (170 nm) compared to the FG1901 surfaces (80 nm), it is well reported in the literature that bactericidal efficiency of NSS increases with the height of the nanostructures, up to a point [72, 82]. Dickson *et al.* had previously developed NSS made using a similar method with the same LightSmyth mould [46]. They used PMMA as the base polymer for the moulding and tested the bactericidal ability against *E. coli*, finding 11% killed after 20 hours of incubation. This appears to be a significantly lower killing degree than the surfaces with near-identical parameters produced here. However, looking at the fold-increase in killing over the respective control surfaces, Dickson *et al.* found a 16% increase, compared to 40% and 36% for the G1657 and FG1901 respectively. These differences are small and could be attributed to the difference in incubation conditions of the bacteria on the NSS. Here, the *E. coli* are resuspended in 0.9% NaCl buffer before incubating on the surfaces, whereas Dickson *et al.* incubated the cells directly in media. Incubation of the cells in media may have allowed some recovery of damaged, but not dead, bacteria leading to a lower killing efficiency for the NSS compared to the ones in buffer (which does not allow cell growth/recovery).

Whilst nearly half of all the *E. coli* on both the Kraton NSS produced from the LightSmyth mould were killed by the nanostructures, there is still room for optimisation to achieve much higher killing levels. Most antibacterial technologies require at least 99.9% of bacteria to be killed, so much improvement is needed in order to accomplish this. One potential route to achieve this is to optimise the parameters of the nanostructures, for example, reducing the spacing between pillars is well reported to increase the killing efficiency [38, 46, 55]. With this moulding technique this would be require changing the dimensions of the master mould, in order to imprint different patterns on the polymers. The next section will discuss the preliminary results of NSS produced with a new master mould, based on the topography of the cicada wing.

4.2.5. The Cicada Replica "mould"

In order to optimise the killing ability of the NSS, a new silicon master mould was fabricated by Dr Paul Fry (Department of Electronic and Electrical Engineering, University of Sheffield) using a previously described technique [145]. Briefly, a 200 nm layer of Silicon Dioxide (SiO_2) was deposited onto a silicon wafer using plasma enhanced chemical vapour deposition (PECVD). A resist layer was then spin-coated onto this and patterned using electron beam lithography (EBL) - this sets the dimensions of the nanopillars. Finally, Reactive Ion Etching (RIE) was used to etch the SiO_2 in the areas not covered by the resist, leaving a pattern of holes on the surface. These holes on this mould are designed to mimic the features on cicada wings, and have a similar depth, diameter and pitch to the nanopillars on the *M. intermedia* wing measured in section 3. The dimensions of the holes on the "cicada replica" (CR) mould, as set by the EBL of the resist, are given in Table 4.2.2 which were confirmed with the SEM and AFM measurements, shown in Figure 4.2.15. The same cleaning and FOTS coating process that was used for the LightSmyth mould was applied here.

Table 4.2.2: Summary of the fabrication values for the CR mould parameters, compared to the sizes of the features on the cicada wing.

Parameter	**CR Mould Value**	**Cicada Nanopillars**
Depth/Height (nm)	200 ± 10%	210 ± 50
Diameter (nm)	130	140 ± 20
Pitch (nm)	160	160 ± 10
Aspect Ratio	1.5	1.5

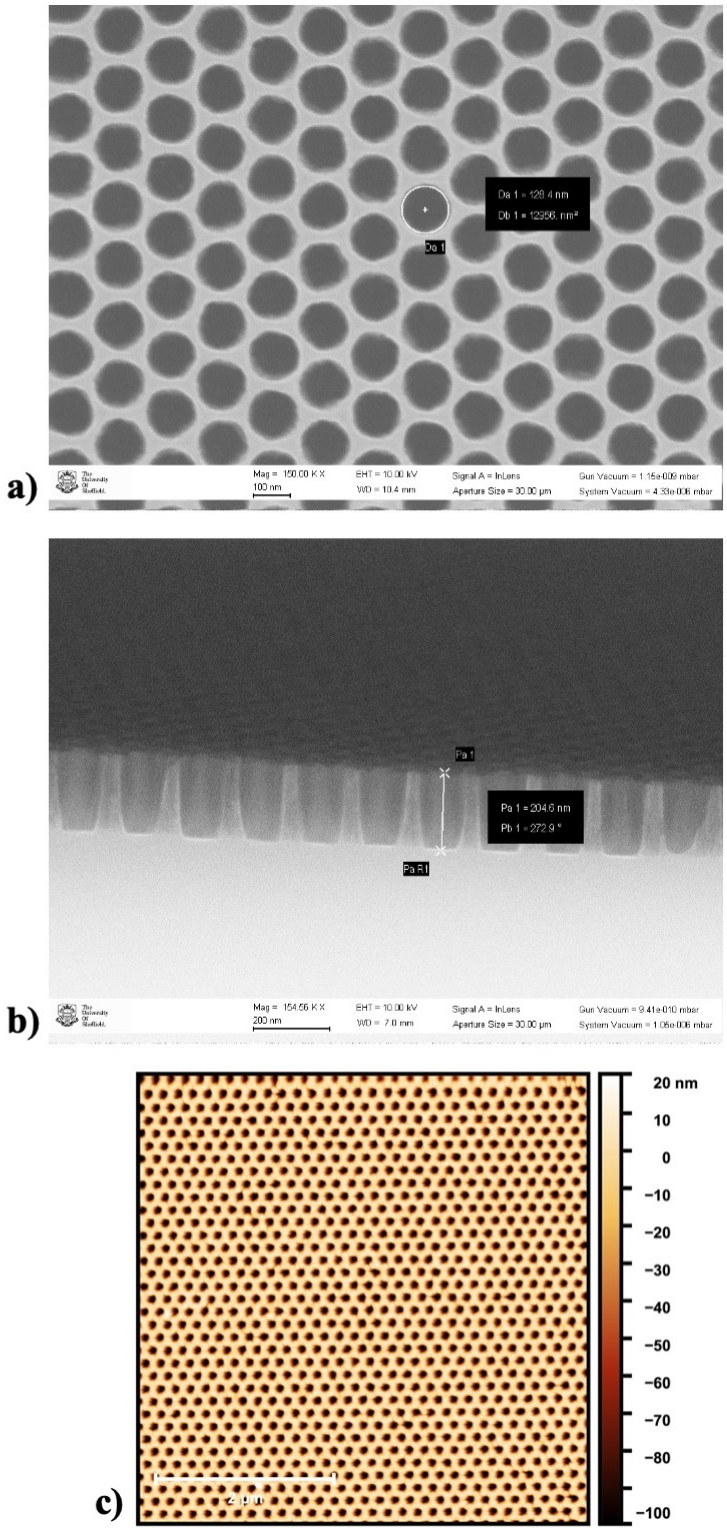


Figure 4.2.15: SEM (a - top view and b - side view) and AFM (c) images of the Cicada Replica master template mould used to make NSS

The first polymer tested on the CR mould was Kraton G1657. Polymer solutions were diluted to different concentrations, which were then cast onto the moulds in the same way as before. After curing at 40°C for 24 h the NSS were removed from the moulds and assessed with AFM. Three different concentrations of G1657 solution were tested - 15, 10 and 5 wt% - to see if this had the same effect on the replication quality as it did for the LS mould. Representative AFM scans of each of the surfaces are shown in Figure 4.2.16.

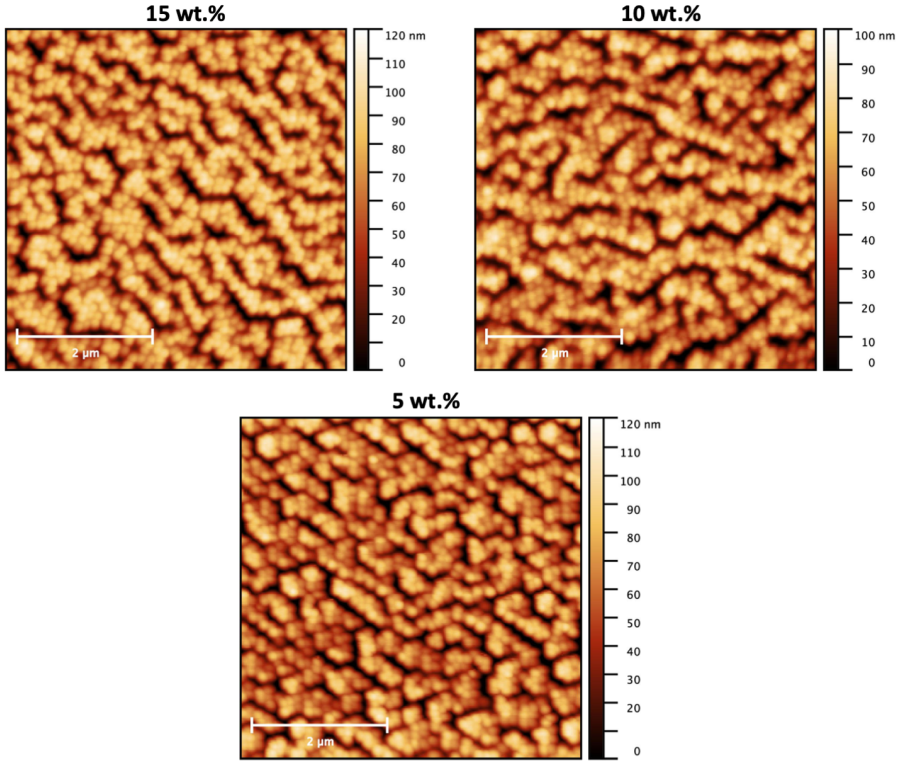


Figure 4.2.16: AFM images of G1657 NSS made with the CR mould using different solution concentrations - 15, 10, and 5 wt%.

It is immediately clear that the replication quality of the CR mould is inferior to the LS mould, when directly comparing the NSS made from G1657. At all solution concentrations there are large defects/gaps in the replication pattern, which take the form of trenches that run across the surface. A possible explanation for these gaps is that the nanopillars have clustered together after being released from the mould, due to the low stiffness of the polymer - G1657 has the lowest PS content of the all the polymers tested and so is the softest. It is clear in Fig. 4.2.16 that the spacing between the nanopillars is not uniform (unlike the mould it came from) which could be attributed to clustering of the tips. This effect was also seen with the G1657 polymer on the LS mould, although to

a lesser extent due to the increased spacing of the pillars.

The AFM measurements of the nanopillar height (Figure 4.2.17) gave an average height of 74 ± 23 nm across all the concentrations. There was a small difference between the nanopillars for the different solution concentrations with the average height measured at 75 ± 23 nm, 63 ± 17 nm and 92 ± 21 nm for the 15, 10 and 5 wt% solutions respectively. This is similar to the result found for the height of the nanopillars vs. solution concentration with the LS mould (Fig. 4.2.11), with a more dilute solution giving better replication of the pattern (i.e. taller features) - although this trend is more subtle for the CR mould. This provides more evidence that reducing the viscosity of the polymer solution helps it to fill into the holes more completely, therefore giving better height replication. However, compared to the LS mould, the replication quality from the CR mould using G1657 was significantly reduced, with the "best" height of the nanopillars <50% the depth of the holes on the mould (~70% filling was achieved on the LS mould).

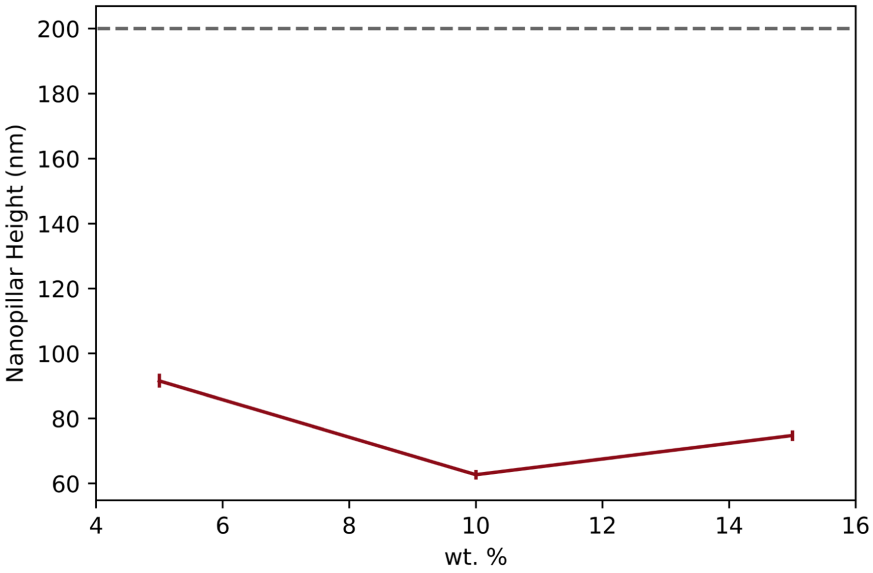


Figure 4.2.17: Nanopillar height for the G1657 NSS made with different concentration G1657 solutions, assessed using AFM. Dashed line represents the depth of the holes in the mould.

Next, imprinting pure polystyrene using the CR mould was tested. The PS (M_w = 350k) was diluted to 10 wt% in toluene and cast onto the surface. It was then placed in a vacuum oven at 200 mBar for 20 min before curing at 40°C for 24 h. The consistency of the pattern replication was much better for the PS than the G1657, with fewer defects, as shown by the AFM and SEM in Figure 4.2.18. As described previously in section 3, the force required to bend a beam/pillar with a fixed end, described by the

Euler-Bernoulli equation (eq. 3.2), increases linearly with the stiffness/Young's Modulus of the beam. Therefore the higher stiffness of the glassy PS compared to the rubbery Kraton G1657, means that higher forces would be required to pull the pillars out of position and cause them to coalesce with their neighbours. This would explain why, generally, the PS surfaces from the CR mould retained good order and uniformity of the nanopillars, however, as Fig. 4.2.18c shows, in the areas with taller pillars some clustering is seen.

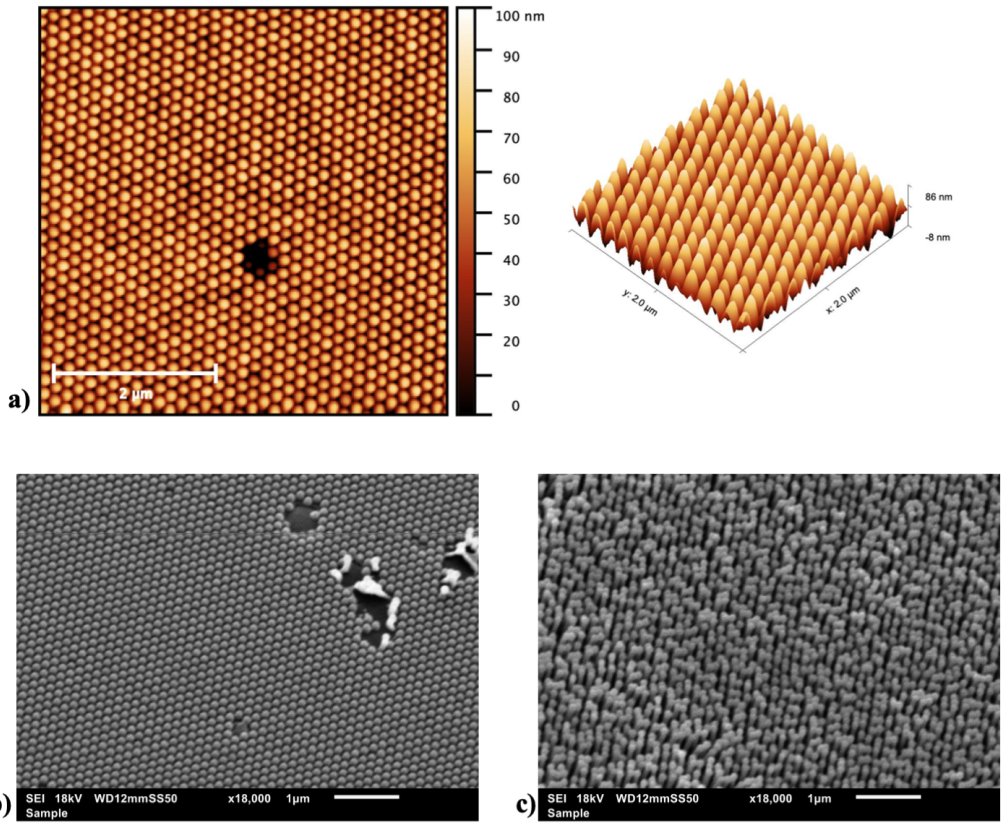


Figure 4.2.18: Polystyrene NSS imprinted using the CR mould, assessed with AFM and SEM. a) Height AFM images of the PS surfaces creating with CR mould. b) and c) SEM images of the same surface.

Measurements of the height of the pillars on the PS surfaces from AFM gave an average of 72 ± 19 nm which is almost identical to the pillars on the G1657 surface. The distribution of pillar heights (Figure 4.2.19) shows two populations, one centred at ∼65 nm and the other at ∼100 nm. These two different height populations are seen in the SEM images in Figure 4.2.18b and c. The pillars in Figure 4.2.18 b) are clearly low aspect ratio, although they appear very ordered, whereas the pillars shown in Figure 4.2.18c protrude much further out from the surface but cluster more.

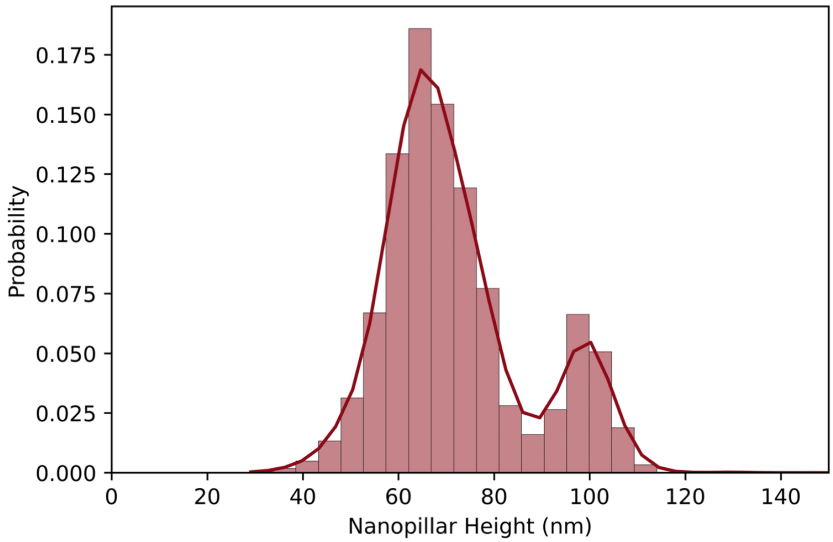


Figure 4.2.19: Distribution of pillar heights on the PS NSS made from the CR mould and measured with AFM.

Despite using the same technique and same polymer solutions that produced good quality nanopillars from the LS moulds, imprinting using the CR mould produced consistently lower quality NSS, with the height of the nanopillars typically $< 50\%$ of the expected value and clustering often seen. The more frequent clustering of the nanopillars on the CR mould compared to the LS mould can be attributed to the reduced spacing between adjacent features. It is possible that small, mechanical disturbances are responsible for pushing the nanopillars closer together so that they touch, but it is also possible that capillary forces between the nanopillars play a role (the NSS are stored in ambient conditions and are typically washed with DI water prior to use). As the distance between the nanopillars is much smaller on the CR mould compared to the LS mould (160 nm vs. 600 nm), these forces do not need to deflect the pillars much for them to come into contact with each other. This is a consideration that would have to be made for all NSS made from softer organic materials whose nanopillars are tightly packed, as this clustering may effect the bactericidal efficiency.

As for the poor filling of the CR mould, this could be explained by the surface tension of the solution preventing it from fully travelling the depth of the hole. As both the PS and G1657 polymers produced nanopillars with nearly identical heights, it is possible that there is a limit on the filling of the holes. If the holes in the mould are considered as narrow tubes/capillaries of radius a, then the pressure difference, ΔP, across the liquid interface is given by a modification of the Young-Laplace equation, Jurin's law (4.1), where γ is the

surface tension of the liquid and θ is the contact angle at the solid-liquid interface [146].

$$\Delta P = \frac{2\,\gamma\,cos(\theta)}{a} \tag{4.1}$$

The FOTS coating on the silicon mould, which helps with release of the cured polymer, lowers its surface energy and takes WCA, θ into the hydrophobic regime. The result of this is that the pressure from the surface tension works against good filling of the mould (for a hydrophilic mould the surface tension would pull the liquid further into the hole, unfortunately this would also prevent good release of the NSS after the polymer had cured). This surface pressure is increased for smaller diameter holes, which could explain why the filling was poorer for the CR mould (diameter = 130 nm) compared to the LS mould (diameter = 160 nm). Given that both the moulds used here are made from silicon, which is not gas-permeable, air may also remain trapped at the bottom of the holes - further preventing filling [147]. Placing the moulds under a vacuum after casting, as attempted here, can improve this by pulling out the air trapped in the holes. However, it also increases the speed at which the solvent evaporates and the surface cures, essentially setting the polymer before it has had chance to penetrate fully into the holes. Another potential improvement is to use a different solvent, with a lower surface tension γ, to dissolve the polymer into. This may help to make filling more favourable by reducing the surface pressure across the capillary, allowing a better replication of the mould.

Typically micro/nanoscale moulding of polymers is achieved through either *injection moulding*, where molten polymer is injected onto a mould before cooling and releasing, *hot embossing*, in which a polymer is heated above its T_g before being imprinted with a mould at high pressure, or simple *casting* as described in this chapter [148]. The results presented in this work have shown that a simple casting process is capable of producing high-quality, repeatable and low cost nanostructured surfaces from a range of different polymers using a commercially-available silicon mould. Further optimisation of this technique is required to produce high quality structures using solution casting into moulds with more densely-packed features. Moving to a hot embossing method could prove to be beneficial as the use of high temperature and pressure can force the polymer to conform to the mould, and therefore give better replication quality. This method would negate the problems associated with the solvents seen in the casting method presented here, such as trapping. This would also be more compatible with techniques such as roll-to-roll imprinting, allowing larger area NSS to be made, which is important when considering how

to scale these antimicrobial surfaces up for use in real-world settings.

One general limitation to any moulding technique is the need to use different moulds when changing parameter size of the nanopillars. This makes it hard to explore the full range of factors which may influence the bactericidal efficiency of these surfaces, and also to optimise them for killing a wide range of bacterial strains. Therefore it is important to test other techniques to produce NSS which allow better tuning of the surface features. The rest of this chapter will discuss trials of Nanosphere Lithography (NSL) as a technique for producing NSS.

4.3. Nanosphere/Colloid Lithography

One method that allows more control over the parameters of the NSS is Nanosphere Lithography (NSL). This is a technique that has previously been described in the literature for making nanostructures in glassy polymer films or inorganic materials such as silicon [77, 78, 149–151]. The basic principal of NSL is illustrated in Figure 4.3.1.

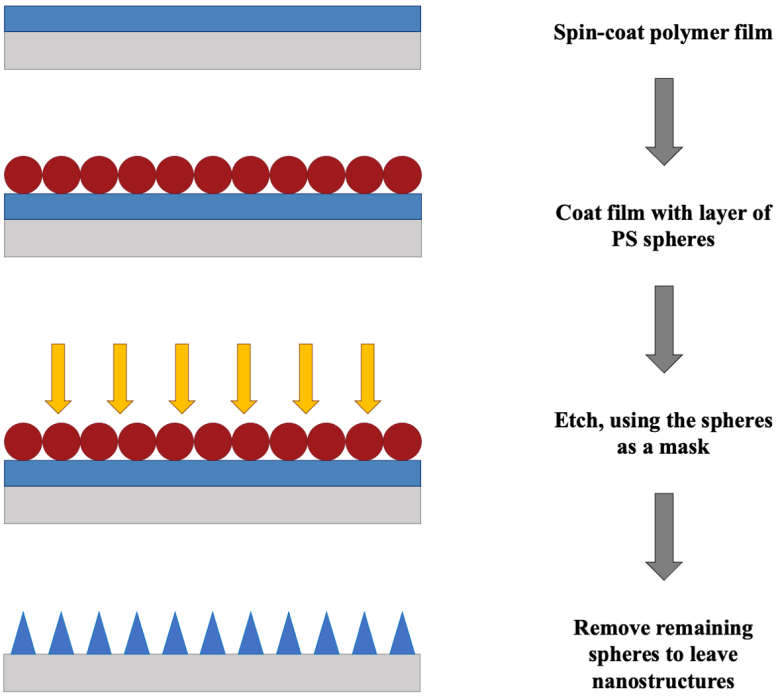


Figure 4.3.1: Process of using NSL to make polymer NSS, highlighting the deposition of the nanosphere monolayer to be used as a mask for etching nanostructures into the base polymer. Adapted from [78].

First, a polymer film (with thickness >> intended height of the nanopillars) is applied

to a clean silicon substrate, typically with spin-coating. Then a monolayer of PS spheres is deposited on top of the polymer film, which can be achieved through various methods such as spin coating or interface coating. The PS nanospheres act as a mask for the dry etching of the polymer film with either plasma or reactive ion etching - the areas between the spheres are preferentially etched as they shrink which leaves a pattern on the surface of the polymer. Finally, the remaining spheres are removed leaving the polymer with an array of surface nanostructures. Because the nanospheres preferentially arrange themselves into a hexagonal array, the resulting nanostructures are also ordered in this way - the same as the ordering of the nanopillars on the cicada wing. The dimensions of these nanostructures is set by the size of the nanospheres and the etching time (e.g. smaller spheres and shorter etching time gives shorter, closer-packed nanopillars) which allows good control over the features. This section will describe the progress made into the development of each aspect of this technique, from synthesising the nanospheres, deposition of a monolayer, to trialling etching of nanopillars.

4.3.1. Nanosphere Synthesis

The first trials of the nanosphere deposition used PS colloids, 500 nm in diameter, diluted to 10 wt% in water, purchased from Sigma Aldrich. 300 nm diameter PS colloids (Sigma-Aldrich) were also tested in this study. However in order to create nanopillars with different sizes and spacings, different sizes of colloids were required. A synthesis process called emulsion polymerisation was used to synthesise further PS colloids. Briefly, 50 ml water, 5 g styrene (monomer) and 2 mg NaCl were added to a round bottomed flask, fitting with a reflux condenser and magnetic stirrer. Whilst stirring, this mixture was heated to 60°C and had nitrogen bubbled through it for 30 min, in order to degas. Then, 50 mg ammonium persulfate in 2 ml water was injected into the mixture to initiate the polymerisation reaction. This was left to continue overnight to grow the size of the colloids, and when finished the liquid turned a milky-colour. This was then passed through a series of filters to remove larger aggregates and then washed by centrifugation and re-dispersion in fresh water in order to remove any unreacted styrene. Measurements of the size of the colloids was carried out with AFM and Dynamic Light Scattering (DLS), and are shown in Figure 4.3.2. The height of the colloids was measured with AFM (as this can be more accurate than the diameter due to tip broadening effects), finding an average value of 690 $\pm$ 250 nm. Fitting a Gaussian function to the peak value from the DLS measurements gave the average size to be 750 $\pm$ 190 nm. These two sets of results are broadly in agreement overall. In future the colloid size can be reduced by adding a surfactant such

as Sodium Dodecyl Sulfate (SDS) during the polymerisation to reduce the size of the monomer droplets. Control of the mixing speed and surfactant concentration allows the polymerisation of colloids with a range of sizes, which could then be used with colloidal lithography to etch different pillar sizes on NSS.

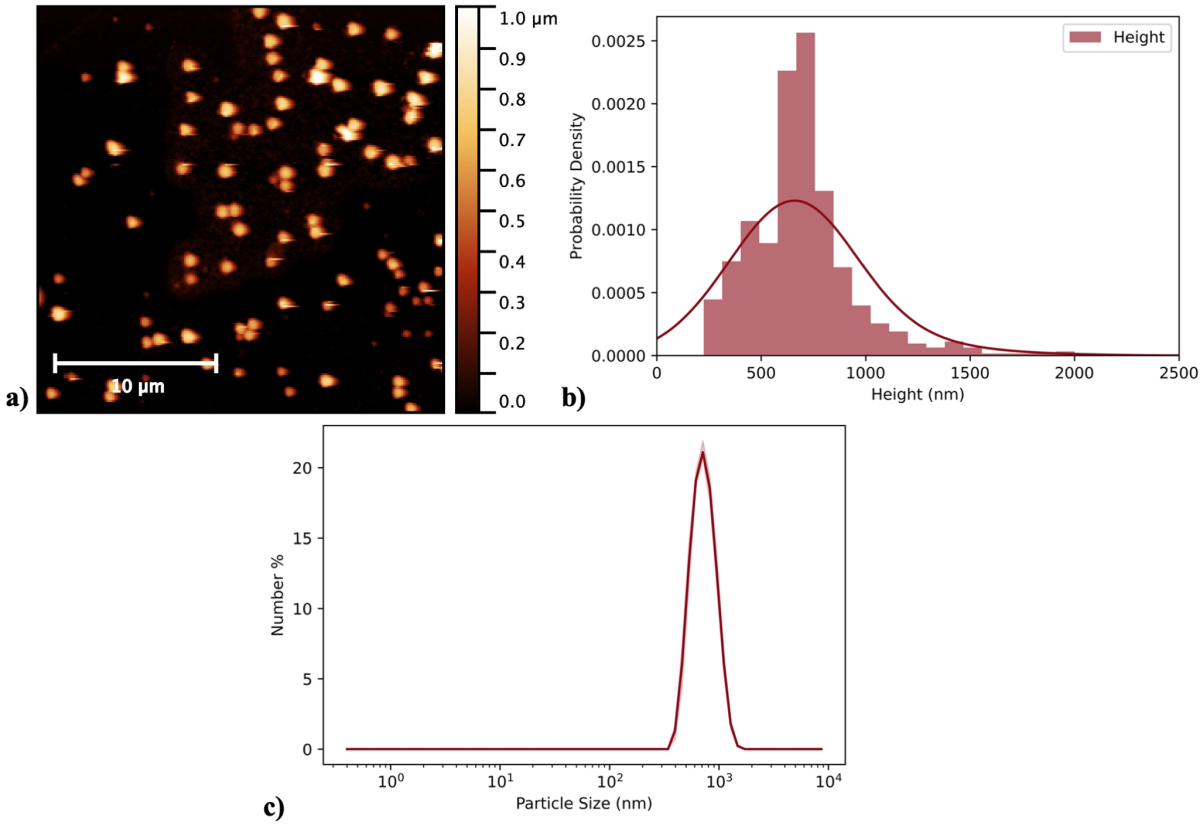


Figure 4.3.2: AFM and DLS measurement to determine the size of colloids produced through emulsion polymerisation. a) AFM height image of the colloids on a glass substrate. b) Histogram of the heights of the colloids measured with AFM. c) DLS data of the particle diameter.

4.3.2. Nanosphere Deposition

In order to produce a good mask for etching nanopillars in to a polymer, the PS nanosphere/colloids must be deposited as a monolayer. Several techniques to achieve this have been described in the literature, but this section will describe the testing and development of spin coating and angled interface coating. The evaluation of the quality of the deposition was carried out with a combination of bright-field optical microscopy and scanning electron microscopy.

Method I: Spin Coating

The simplest method for applying a monolayer of nanospheres to a surface is through spin coating. In the simplest form, a solution of the PS nanosphere (usually in water) is added to the substrate which is then rotated, casting off the solvent and leaving a layer of the colloids on the surface. This process is illustrated in Figure 4.3.3.

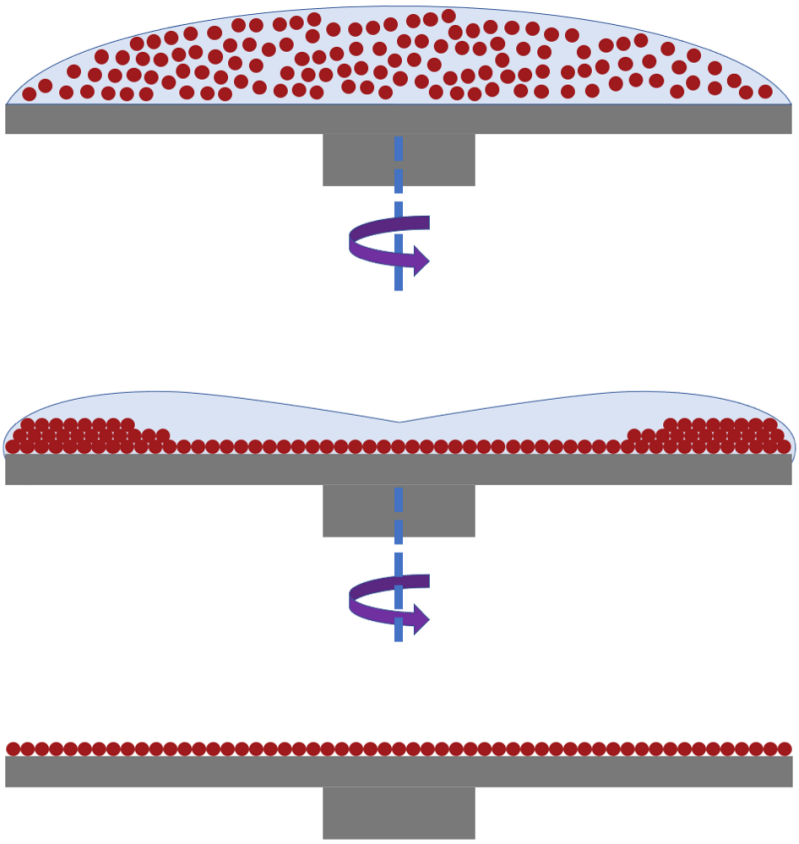


Figure 4.3.3: Process of depositing a monolayer of PS beads with spin coating. A solution of PS colloids is applied to a substrate which is then rotated in a spin-coater. This orders the colloids and drives the remaining solvent away, giving good ordering in the final monolayer. Adapted from [152].

The 500 nm PS colloids, diluted to 10 wt% in water (Sigma Aldrich) were used for this spin coating study. To create different concentrations of the colloids, the solution was centrifuged at 3500 rpm for 5 min to pellet the colloids. This pellet was then re-dispersed in different quantities of water to give different final wt%, and the solutions were sonicated for 15 min to ensure that the colloids were not aggregated. The spin coating was carried out with an Ossila spin coater. The first trial of the spin coating was carried out with 4 different concentrations of the colloids in water - 1, 2, 10 and 20 wt%. For each, ~100 µl

of the solution was deposited and manually spread across a cleaned glass coverslip and then spun at 3000 rpm for 30 seconds. The optical microscopy images in Figure 4.3.4 show the results of this test.

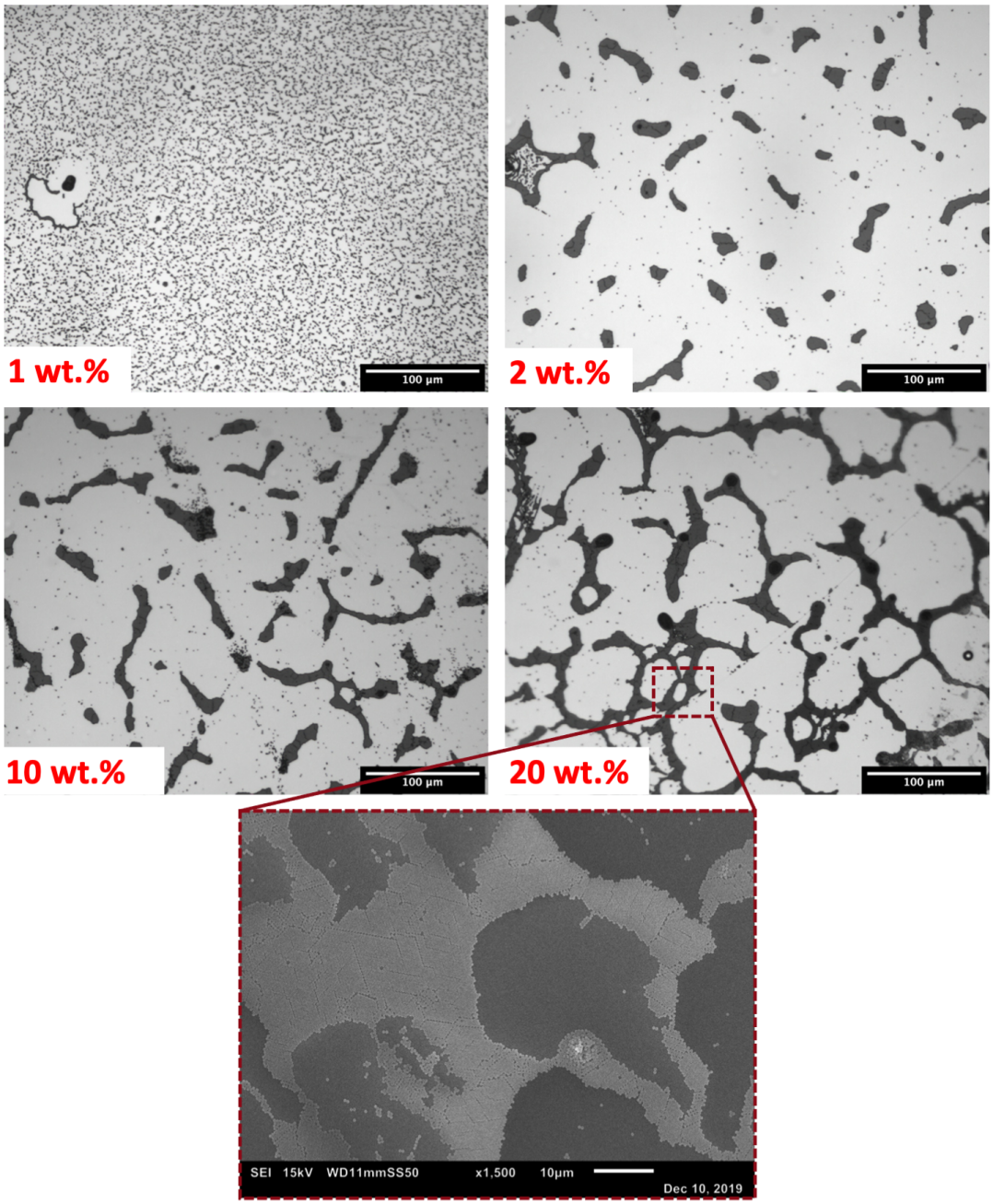


Figure 4.3.4: First trial of spin coating 500 nm PS beads onto glass substrate. Different concentrations of PS bead solutions were tested, spinning at 3000 rpm for 30s. The images here are from optical microscopy assessment of the distribution of the nanoparticles.

Firstly, the lowest concentration solution (1 wt%) showed a good homogeneity in the

dispersion of the colloids across the surface and there was only the occasional large aggregate seen which caused large gaps to form. However, there was no tight-packing of the colloids apparent. With the increasing solution concentration, the colloids moved from a uniform dispersion across the surface to islands of packed particles. The size of these islands increased with the solution concentration, indicating that the higher percentage of colloids in the solution aided their ability to tightly pack together into an ordered pattern. The inset of the 20 wt% sample is an SEM image of these islands, which shows that the colloids are well packed into monolayer in these areas. Toolan *et al.* described how spin coating low concentration solutions of colloids in a low volatility solvent (such as water) can lead to ordering being mainly due to "drying fronts" [153]. Capillary forces, from the surface tension of water between two colloids, are responsible for pulling neighbouring nanospheres into close packing. However, as the film dries the receding water line displaces these packed regions along the drying front, creating the large voids seen in Fig. 4.3.4.

To try and improve the packing quality of the monolayer, the 500 nm PS colloids were resuspended in a 50/50 mixture of water and ethanol, which is more volatile than water alone and so will evaporated faster, whilst still allowing the formation of the capillaries which pull the colloids together. A more complex spin coating routine was also used, which had previously been described by Shinde and Park [154] (given in Table 4.3.3). The first step involves spinning the substrate slowly (200 rpm) to spread the colloids uniformly over the surface. Next, the substrate is spun at 1000 rpm which begins to order the monolayer and make it more compact. The final step is at 6000 rpm which drives off the final solvent, pulling the colloids together into a tightly packed arrangement. This 3-step spin coating method was tested with PS colloid concentrations of 1, 5, and 10 wt% deposited onto cleaned glass coverslip, as before.

Table 4.3.3: 3-step spin coating parameters for applying monolayer of PS colloids. (From [154])

Step	**Speed (rpm)**	**Duration (s)**	**Role**
1	200	30	Spreading Colloids
2	1000	60	Ordering into Monolayer
3	6000	10	Tightly Packing

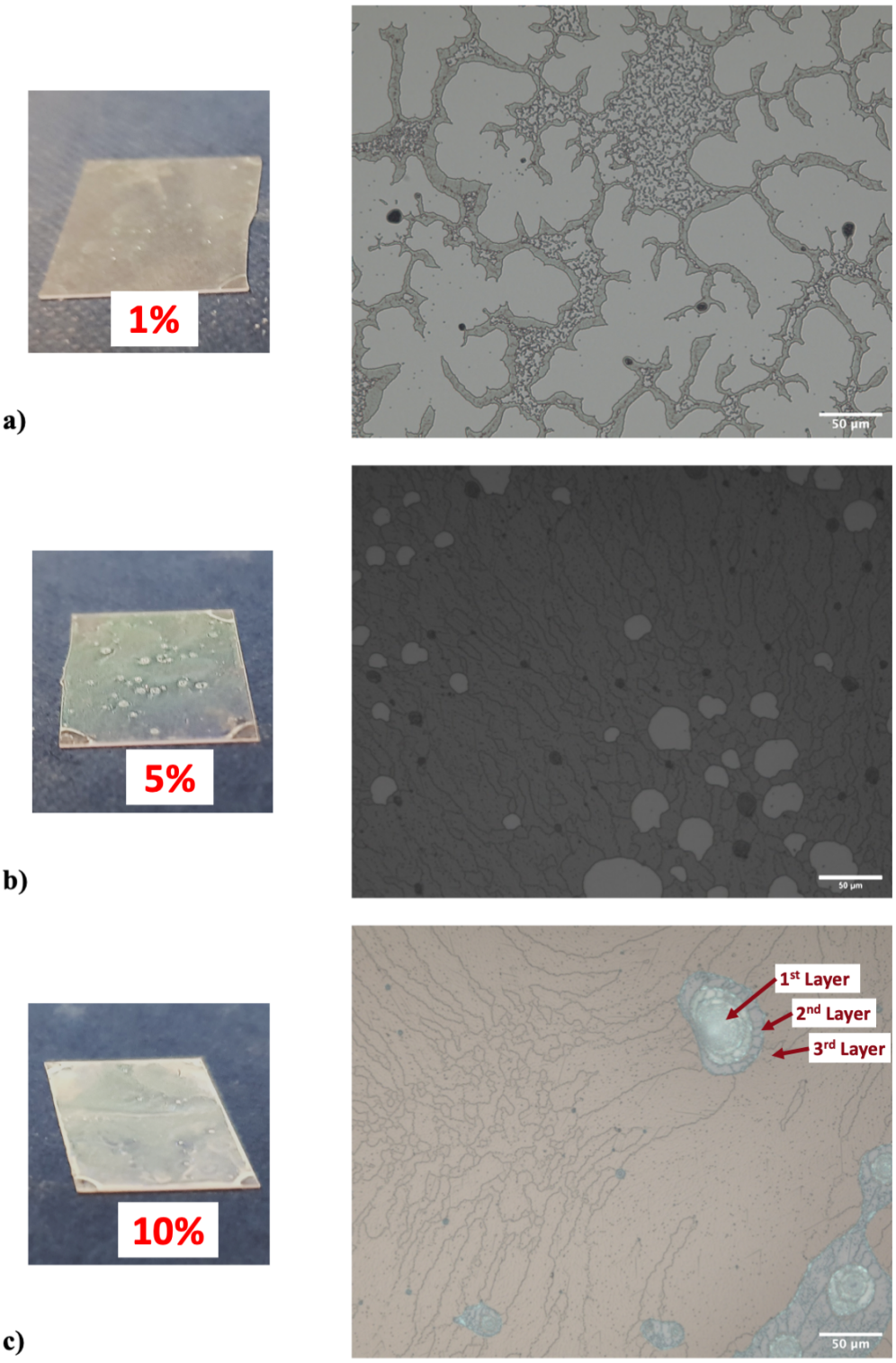


Figure 4.3.5: 3-step spin coating process for depositing PS colloids onto glass substrate. The concentration of the colloids (in a 50/50 water/ethanol solution) was changed from 1, to 5 to 10 wt%. The left column show photographs of the colloid layer on the glass substrate and the right column shows optical micrographs of those same layers.

Figure 4.3.5 shows example optical microscopy images as well as what the layer of colloids looks like on the substrate. For the lowest concentration (1 wt%), there is still not a uniform layer of colloids deposited across the surface and a similar drying pattern is found to what was seen for the 20 wt% solution for the 1-step spin coating procedure. This is likely due to the low concentration of colloids which results in the same drying front effect described above. However, for the higher solution concentrations, it was found that a successful layer of colloids was deposited onto the substrate. In particular, using the 3-step spin coating process with the 5 wt% solution gave a good monolayer of colloids across most of the substrate. Again, Toolan *et al.* described that when using a more volatile solvent system (such as 50/50 water/ethanol) the ordering of the monolayer is dominated by the shear forces from the spin coating [153]. After the colloids have spread across the surface, the shear forces allows the monolayer to flow and re-order into a tight Hexagonally Closed Packed (HCP) regime. There are still some defects/holes in the monolayer, as well as some large aggregates which can be seen in the photograph of the substrate but these do not seem to effect the quality greatly. AFM measurements were taken of the 5 wt% colloid film to investigate how well the nanospheres are ordered in the monolayer (Figure 4.3.6).

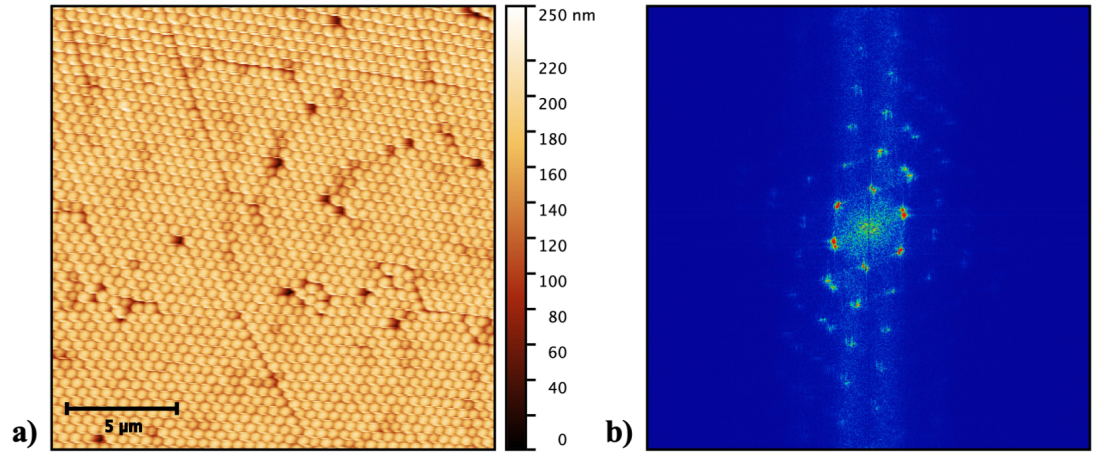


Figure 4.3.6: AFM data showing the well ordered structure of the colloid monolayer, spin coated (3-step) from 5 wt% PS in 50/50 H_2O/EtOH solution. a) AFM Height data, b) the resulting FFT from the height data.

As Figure 4.3.6a shows, the colloids are very well packed in the monolayer in a tight HCP arrangement. There is the occasional small defect but these appear not to have disturbed the overall arrangement. Taking the Fast Fourier Transform (FFT) of the AFM data (shown in Figure 4.3.6b) results in a series of discrete points which confirms the extremely well ordered, hexagonal structure of the colloids. The highly ordered nature of the colloid monolayer is also implied by the photograph of the 5 wt% film in Fig. 4.3.5b, which shows a slight iridescence pattern due to the diffraction and interference of light due to the colloids.

For the 10 wt% solution, the 3-step spinning procedure resulted in a colloid film with multiple layers stacked onto each other. This is clearly seen in the optical microscopy image in Fig. 4.3.5c, where the different layers are indicated by the different colours in the image. The blue areas indicate the base monolayer, the pink area that surrounds them are bilayers, and then the red layer which covers most of the image is the top layer. It is possible that the shear forces of the spin coating were not great enough to allow good ordering of the colloids into a monolayer at this increased concentration. Having multiple layers of colloids like this is not suitable for use as a mask for lithography as the etch would have to go through more layers in some areas than others, making the resulting structures inconsistent.

Whilst good results were achieved for spin coating of the colloids, large defects in the monolayer were still common. The inherent issues with spin coating as a technique, such as pinhole formation and comet streaks from sub-optimal substrate preparation, can cause defects when trying to assemble a large area monolayer of colloids. Any aggregation in the solution, which is common with colloid solutions, further enhances these issues. Therefore an alternative technique for assembling a colloid monolayer was tested.

Method II: Interface Coating

Interface coating, or Langmuir-Blodgett coating, is a technique in which a monolayer of colloids is assembled at the air-water interface and then transferred onto a substrate. An illustration of the process is given in Figure 4.3.7. First, a glass dish is filled with deionised water and a glass microscope slide is placed at the edge so that it meets the water interface at roughly a 45° angle. Then, $\sim 20\,\mu l$ of a 10 wt% solution of PS colloids (in H_2O/EtOH) is slowly dropped onto the slide. This is done in small drops to ensure that all of the previous drop is spread over the surface of the water before the next is

added, to avoid too much turbulence at the surface. As the PS colloids reach the water interface they diffuse and spread out across the surface. Once all of the PS solution was added, everything was left for 10 min to allow an equilibrium to be reached and the fast diffusion of the colloids across the surface to stop. During this time domains of ordered colloids begin to form and draw in other domains due to the surface tension of the water that surrounds them, resulting in a loosely packed layer which covers most of the water surface. Then, $\sim 20\,\mu l$ of surfactant (in this case 2 wt% SDS) is added to the water which pushes the colloids together and increases the ordering and strength of the monolayer. This good ordering is shown by the photograph in Figure 4.3.8, which shows the strong iridescence pattern due to the colloids on the water surface. Finally, the target substrate is inserted in the water before being slowly withdrawn at a shallow angle ($\sim 20^{o}$), transferring the monolayer onto its surface. This is then left to dry, which pulls the colloids together one final time and loosely fixes them to the substrate.

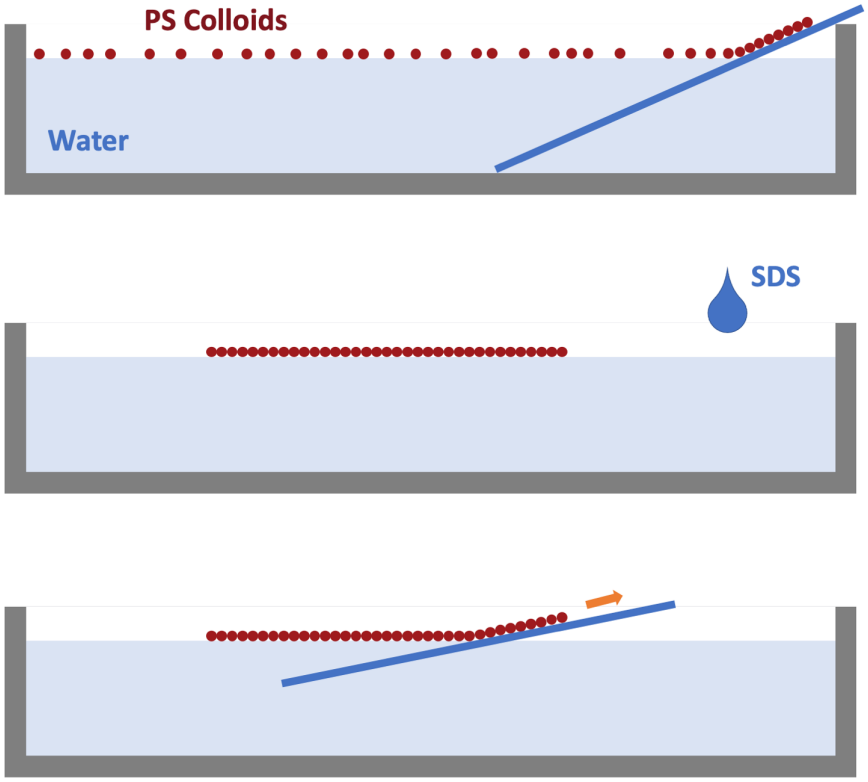


Figure 4.3.7: Process of depositing a monolayer of PS beads with interface coating. Adapted from [77].

This technique has a big advantage over spin coating because the assembly of the monolayer is well controlled before it applied to the substrate, reducing the chances of

defect formation. This is because the small aggregates are often dispersed by the diffusion across the water surface and the larger aggregates usually sink, and so do not form part of the monolayer. The pre-forming of the monolayer also makes the substrate requirements for interface coating less restrictive than for spin coating with the coating of irregular and non-uniform surfaces possible [77].

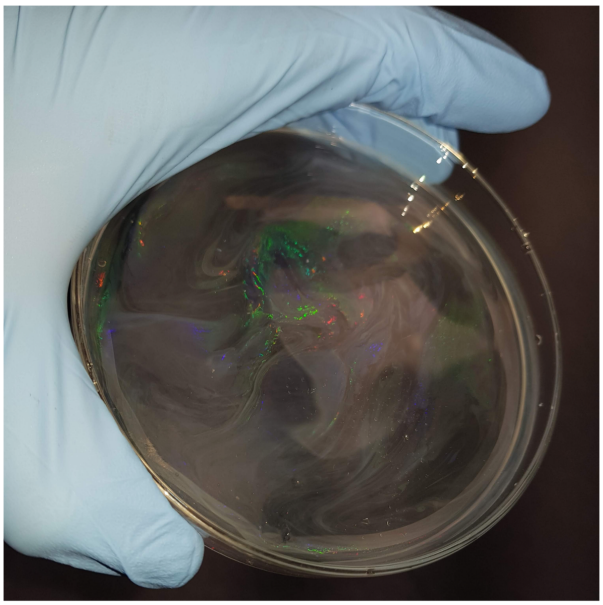


Figure 4.3.8: Iridescence pattern caused by the diffraction of light from the well ordered colloids on the water surface, after the application of SDS.

Results

The first tests of this technique were carried out using 500 nm colloids. The substrate chosen was a silicon wafer coated in a layer of PS. This layer was applied by spin coating a 3 wt% solution of PS (M_w = 350,000) diluted in toluene, at 3000 rpm for 60 s. This resulting film was hydrophobic, which resulted in the colloids being pushed away from the substrate because of the high contact angle with the water. To counter this, the film was treated with UV ozone for 5 min to render it hydrophilic. This ensured a lower contact angle between the water surface and the substrate - allowing the colloids to be picked up. Figure 4.3.9a shows an image of the colloids deposited onto the thin film of PS.

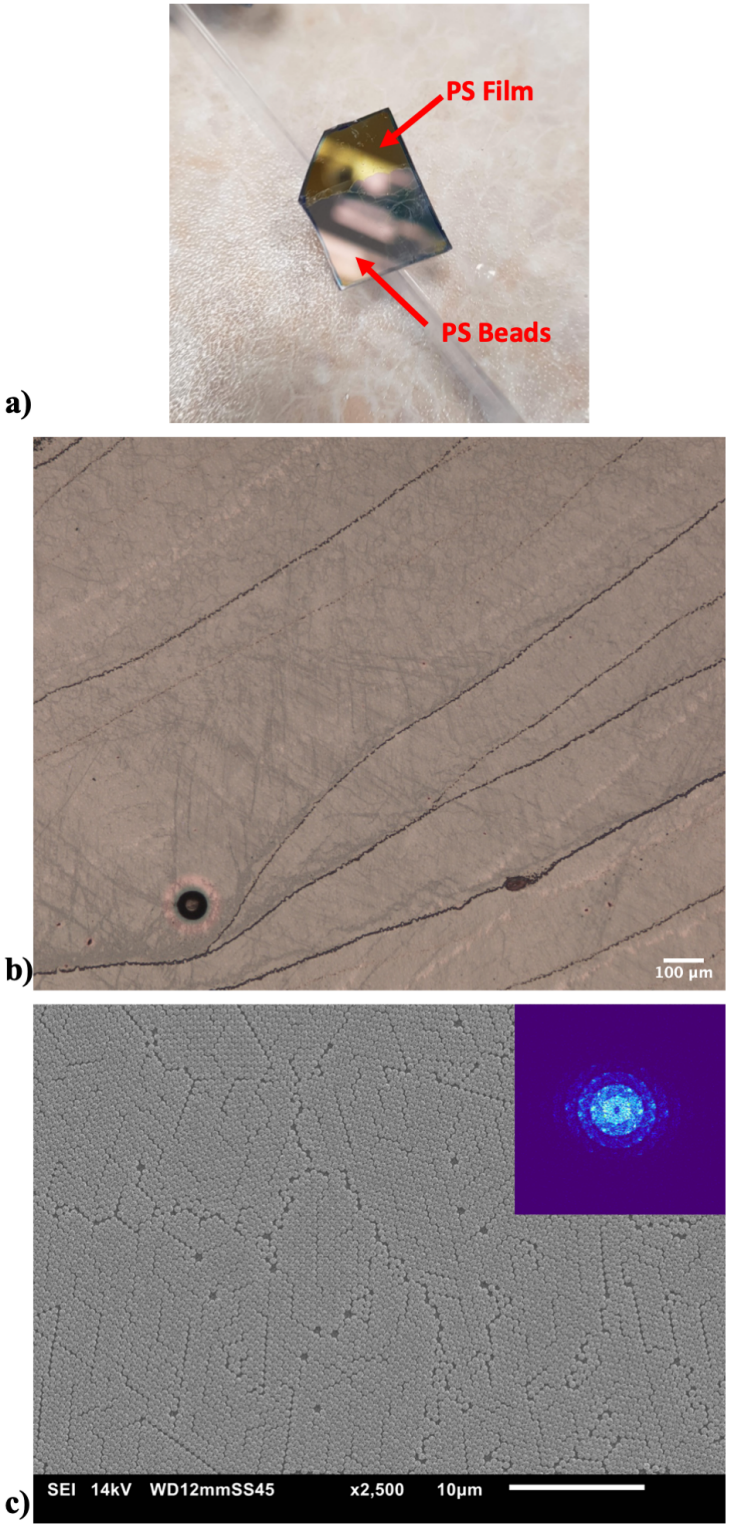


Figure 4.3.9: Monolayer of 500 nm PS colloids deposited onto a thin PS film with interface coating. a) Photograph of the colloid monolayer on the PS film, b) Optical micrograph of the layer of colloids, c) SEM showing the good packing of the colloids in the monolayer, with FFT inset.

The yellow colour is region of the PS thin film only, whereas the blue region has the colloids deposited on it. The solid blue colour indicates that there is a layer of uniform thickness. Optical microscopy images of the colloid layer (Figure 4.3.9b) confirm that the majority is indeed a single layer, which was consistent over the whole film. The dark lines across the image do indicate areas of stacked colloids, but the total coverage of these is negligible compared to the rest of the film. SEM analysis of the monolayer (Fig. 4.3.9c) show very good packing of the colloids across the whole surface, with only a few point defects (from a single missing colloid) or line dislocations in the HCP structure. Taking the FFT of the SEM again confirms this good HCP ordering. Unlike the layers formed with the spin-coating technique, there were no large gaps or defects found in the monolayer, which makes it highly attractive for colloid lithography. This technique also required much less optimisation of the deposition parameters, as the monolayer is pre-assembled, which also means that the requirements of the substrate are less restrictive.

4.3.3. Etching

The final stage in the colloidal lithography process is etching the base polymer film, using the previously deposited PS colloids as a mask. To understand the parameters required for the etching, the etch rates of both the different polymer films and the colloids themselves need to be understood. The etching here was carried out using O_2 plasma which reacts with organic components on the surface and breaks them down into species which are removed by the vacuum in the plasma chamber.

Bead Etching

To test the etching rate of the PS nanospheres themselves, a monolayer of the 300 nm colloids was deposited onto several silicon substrates using the interface coating method described earlier. Each substrate was then exposed to the same O_2 plasma treatment as the polymer films, for different times - 5, 10 and 20 min. The size of the colloids on each was then assessed using SEM, and analysis performed using the particle analysis feature in FIJI. Example SEM images of each stage of etching can be seen in Figure 4.3.10. As the etching time increases, the colloids clearly reduce in diameter, to almost half of the starting value by 20 min of exposure to the O_2 plasma. The graph in Figure 4.3.10 shows the results of the measurements of the colloid diameter across the whole film, along with a least-squares linear fit. From this fit it is estimated that the colloids are being etched at a rate of $\sim$7 nm/min.

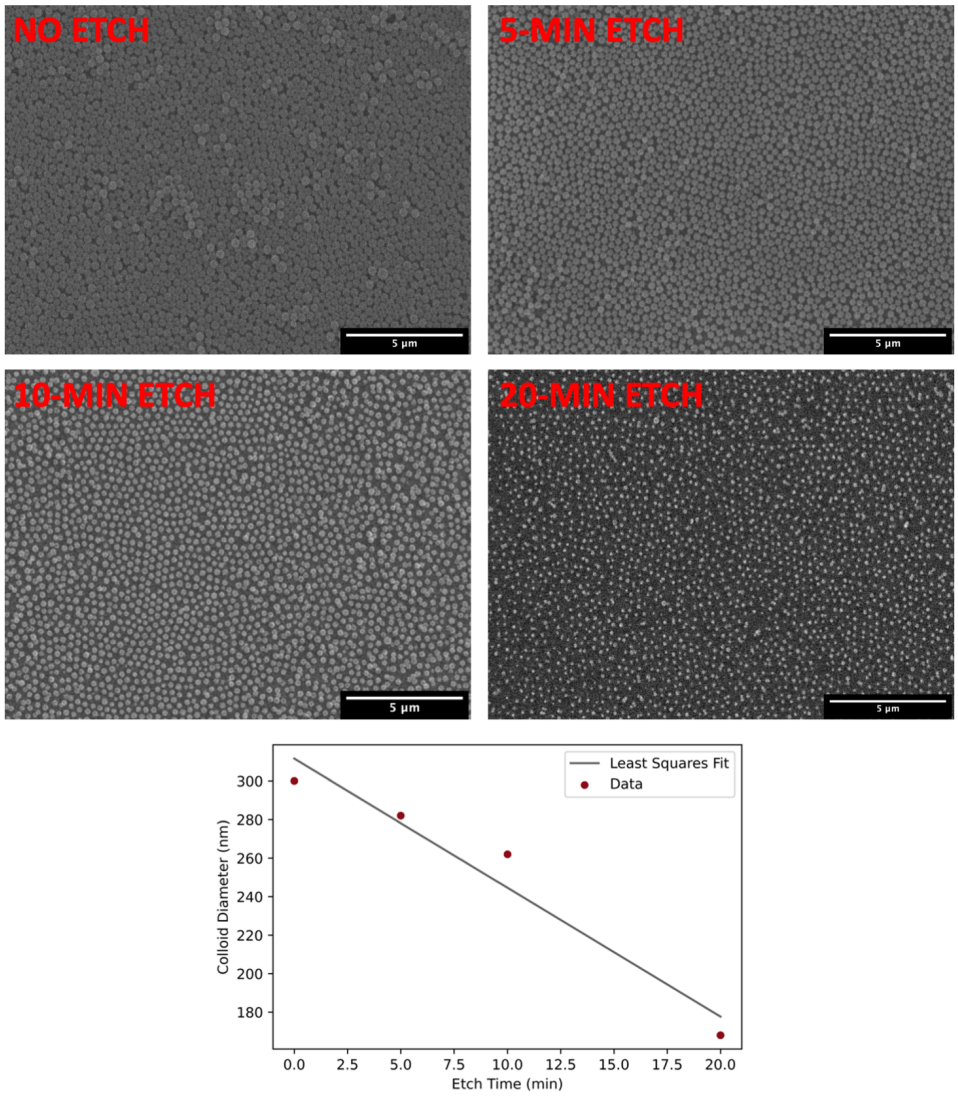


Figure 4.3.10: PS Colloid Etching under O_2 plasma for different times, assessed using SEM. The size of the colloids were measured in FIJI, the fit to the data is a straight-line least squares fit.

Film Etching

The etch rates of various polymers was established by spin coating films onto silicon substrates, placing under the O_2 plasma for different times and then measuring the change in thickness with ellipsometry. Three different polymers were tested high-molecular weight polystyrene (HMW PS) with M_w = 350k, low molecular weight polystyrene (LMW PS) with M_w = 35k, and PMMA with M_w = 120k. The HMW PS was cast from a 5 wt% solution spinning at 1500 rpm for 60 s. The LMW PS was cast from a 10 wt% solution at 2000 rpm. The PMMA film was cast from a filtered 10 wt% solution at 2000 rpm. These were repeated in triplicate for both the PS films and in duplicate for the PMMA

film. Once the films were cast, their starting thickness was measured and then they were placed under the oxygen plasma at set time intervals up to 30 min. After each time point under the plasma, the thickness of the films were measured. The data from this is given in Figure 4.3.11. Fitting a linear regression to this data and finding the gradient gives a value for the etch rates of these polymers under the oxygen plasma. The HMW PS was etched at a rate of 14 nm/min, the LMW PS at 13 nm/min and the PMMA at 53 nm/min. There seemed to be no dependence of the polymer molecular weight on the etching rate, but the PMMA etch was around 4 times faster than the PS film. The etching rate of both the PS and PMMA are higher than that of the PS colloids. This is important when using the colloids as a mask as it ensures that the film is etched deeper before the spheres are completely removed, thus leading to higher aspect ratio nanofeatures. As the PMMA film had the higher etching rate, this was chosen to be trialled for etching nanopillars.

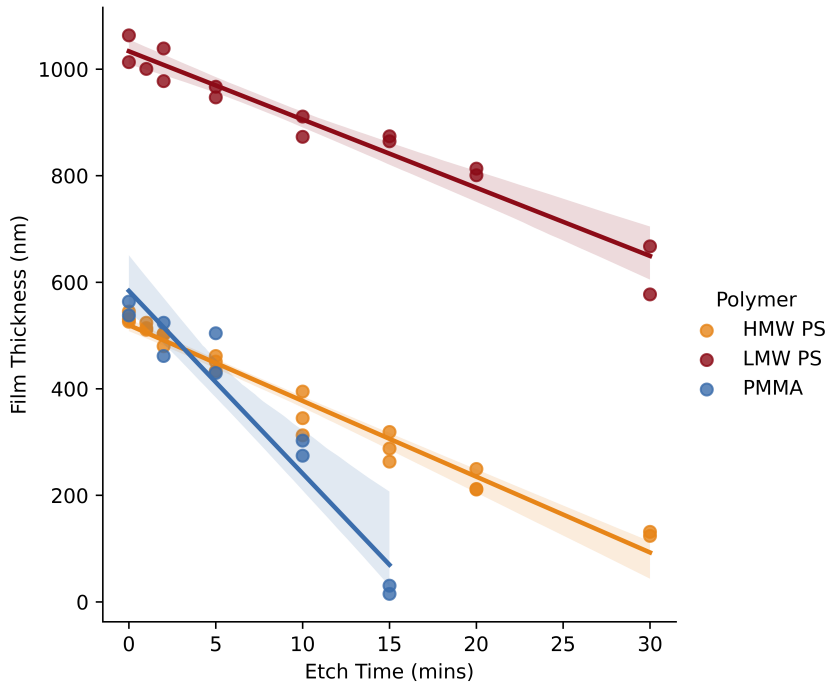


Figure 4.3.11: Etching rates of HMW PS, LMW PS, and PMMA under O_2 plasma, measured by ellipsometry. The fit is a straight-line least squares fit, with the error band as the standard deviation.

Etching Nanopillars - Preliminary Results

To test the capability of this method for producing nanopillars in polymer films, 300 nm PS colloids were deposited onto a ~500 nm thick PMMA film using the interface coating approach. This system was then etched for 5 min with the O_2 plasma, as described previously, to attempt to achieve nanopillars. AFM was then used to assess the

morphology of the polymer surface. Figure 4.3.12 shows preliminary results from this process.

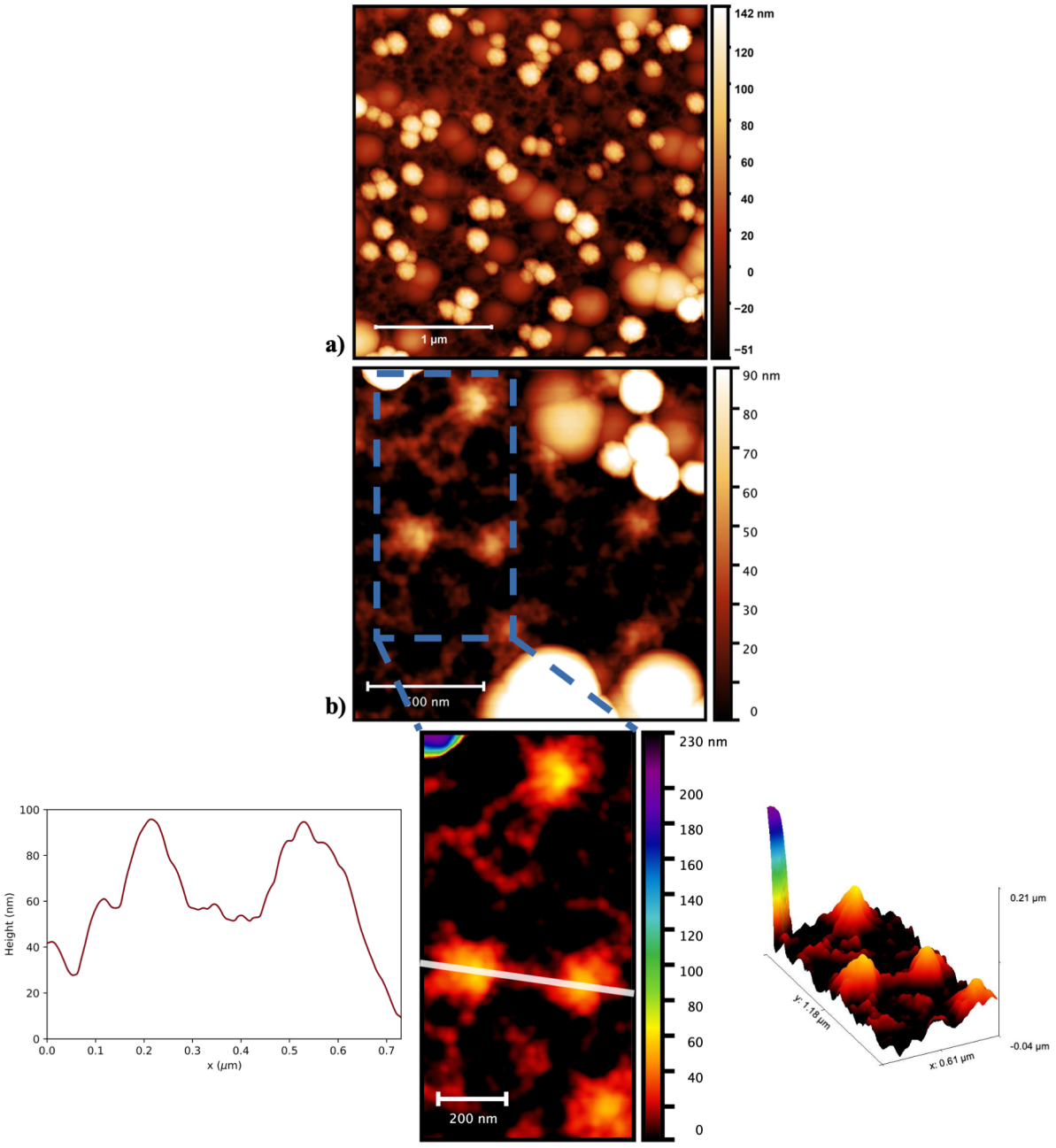


Figure 4.3.12: Etching a PMMA film using O_2 plasma, using a monolayer of 300 nm HCP colloids as a mask. a) Most areas do not show any etched features. b) Some etched nanopillars were found, although they were generally low aspect ratio.

The majority of the PMMA film surface was found to still be covered in the debris of the colloids, most of which had shrunk from their original 300 nm diameter, however there were also some still present at full size (Fig. 4.3.12a). It also appeared that the

colloids had shifted away from their ordered positions during the etching process, possibly due to the pumping of the vacuum required to create the O_2 plasma. Looking past the colloids to the base film in Fig. 4.3.12a, there does appear to be some gaps/holes which could be due to masked etching. A more high-resolution image of another area of the film, shown in Fig. 4.3.12b, showed what appeared to be pillars in the PMMA film. The cross sections taken of them showed a pointed peak, which indicates that they are not simply small colloids that had not been removed. The peak to peak distance of these features is ∼300 nm, which is to be expected given the spacing of the features fabricated using this technique is set by the diameter of the colloids used, in this case 300 nm. The features protruded around 100 nm from the surface of the polymer and had a diameter at the base of 200-300 nm, giving them a much lower aspect ratio than the pillars on the *M. intermedia* wing and those produced by the LS mould by solution casting.

Overall, there was limited success using this colloidal lithography technique to produce NSS, however with some additional development it could be very powerful. Nowlin and Lajeunesse described how the anisotropic etching of O_2 plasma produces nanofeatures with a pyramid-like morphology that are generally not very high aspect ratio [77]. Similar results were found here, with the pillars being wider than they were tall. Because the O_2 plasma etches anisotropically, it degrades the sides of the colloid as quickly as it is the base film causing the pillar to narrow quickly, leaving it with the pyramidal shape. RIE (under oxygen) is an alternative option, as this provides vertical isotropic etching that etches through the polymer film much quicker than decreasing the size of the colloid. This would result in much higher aspect ratio nanopillars, more like those found on the *M. intermedia* wing.

4.4. Summary of Findings and Conclusions

In this chapter two different technique for the fabrication of polymer nanostructured surfaces have been explored and developed - solution casting and colloidal lithography. The topographies of the NSS produced were assessed with a combination of AFM and SEM. The bactericidal efficiency of the successfully fabricated NSS was determined against *E. coli* using LIVE/DEAD staining. The key conclusions are as follows -

- Solution casting into nanopatterned silicon moulds was found to be a quick and low-cost method of producing NSS.
- A method of preparing the master moulds, involving O_2 plasma cleaning and vapour coating with FOTS was developed that allowed good release of the polymer NSS.
- Casting glassy polymers, such as PS, often resulted in residual trapped solvent especially when casting from high concentration solutions. This trapped solvent then led to stretching of the pillars upon removal from the mould.
- Applying a vacuum during the curing process aids with the full removal of solvent, and prevents the extreme stretching of the nanopillars. Using this method with a 10 wt% PS solution gave an average nanopillar height of 360 $\pm$ 60 nm.
- As well as glassy polymers, thermoplastic elastomers were also moulded by solution casting. These materials can provide a range of mechanical properties for the NSS.
- With Kraton G1657 (PS content = 13%), nanopillars were replicated over 10 repeat moulding processes showing the consistency of this method for elastomers.
- Lower solution concentration improved the replication quality for the elastomeric materials, likely due to better filling because of lower viscosity.
- The nanostructured G1657 was found to enhanced the percentage of dead *E. coli* compared to a glass control by 2.2-fold. >40% of bacteria were inactivated on average on the structured surface.
- Good replication was also achieved for an elastomer with a higher PS content (30%). This FG1901 polymer was found to have a 1.36 fold enhancement in killing of *E. coli* when nanostructured, compared to a flat control.
- This casting process was also tested on a custom silicon mould, made to match the dimensions of the cicada wing.

- The replication quality from this mould was poorer overall, with tip clustering and poor filling of the mould likely problems.
- One limitation of this solution casting method is the difficulty in quickly changing the nanopillar size, without the fabrication of additional moulds.
- Colloidal Lithography was explored as an alternative technique which would allow the nanopillar size to be changed more easily.
- A method of producing PS colloids of different sizes were tested and produced nanospheres with $\sim$ 700 nm in diameter.
- Two techniques of depositing a monolayer of the colloids was tested - Spin Coating and Interface Coating.
- Spin Coating can achieve a monolayer of colloids, however it requires fine adjustment of both solution concentration and spin parameters to optimally balance the capillary and shear forces.
- Interface Coating is an easier method as the monolayer is formed on a water surface before deposition on the substrate. This allows a monolayer to be placed on imperfect or non-planar surfaces.
- The etching rate of both the colloids and various polymer films under O_2 plasma treatment was established. This was 7 nm/min for the PS colloids and 14 nm/min and 53 nm/min for PS and PMMA films, respectively.
- A trial of etching nanopillar into a PMMA film using the PS colloids as a mask had limited success, however some nanopillars were found on the surface of the film.
- Overall, effective nanostructured surfaces were produced for a range of polymers, with different properties, using a low-cost and quick production method. However the ability to change the topographical parameter of the surface is currently limited.

The next chapter will utilise the casting method developed here to investigate the role of nanopillar stiffness in the bactericidal effect of NSS.

Chapter 5

Effect of Nanopillar Stiffness on Bactericidal Efficiency

5.1. Introduction

To date, antibacterial nanostructured surfaces have been fabricated from a range of materials such as black silicon [14], diamond [49], gold [66], TiO_2 [44, 75], ZnO [73], PMMA [46], PET [59] and cellulose acetate [65]. These surfaces were made with a wide range of techniques which resulted in NSS with a variety of topographies. Understanding the many factors that are involved in making effective bactericidal surfaces is important, as it may provide more insight into the mechanism of cell death and aid in the production of highly effective antibacterial surfaces. Previous work has demonstrated how the degree of bacterial killing by NSS is influenced by factors such as height, pillar radius and spacing of the nanopillars (discussed in more detail in section 1.7.1). Generally, narrower nanopillars (smaller radius) have been found to lead to higher killing efficiencies [38, 46, 57, 59]. For example Hazell *et al.* found that decreasing the tip diameter of PET nanocones from 54 nm to 22 nm increased the killing of *E. coli* from 22% to 28% [59]. The height of the nanopillars seems to influence killing efficiency but only up to a point, with Cui et al. finding that features taller than 200 nm did not further enhance the bactericidal efficiency [72]. Nanopillar spacing was found to affect killing in a similar way, generally closer spaced (denser) nanopillars lead to higher killing efficiencies [38, 46, 55], but in some cases the most densely packed nanopillars lead to a reduction in killing [57, 58, 72]. The literature survey carried out in section 1.7.1 (shown in Fig. 1.7.1) found that across all the types of surface, only the spacing/pitch had a noticeable influence on the killing efficiency, with closer features conferring an increased ability to kill bacteria.

One factor that has has been often overlooked is the role of nanopillar stiffness on the bactericidal efficiency. The NSS described in the literature are made from a range of different materials which have large differences in mechanical properties. For example, a common organic material used to make NSS is PMMA, which has a Young's modulus of ∼3 GPa [119]. Whereas silicon, an inorganic material which has been widely used for NSS, has a Young's Modulus >130 GPa [121]. Therefore it is key to understand what effect these differences in mechanical properties could have on the bactericidal efficiency of the NSS. Ivanova *et al.* recently reported that an increase in flexibility of high-aspect ratio silicon nanopillars was responsible for an increase in bactericidal efficiency against both *P. aeruginosa* and *S. aureus* [155]. They found that increasing the height of the nanopillars led to an increase in their flexibility, and the amount of elastic energy stored in them when bent due to the interaction with the bacteria. They concluded that this additional elastic energy stored in the nanopillars could lead to extra stress on the bacterial membrane. Linklater *et al.* similarly reported that super high aspect ratio carbon nanotubes, that were able to store a greater amount of elastic energy, killed a greater percentage of both *P. aeruginosa* and *S. aureus* [56]. Both of these studies do not change the intrinsic stiffness of the nanopatterned material, only the elasticity of the pillars by increasing their height. Additionally, the investigated materials both have very high Young's modulus values - 66.5 GPa for silicon [155] and 1 TPa for carbon nanotubes [56]. Most of the other NSS used in the literature are lower aspect ratio and made of very stiff materials (e.g. Black Silicon) so do not bend when they come into contact with bacteria.

Very recently, Lohmann *et al.* created NSS from a range of UV-cured resins with differing Young's modulus. Unlike the other studies on the flexibility of the nanopillars, here the surface topography is kept constant and the pillar stiffness changed between 208 MPa and 4 GPa [156]. When testing the killing effect of these NSS against *E. coli*, they found that only the pillars with a stiffness $\geq$ 1.3 GPa were able to kill significantly more bacteria than the flat control surfaces. They concluded that, due the their increased stiffness, these surfaces were able to exert stronger shear forces on the bacterial membrane, increasing the chance of rupture.

In this work, nanostructured surfaces are formed from 4 thermoplastic elastomers with varying polystyrene content, along with pure polystyrene, in order to evaluate the importance of nanopillar stiffness on bactericidal efficiency. The Young's modulus of the chosen polymers ranged from ∼3 MPa to ∼3 GPa, therefore exploring a wider range of stiffness

than the current literature [56, 155, 156]. The NSS were formed using the previously developed drop casting and moulding method (section 4.2.1), which was optimised for each of the polymers. After characterisation of these surfaces with AFM, the LIVE/DEAD bacterial viability assay was used to assess the killing ability of the different polymers. Finally, SEM was used to visualise the morphology changes of both the adhered bacteria and the nanopillars that they are in contact with.

5.2. Experimental Methods

5.2.1. Materials

The nanostructured surfaces were fabricated using Polystyrene (M_w = 710,000, Sigma Aldrich) and Kraton polymers (A1535, A1536, FG1901 and G1657) which were kindly supplied by Arwin van der Waal (Kraton Polymers Research, Amsterdam, The Netherlands). The polymer solutions were produced by dissolving in toluene (Sigma Aldrich UK) at various wt%.

5.2.2. Polymer Mechanical Characterisation

To assess the Young's modulus (YM) of each of the polymers a technique was used based on the capillary wrinkling of films, which had previously been described by Huang *et al.* [157]. In this method, a thin polymer film is floated on the surface of water, whereby it is stretched out by surface tension. Then, a small droplet of water was placed in the centre of the film, which induces wrinkles in the film around the drop, as seen in Figure 5.2.1.

The wrinkles form due to the capillary forces acting on the film because of the surface tension of the droplet. The length of these wrinkles is determined by the properties of the polymer film (it's thickness and YM) and the size of the droplet. The previous work showed the following relationship between the parameters -

$$L = C_L \left(\frac{E}{\gamma}\right)^{\frac{1}{2}} a h^{\frac{1}{2}} \tag{5.1}$$

where L is the wrinkle length, C_L is a numerical constant (0.031), E is the YM, γ is the surface tension of water (72 mN/m), a is the radius of the droplet and h is the thickness of the film. In this work, given that the nanopillars produced from the LS

mould have a width of ∼200 nm, the Young's modulus of thin PS films of a similar thickness was assessed and compared to the expected bulk value. Firstly, a thin layer of poly(3,4-ethylenedioxythiophene) polystyrene sulfonate (PEDOT:PSS) was spin-coated onto a silicon substrate which acts as a release layer. Then at 3 wt% solution of PS (M_w = 710k) was deposited by spin coating. A series of films were created using a range of different spin speeds which gave a range of thicknesses, which were measured with ellipsometry. A razor blade was used to cut the edge of each of the films before they were lowered into a dish of water. This cut allows the water to access the PEDOT:PSS layer and release the PS film onto the water surface. Once the film was floating, small droplets (∼20 μl) of water were placed on the surface and the images of the wrinkles captured with a Nikon DSLR camera which was placed at a fixed distance from the surface. A scale was also placed in the image to allow conversion from pixels to millimetres. These images were analysed in FIJI to measure the size of the droplets and the length of the wrinkles.

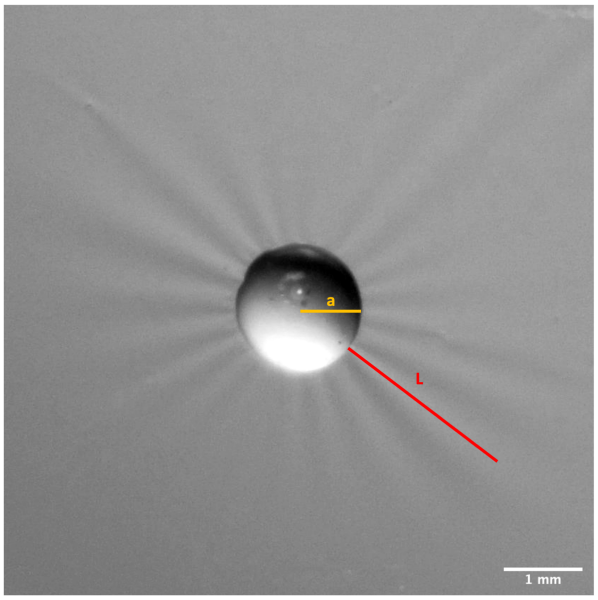


Figure 5.2.1: Photograph of droplet of water on PS thin film causing capillary wrinkling. From this the radius of the water droplet, a, and the length of the wrinkle in the film, L, were measured in order to calculate the Young's modulus of the polymer.

This "wrinkling" technique to find the YM was also attempted on films of the Kraton polymers, however due to their softness compared to the PS, no wrinkles were observed. Therefore, the mechanical properties of the bulk Kraton polymers was determined with a mechanical pulling method, using the standard ASTM D882-18 [158]. For this, each of the polymers were formed into thin bars by casting the solution either into a mould or as

a sheet which is then cut to size. The width and thickness of the bars were measured with a digital calliper prior to stretching. The samples were then mounted in a tensile tester (Tinius Olsen H5k) with a 250 N load cell to measure the applied force. The length of the sample between the two grips on the tester was measured and recorded as the initial length. The samples were then stretched at 300 mm/min and the force and change in the length of the sample was recorded through the Tinius Olsen's Horizon software. The stress and strain of the samples during testing were later calculated using equations 5.2 and 5.3, where ΔL is the change in length from the initial L_0, F is the applied force and A is the cross-sectional area of the beam.

$$\text{Strain}, \varepsilon = \frac{\Delta L}{L_0} \tag{5.2}$$

$$\text{Stress}, \sigma = \frac{F}{A} \tag{5.3}$$

Using these, the Young's modulus, E, of the sample can be calculated using equation 5.4. This is only valid when the sample is undergoing elastic deformation, i.e. when the stress increases linearly with strain.

$$\text{Young's modulus}, E = \frac{\text{Stress}}{\text{Strain}} = \frac{FL_0}{A\Delta L} \tag{5.4}$$

There were some issues with non-uniformity in the thickness of the samples, which caused inconsistencies in the strain measurements along with twisting of the samples. To counter this, it was ensured that the beams were of uniform thickness after casting before they were tested.

5.2.3. Fabrication of Polymer NSS

To create the NSS for this experiment, the drop casting method previously developed as part of this project and described in section 4.2.1 was used. Briefly, a silicon master mould (S2D-24C2-0808-350-P, Lightsmyth) was first cleaned with oxygen plasma treatment (Henniker HP-200, Runcorn UK) for 10 min, after which it was vapour coated with 1H,1H,2H,2H-Perfluorooctyltriethoxysilane (FOTS) (Sigma Aldrich) for 24 h, to render it hydrophobic and ensure easier release of the NSS. The polymer solutions were then

drop-cast onto the mould and put in a vacuum oven at 200 mBar for 20 min to ensure the mould is fully filled and no air gaps or bubbles remained. The polymers were then left to cure at 40°C for between 1-5 days to allow all of the remaining solvent to be released. The polymer was then released from the silicon mould, with nanopillars now imprinted in its surface. An optimisation process of the fabrication parameters for each of the polymers was first carried out, with the details given in more detail in section 5.3. Once the optimal process for making the NSS was determined, several nanostructured replicas of each polymer were made to use in the bacterial studies.

5.2.4. Polymer NSS Characterisation

The nanopillars on the NSS were characterised using tapping-mode AFM (Veeco Dimension 3100) with a NuNano Scout 350 cantilever (spring constant 42 N m^{-1}, resonant frequency 350 kHz). For each surface, 5 different areas of 10 µm × 10 µm were scanned, with the average height of the nanostructures found using the grain threshold feature in Gwyddion [99]. A selection of surfaces were also imaged with SEM to determine the morphology of the nanopillars. This was carried out using a JEOL InTouchScope Scanning Electron Microscope, with surfaces mounted onto SEM stubs using conductive carbon tape and a 50 nm layer of gold evaporated onto the surface (Edwards Auto 306 bell-jar evaporator) to ensure good conduction.

5.2.5. Bacterial Culture

All of the antibacterial testing in this study was performed using *E. coli* K12 MG1655 (wild-type) strain. Before each experiment, a single bacterial colony was used to inoculate LB media (Miller) and grown overnight at 37 °C, shaking at 200 rpm. This culture was then diluted to OD_{600} = 0.05 in fresh media and grown to mid-exponential phase (OD_{600} = 0.4 - 0.5). At this point, the culture was added to the test surfaces and incubated for 2 h at 37 °C, without shaking. After this time the cells were aspirated and the surfaces washed 3 times with 0.9% NaCl buffer to remove any non-adhered bacteria, prior to carrying out any assays.

5.2.6. Bacterial Viability Assay

To quantify the bactericidal efficiency of the nanostructured surfaces a Live/Dead fluorescent stain assay was performed (described in Section 2.3). The LIVE/DEAD™ BacLight™ Bacterial Viability Kit (L7012 for microscopy, Thermofisher Scientific) was

prepared according to the manufacturer's instructions (details given in section 2.3). After bacterial incubation, the combined SYTO9 and PI solution was incubated on the surfaces for 30 min in the dark before rinsing 3 times with 0.9% NaCl buffer and mounting between a glass slide and a coverslip for imaging. The microscopy was carried out with a Nikon Ti Eclipse Wide-field system at 10x magnification, 8 different areas of each sample were captured. Counts of the number of live and dead cells were made using the "Analyse Particles" feature in the image analysis software FIJI [103], with the killing percentage calculated using equation 2.4. The same killing assay was also carried out on unstructured controls of the same polymers for comparison. Statistical differences between the bactericidal efficiency of the different surfaces were found using a 2-way ANOVA with Šídák's multiple comparisons test.

5.2.7. Visualising Bacterial Interaction with Nanostructures

After bacterial incubation and washing, 4% paraformaldehyde in PBS was added to the surfaces for 30 min to fix the cells. The surfaces were then washed 3x with 0.9% NaCl to remove excess fixative. For SEM (JEOL InTouchScope) the samples were dehydrated with an ethanol series (20%, 40%, 60%, 80%, 100% - 10 min incubation at each step) which slowly replaces all of the water in the cells with ethanol, before air drying and mounting onto a stub. The surfaces were then coated with a 30 nm layer of gold using a thermal evaporator (Edwards Auto 306 bell-jar evaporator).

5.3. Fabrication of Polymer NSS with Varied Stiffness

5.3.1. Selection of Polymer Materials

In order to achieve a large range of nanopillar stiffness, several different polymers were used to fabricate the surfaces. Thermoplastic elastomers are an ideal candidate material for this purpose as they exhibit the properties of both plastic and rubbery polymers. The Kraton polymers chosen for this study are thermoplastic elastomers which possess rubbery (ethylene-butylene) and glassy (styrene) blocks. By altering the ratio of the rubbery block to the glassy block, it is possible to reliably tune the stiffness of the polymer. As discussed in section 4.2.1, Kraton polymers were tested and found to produce good NSS from the Lightsmyth mould. The polymers chosen for this experiment had a PS content of 13%, 30%, 40%, and 60% for the G1657, FG1901, A1536, and A1535 respectively. Additionally,

pure PS (M_w = 710k) was chosen in order to test a purely glassy polymer, which will possess a much higher stiffness.

5.3.2. Mechanical Characterisation of Polymers

Using the capillary wrinkling method on a series of PS film of different thickness yielded a range of wrinkle lengths. Wrinkle length, L was plotted against the product $ah^{1/2}$ and the gradient found to be 6800 $m^{-1/2}$ (shown in Figure 5.3.1). From equation 5.1, this gradient equates to $C_L \left(\frac{E}{\gamma}\right)^{\frac{1}{2}}$. Inputting the constants yields a value for the YM of PS of 3.35 ± 0.77 GPa. Despite larger variation in the data compared to the original method by Huang *et al.* [157] (which is likely due to a less sophisticated experimental setup), this value is in very good agreement with the literature values of the bulk YM of PS, ~3.4 GPa [119, 159].

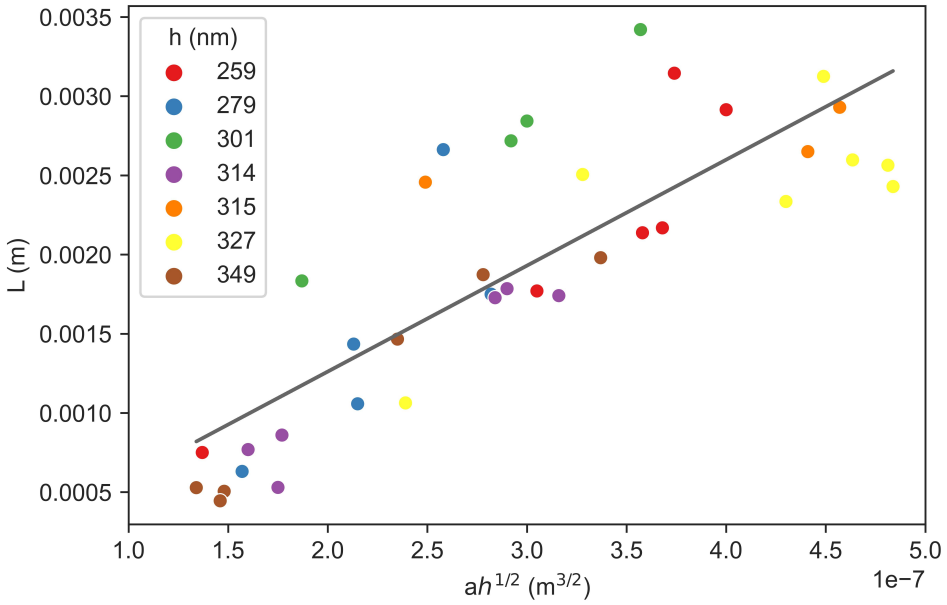


Figure 5.3.1: Results of the capillary wrinkling method to determine the Young's modulus for PS. The measured length of the wrinkle, L, on the thin polymer film as a result of the water droplet linearly increases with the factor $ah^{1/2}$, describing the size of drop and the thickness of the film.

The bulk mechanical properties of the Kraton polymers were evaluated by calculating their YM from force vs. extension measurements (converted into stress vs. strain, Figure 5.3.2). Taking the gradient of the linear portion of the stress-strain curve yields the YM of the material, and provides a measure of its stiffness.

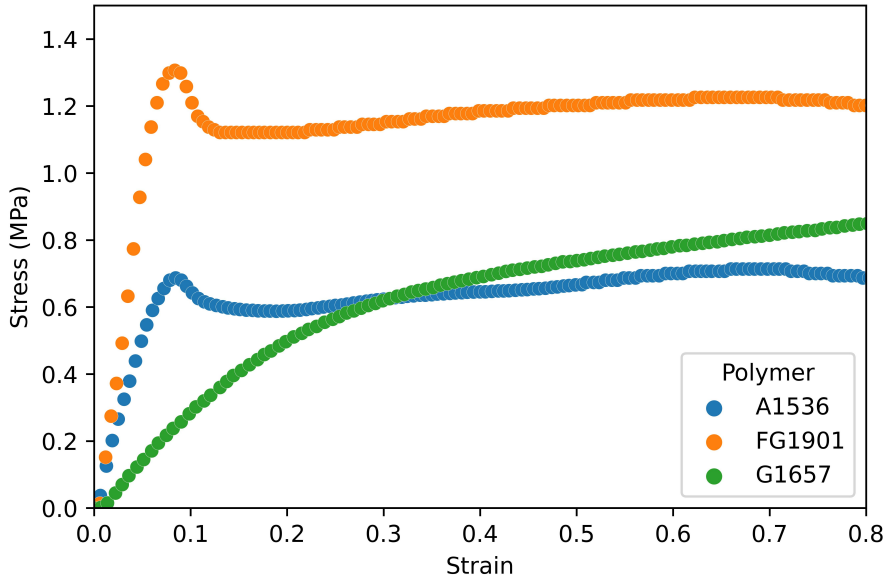


Figure 5.3.2: Stress-Strain curves from the tensile testing of the Kraton polymers used in this study.

The YM values for all of the polymers used in this study are shown in Figure 5.3.3 and summarised in Table 5.3.1.

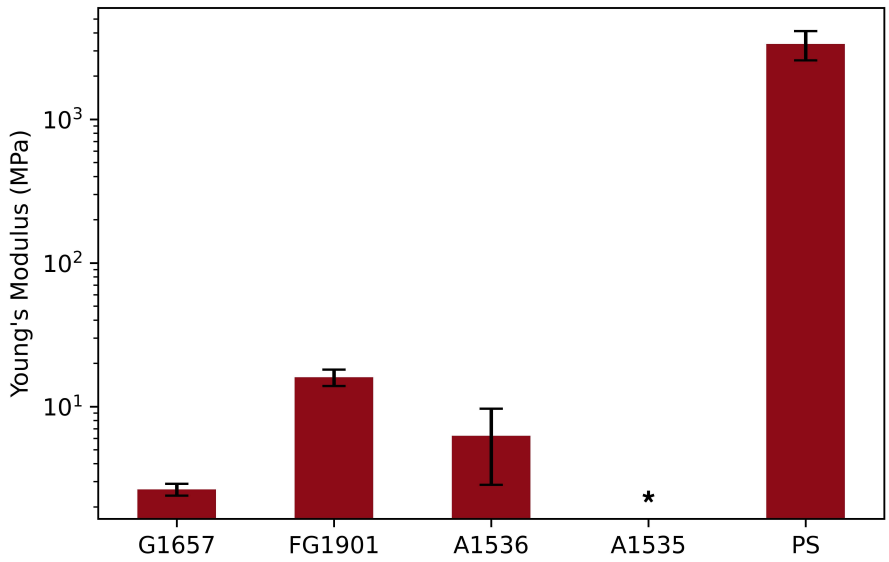


Figure 5.3.3: Young's modulus values for the polymer used to form NSS in this study.

For the polymer with the lowest PS content, G1657, the YM was found to be 2.7 ± 0.3 MPa. Interestingly, the next highest YM value was for the A1536 (40% PS) which was measured to be 6.3 ± 3.4 MPa. Then the FG1901, which has a lower content of 30%, was found to have a YM of 16 ± 2 MPa. It is possible that the arrangement of the styrene and

ethylene-butylene blocks are different for the FG1901 compared to the A1536, enhancing the former's mechanical properties, despite having a lower percentage of PS [160]. Finally, the YM of the pure PS was measured to be 3.35 ± 0.77 GPa. This is expected due to the fully glassy nature of the PS, which will significantly increase its stiffness. Unfortunately, due to issues with the the A1535 samples slipping out of the tensile tester, no YM values were obtained for this material at this time. However this still provided a good range of YM values over which to test the effect of nanopillar stiffness on bactericidal efficiency. In previous work NSS have generally been formed from high YM materials such as titanium, silicon or glassy polymer (i.e. PMMA), and there have been very few reports to date of NSS formed from pure polymer systems (that are free from small molecules that could contribute to the bactericidal effect through a chemical pathway) with YM values as low as those studied here.

Table 5.3.1: Summary of Young's modulus values for 5 different stiffness polymers. (Value for the A1535 polymer could not be obtained at this stage.)

Polymer	**Young's Modulus (MPa)**
Kraton G1657	2.7 ± 0.3
Kraton FG1901	16.0 ± 2.1
Kraton A1536	6.3 ± 3.4
Kraton A1535	*
Polystyrene	3350 ± 770

5.3.3. Optimisation of Procedure to Produce NSS

In order to test the effect of the NSS mechanical properties on bactericidal efficiency, it was vital that the other, topographical, parameters of the nanopillars were kept constant, as they each could have an effect on the amount of bacteria killed. The moulding technique used to create the NSS for this study (as previously described in section 4.2.1) produced pillars with a similar hexagonal arrangement to those found on the cicada wing, although with straight edges and a flat tip. The spacing of the pillars was set by the dimensions of the LightSmyth mould to 600 nm, and therefore was the same for all of the surfaces. However, despite the same moulding procedure being used for each polymer, the heights of the nanopillars showed a lot of variation depending on the parameters of the moulding process. As previously discussed, the concentration of the polymer solution had an effect on the height of the nanopillars, due to the difference in the viscosity of the solution changing how well it filled into the mould. This effect was different for each of the

different polymers due to the differences in molecular weight. Therefore, it was important to optimise the process for each polymer in order to get a consistent feature height and to be able to effectively probe the effect of surface stiffness on the bacterial killing efficiency of NSS. Figure 5.3.4 summarises the mean feature height of surfaces made from different solution concentrations for each of the polymers.

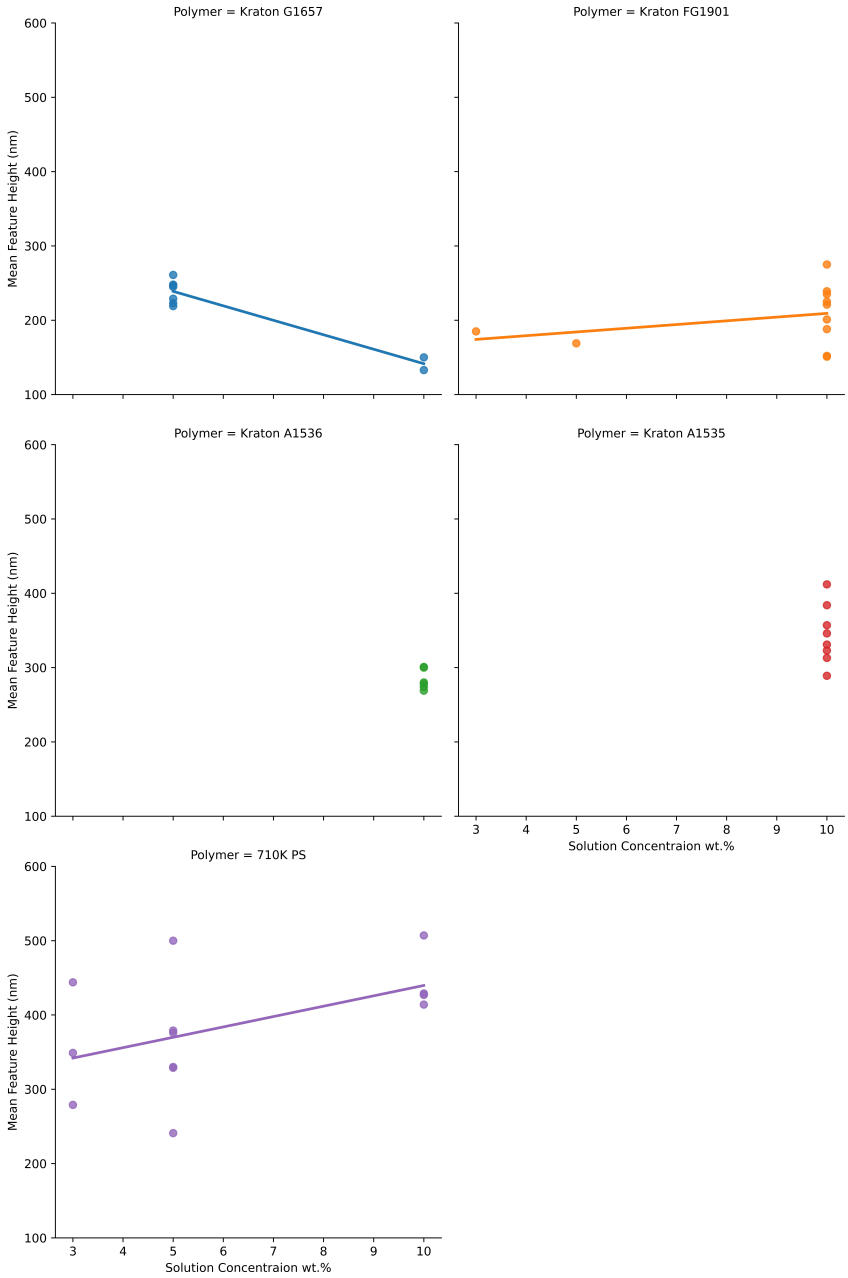


Figure 5.3.4: Optimisation of solution concentration for each polymer in order to make consistent NSS. This shows the mean feature height on the NSS for each solution concentration.

As was found in Chapter 4, the mean pillar height for the surfaces made with PS

decreased with decreasing solution concentration. The 5 wt% PS solution was ultimately chosen as it provided the pillar heights that most closely matched the rest of the polymers. Kraton G1657 also showed the same effect as found in Ch. 4, with increasing pillar height at lower concentrations. This is attributed to better filling of the mould due to a lower polymer solution viscosity. The 5 wt% provided the most suitable pillar heights here. As for the FG1901, A1535 and A1536, the 10 wt% solutions gave pillar heights which were very close to the other polymers. No other concentrations were tested for the A1536 and A1535 as the first one used provided the desired results. For all the polymers a 1 day cure time was used, as it was found that this time, in combination with the vacuum, was sufficient for full evaporation of the solvent.

Final Surfaces

The optimisation of the moulding process for each of the polymers gave greater control over the height of the produced nanopillars. However, as the pillars were not exactly the same height on each of the fabricated surfaces, a range of "acceptable" average pillar heights was chosen in order to select the surfaces to use for bacterial testing. It was decided that a $\sim \pm 50$ nm variation in the pillar height was an acceptable range over which it could be assumed that the height differences would not lead to significant differences in bactericidal efficiency. By measuring the average height of the pillars on all of the surfaces and counting the number that fall within a $\pm$ 55 nm range of a certain height, a midpoint for the range could be determined. Figure S5.1 on page 150 shows that most surfaces had features whose heights fell within $\pm$ 55 nm of 276 nm, so the final selection window was between 221 and 331 nm. As previously discussed, this $\sim$ 100 nm difference in pillar heights should not play a big role in differences in BE - it has been reported there is a "critical height" for features on NSS of $\sim$200nm, above which no additional killing of *E. coli* was found [72]. After picking this "selection window", any of the NSS whose average pillars height fell within the range were used for the future studies. Figure 5.3.5 shows the average heights of the nanopillars (measured using AFM), and Table 5.3.2 summarises the other key parameters of the nanopillars for these NSS made with each polymer used in this study. Representative AFM height images of the NSS are shown in Figure 5.3.6. These images show the hexagonally-packed nature of the nanopillars, mimicking the structures on the cicada wing, with very few defects or missing features, indicating good mould replication.

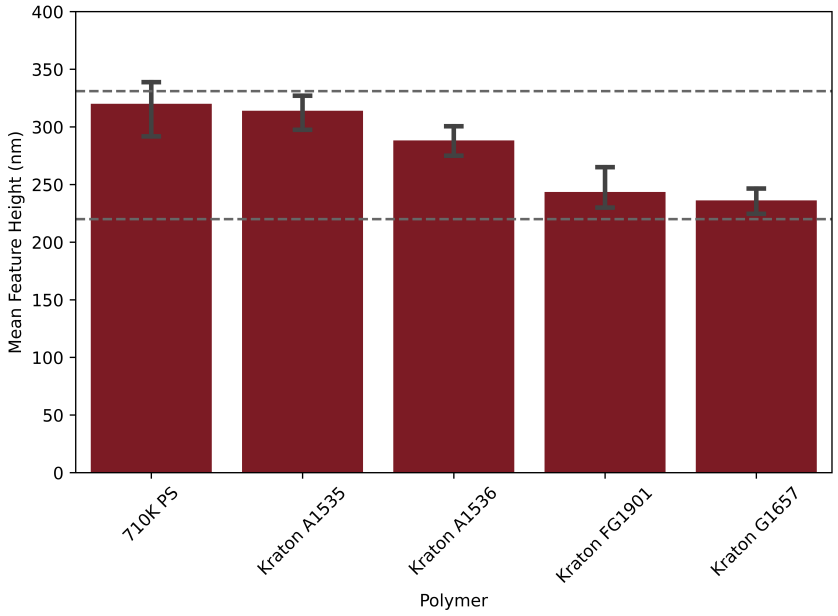


Figure 5.3.5: Average feature height for the surfaces made from the 5 different stiffness polymers. The grey lines indicate the selection window that was used to pick surfaces with a similar average height.

Compared to the features on the cicada wing (studied in section 3.3), these nanopillars are similar in height (240-320 nm for the polymer NSS vs. 210 nm for the *M. intermedia* wing) but are spaced much further apart (600 nm for the polymer NSS vs. 160 nm for the *M. intermedia* wing). The pillars on the polymer NSS are also wider than those on the cicada wing, diameters of 270-360 nm and 140 nm respectively. The resulting roughness factor, r is much lower on the polymer surfaces than the cicada wing, 1.4-1.5 and 5.6, respectively. Additionally, the areal density of features is much lower on the polymer surfaces, with only 2-3 features/μm^2 compared to 34 features/μm^2 on the *M. intermedia* wing. Given these dimensions it would be expected, based on the literature, that the LS moulded polymer surfaces will have a reduced killing ability compared to the cicada wing. However, they do meet the key requirement for antibacterial nanostructures set out by Watson *et al.*, which states that the spacing of the pillars must be less than the size of the bacteria in order for several nanopillar to make contact [85]. Given that the *E. coli* cell is $\sim$ 1 μm in diameter and $\sim$ 1.5-2 μm long, these nanopillars are sufficiently closely spaced to provide several contact points with the bacteria. Importantly, these surface parameters do not vary greatly between the different polymers. Therefore, from a topography perspective, the surfaces for each polymer will appear very similar to the bacteria and any differences will not have a large impact on the killing efficiency. The most significant difference between the NSS is the stiffness of the polymer which was used to mould it, which is the key parameter being tested here.

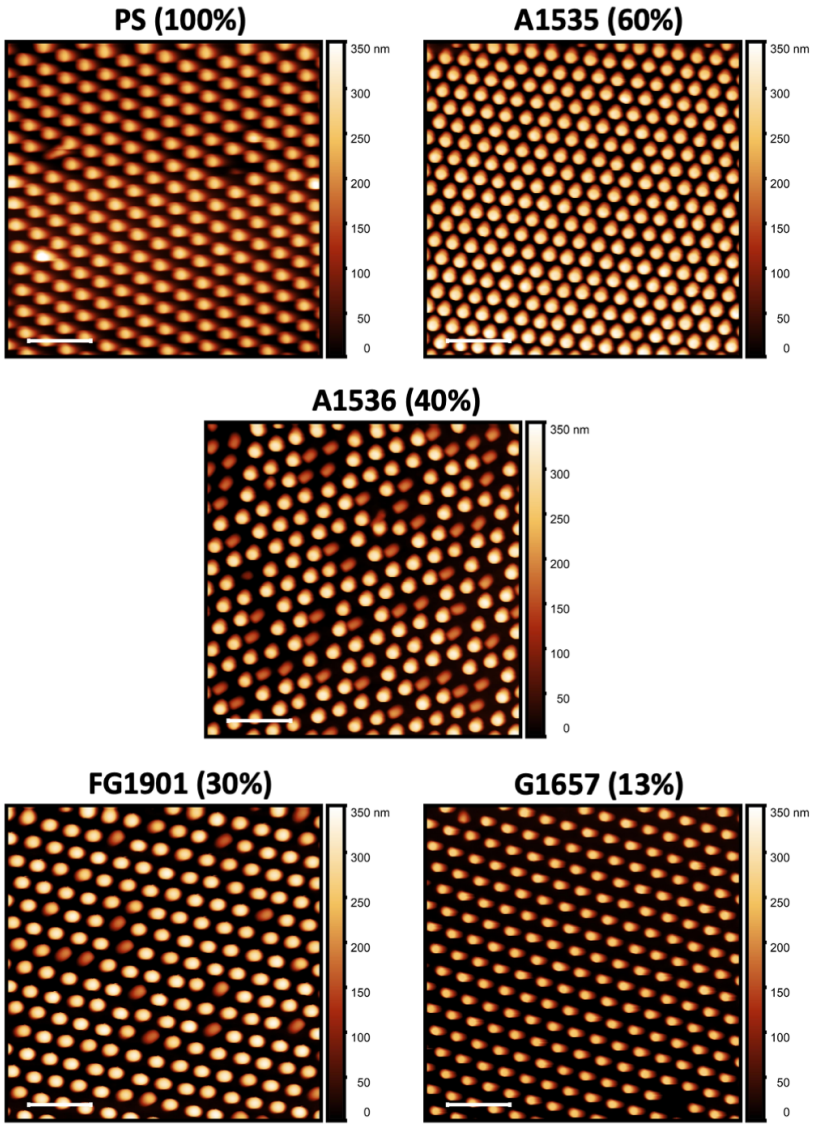


Figure 5.3.6: Representative AFM height images of the NSS made from the various polymer tested in this study.

Table 5.3.2: Summary of geometry of NSS made from 5 different stiffness polymers.

Parameter	**Polystyrene**	**Kraton A1535**	**Kraton A1536**	**Kraton FG1901**	**Kraton G1657**
Height (nm)	320 ± 30	310 ± 20	290 ± 10	240 ± 20	240 ± 10
Diameter (nm)	280	280	270	330	270
Pitch (nm)	600	600	600	600	600
Aspect Ratio	0.97	1.0	1.1	0.67	0.83
Wenzel Roughness Factor, r	1.5	1.5	1.4	1.4	1.4
Feature Density (/μm^2)	2.5	3.6	2.6	2.3	3.4

5.4. Effect of NSS Stiffness on Bactericidal Efficiency

Once a suitable set of NSS were produced from each polymer, the effect of nanopillar stiffness on their ability to kill exponential-phase (OD_{600} = 0.4 - 0.5) *E. coli* MG1655 was tested. The bacteria were incubated on each of the different polymer NSS and an equivalent flat control surface for 2 h. Subsequent staining with the LIVE/DEAD™ BacLight™ Bacterial Viability Kit was used to determine the percentage of bacteria adhered to the surfaces that had been killed. The results of this are shown in in Figure 5.4.1a.

The pure PS NSS was found to exhibit the greatest degree of killing with 34 ± 3% of the *E. coli* cells killed. Whereas, the G1657 NSS showed the least amount of killing at 14 ± 3%. The FG1901, A1535 and A1535 NSS killed 29%, 25% and 20% of the *E. coli* cells, respectively. The PS ($p = 0.0021$), FG1901 ($p = 0.0026$) and the A1535 ($p = 0.0085$) NSS were all found to kill significantly more *E. coli* than their respective flat control surfaces. Compared to the killing efficiency of the cicada from Chapter 3, the PS NSS here killed a similar percentage of the *E. coli* cells, with 34% vs. 38% for the cicada wing. When considering that the *E. coli* on the cicada wing were incubated for 20 h compared to only 2 h here, this gives a suggestion that these PS NSS are at least as good, if not more effective, in terms of their antibacterial ability. However, as previously discussed, the dimensions of these surfaces should make them inferior at killing bacteria compared to the cicada wing, given their wider spacing/lower density of features. Measurements of the YM of the cicada wing in Chapter 3 found that they are relatively soft, with $E \sim 40$ MPa, compared to the PS surfaces which are almost 100 times stiffer at $E \sim 3$ GPa. This hints that the increased stiffness of the nanopillars is able to enhance the bactericidal ability of surfaces that may not have the optimal killing parameters (i.e. those with reduced feature density as shown here). It is possible that differences in bacterial attachment between each polymer could be responsible for the variation in killing efficiency, in that surfaces which are highly undesirable for bacterial attachment may cause them to leave the surface before they are killed. Figure S5.2 shows the total number of bacteria (both dead and alive) imaged on each of the polymer surfaces. There appears to be no correlation between the attachment on each surface and no significant differences were found (tested with 2-way ANOVA). It is therefore unlikely that the differences in attachment contributed to the differences in killing efficiency between the surfaces.

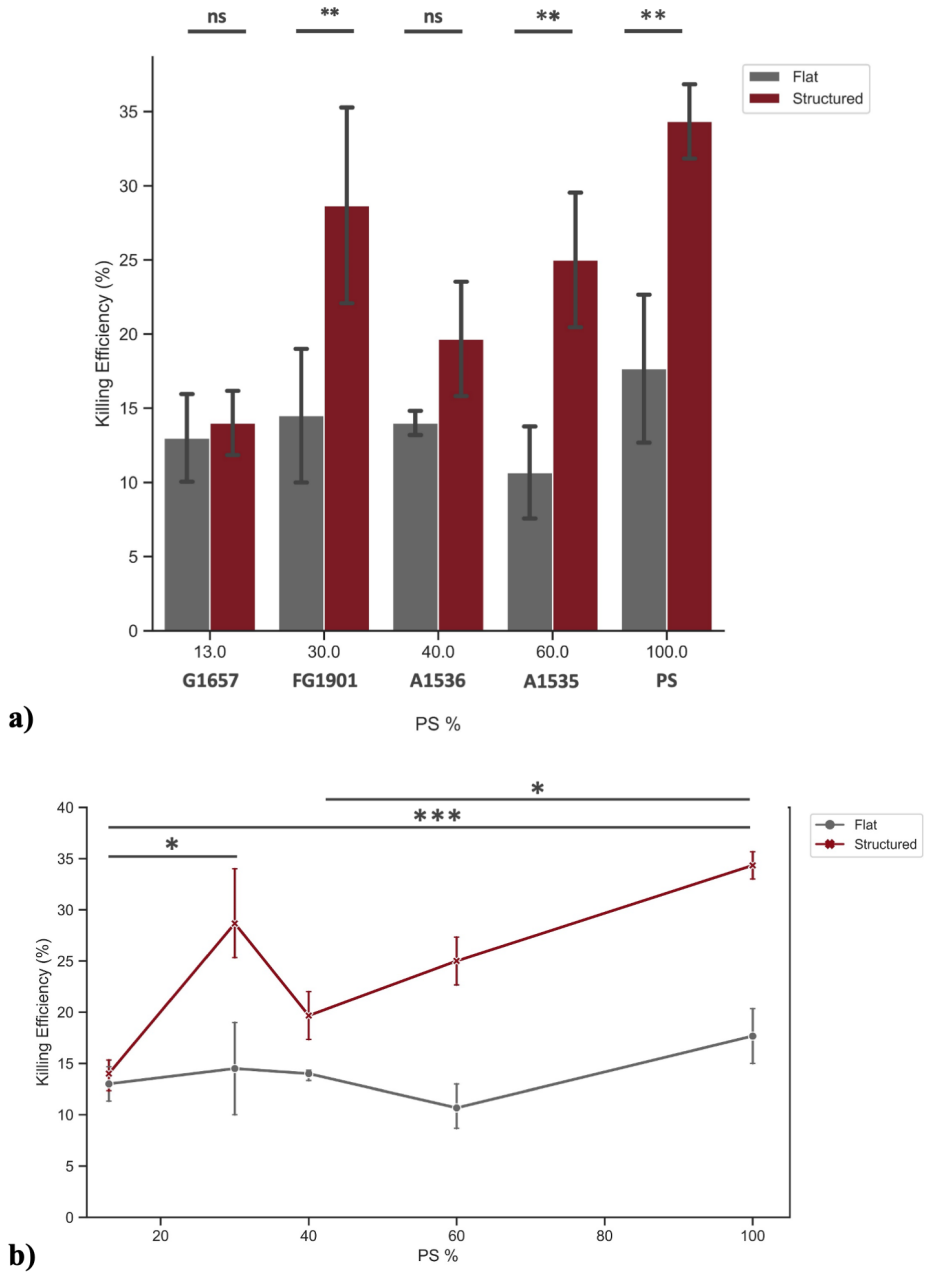


Figure 5.4.1: Killing Efficiency of the nanostructured surfaces made from polymers with different ratios of the glassy polystyrene block. a) The killing efficiency for the structured and flat controls for each of the polymer, based on 3 repeat measurements. Statistical tests performed with a 2-way ANOVA, comparing the killing efficiency of the flat and structured surfaces of each polymer. b) Killing efficiency of the flat and structured surfaces against the proportion of PS in the polymer. Statistical tests performed with a 2-way ANOVA, comparing the killing efficiency of each structured polymer against one another.

Exploring the role of nanopillars stiffness on bactericidal efficiency further, Figure 5.4.1b shows the killing ability of the NSS vs. the proportion of PS within the polymer. In general, the killing efficiency of the NSS increases with the PS content of the polymer,

with the exception of the FG1901 polymer which killed 29 ± 8% of the *E. coli*, higher than both the A1536 and A1535 which have a larger PS content. The PS NSS were able to kill significantly more bacteria than both the A1536 and G1657 polymers and the FG1901 killed significantly more than the G1657. There was no significant differences found between the levels of killing on the control surfaces for each polymer, with the bactericidal efficiencies ranging between 10-17% overall. As Figure 5.3.3 shows, the stiffness of the polymers was not found to directly increase with PS content. Therefore the relationship between the killing efficiency and YM of each polymer is plotted in Figure 5.4.2.

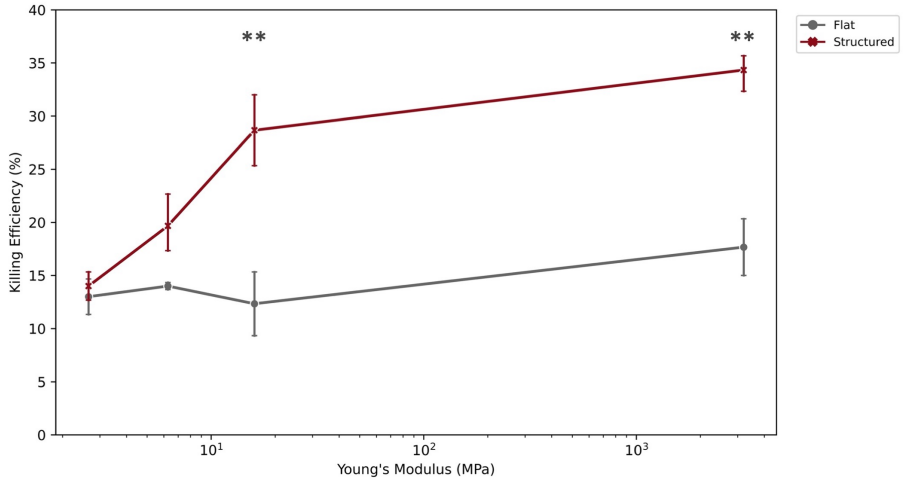


*Figure 5.4.2: Killing efficiency of the nanostructured surfaces and the control surfaces vs. the Young's modulus of the polymer. ** highlights significant killing over the control surfaces determined with a 2-way ANOVA.*

This shows that the killing efficiency of the NSS increases with the stiffness of the nanopillars. The lowest YM polymer (G1657) was able to kill the lowest proportion of *E. coli*, whereas the stiffest polymer (pure PS) was able to kill the highest. To verify that these differences are due to the changing stiffness of the polymers and not due to any topographical differences the relationship between the feature height of each surface and it's bactericidal efficiency was investigated. As Figure 5.4.3 shows there appears to be no correlation between feature height and the killing efficiency, meaning that it is very likely that the differences in killing between the polymers are due to the differences in stiffness. This strongly indicates that nanopillar stiffness plays an important role in the antibacterial effect of NSS. Given that only the FG1901 and PS NSS were able to kill significantly more bacteria than the control surfaces, it is possible that there is some "minimum" stiffness of the polymer which is required to activate the killing effect of the NSS. From this data, this "minimum" stiffness may be $\sim$ 10 MPa.

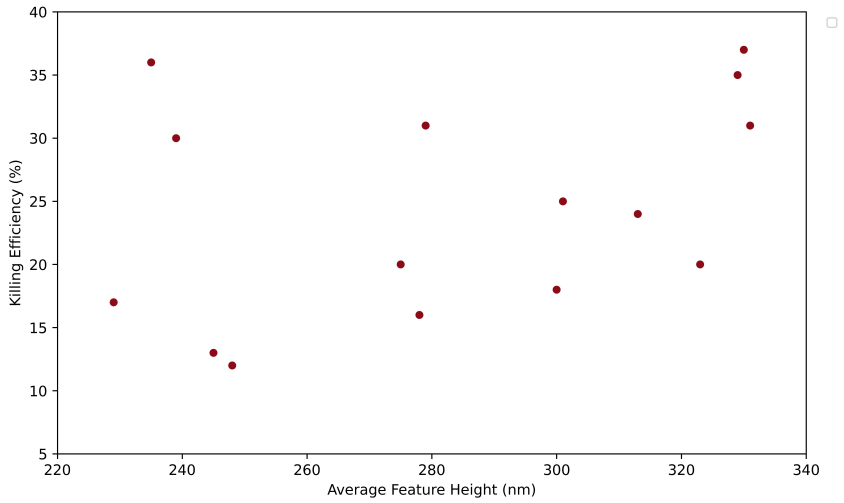


Figure 5.4.3: Killing Efficiency vs. nanopillar height for all the polymer NSS from this study.

Considering the currently accepted mechanism for bacterial death on NSS [80], these results could be explained by the fact that the stiffer nanopillars are able to push into the bacteria and stretch the membrane to breaking point, whereas the softer pillars may not provide enough rigidity for this and may fold underneath the bacteria, thus providing no stretching effect. This could explain why a steep increase in killing efficiency is seen as the YM of the NSS increases from 3 - 16 MPa. However, there is not a large increase in killing found between the FG1901 ($\sim$ 16 MPa) surface and the PS ($\sim$ 3 GPa) surface, despite a 2-orders of magnitude difference in the Young's modulus. It is possible that once the "minimum" stiffness requirement is met, other factors (such as pillar spacing or height) have a more dominant effect on the bactericidal efficiency. For example, the spacing of these nanopillars is large (600 nm) compared to many other NSS studied in the literature, and this may place an inherent limit on the bactericidal efficiencies that they can achieve, regardless of the material they are formed from.

5.5. Bacterial Interaction with NSS

To further probe the reasons why the NSS with stiffer nanopillars are able to kill a greater proportion of bacteria, the morphology of the *E. coli* and their interaction with the nanopillars after incubation on the NSS for 2 hr was assessed using SEM. Representative SEM images of the *E. coli* on each of the polymer NSS are shown in Fig. 5.5.1.

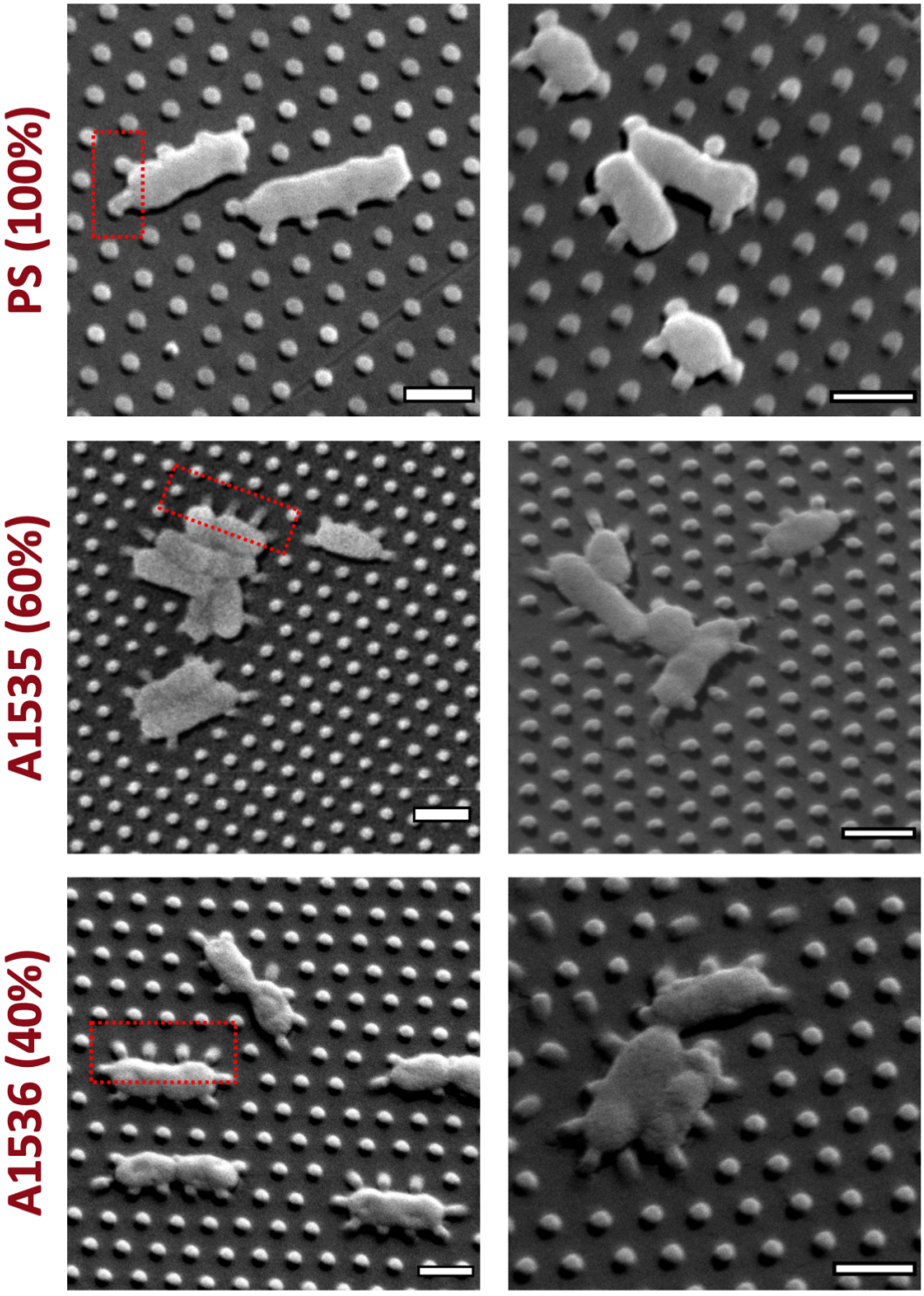


Figure 5.5.1: SEM of E. coli incubated for 2 hr on different stiffness NSS. The red box highlights how the nanopillars appear to bend to conform to the shape of the bacteria which are situated upon the surface. Scale Bar = 1 µm

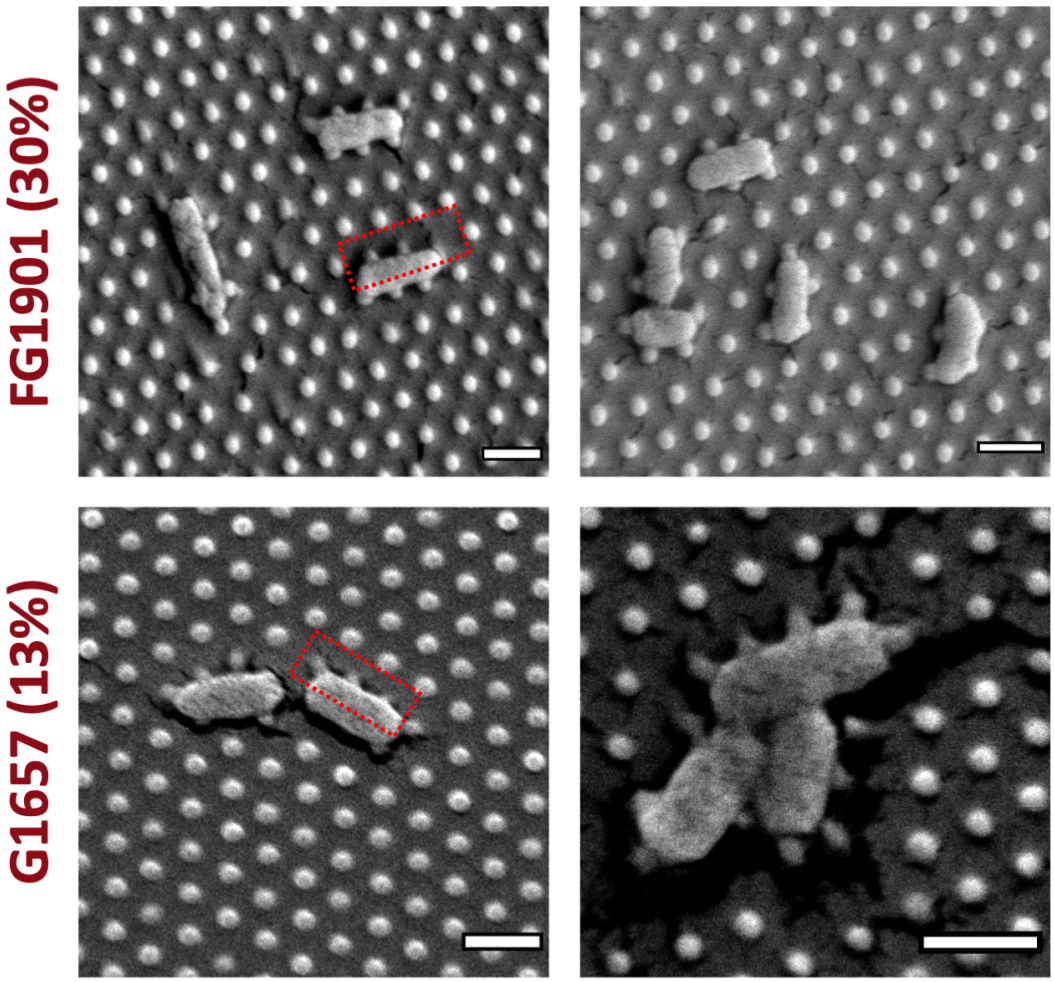


Figure 5.5.2: SEM of E. coli incubated for 2 hr on different stiffness NSS. The red box highlights how the nanopillars appear to bend to conform to the shape of the bacteria which are situated upon the surface. Scale Bar = 1 µm

Unlike the *E. coli* incubated on the cicada wing (Fig. 3.6.2 in Chapter 3), the bacteria on the polymer surfaces do not show any major changes in morphology due to their interaction with the nanopillars. The cicada wing features seemed to cause tears in the bacterial membrane which lead to deflation of the cell, however the polymer NSS features do not seem to cause such extreme effects. This is even more apparent when comparing to the *E. coli* incubated on the flat control surfaces (Figure S5.3), which show the bacteria in their "normal" state. It could be that this is due to the difference in incubation time compared to the experiment on the cicada wing. For that study the *E. coli* was incubated on the wing for 20 h, whereas here the cells are only on the NSS for 2 h. This may result in less overall damage being inflicted to the bacterial envelope. However, despite the fact that less membrane damage is seen for the cells incubated on the polymer NSS

compared to the cicada wing, similar levels of bactericidal efficiency are reported (for the PS, FG1901, and A1535). This indicates that total membrane rupture and full loss of turgor pressure seen in Figure 3.6.2 may not be an essential part of the bactericidal process, but a result of prolonged incubation on the nanostructures. For example Ivanova *et al.* incubated *P. aeruginosa* on the cicada wing for 60 min and did not see large-scale changes in the cell morphology with SEM, despite finding efficient killing with the LIVE/DEAD stain [11]. Kelleher *et al.* also found that *E. coli* incubated on cicada wings with widely spaced features for 30 min did not show obvious damage when imaged with SEM [38].

5.5.1. Cell Length and Orientation

The SEM imaging of the *E. coli* cells on the polymer nanostructures also allowed information about the bacterial morphology to be obtained. The length of the cells that had been incubated for 2 hrs on both the NSS and the flat control surfaces were measured using FIJI and are summarised in Figures 5.5.4 and 5.5.3.

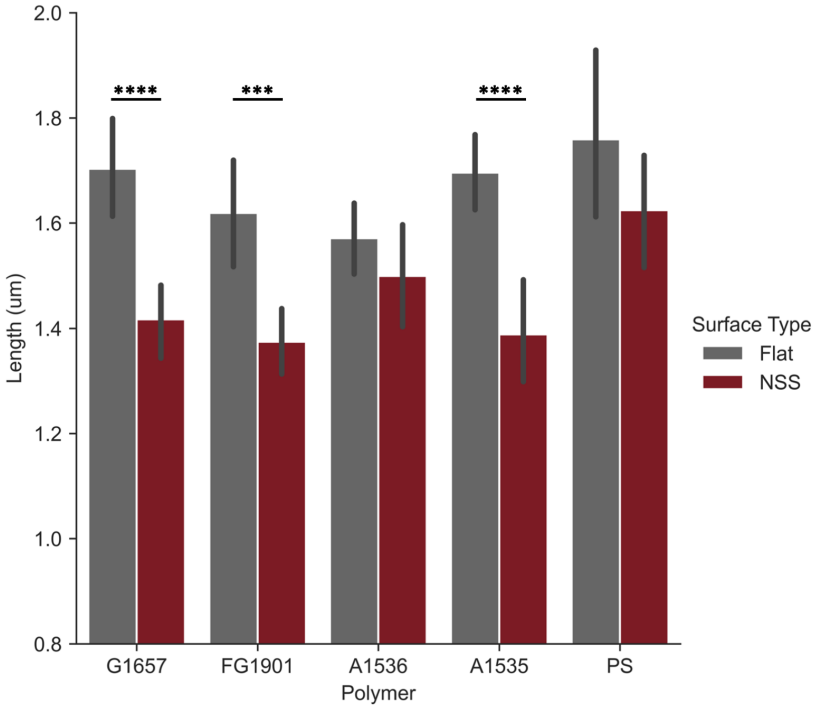


*Figure 5.5.3: Average length of the cells on the NSS compared to the flat surfaces for each of the different polymers. Error bars correspond to standard deviation. Statistical significance tested with two-way ANOVA. *** $p = 0.0004$, **** $p < 0.0001$.*

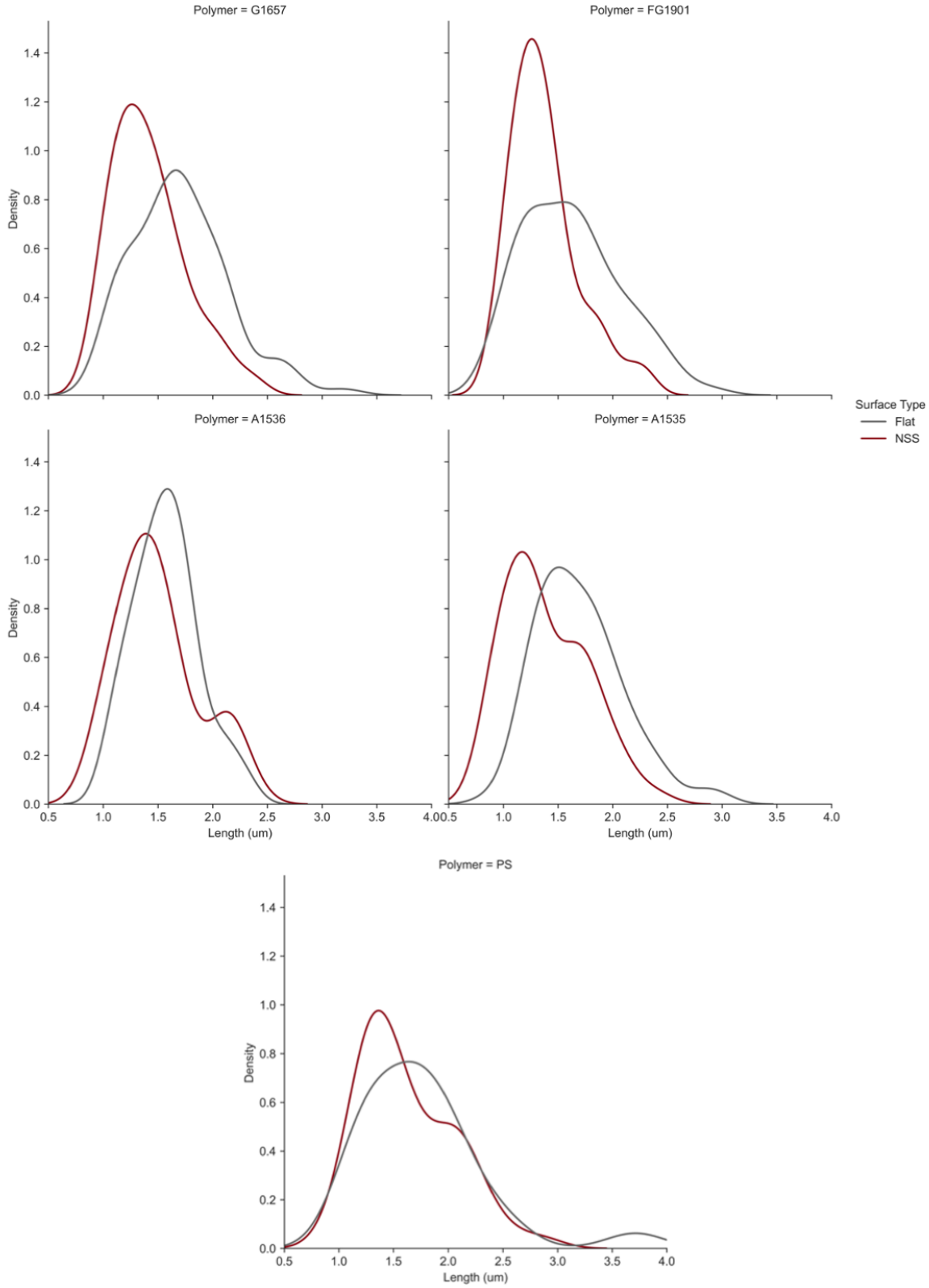


Figure 5.5.4: Distribution of lengths of the cells on the NSS compared to the flat surfaces, for the 5 different polymers used in this study.

Firstly, there was no significant difference found between the lengths of the cells between the flat polymer surfaces, with an average *E. coli* length on the control surfaces of 1.67 ± 0.42 μm. This is typical for the size of an *E. coli* cell. The consistency of the cell lengths on the flat control surfaces show that any changes in length are not due to the differences in polymer chemistry. As for the NSS, the length of the *E. coli* cells was found to be significantly shorter that on the control surfaces for the G1657 (1.42 ± 0.34 μm), FG1901 (1.37 ± 0.31 μm) and the A1535 (1.39 ± 0.37 μm) polymers. In addition, the A1536 (1.5 ± 0.37 μm) and PS (1.62 ± 0.43 μm) NSS also displayed shorter cells than the controls, although these differences were not significant.

Jenkins *et al.* has previously suggested that nanopillars may surround and trap bacteria, impeding the growth of the cells [75]. It is possible that the shorter cells seen here are a result of this impedance, as they have been prevented from fully growing and dividing. It would perhaps be expected that the amount of impedance of the bacteria would increase with the stiffness of the nanopillars (as they would be able to resist the growth of the bacteria better) and that this would lead to more killing. However no correlation was found between the average percentage difference in length of the cell between the NSS and the control, and the bactericidal efficiency of that polymer (shown in Figure S5.4 on page 152). This suggests that either - impedance does not play a role in the bactericidal mechanism of this type of surface, or that the change in cell length is not indicative of the levels of bacterial killing through the impedance mechanism. If the former is the case, the change in cell length seen here may just be a result of dehydration of the cell as it is prepared for imaging with SEM - if the bacterial envelope has been ruptured then it may shrink more that it would on the control surfaces. Further experiments would be required to investigate the link between the growth of the cells (or the impedance of growth) and bactericidal efficiency of NSS.

From the SEM images it was also possible to measure the orientation of the bacteria, relative to the array of nanopillars. The angle at which the *E. coli* sat on the nanopillar array was measured for all of the polymer NSS and the distribution is shown by the heat map in Figure 5.5.5. The brighter colours indicate a higher count of cells with that particular orientation. An angle of 0°, 60°, 120°, or 180° signifies that the cell is lying in-line with the orientation of the nanopillars - as shown in Fig. 5.5.5.

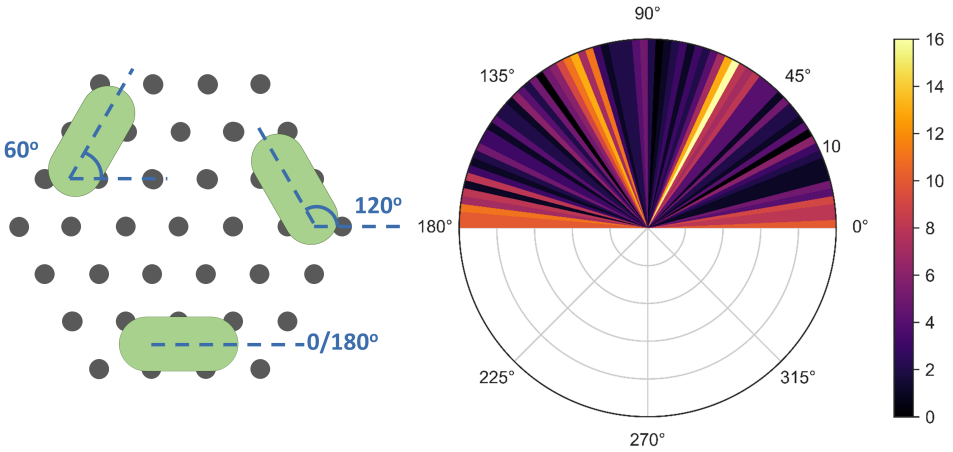


Figure 5.5.5: Orientation of the E. coli on the NSS relative to the array of nanopillars. The heat map show the most common orientations with which the bacteria sat on the nanopilllars.

As the heat map shows, the majority of the *E. coli* cells found on the NSS were seen to orientate themselves with the nanopillars and are strongly polarised in their orientation. This is an interesting result as this preferential orientation was not seen for the *E. coli* that were incubated on the cicada wing surface in Chapter 3. It is possible that because of the wide spacing of these NSS formed from the LS mould (i.e. low density of features), that it is favourable for the bacteria to sit in the "trenches" between the pillars. However, as shown by Fig. 5.5.14 this also results in the largest number of contact points between the bacteria and the NSS. For any other orientation, there are fewer pillars in contact with the bacteria. This may help to increase the bactericidal efficiency of these "lower density" NSS by increasing the points of contact, and therefore the mechanical stress that is imparted on the bacteria.

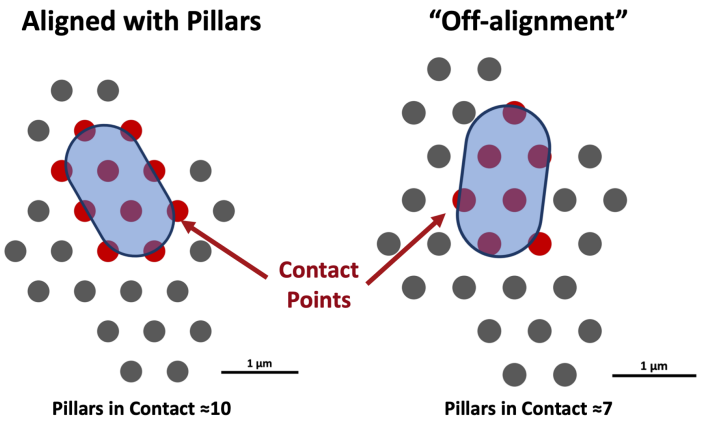


Figure 5.5.6: Illustration of the number of contact points between the LS nanopillars and the bacteria for different orientation angles. Drawn to scale with the measured size of the nanopillar ("bacteria" length = 1.8 µm and width = 1 µm.)

5.5.2. Nanopillar Bending and Forces

The SEM images of the interaction of the NSS with the *E. coli* cells also revealed that the nanopillars appear to bend into contact with the bacteria. This effect was observed for all of the different polymer NSS (highlighted by the red boxes in Fig. 5.5.1 on page 131) and was previously observed for the cicada wing (Fig. 3.6.2 in section 3) and elsewhere in the literature [11, 56, 155]. This effect was also seen on the polymer NSS when imaged with environmental SEM (E-SEM), which is carried out at ambient pressure and without the need for specimen coating (see Figure S5.5 on page 153) [161]. This shows that this bending is not due to the dehydration of the sample or due to the vacuum of the conventional SEM. This nanopillar flexibility and bending is not considered in the biophysical "stretching" model of cell death on NSS [80]. In this model, the pillars are seen as straight and rigid with the bacteria adsorbing downwards onto them, causing the membrane rupture. Here we see that some pillars bend into contact with the side of the bacteria, highlighting that the forces involved in this interaction cannot purely be in the vertical direction. This shows limitations in the current and dominant theory of the bactericidal mechanism.

In order to explore if the bending of the nanopillars into contact with the bacteria could be involved in the killing process, the distance the pillars deflected was measured from the SEM images. The average bend lengths for each of the polymer NSS are shown in Figure 5.5.7.

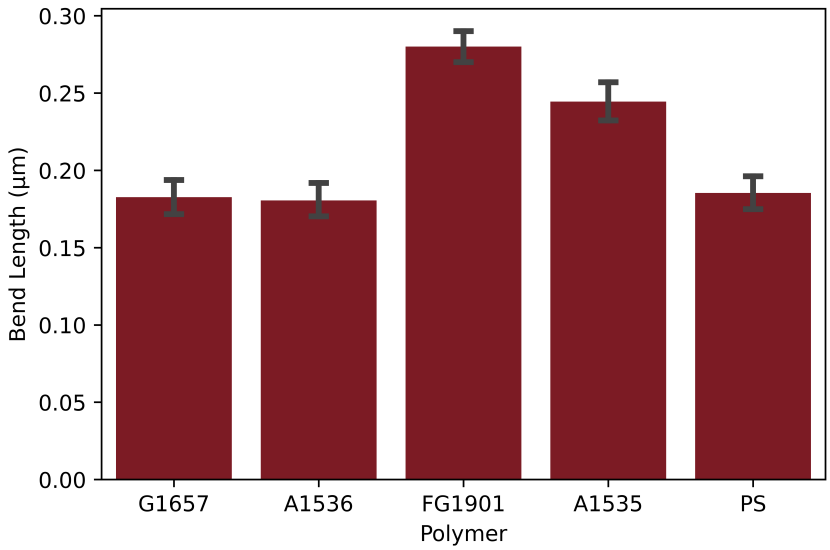


Figure 5.5.7: Magnitude of the average length of nanopillar bending on different polymer NSS.

For the G1657, A1536 and PS surfaces, the magnitude of the nanopillar bending is very similar with mean values of 0.183 ± 0.048 µm, 0.181 ± 0.057 µm, and 0.185 ± 0.055 µm respectively. The pillars on the FG1901 (0.280 ± 0.058 µm) and the A1535 (0.244 ± 0.062 µm) surfaces were found to bend further. There is no correlation between the stiffness of the polymer and the bending length of the nanopillars. The distance that the nanopillars bend does not provide much information alone, therefore it is important to consider the forces involved in the bending. For elastic deformation of the nanopillars, the bending distance is proportional to the applied force. This was first considered using the Euler-Bernoulli beam theory, which is a simple model for describing the deflections on beams that are subject to a load force (illustrated in Figure 5.5.8).

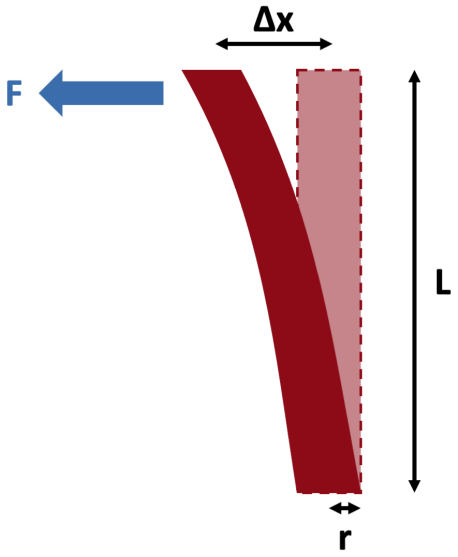


Figure 5.5.8: Euler-Bernoulli Beam Theory for the force (F) required to bend a beam with a fixed end of length (L) and radius (r), a distance (Δx).

Using the Euler-Bernoulli model, in the case of a cylindrical beam with a fixed end, the deflection depends on the force of the applied load (F), the length of the beam (L), the radius of the beam (r), and the elastic/Young's Modulus of the beam (E). Therefore the force required to deflect a beam by a distance Δx, is given by equation 5.5 [123, 124].

$$F = k\Delta x = \frac{3EI}{L^3}\Delta x = \frac{3}{4}\frac{\pi E r^4}{L^3}\Delta x \tag{5.5}$$

Here, k is a parameter describing the elasticity of the beam.

$$k = \frac{3EI}{L^3} = \frac{3}{4}\frac{\pi E r^4}{L^3} \tag{5.6}$$

And I is the area moment of inertia for a circular rod, describing the resistance to bending.

$$I = \frac{\pi r^4}{4} \tag{5.7}$$

However, as discussed by Schoen *et al.*, the bending of pillars on elastic substrates is more complex than simple deflection at the tip [124]. Shear forces on the pillar and tilting at the base of the pillar due to deformation of the substrate also contribute to how far the nanopillar bends overall, and by not taking these into account the forces involved can be overestimated. Considering these effects, a new "reduced" value for k is given.

$$k_{red} = \frac{\left(\frac{\pi}{4}\right) Ed}{\frac{16}{3}\left(\frac{L}{d}\right)^3 + \frac{(7+6\nu)}{3}\frac{L}{d} + 8T_{tilt}\left(\frac{L}{d}\right)^2} \tag{5.8}$$

As before, L is defined as the length of the beam and E as the Young's modulus. d is diameter of the beam and ν is Poisson's ratio for the material, which describes deformation in the plane opposite to the applied force. T_{tilt} is the "tilting coefficient" which describes how the pillar moves due to the deformation of the bulk material at its base.

$$T_{tilt} \approx 1.3\left(\frac{1+\nu}{2\pi}\right)\left[2(1-\nu) + \left(1 - \frac{1}{4(1-\nu)}\right)\right] \tag{5.9}$$

Using this more thorough method leads to significantly different values for the elastic constant. For polystyrene, with a Poisson's ratio of 0.34, the elastic constant calculated with the Euler-Bernoulli method, k_{EB} = 74.5 N/m, whereas using the reduced method, k_{red} = 36.4 N/m. For the SEBS block copolymers, the Poisson's ratio was assumed to be 0.48 [162], which for the G1657, gave k_{EB} = 0.19 N/m and k_{red} = 0.07 N/m. So for the stiffer polymer (PS) the reduced elastic constant was 51% lower and for the softer G1657 it was 63% lower. This illustrates how the additional deformations of the substrate need to be taken into account, especially when considering more elastic materials. This reduced elastic constant is therefore used for the remaining calculations.

$$F_{red} = k_{red}\Delta x \tag{5.10}$$

Using equation 5.10, it is possible to approximately calculate the force required to bend the nanopillars by the amount measured from the SEM images, given their respective length and the Young's modulus of the polymers previously obtained. The average bending force calculated for each of the polymer NSS is shown in Figure 5.5.9.

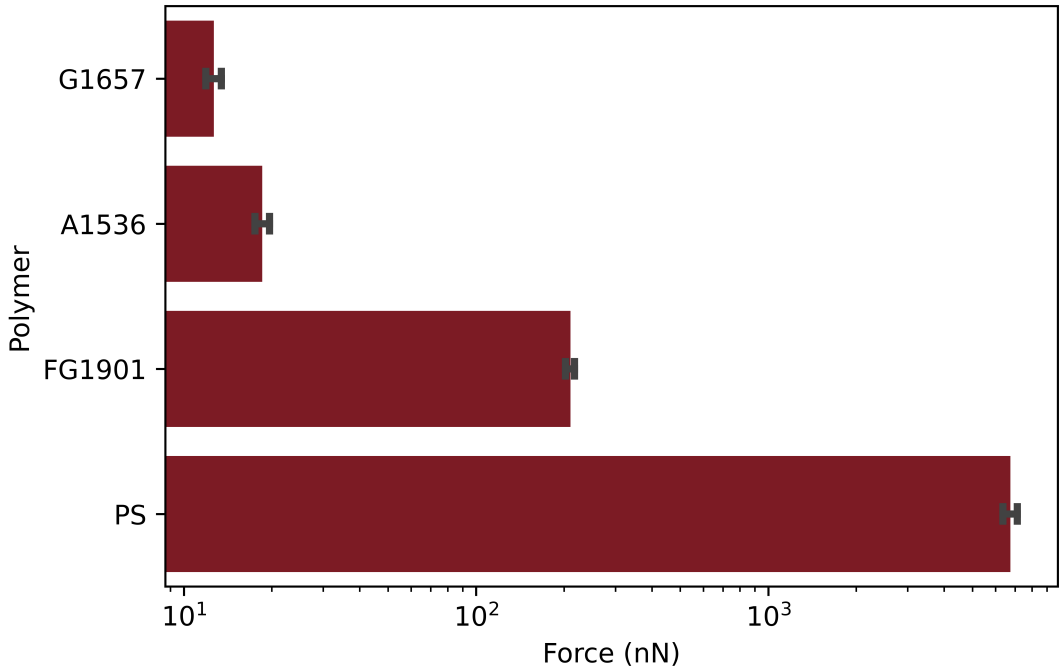


Figure 5.5.9: Magnitude of the length of pillar force on different polymer NSS. Error bars = SE.

Given that the PS has a significantly higher Young's modulus than the Kraton elastomers (by two orders of magnitude), it is not surprising that the highest bending force is found for these NSS at 6.7 ± 2.0 μN. The next stiffest polymer, FG1901, required 210 ± 44 nN to bend the pillars. The two softest NSS, A1536 and G1657, required a force of 18.5 ± 5.9 nN and 12.7 ± 3.3 nN, respectively. As early bacterial attachment to surfaces is driven by van der Waals and electrostatic interactions [163], it is likely that the same forces cause the bending of the nanopillars into contact with the bacterial envelope. This force must be at least 6.7 μN, as this is what is required to bend the stiffest polymer, and there is no reason why the interaction would be stronger for the different polymers. Because the bending here is assumed to be elastic, there will be stored elastic energy in

the pillar due to this process, which in turn, will cause a reactionary force to be exerted on the bacterial envelope as the pillar tries to restore to its original position. This stored "mechanical" energy has previously been linked with a role in the killing mechanism of NSS [56, 155]. Equation 5.11 can be used to calculate an approximate value for the elastic potential energy of a beam.

$$U = \frac{1}{2}k\Delta x^2 \tag{5.11}$$

Using this equation, the stored elastic energy for the pillars on each of the polymer NSS was calculated and are shown in Figure 5.5.10.

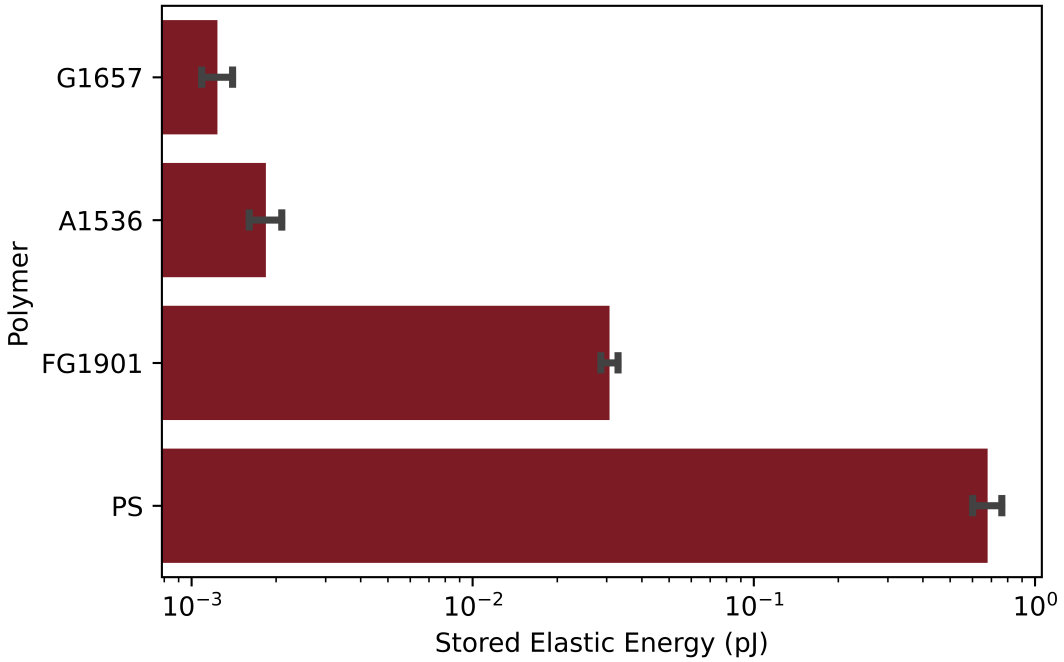


Figure 5.5.10: Magnitude of the stored elastic energy of the pillars on different polymer NSS.

The elastic energy which is stored in the PS pillars as a result of the bending is calculated to be 0.67 ± 0.41 pJ. This is much higher than the value reported by Ivanova *et al.*, when looking at the bending of 360 nm tall silicon nanopillars. They found that the maximum stored elastic energy was 1.2 fJ (0.0012 pJ) [155]. Whilst the silicon that Ivanova *et al.* studied had a higher YM than the PS NSS used here (66.5 GPa vs. ∼3 GPa), the nanopillars themselves were much thinner, with a diameter of 35.9 ± 2.2 nm. This significantly decreases the elasticity, k, to 0.31 N/m - much lower than the 36.4 N/m

for the PS nanopillars and means that much less energy is stored upon bending. The amount of stored elastic energy in the G1657 nanopillars is actually measured to be the same as was reported for the silicon nanopillars, at 1.2 fJ. However, the G1657 NSS was not found to kill a significant amount of *E. coli*, whereas the Ivanova *et al.* reported the silicon nanopillars killing up to 95% of *P. aeruginosa* cells. This is an indication that stored elastic energy may not be solely responsible for the killing of bacteria on NSS.

Once the pillar has built up this elastic potential energy it must exert a force on the bacterial envelope in order to cause damage. Given that the pillar is attached to the bacteria by its tip, all of the force it exerts on the envelope as it tries to pull away will be over the attachment area. This can be described by a shear stress, σ_{shear} given in Equation 5.12 and illustrated in Figure 5.5.11 [156].

$$\sigma_{shear} = \frac{F}{A_{\text{Cross-Section}}} = \frac{F}{\pi \left(\frac{d}{2}\right)^2} \tag{5.12}$$

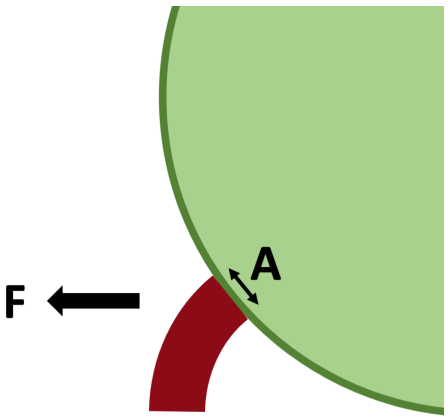


Figure 5.5.11: Illustration of the shear stress imparted on the bacterial membrane as a result of the release of potential energy in the bent nanopillar.

Here F is the force from eq. 5.10 and d is the diameter of the nanopillar (which is used to calculate the cross-sectional area of the pillar, A). The value of the average shear stress for each of the polymer NSS is calculated and shown in Figure 5.5.12. Additionally, using the SEM images of the *E. coli* on the cicada (*M. intermedia*) wings from Chapter 3, it was also possible to measure the bending of those nanopillars. Then, using the measured value of the YM of the cicada wing features, calculate the approximate shear stress acting on the bacteria. These results are also displayed in Fig. 5.5.12.

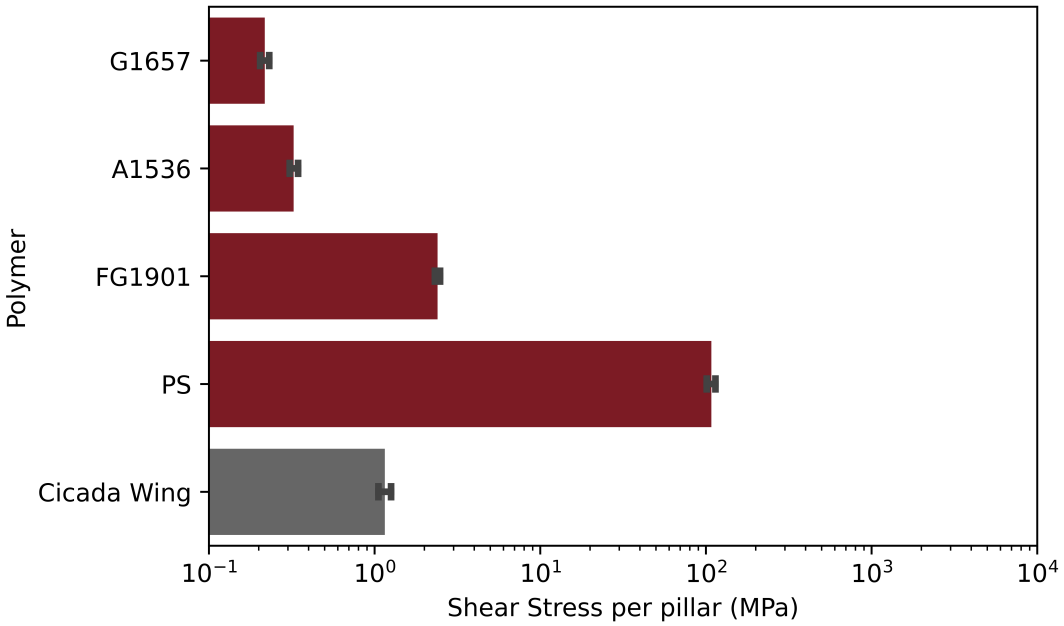


Figure 5.5.12: Approximate shear force acting on bacterial envelope as a result of nanopillar bending, for the various polymer NSS and the cicada (M. intermedia) wing.

For the PS nanopillars, the shear stress exerted on the bacterial envelope was calculated to be $\sim$ 100 MPa, per nanopillar. For the cicada wing and the FG1901 NSS, which both killed a significant proportion of *E. coli*, were calculated to have a shear force per nanopillar of $\sim$ 1 MPa and $\sim$ 2 MPa, respectively. It is important to consider these values for the stress imparted on the membrane by the pillars in the context of the bactericidal efficiency found for each NSS. Figure 5.5.13 shows the calculated shear stress per nanopillar against the bactericidal efficiency of the surface.

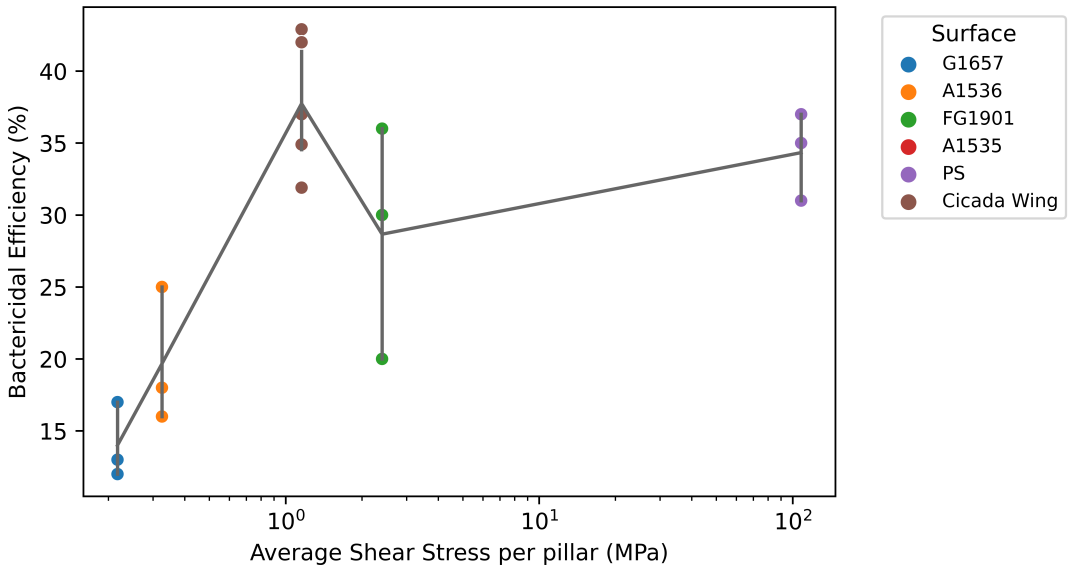


Figure 5.5.13: Average shear stress per nanopillar imparted by the NSS, including the cicada wing, compared to the bactericidal efficiency.

It is clear that with the polymer NSS, whose surface topography is nearly identical, the bactericidal efficiency increases with the average stress imparted on the cell by each nanopillar. However, the cicada wing was found to have a bactericidal efficiency slightly greater than the PS NSS but, as their nanopillars were measured to be much softer, the average stress that they impart is two orders of magnitude lower. The previously discussed work on silicon nanopillars by Ivanova *et al.* found that a force of 27 nN was required to bend the nanopillars, which can be used to calculate that the shear force imparted in this interaction is $\sim$ 30 MPa [155]. Despite having a lower stored potential energy than all of the nanopillars studied here, because of their significantly smaller diameter, the silicon pillars are able to exert a high amount of shear on the bacterial membrane. Lohmann *et al.* also recently reported that nanopillars formed from a UV cured resin with a YM of 4 GPa displayed the same bending towards the bacterial membrane [156]. They calculated (with the same method used here) that the shear stress imparted by these pillars on *E. coli* cells was 80 - 120 MPa, depending on the parameters of the nanopillars. This is in very good agreement with the stress imparted by the PS pillars in this study (which have a similar value of YM).

However, the bactericidal efficiency of the silicon nanopillars [155] and the UV resin nanopillars [156] were both found to be significantly higher than the bactericidal efficiency for the PS nanopillars found here. The silicon nanopillars were able to kill $\sim$ 95% of *P. aeruginosa* and the UV resin nanopillars were able to kill up to 80% of *E. coli* cells,

whereas the PS nanopillars here were only found to kill 34% of *E. coli* cells. These results can be reconciled by taking into account the relative number of contact points between each surface and the bacteria. For example, the density of features on the cicada wing is much higher (closer spacing) than those of the NSS produced from the LS mould, as is illustrated in Figure 5.5.14.

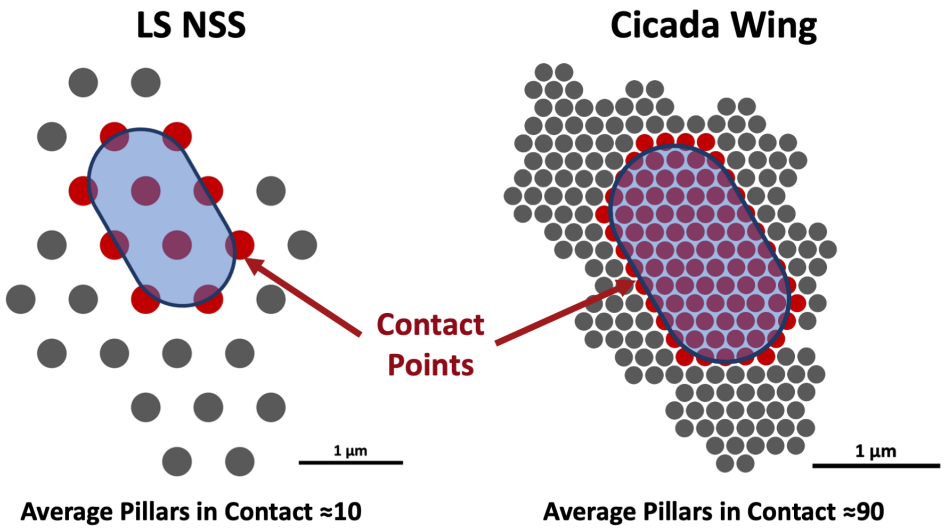


Figure 5.5.14: Illustration of the number of contact points between the nanopillars and the bacteria. Drawn to scale with the measured size of the nanopillar ("bacteria" length = 1.8 µm and width = 1 µm.)

This shows that there will be many more pillars in contact with the bacteria on the cicada wing than the LS NSS. For a 1 x 1.8 μm bacteria (typical for *E. coli*), roughly 10 pillars will come into contact on the LS surfaces compared to $\sim$ 90 on the cicada wing. Similarly, given that their spacing is much closer than the LS surfaces, the silicon and resin surfaces reported in the literature would also have many more pillars in contact with the bacteria [155, 156].

Whilst it has been shown, with cross-sectional FIB-SEM, that the nanopillars directly underneath the bacteria do not bend to the same extent that those around the perimeter do [155], it would be expected that they still exert some force on the membrane. If it is approximated that each of the pillars in contact with the bacteria exerts the same force, a "total" force acting on the bacterial envelope can be estimated by multiplying σ_{shear} by the number of contact points. The value of this is estimated for each surfaces here and is shown in Figure 5.5.15.

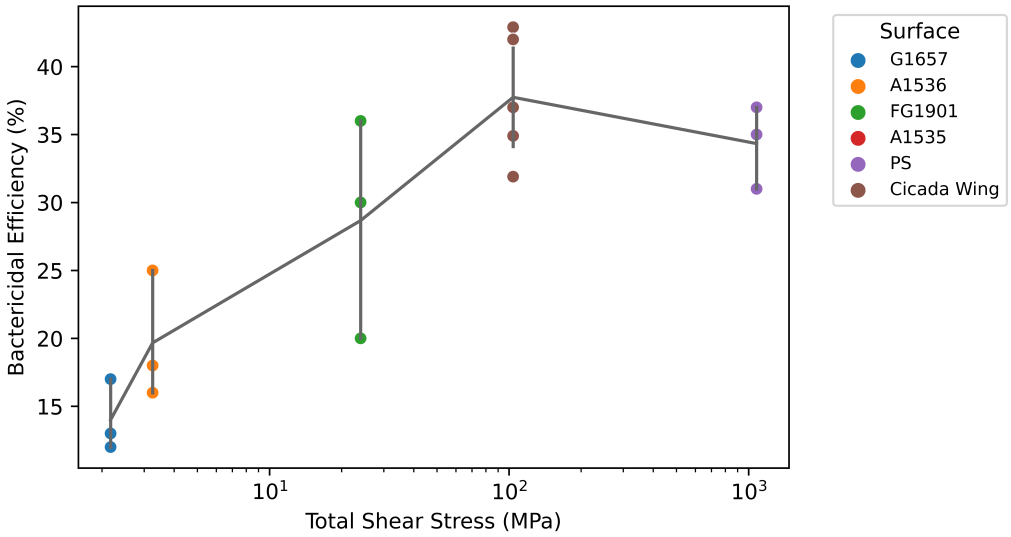


Figure 5.5.15: "Total" shear stress imparted by all nanopillars in contact with bacterial membrane.

This is likely to be an overestimation (especially for surfaces with denser features) as the perimeter pillars will bend further and because the stress imparted by a particular nanopillar will depend in some way on the stress of the surrounding nanopillars [156]. However, it does provide some information when used as an approximation. Fig. 5.5.15 shows that the bactericidal efficiency increases with the "total" shear stress imparted on the membrane. When considering the mechanisms of cell death on NSS set out in Section 1.6, this perhaps aligns best to the theory of Bandara *et al.* who suggest that shear forces were responsible for killing [41]. In that case it was thought that strong adhesion between the bacteria and nanopillars was due to release of EPS, which in turn caused damage to the bacteria as it tried to move. Here, it appears that the shear forces may arise from bending of the nanopillars into the bacteria, and the subsequent stress associated with restoring the pillars back to their original position. Thus, increased shear forces acting on the bacterial envelope are more likely to cause damage and cell death. This also suggests that the ability of a surface to kill bacteria may depend on an interplay between nanopillar stiffness and spacing. It has been shown here that the PS NSS (with a wide pillar spacing) showed similar levels of killing of *E. coli* to the cicada wing, despite having almost 10x fewer contact points, possibly due to it having a higher stiffness and therefore a greater ability to exert shear stress on the bacterial membrane. This could also explain why NSS in the literature which have similar dimensions to the cicada wing are able to kill significantly more bacteria [58, 72, 156]. For example, Cui *et al.* demonstrated 98% killing efficiency using polycarbonate surfaces (YM $\sim$ 2 GPa) with pillars 200 nm tall and 170 nm in spacing [72] - almost identical to the cicada wing measured in

Chapter 3. However, at a certain point, the spacing of the nanopillars becomes a limiting factor. As Fig. 5.4.2 shows, the killing efficiency of the polymer NSS does not continue increasing with the YM - the spacing of the pillars must be reduced to increase the killing.

As suggested previously by Ivanova *et al.* [155], it is possible that there are multiple bactericidal mechanisms at play on NSS. For example, with NSS made from very stiff materials, with a Young's modulus >> 100 GPa, or those with a wide base, the initial interaction force between the bacteria and the nanopillars is likely to be insufficient to cause bending (and the subsequent release of energy). Therefore, the bactericidal mechanism on these surfaces may be as described by the "stretching" theory, where the membrane is ruptured as it adsorbs to the nanopillars [80]. Further work undertaken to learn more about the bactericidal mechanism of NSS is described in Chapter 6.

One final point to make here is that, regardless of the bactericidal mechanism, it has been shown that effective antibacterial surfaces can be fabricated from rubbery materials. Both the A1535 and FG1901 showed significant killing over the control surface, despite not having optimal spacing of their features. This is an important result when considering the practical uses of these antibacterial surfaces. As discussed earlier, medical devices often have lots of issues when it comes to the formation of biofilms and these generally lead to further infections for the patient. Many of these devices, such as catheters or ventilator tubing, have to formed from flexible materials to allow them to be placed in the body. This could not be achieved with the range of inorganic materials, such as titanium or silicon, that has been previously used to form NSS. These rubbery elastomers provide a practical material as well as the ability to make antibacterial NSS, as shown here. Future work will look to improve their bactericidal efficiency by optimising the pillar spacing *and* by tuning the mechanical properties with different block copolymers, such that their rubbery qualities can be maintained but with a higher Young's modulus.

5.6. Summary of Findings and Conclusions

In this chapter the role of nanopillar stiffness and its link to bactericidal efficiency of NSS has been investigated. This was achieved by forming NSS from a series of SEBS block copolymers using the previously discussed solution casting method onto the LS mould. The bactericidal ability of the NSS were then tested against *E. coli* using a Live/Dead assay. Finally, the morphology of both the bacteria and the nanopillars after incubation were assessed using SEM. The key conclusions are as follows -

- A range of polymers were selected to provide different mechanical properties. A fully glassy polymer, PS, provided high stiffness and then a set of SEBS block copolymers where chosen, which had a range of PS contents, to test more flexible material.
- The mechanical properties of the PS was assessed using a capillary wrinkling technique, with the Young's modulus measured to be 3.34 ± 0.77 GPa, which is in very good agreement with the literature.
- The Young's modulus of the block copolymers were assessed in bulk with a tensile tester giving values ranging from 2.7 - 16 MPa. It was found that the Young's modulus did not scale with the percentage of PS in the polymer, possible due to the block architecture.
- The NSS fabrication process was optimised for each of the polymers in order to produce nanopillars that were consistent in height across all of the surfaces. This was to insure that the only difference between each NSS was the stiffness.
- Each NSS was assessed for killing ability against *E. coli* after 2 h of incubation. The PS, FG1901 and A1535 polymers were all found to kill significantly more bacteria than the control surface.
- Comparing the killing rate to the stiffness found that the NSS with a higher Young's modulus were able to kill more *E. coli*.
- Importantly, no correlation was found between the height of the pillars on the NSS and the killing ability - suggesting the stiffness was the factor which causes the increase in bactericidal efficiency.
- No large scale morphological changes of the bacteria were found after incubation on the NSS for 2 h - it is possible that the "tears/ruptures" in the membrane occur after longer incubation times.

- The bacteria incubated on all the NSS were found to be shorter than those incubated on the control surfaces.
- No correlation was found between the change in cell length and the killing ability, so it is possible that this could be a drying effect.
- The bacteria on the LS NSS were found to have preferentially orientate themselves along the direction of the nanostructure array, i.e. they lay along the trenches of the pillars. This increases the number of contact points between the bacteria and the surface.
- Bending of the nanopillars towards the bacterial envelope was observed on all NSS.
- The forces involved in these interactions were calculated by considering the bending distance and the elastic constant of the nanopillars.
- Using this method it was also possible to calculate the potential energy of the pillar after bending, and the amount of shear stress that the nanopillar will impart on the bacteria as it tries to restore its position.
- For the PS nanopillars this stress was measured to be $\sim$ 100 MPa, which is similar to what has previously been measured in the literature.
- To reconcile the differences in bactericidal efficiency of surfaces with different stiffness pillars, the density of the nanopillars, or the number of contact points with the bacteria were also taken into account. By looking at this as a combination an increase in killing with the "total" shear stress is seen.
- For NSS with flexible nanopillars, a bactericidal mechanism is proposed which suggests that both the flexibility and spacing of the nanopillars play important roles. This may be different to the mechanism of NSS with high stiffness or inflexible nanopillars.

More work is required to untangle the bactericidal mechanism of different surfaces, with some experiments untaken in the next chapter.

S5. Supplementary Figures

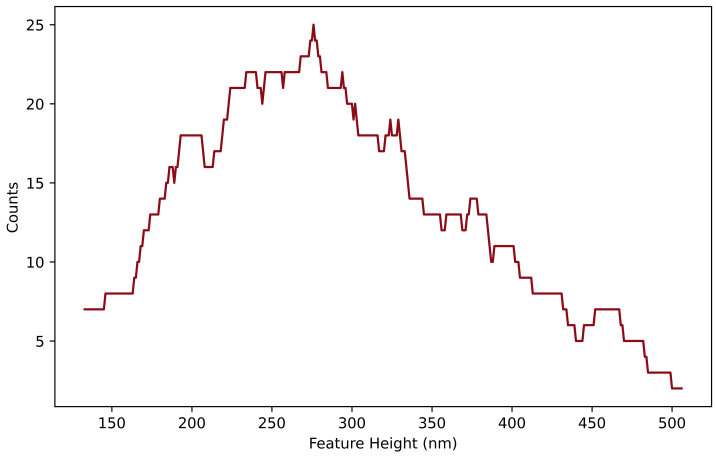


Figure S5.1: Counts of the number of surfaces, made from all of the polymers, whose average pillar height fell within a ± 55 nm window of a certain value. The highest count represents the greatest number of surfaces which fall in the window of the corresponding height and so gives the greatest number of surfaces for use in the study.

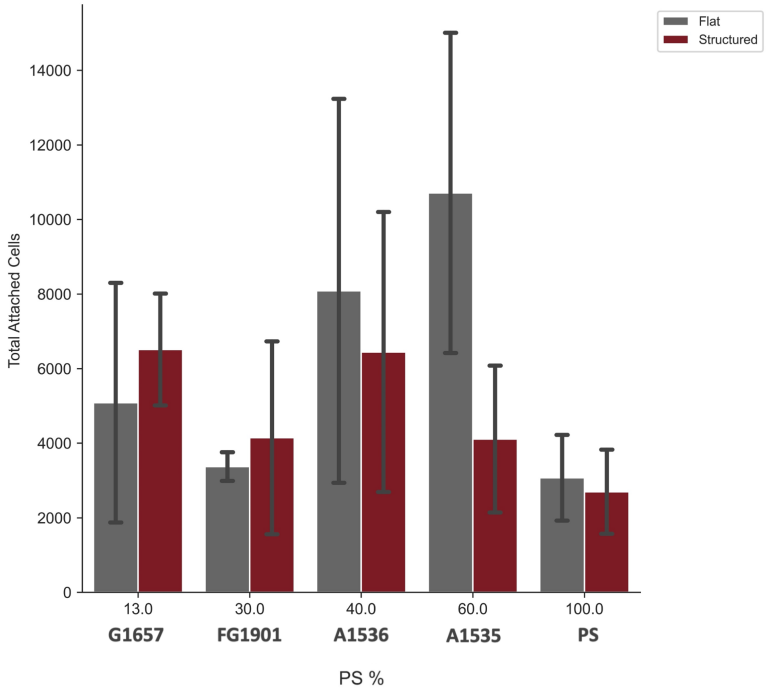


Figure S5.2: Total number of attached cells found on each of the different polymer nanostructured and control surfaces. Statistical tests performed with a 2-way ANOVA, which found no significant differences between any of the values.

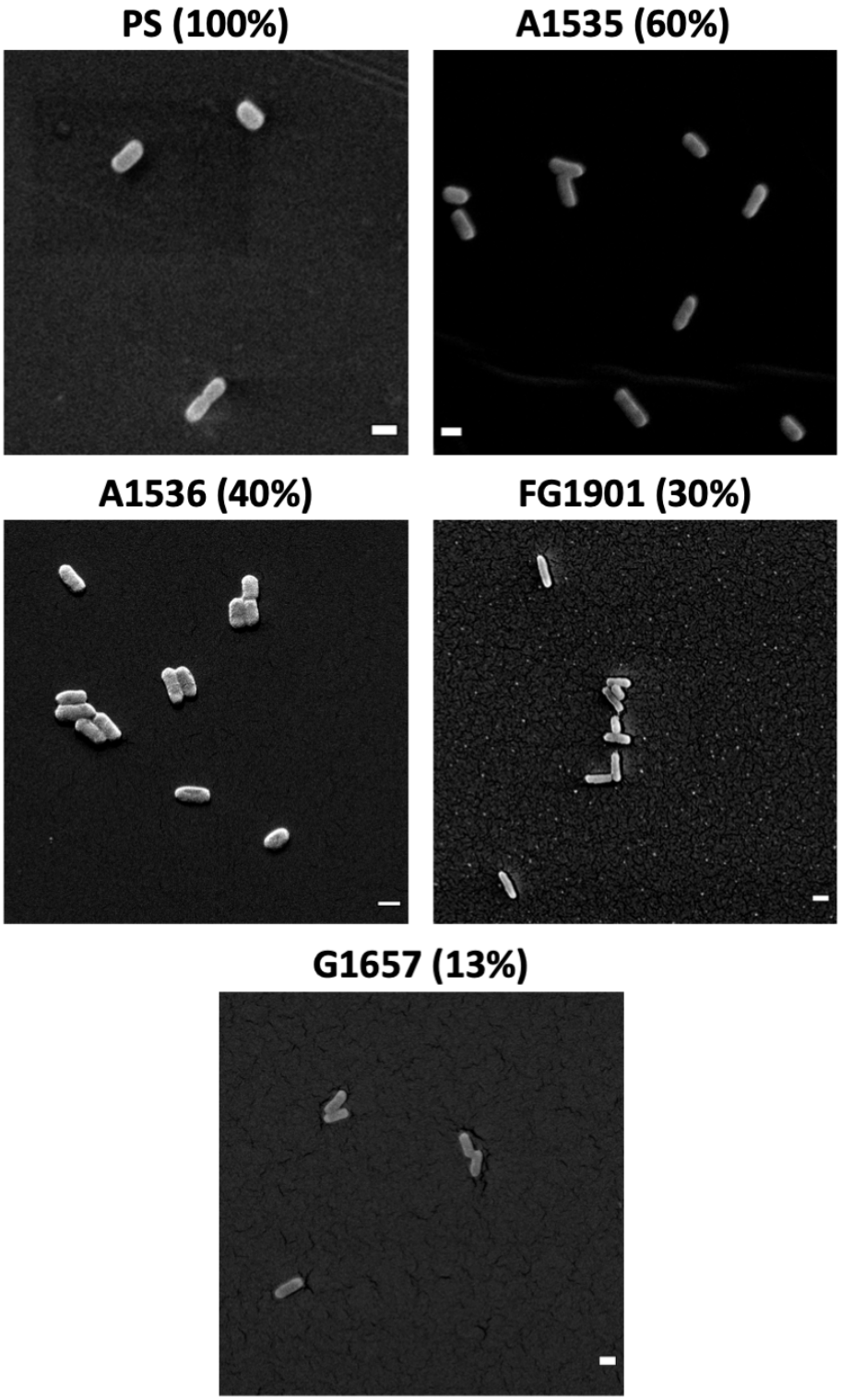


Figure S5.3: SEM of E. coli on different stiffness flat surfaces. Scale Bar = 1 µm

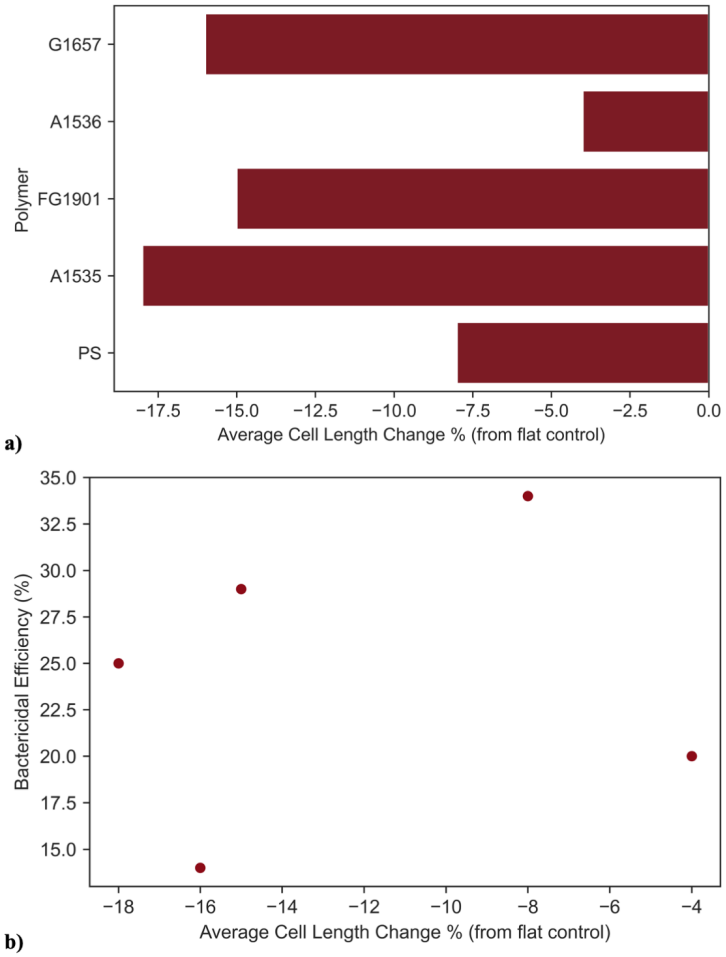


Figure S5.4: Change in cell length of E. coli incubated on NSS compared to flat surfaces

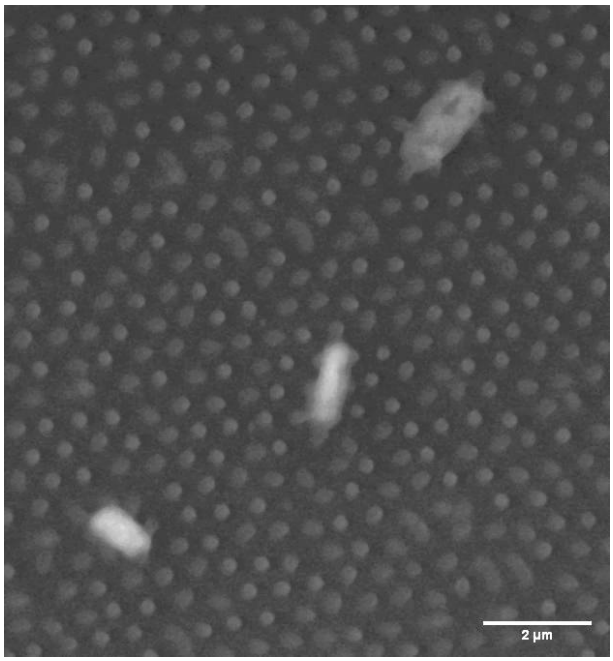


Figure S5.5: E. coli on FG1901 NSS imaged with environmental SEM. This work was carried out by Samuel Davis at Department of Materials, Loughborough University.

Chapter 6

Elucidating the Bactericidal Mechanism of Nanostructured Surfaces

6.1. Introduction

Despite the large number of studies undertaken into nanostructured surfaces and the ability to probe numerous factors that may influence the efficiency with which they kill bacteria, there is still uncertainty as to the exact mechanism by which bacteria are killed by NSS. As discussed previously (in section 1.6), the generally accepted theory is that the outer bacterial membrane is stretched to breaking point as it adsorbs to and is pulled over the nanopillars [80]. However, there is conflicting evidence that a number of other factors, such as the adhesion forces between the bacteria and the nanopillars [39, 41], bacterial growth [90] and oxidative stress [75], may also play important roles. The work in the previous chapter has also suggested that the nanopillar stiffness and the shear forces that arise from their bending may play a role in the bactericidal effect.

The main factor that is holding back insight into the bactericidal mechanism is the difficulty in visualising the interaction between nanopillars and the bacterial membrane *in situ*. Most studies in the literature to date have determined the bactericidal mechanism through either computational modelling or with *ex situ* imaging with techniques such as TEM and SEM. Whilst these imaging techniques can provide a high resolution picture of the bacterial membrane after the interaction with the nanopillars, it can only do so after they have been treated with fixatives and other sample preparation chemicals required

for this type of imaging (which are also often carried out under a vacuum). Additionally, these techniques only provides an "end-point" view of this interaction, not what is happening during the actual death of the bacteria. However, imaging these interactions *in situ* is challenging as the length-scales involved are very small, often in the nanometre range, which is at the limit of most fluorescent microscopy techniques.

This chapter will discuss various experiments that have been carried out to shed more light on the bactericidal mechanism of these nanostructured surfaces. Firstly, a high-throughput testing regime was developed using the LIVE/DEAD stain in a microplate reader, to assess the killing of numerous bacterial strains by a commercial NSS - g.moth. Some of these were mutant strains that had cell membrane defects, allowing the exploration of the bacterial characteristics that are most important in rendering cells susceptible to killing by NSS. Next, the link between the bacterial growth cycle and the susceptibility to NSS is investigated, as it was previously suggested that cell division plays a key role in the damage sustained by bacteria on NSS [90]. This was examined by growing *E. coli* to different points in the growth cycle (where the growth rates are different) before incubating them on the *M. intermedia* wing and assessing the amount of killing with the Live/Dead stain assay. Finally, attempts to capture the interaction between the nanopillars and bacterial membrane *in situ* will be discussed. This involved using high-resolution fluorescence microscopy to image the *E. coli* membrane interacting with fluorescently labelled nanostructures.

6.2. Susceptibility of Different Bacterial Strains to NSS

6.2.1. Introduction

Most of the investigations into the mechanism of action of antibacterial nanostructured surfaces has focussed on the structures themselves, and how changing their parameters could alter this effect. What has been scrutinised far less is the characteristics of the other participant in the interaction - the bacteria. By revealing which, if any, bacterial characteristics make them more susceptible to killing by NSS, it may be possible to learn more about the effect itself. Hasan *et al.* reported that whilst the cicada wing was able to effectively kill gram-negative bacteria such as *E. coli* and *P. aeruginosa*, it did not kill any gram-positive bacteria, such as *S. aureus* [37]. They also reported that the shape of

the bacteria (rod or coccus) did not affect whether the cells were killed or not. Nowlin *et al.* later reported that strains of the yeast, *S. cerevisiae*, which had higher binding affinities to substrates were more susceptible to killing by a NSS [39]. Another report by Jindai *et al.* investigated *E. coli* strains with differences in flagellation and motility, finding that the more motile bacteria died quicker on silicon nanopillars. This finding was attributed to the assumption that the more motile cells move faster towards the surface and therefore are killed more quickly. The results in the literature indicate that the adherence and movement (growth and motility) clearly play an important role in the bacteria-nanopillar interaction, and therefore the mechanism of cell death. The leading theory as to the mode of death on NSS implicates the stretching of the cell wall over the nanopillars to the point of breaking and does not account for bacterial movement. However, investigating bacterial strains with different cell wall characteristics could provide more important information about the bactericidal mechanism.

This section will discuss the testing of a range of bacterial strains, including knock-out strains that have cell wall defects, against a commercially available nanostructured surface, termed g.moth. This particular NSS was used to allow the testing of numerous bacterial strains, as it was available as large-area sheets, that were consistent in topography. In conjunction with this, a high-throughput testing regime was developed that used the LIVE/DEAD stain with a microplate reader instead of the typical fluorescence microscopy, allowing more samples to be measured in a shorter time. To confirm the results, LIVE/DEAD staining was also used, as previously, with fluorescence microscopy. Additionally, each of the strains was imaged on the g.moth surfaces using SEM to assess any changes in morphology of the bacteria. The work in this section was carried out in conjunction with a 3rd Year Undergraduate project student, William Mann.

6.2.2. g.moth^{TM} Surfaces

The nanostructured surface used in this study was the commercially available g.moth^{TM} films (purchased from GEOMATEC). These are PET films which are imprinted with nanostructures using a roll-to-roll, hot-embossing, production method, which allows very large areas to be fabricated with a consistent topography. g.moth is designed as an anti-reflective surface, however as Figure 6.2.1 shows, the topography (which was assessed with AFM and SEM as described in section 5.2) is similar to many antibacterial NSS.

The AFM and SEM analysis on the g.moth surface reveals a random array of features

with inhomogeneous spacing, much like those on the dragonfly wing. The average feature height was measured at 120 ± 50 nm, which is lower than those on the *M. intermedia* wing but still sufficient to have a bactericidal effect according to Watson *et al.* [85]. The morphology of the features takes the form of thin pillars with a rounded tip, similar to those on the cicada wing or the moth-eye (upon which this technology is based). The films themselves are backed with an adhesive layer which allowed them to be secured to a substrate for testing.

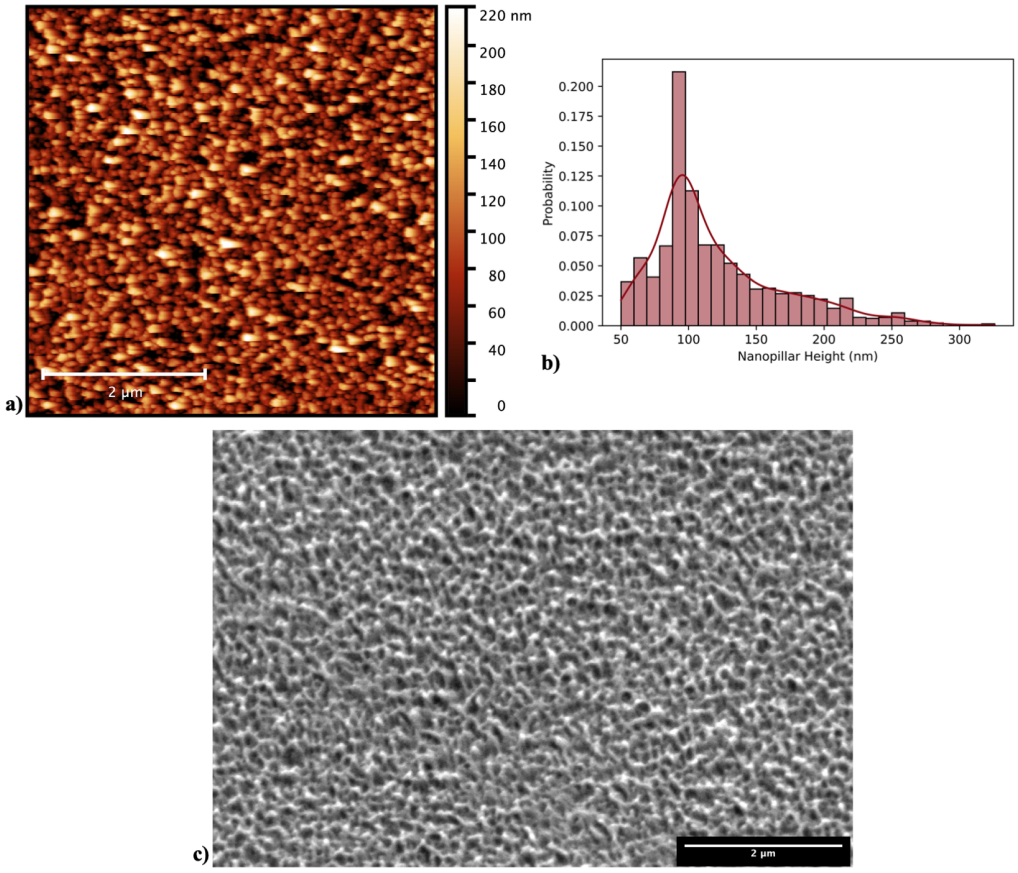


Figure 6.2.1: Characterisation of the g.moth surfaces. a) AFM scan of the surface. b) Histogram of the average feature heights and c) SEM image showing the morphology of the features.

6.2.3. Bacterial Strains

The aim of this study was to explore the importance of a wide range of bacterial characteristics on the killing efficiency of NSS, especially those relating to the bacterial cell wall. With that, the strains in Table 2.4.1 on page 45 were chosen for testing. The wild-type (WT) *E. coli* strain (MG1655) which has been used throughout this work so far, was chosen to provide a reference point as a bacterium that is known to be suscep-

tible to killing on NSS. Additionally, a clinical isolate of UroPathogenic *Escherichia coli* (UPEC), which is a leading cause of hospital-acquired infections and therefore a very relevant pathogen for this research, was also selected. UPEC strains tend to have a range of virulence factors, including increased cell-surface features such as fimbriae that promote adhesion to surfaces, leading to stronger biofilm formation [164]. As well as these two gram-negative strains, several gram-positive bacteria were also chosen. Gram-positive bacteria have a thicker cell wall than gram-negative bacteria, owing to the thicker layer of peptidoglycan (discussed in section 1.3), so would be expected to be more resilient to killing by NSS. *S. aureus* was chosen to probe this, with the methicillin-susceptible laboratory strain, RN4220, tested alongside the methicillin-resistant strain, Je2. As antibiotic resistance is conferred from changes in enzymes that synthesise the cell wall, but not the final cell wall structure, MRSA should be as susceptible to NSS as the MSSA (non-resistant) strains [165].

In addition to the wild-type MRSA Je2 strain, several mutant strains that had cell wall defects were also tested. Penicillin Binding Proteins (pbp) are transpeptidases which are involved in peptidoglycan (PG) synthesis during the cell cycle. Pbp3 is involved in insertion of new PG into the sidewall of the cell during elongation. The $\Delta pbp3$ mutant strain shows few morphological changes, other than being slightly less elongated [166]. The role of Pbp4 is in the high level cross-linking of PG in the cell wall. The $\Delta pbp4$ strain has much less cross-linking and has been shown to have reduced cell wall stiffness as a result [167]. SagB is a glucosaminidase involved in cleaving glycan chains. The $\Delta sagB$ mutant presents with longer glycan strands that gives the bacteria a stiffer cell wall and irregular morphology [168, 169]. Atl is also a glucosaminidase and is involved in the separation of daughter cells during division [170]. The Δatl mutant is characterised by clusters of cells due to poor separation. Finally, ppGpp is an alarmone which triggers a stress response (known as the stringent response) when bacteria are in nutrient poor conditions, such as amino acid deprivation or osmotic stress [171], slowing down growth and other metabolic processes. The ppGpp null strain, ppGpp^o, cannot initiate the stringent response, and therefore is less resilient when placed in stressful conditions.

All of the chosen strains were grown from a single colony in the appropriate media (LB for the *E. coli* strains and Tryptic Soy Broth (TSB) for the *S. aureus* strains) overnight, at 37^{o}C shaking at 200 rpm. The growth media for the mutant strains was supplemented with 10 μg/ml of Erythromycin (erm) in order to select for the correct strain. These overnight cultures were then used as described later.

6.2.4. Developing High-Throughput Testing Procedure

The typical method for measuring the bactericidal efficiency of NSS, used previously here and throughout the literature, uses a Live/Dead stain in combination with fluorescence microscopy. This is a highly effective method as the "Live" or "Dead" state of individual bacteria can be observed and counted, giving an accurate assessment of the percentage of dead cells. However, the process of imaging and analysing multiple regions of many samples is time consuming, which means that this method is not conducive to testing ∼10s of NSS (along with controls). To allow the screening of many NSS at once, or to investigate killing against many different bacterial strains, a high-throughput Live/Dead assay was developed using a microplate reader. By placing the test surfaces in the wells of a 96-well plate, it becomes possible to screen many more parameters than if individual samples had to be prepared for microscopy.

Method 1:

The first method tested, illustrated in Figure 6.2.2, is similar to the technique used to prepare samples for fluorescence microscopy. Firstly, the surfaces (NSS and controls) were added and secured inside the wells. A black well plate was used for this to prevent signal cross-talk between the wells. Next, a bacterial suspension was added to cover the surface. For this, an overnight suspension of bacterial culture was diluted in fresh media and grown to mid-exponential phase (OD_{600} = 0.4-0.5). As most growth media can interfere with the binding of the LIVE/DEAD stain [172] and also tend to auto-fluoresce, which would create a high background signal, the bacteria were pelleted and resuspended in 0.9% NaCl to the desired concentration, before 200 µl was added to the wells. The bacteria were then incubated on the surfaces at room temperature (RT) without shaking. After the chosen incubation time, the suspension was removed and the wells gently rinsed with buffer. Then 200 µl of the BacLight LIVE/DEAD stain was added and left for 30 min in the dark to bind to the cells. It was then aspirated and the well gently washed with buffer for a final time. To improve the fluorescence signal, 200 µl of buffer was added to the wells before putting in the microplate reader (Hidex Sense). This was set to the excitation wavelength of both dyes (485 nm), and to measure the fluorescence intensity at the emission wavelengths of each ($\lambda_{\text{em. SYTO9}}$ = 530 nm, $\lambda_{\text{em. PI}}$ = 630 nm). As the dyes can bind to the test surfaces it was important to have "background" wells which contained the test surface, but had not been inoculated with bacteria. The LIVE/DEAD stain was added to these to obtain a background signal that was then subtracted from each of the other wells. Once the background was removed, the SYTO9 and PI signal

intensities needed to be converted into a percentage of dead cells.

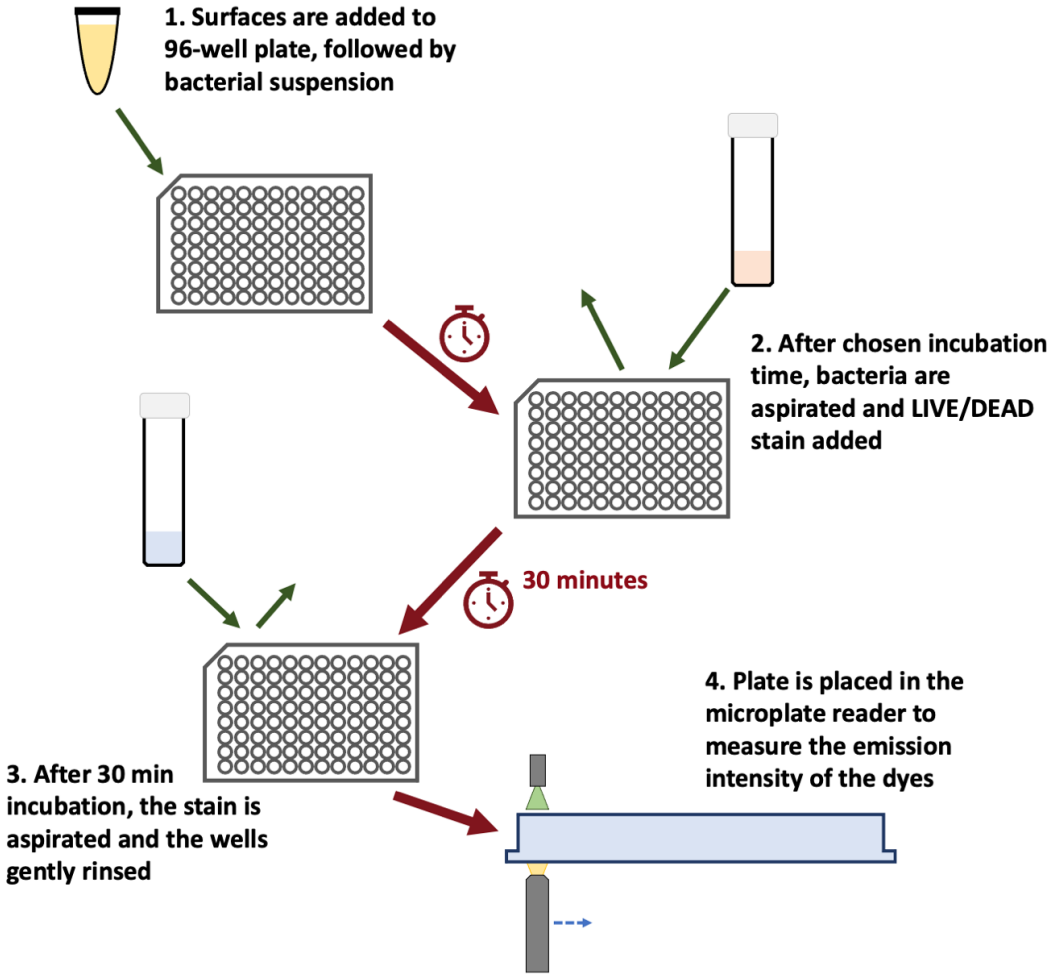


Figure 6.2.2: Method 1 for the high-throughput assay to test the viability of bacteria on NSS. In this, the Live/Dead stain is removed from the wells before imaging in the plate reader.

In order to assess the response of the dyes to different amount of live and dead bacteria, a "calibration" experiment was performed. The procedure for this is as follows -

- Grow *E. coli* cells to mid-exponential phase
- Wash out the growth media from 25 ml of the bacterial suspension by centrifuging into a pellet at 4000 rpm for 10 min and resuspending in 1 ml of 0.9% NaCl. This is repeated 3 times.
- Divide this suspension in two, putting 0.5 ml in 10 ml of buffer and the other 0.5 ml in 10 ml of 70% ethanol, leaving for 1 h at RT. This creates a live and dead population of bacteria.

- Wash the cells again to remove the ethanol by centrifuging into a pellet at 4000 rpm for 10 min and resuspending in buffer (x3). Then adjust to OD = 1.
- Make 5 mixtures of the live and dead bacteria at ratios of 0:100, 20:80, 50:50, 80:20, 100:0.
- Add 100 µl of the bacteria mixtures and 100 µl of a 2X LIVE/DEAD stain solution to a 96-well plate, in triplicate.
- Incubate for 15 min at RT to allow the dyes to bind.
- Measure the signal intensity of both the SYTO9 and PI for each mixture.

This test was performed on the *E. coli* MG1655 strain, with the fluorescent intensities of the SYTO9 and PI stains plotted against the percentage of dead cells in Figure 6.2.3.

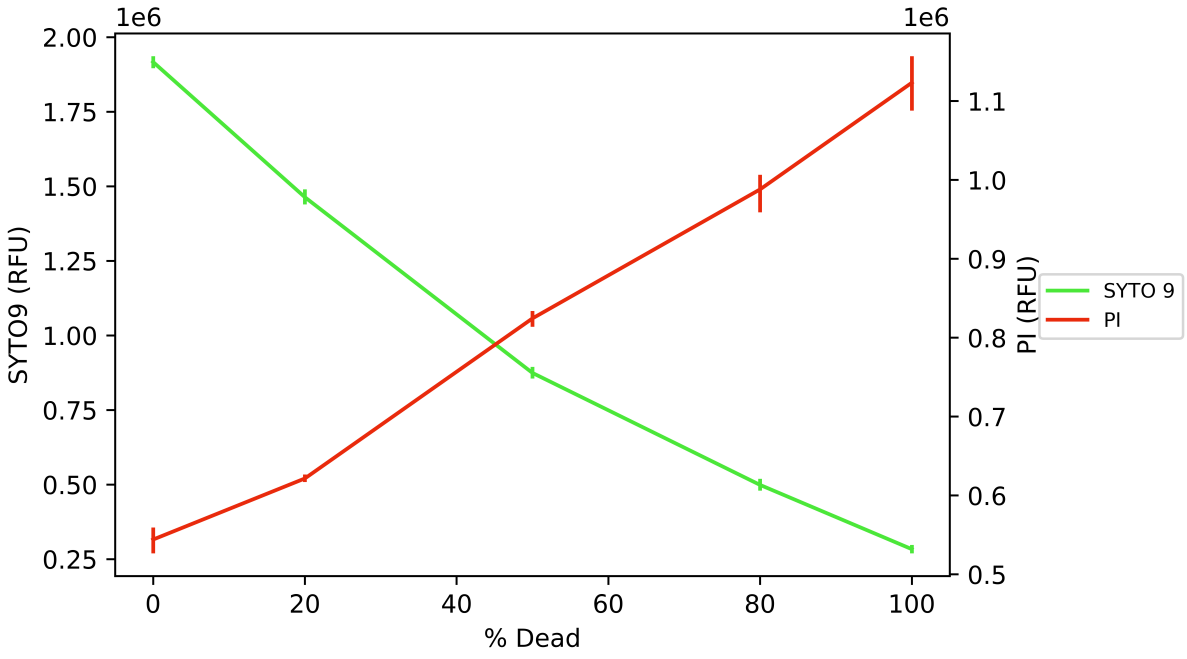


Figure 6.2.3: Fluorescence intensity of the SYTO9 and PI signals from E. coli MG1655 cells changes linearly with the proportion of dead cells in the suspension.

This shows that the signal of both the SYTO9 and PI dyes change approximately linearly with the proportion of dead cells. Therefore in order to convert the signal intensity into the percentage of cells, it is possible to use the same approximation that is used for the fluorescence microscopy. This expression is given by equation 6.1.

$$\% \text{ of Dead Bacteria} \propto \frac{\text{PI}_{\text{Intensity}}}{\text{PI}_{\text{Intensity}} + \text{SYTO9}_{\text{Intensity}}} \tag{6.1}$$

The first trial using high-throughput method 1 was carried out with the *E. coli* MG1655, UPEC and *S. aureus* RN4220 strains, which were incubated at a concentration of $OD_{600} = 1$ on the g.moth surfaces (+ empty well controls) for 24 h. Figure 6.2.4 shows the combined fluorescence intensity of the SYTO9 and PI for the g.moth and control surfaces, along with the respective backgrounds.

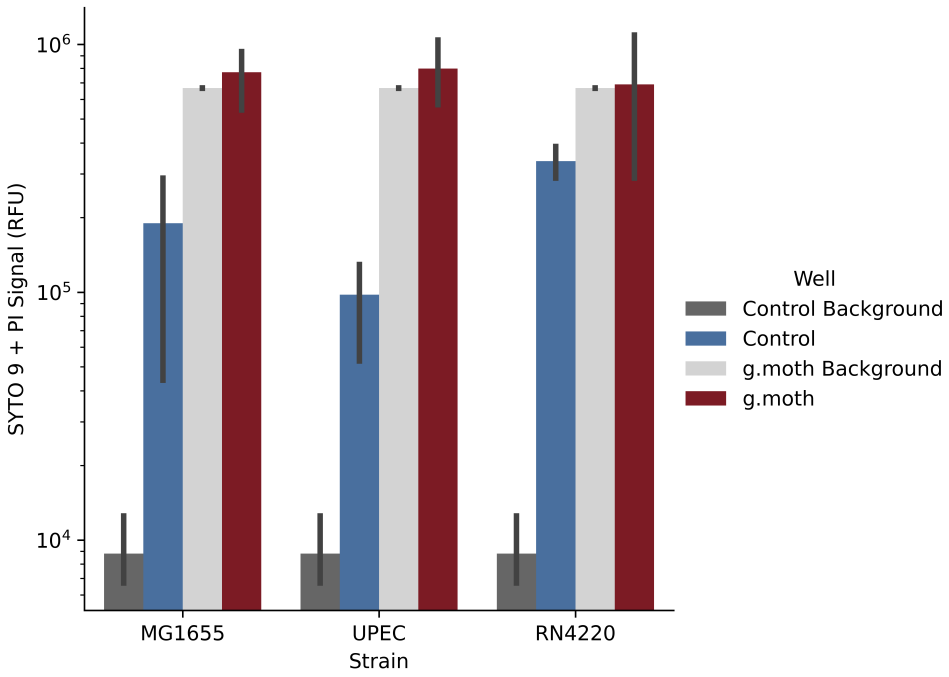


Figure 6.2.4: Combined SYTO9 and PI signal intensity for the g.moth and control surfaces, along with the "blank" background, for method 1 (OD = 1 suspension, 24 h incubation).

Generally, the "signal" from the g.moth surfaces exceed the levels of the "background" wells (with no bacteria present) which allows measurement of the percentage of dead cells on the test surfaces. However, for some of the individual repeats (especially for the RN440 strain) the "background" did exceed the signal. This indicates that the g.moth surface is absorbing some of the dye, giving a high background, which is problematic when the number of cells on the surface is low. As the absorption of the dye into the g.moth cannot be prevented, the signal needed to be increased in order for it to exceed the background levels. An improved version of this plate reader method was therefore developed.

Improved Method (Method 2):

An alternative procedure was devised to try and improve the signal further, which is illustrated in Figure 6.2.5. Method 2 is the same as method 1 up to the point where the bacterial suspension is removed from the surfaces after incubation. For method 2 the LIVE/DEAD stain solution is added to the surfaces and put directly into the microplate reader. This is used to incubate the stain on the surfaces whilst shaking at 600 rpm in order to ensure that all of the adhered cells are exposed to the dye. The signal intensity of each dye is measured after 15 min of incubation with the dye, *without* removing the dye. The aim of this was to try and prevent too many of the cells from being washed off during the cell staining phase.

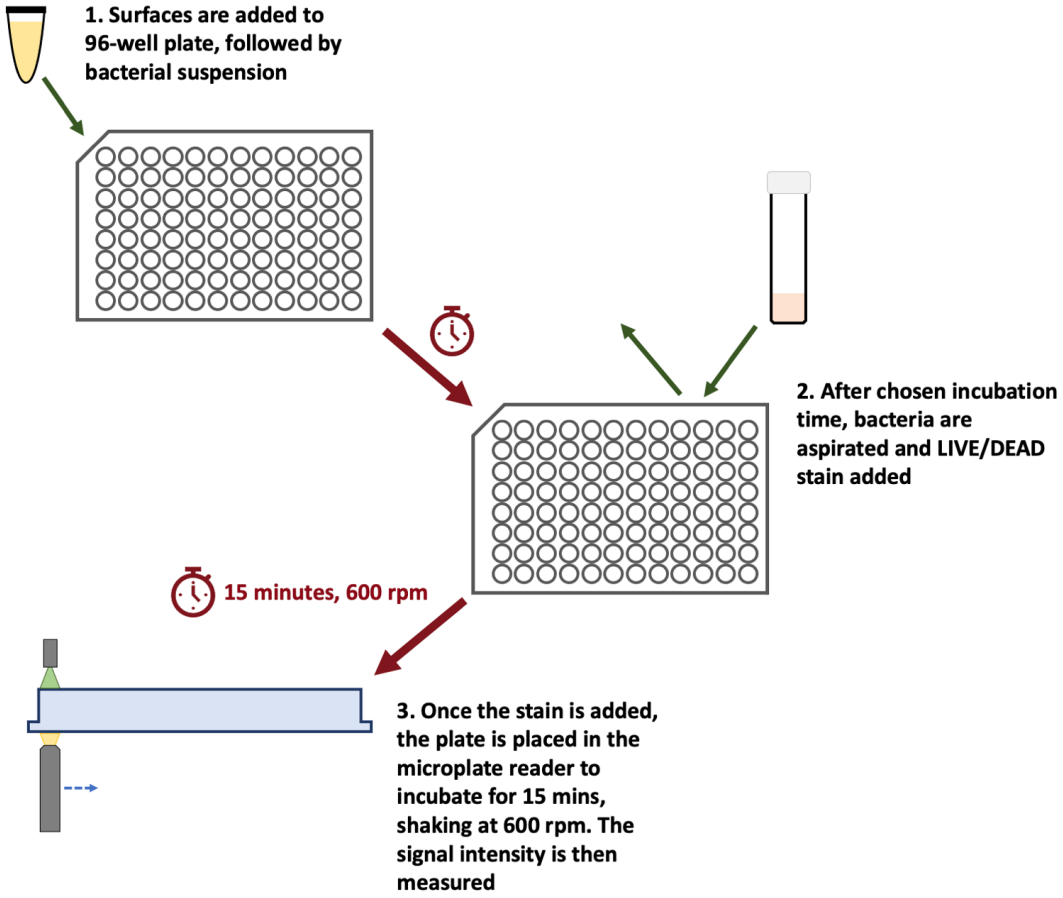


Figure 6.2.5: "Improved" Method 2 for the high-throughput assay to test the viability of bacteria on NSS. In this the Live/Dead stain remains in the wells before imaging in the plate reader.

Figure 6.2.6 shows the signal and background intensities measured from a trial using the Je2 WT, Δ*pbp3*, and Δ*sagB* strains. It was found that the signal received from the bacteria-laden surfaces (both the g.moth and the control) exceeded the background (with

no cells) greatly, indicating that this method is able to detect the number of live and dead bacteria on the surfaces from within the well-plate, and therefore can also be used as a high-throughput viability assessment for NSS.

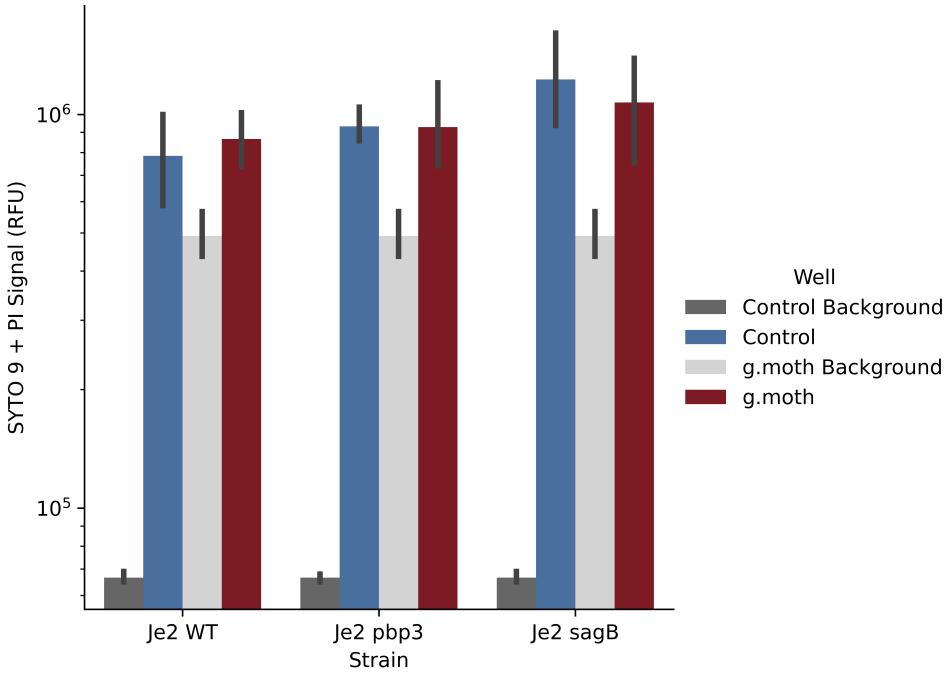


Figure 6.2.6: Combined SYTO9 and PI signal intensity for the g.moth and control surfaces, along with the "blank" background, for method 2 (OD_{600} = 1 suspension, 24 h incubation).

6.2.5. Assessing Viability of Bacterial Strains with a Microplate Reader

Once procedures for using the microplate reader with the Live/Dead stain had been established, the viability of the various bacterial strains, after incubation on the g.moth surfaces, was assessed. The g.moth films were cut to the size of the wells on the 96-well plate using a hole-punch and the adhesive layer on the back of the film was used to secure each disc to the bottom of the well. For this study, blank wells were used as the control (i.e. flat polystyrene). It was found that method 1, whereby the LIVE/DEAD stain is removed and buffer used to rinse the well before putting in the plate reader, was effective for studying both the *E. coli* strains, and the *S. aureus* RN4220 strain. Each strain was prepared as described above adjusted to OD_{600} = 1 and incubated for 24 h at RT. Due to the differences in fluorescence signal intensity from each of the strains (because of differences in size of the bacteria), the bactericidal efficiency is represented as a fold killing enhancement over the control surfaces. The fold enhancement in killing for these

strains, found from 4 repeat measurements, is shown in Figure 6.2.7.

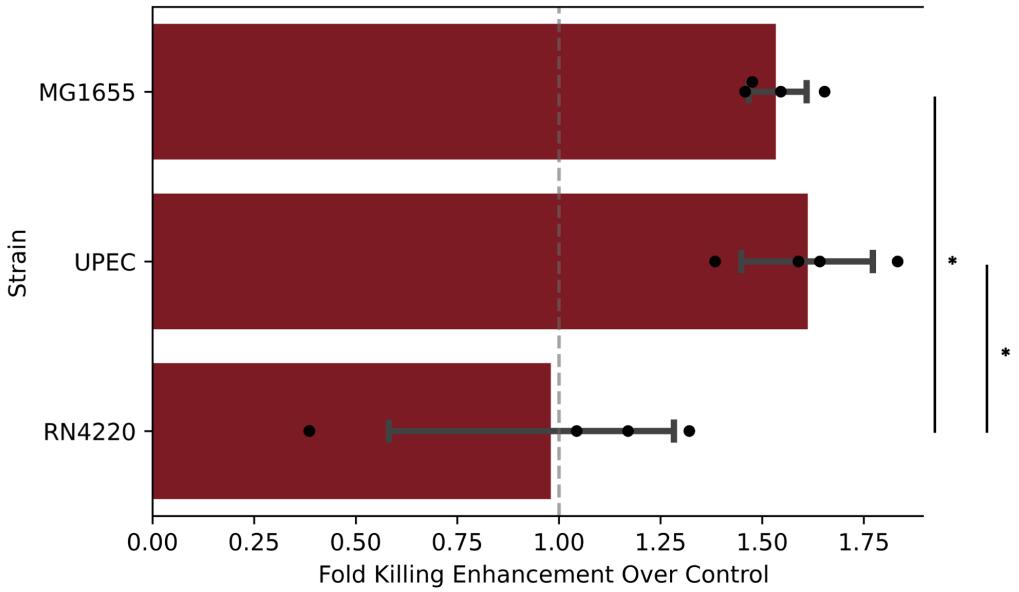


Figure 6.2.7: Fold enhancement in the percentage of dead bacteria on the g.moth surface compared to a control. E. coli strains MG1655 and UPEC, are compared to S. aureus RN4220. Statistical differences were assessed with a one-way ANOVA from n = 4 repeat measurements.

For the *E. coli* MG1655 and UPEC strains, the g.moth surfaces showed a 1.5-fold increase in the number of dead bacteria compare to the flat control surface. This confirms that g.moth is an effective antibacterial NSS against *E. coli*. The *S. aureus* RN4220 strain, on the other hand, showed no fold enhancement (~ 1) on the g.moth surface, indicating that the nanostructures were not able to kill any more bacteria than the control surfaces. The fold increase was significantly higher for both the MG1655 and the UPEC compared to the RN4220. Given that the killing mechanism of NSS in some way results in damage to the bacterial cell wall, it is not surprising that the gram-negative *E. coli* are killed more easily than the gram-positive *S. aureus*, considering their relative thickness (see section 1.2). What is of interest is whether defects in the cell wall of gram-positive bacteria make them more susceptible to killing by NSS.

To explore this, the mutant strains of Je2 were tested against the g.moth surface. Using method 1 with the *S. aureus* Je2 and the mutant strains yielded inconsistent results, as previously mentioned. Therefore the improved method 2, in which the LIVE/STAIN is left in the well during the measurements in the plate reader to increase the overall signal, was used for this set of strains. Again, each strain was grown to exponential phase, resuspending in 0.9% NaCl to $OD_{600} = 1$, and incubated on the surfaces for 24 h at RT,

as described above. The result of 3 repeat measurements is shown in Figure 6.2.8.

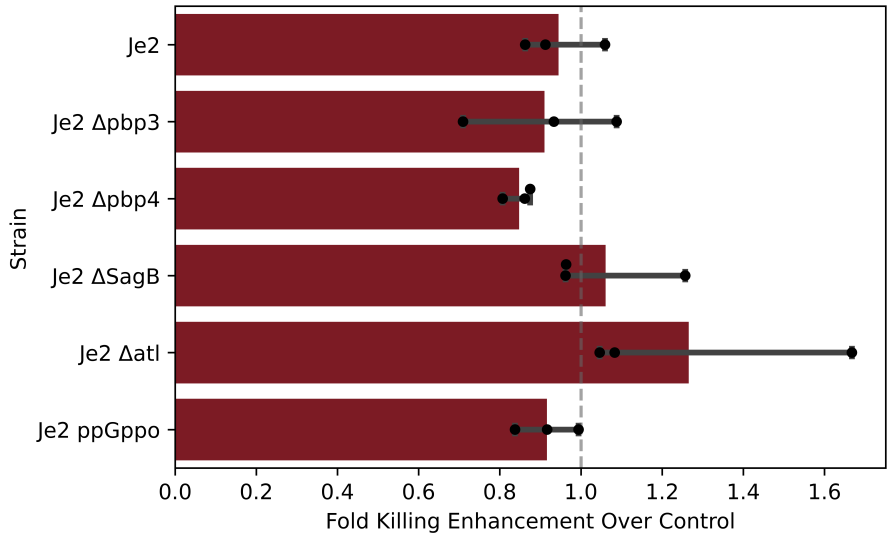


Figure 6.2.8: Fold enhancement in the percentage of dead MRSA S. aureus and cell wall mutant strains on the g.moth surface compared to a control. Statistical differences were assessed with a one-way ANOVA from n = 3 repeat measurements.

Here, only the Δ*sagB* and the Δ*atl* strains were killed at higher levels on the g.moth surface compared to the flat controls, at 1.1 and 1.3-fold respectively. The rest of the mutant strains were not killed any more on the g.moth than the control, suggesting that they were not susceptible to killing by the nanostructures. There was no significant difference in the levels of killing of the mutant strains compared to the "wild-type" Je2 strain, and only the Δ*sagB* and the Δ*atl* strains were killed at higher levels. Both the Δ*pbp3* and Δ*pbp4* strains have mutations which effect the amount of insertion or cross-linking of the peptidoglycan in the cell wall. Given that the leading theory as to the bactericidal mechanism of NSS is that the cell wall is stretched to breaking over the pillars, it could be expected that these mutant strains would be more susceptible to killing by the NSS. Additionally, if the nanostructures initiate a stress response in the bacteria which contributes to cell death, it would be expected that the ppGpp^0 strain would be more susceptible because it cannot trigger the stringent response. The fact that none of these mutant strains were killed at significantly higher rates than the "WT" Je2 strain indicates that, despite the mutations in the cell wall synthesis, the fact that they are gram-positive bacteria with thick cell walls is enough to make them resilient to killing by the g.moth NSS. Previously, gram-positive bacteria have been shown to be killed by NSS but this often requires high-aspect ratio inorganic surfaces such as black silicon [14]. Despite being able to kill *E. coli* strains effectively, it is likely that the parameters of the

g.moth surfaces are not sufficient to be able to kill gram-positive bacteria.

6.2.6. Assessing Viability of Bacterial Strains with Fluorescence Microscopy

Methods

To support the results that were obtained with this new technique and verify their accuracy, the bactericidal ability of the g.moth surfaces against the different bacterial strains was also assessed with the traditional LIVE/DEAD microscopy assay. The samples were prepared in a similar way as the microplate reader assay to allow good comparison. The overnight cultures of each of the strains were diluted in fresh media and grow to mid-exponential phase (OD_{600} = 0.4-0.5). The media was then washed out and replaced with 0.9% NaCl buffer by centrifugation three times. The final suspension was then adjusted to $OD_{600} = 0.5$. This bacterial suspension was then transferred to 6-well plates containing either a glass coverslip (control) or a coverslip coated with the g.moth film. The bacteria were left to incubate in the plates for 24 h before the surfaces were removed and rinsed x3 with buffer. A solution of the BacLight LIVE/DEAD stain (made as before) was added to each of the surfaces and left to incubate in the dark for 30 min, after which time it was rinsed off and the surfaces mounted onto slides for imaging. The results of a single repeat of this experiment, using all of the strains, are shown in Figure 6.2.9.

Results

Looking at the fold-increase in killing (Figure 6.2.9b) is useful here as it allows direct comparison of the results obtained with the plate reader. As seen with the plate reader assay, both of the *E. coli* strains are highly susceptible to killing by the g.moth surfaces, with 3x as many of the MG1655 and UPEC bacteria killed compared to the flat control. The *S. aureus* strains however, were more resilient against the g.moth, which was also found when using the microplate reader method. Only the RN4220 and the Je2 ppGpp^o strains were found to have a fold change > 1, indicating that g.moth has killed more bacteria than the control surface. The Je2 strains and the rest of the mutant strains were found with a fold enhancement < 1, signifying that the nanostructures did not kill any more bacteria than the flat surface. Interestingly, the Δ*pbp3*, Δ*pbp4*, Δ*sagB*, and ppGpp^o knockouts of the Je2 strain all had a higher killing enhancement than the "wild-type" Je2 strain, which could be an indication that these mutations made the bacteria more susceptible to killing by the NSS. Although no comment can be made on the significance of

these results at this stage, this would be in line with what was found with the microplate reader, in that certain strains could be more susceptible due to their defects, but their thicker gram-positive cell wall still provides enough protection.

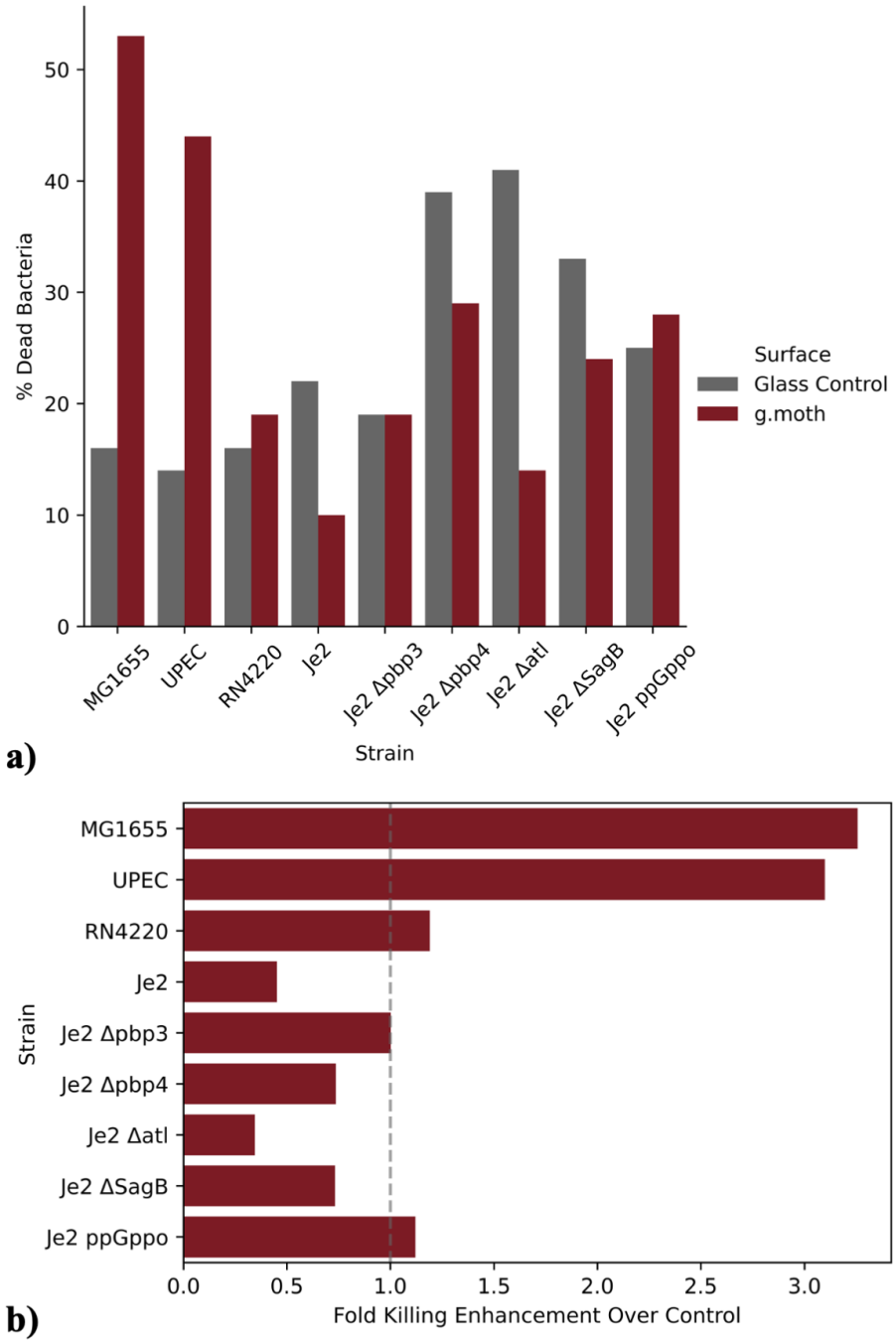


Figure 6.2.9: Bacterial Viability of bacterial strains on g.moth, assessed with fluorescent microscopy. a) percentage of dead bacteria found on the glass control and g.moth surfaces and b) Fold change in the amount of dead bacteria between the g.moth and the control.

These microscopy results also confirm that the high-throughput viability assay developed here is sensitive enough to detect the killing of different bacterial strains by NSS. In particular, the relative levels of killing of the MG1655, UPEC and RN4220 strains were found to be very similar for both the microplate reader and the microscopy assay. Whilst the accuracy of the microscopy is much higher, due to the ability to count individual cells, this microplate reader still provides useful results. It could be most useful as a pre-screening assay to determine parameters which may provide a killing enhancement or strains which are more susceptible to NSS, before completing a full Live/Dead microscopy assay to establish the true bactericidal efficiency.

6.2.7. SEM Imaging of Bacteria on g.moth

Methods

The morphology of the bacterial strains after incubation on the surfaces was assessed using SEM. After a suspension of $OD_{600} = 0.5$ bacteria was incubated on a g.moth surface for 24 h, non-adherent cells were rinsed away with buffer. The samples were then fixed with PFA and dehydrated with ethanol as described in section 5.2. Finally, a thin ($\sim$ 20 nm) layer of gold was sputter coated onto each sample to ensure good conduction. Representative SEM images of each of the bacterial strains investigated here are shown in Figures 6.2.10 - 6.2.12.

Results

As Fig. 6.2.10a) and b) shows, the g.moth surface caused a large amount of damage to the *E. coli* MG1655 cells. There is evidence of both cell wall damage (red arrows) and possible cytoplasm leakage from the cells (blue arrows) similar to that seen in cells incubated on the *M. intermedia* wing. The UPEC cells (Fig. 6.2.10c) and d)) also showed similar damage, with one of the cells almost completely deflated (indicating a total loss of turgor pressure) after the interaction with the NSS. This extent of damage is consistent with the Live/Dead stain assays for both strains. For the RN4220 strain, most of the cells retained their normal morphology which is expected given that the Live/Dead assay found little increase in killing compared to the control. However, there is still some evidence of possible cytoplasm leakage showing that the g.moth surface is able to inflict some damage on the *S. aureus* cells. The *S. aureus* Je2 cells (Fig. 6.2.11a) and b)) remained largely unaffected by the g.moth surface, with any damage occurring with a low frequency. This corresponds well to the Live/Dead data which indicated that the Je2 strain was not killed

significantly by the g.moth. The cell wall mutant strains showed similar results, with no significant changes in morphology seen, which again is in agreement with the previous data. Interestingly, for the ppGpp^0 samples (Fig. 6.2.12e) and f), there was several regions which looked like deflated cells (green arrows). It is not clear whether these are actually damaged cells or just debris on the surface, but the Live/Dead microscopy assay suggested that the ppGpp^0 strain could be susceptible to killing by the g.moth and this SEM could be further evidence to that effect. If this is the case, it may suggest that the killing mechanism of NSS may be linked in some way to bacterial stress - although it is unclear how this is linked to the mechanical damage that the bacteria sustains.

Unlike the NSS in Chapter 5, no deformation/bending of the nanopillars is evident here. This is likely because they are very short $\sim$ 100 nm and seem to form a mesh of spikes rather than distinct pillars. Therefore it is unlikely that the mechanism proposed in Chapter 5, whereby the bending of the nanopillars is able to impart shears forces on the bacterial membrane resulting in enhanced killing, is at play here. This further suggests the presence of multiple bactericidal mechanism for NSS, depending on the type of surface.

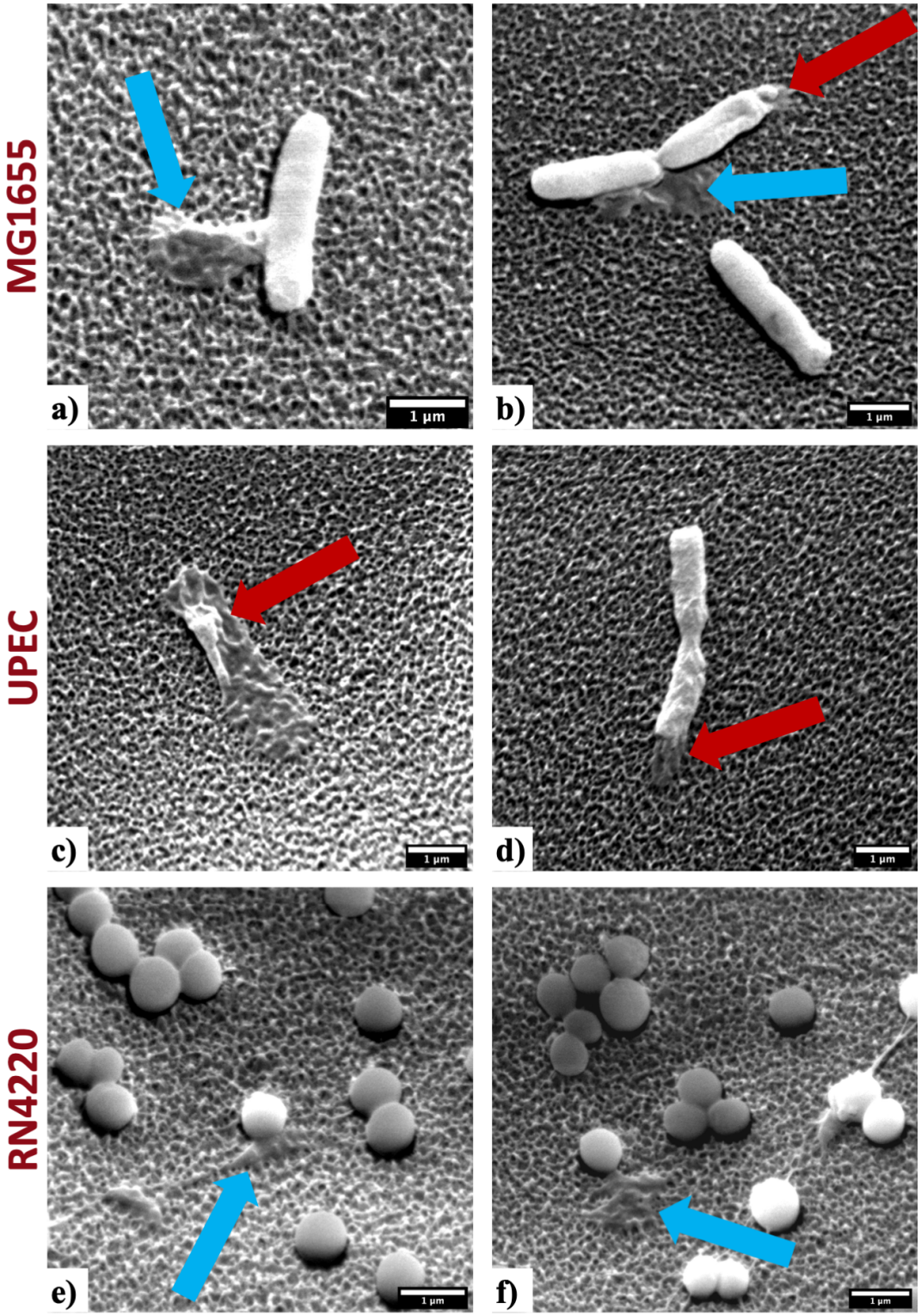


Figure 6.2.10: Morphology of the different bacterial strains assessed with SEM. a) + b) E. coli MG1655, c) + d) UPEC, e) + f) S. aureus RN4220. Blue arrows indicate potential cytoplasm leakage and red arrows indicate cell wall damage.

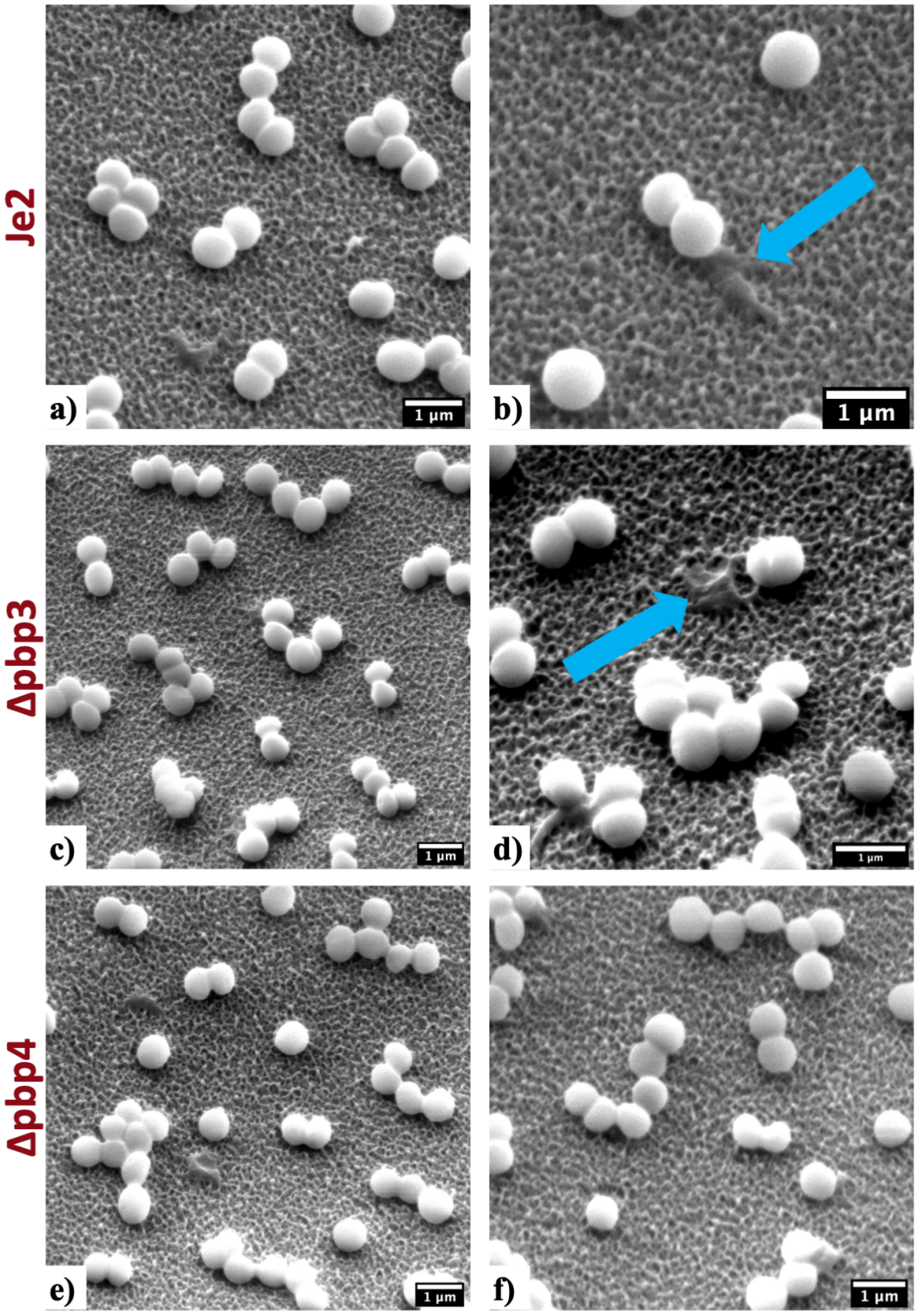


Figure 6.2.11: Morphology of the different bacterial strains assessed with SEM. a) + b) S. aureus Je2, c) + d) Je2 Δpbp3, e) + f) Je2 Δpbp4.Blue arrows indicate potential cytoplasm leakage.

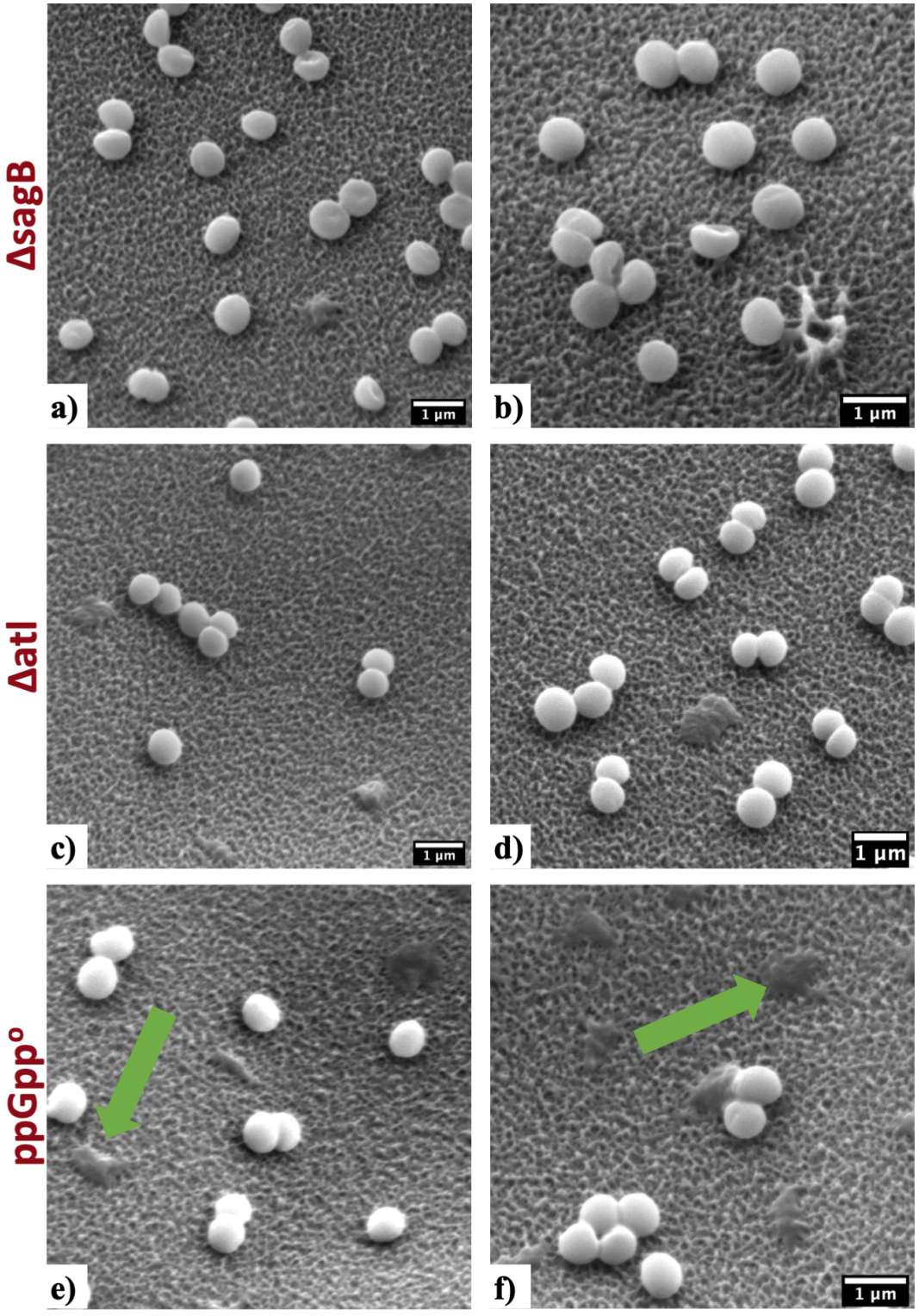


Figure 6.2.12: Morphology of the different bacterial strains assessed with SEM. a) + b) Je2 ΔsagB, c) + d) Je2 Δatl, e) + f) Je2 ppGpp°. Green arrows indicate potential deflated cells.

6.2.8. Summary of Findings and Conclusions

In this section a new high-throughput method for assessing the viability of bacteria on NSS was developed. This was then used to evaluate the susceptibility of various bacterial strains against a NSS with the aim of gaining more information about the bactericidal mechanism. The key conclusions are as follows:

- A commercially available anti-reflective surface, g.moth, was characterised and found to be covered in a random array of nanopillars $\sim$ 120 nm tall.
- A new high-throughput assay to determine the bactericidal ability of multiple NSS at once was devised, based on Live/Dead staining and a microplate reader.
- Optimisation of this technique was carried out to improve the signal intensity compared to the background to ensure more accurate measurements.
- This assay was used to determine the bactericidal efficiency of the g.moth surfaces against a range of bacterial strains.
- Two *E. coli* strains, MG1655 and UPEC, were both found to be killed at higher levels ($\sim$ 1.5-fold increase) on the g.moth than a flat control. No killing enhancement was found for *S. aureus* RN4220. This would be expected given the differences in cell wall thickness between gram-positive and gram-negative bacteria.
- Mutant strains of *S. aureus* Je2 that had cell wall defects were also tested in order to see if they had any effect on the susceptibility to NSS. This could shed more light of the bactericidal mechanism.
- None of the mutant strains were killed significantly more than the "wild-type" Je2 strain, indicating that the cell wall defects did not make gram-positive bacteria more susceptible to NSS.
- The fluorescence microscopy viability assay was carried out on all the strains to verify the results from the microplate reader. This also showed the *E. coli* strains killed at much higher levels than the control ($\sim$ 3-fold increase), and showed no enhancement for the *S. aureus* strains.
- This confirms that the high-throughput microplate assay is sensitive enough to assess the killing by NSS. It could find use as a screening step to determine strains/parameters of interest for future testing.

- SEM imaging of the bacteria on the g.moth surfaces showed extensive damage for the strains which were previously found to be killed in high levels by the NSS. This included cell wall rupturing and cytoplasm leakage.

- In general, it appears that the thicker cell wall of gram-positive bacteria is sufficient to protect them against killing by NSS, even when there are defects in that wall. This suggests that the bactericidal mechanism does involve the mechanical breaking of the cell wall by some pathway.

6.3. Effect of Bacterial Growth Cycle on Susceptibility to NSS

6.3.1. Introduction

The link between the growth cycle of bacteria and and the amount of killing by NSS was suggested by Köller *et al.* [90]. They found that the percentage of *E. coli* killed on nanostructured titanium surfaces was higher when the cells were incubated on the surface in nutrient rich media (brain heart infusion (BHI)) compared to a non-supplemented media (RPMI1640). They claimed this was due to an increased rate of bacterial growth and division in the rich BHI media. They then incubated *E. coli* in BHI + DL-serine hydroxamate (SHX) (which halts cell growth by inhibiting the seryl-tRNA synthetase), and also found that the percentage of dead cells was decreased compared to the actively growing bacteria. It was therefore concluded that the cell growth and division cycle plays a role in how the cell membrane becomes damaged by the surface nanostructures, with disruption of the peptidoglycan synthesis mechanics or damage due to the motion of the bacteria on the NSS during division postulated as potential explanations. It should be noted that this study did not compare the killing of the NSS in each condition to any control surfaces. Truong *et al.* had also previously demonstrated that *S. aureus* and *P. aeruginosa* cells that had been grown for different times (1, 6, 12, 18 and 24 h) in media before being incubated on the nanostructured wing of the damselfly *Calopteryx haemorrhoidalis* displayed varied levels of killing [173]. They found that for both bacterial species, the highest percentage of dead cells was found in the young (1 h of growth) and old (24 h of growth) populations of bacteria. The increased killing of the young (late lag phase/early exponential phase) cells was attributed to the changes in the cell wall during growth, such as the increased incorporation of new peptidoglycan, which may weaken the bacterial envelope and make it more susceptible to mechanical breaking.

This section describes an experiment in which GFP-expressing *E. coli* were grown to different points in their growth cycle, before being incubated on section of the *M. intermedia* wing. At these different points, the growth rates of the bacteria are different, which allows investigation into whether it is the growth rate of the cells which plays a role in the killing mechanism. This experiment was also repeated by adding the bacteriostatic antibiotic Chloramphenicol (cam), which prevents bacterial growth by inhibiting protein synthesis, to the *E. coli* as it is incubated on the cicada wing. The bactericidal efficiency

in both cases was assessed by adding Propidium Iodide after incubation, to stain the dead cells, and imaging with fluorescence microscopy.

6.3.2. Methods

Nanostructured Surfaces

The nanostructured surfaces used in this study were sections of the *M. intermedia* wing which was previously characterised in chapter 3. The wings were washed with DI water and dried with nitrogen before being cut and fixed to a glass coverslip with double-sided tape.

Bacterial Strain and Growth

For this study, a Green Fluorescent Protein (GFP)-expressing *E. coli* strain was used. The *gfp* gene is located next to a kanamycin (kan) cassette, allowing for strain selection during growth. A single bacterial colony (grown on LB-agar supplemented with 50 μg/ml kan) was used to inoculate LB media (also supplemented with 50 μg/ml kan) and grown overnight at 37°C, shaking at 200 rpm. To establish the growth rate of the GFP-expressing *E. coli* strain, a growth curve was performed. For this the overnight culture was diluted to OD_{600} = 0.05 in 50 ml of fresh media and incubated at 37°C, shaking at 200 rpm. Every hour after the inoculation, a sample of the culture was taken and its optical density (OD_{600}) was measured. This experiment was replicated in triplicate.

Bacterial Viability Assay

To determine the bactericidal effect of the cicada wing at each point during growth, the overnight culture of *E. coli* was then diluted to OD_{600} = 0.05 in 50 ml of fresh media and incubated at 37°C (shaking at 200 rpm). At each of the chosen time points, 5 ml of the culture was removed and added to a well of a 6-well plate, along with a section of cicada wing attached to a coverslip (and a plain coverslip acting as a control). This well plate was then incubated statically at 37°C for 2 h before the cicada wing was removed and gently rinsed. A Propidium Iodide solution was then prepared (at 1.5 μl/ml from 20 mM stock) and added to the surface for 30 min in the dark, before a final rinse. The samples were then mounted to a glass microscope slide for imaging. In this experiment the expression of GFP in the *E. coli* acts in the same way as the SYTO9 does in the LIVE/DEAD kit, strongly fluorescing any bacteria with undamaged membranes. The microscopy was carried out with a Nikon Ti Eclipse Wide-field system at 10x magnification. Counts of

the number of live and dead cells were made using the "Analyse Particles" feature in the image analysis software FIJI [103], with the killing percentage calculated with equation 2.4.

6.3.3. Results and Discussion

The result of the 3 repeats of the growth curve for the GFP-expressing *E. coli* strain is shown in Figure 6.3.1a. This follows the typical shape of a bacterial growth curve, starting with a *lag* phase where the cells begin to adapt to the fresh media and prepare for growth metabolically. Next the *log/exponential* phase where the cells begin to divide readily and the population number increases exponentially. Finally, as the nutrients available in the media decrease, the growth of new cells begins to plateau and the bacteria enter the *stationary* phase. The doubling time of the bacteria at each of these points is calculated with equation 6.2, where t is the sampling time and C is the measured concentration (in OD_{600} in this case). This doubling rates for this growth curve at each time point is shown in Figure 6.3.1b.

$$\text{Doubling Time} = \frac{(t_2 - t_1)\, ln(2)}{\ln\left(\frac{C_2}{C_1}\right)} \tag{6.2}$$

As Figure 6.3.1b shows, within the first 2 hours of growth the *E. coli* are in lag-phase with a doubling time of nearly 4 h. After this point the cells start to enter the exponential phase of growth, with early-exponential starting after 2 hours of growth. The growth rate clearly starts to increase at this point, with the doubling time now only 55 min. Between 2-4 h the cells are growing exponentially with a doubling time of 30-40 min. After 6 h of growth the cells begin to enter stationary phase, with the growth rate slowing significantly. By 9 h the doubling time has increased to 6.5 h, indicating that the growth of the *E. coli* population has plateaued.

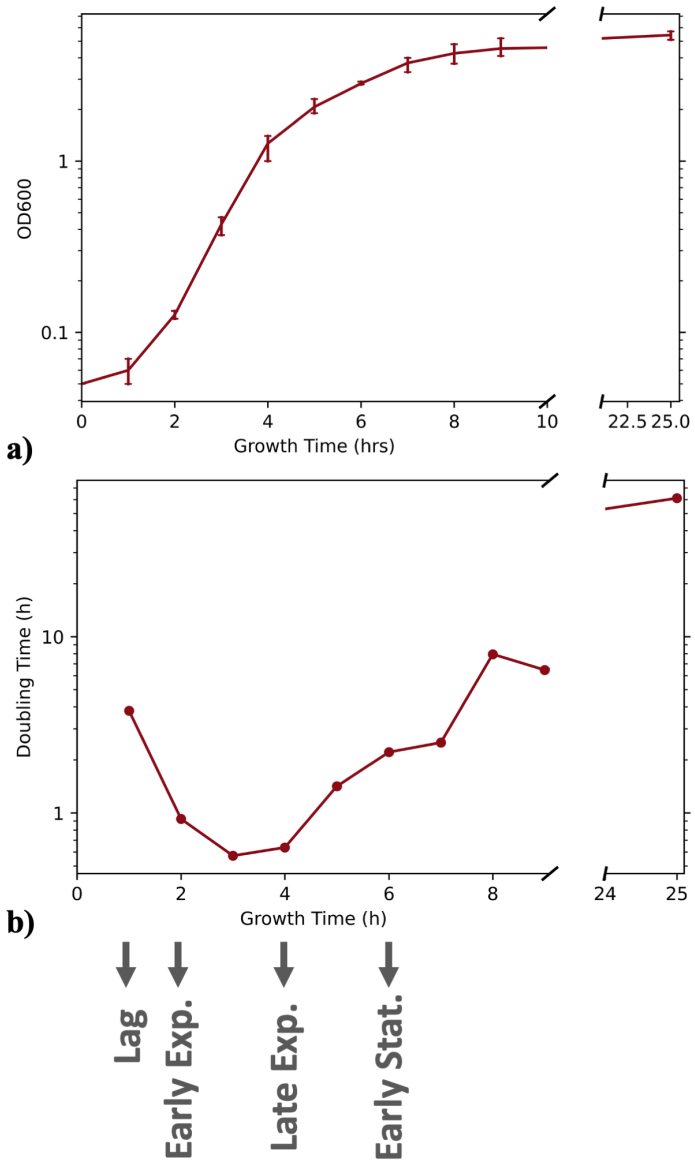


Figure 6.3.1: Growth Curve (a) for the GFP expressing E. coli strain, along with the doubling time at each point (b). The key points in the growth curve are highlighted by the arrows.

To explore the potential effects of this changing growth rate on the killing by NSS, several time-points of this cycle were picked out. These were 30 min, 2 h, 4 h, 6 h, and 21 h post-inoculation in the fresh media. After these growth times were reached, samples were removed from the main culture but kept in media (not resuspended in buffer) and incubated on the cicada wing at 37°C for 2 h. This was to allow the bacteria to carry on growing at a similar rate whilst in contact with the NSS. The 5 time points chosen covered the key stages of the growth curve, from lag phase to stationary phase (details given in Table 6.3.1).

Table 6.3.1: Growth phase of the sample time points taken from the growth curve of the GFP-expressing E. coli, along with the calculated doubling time.

Sample Time (hrs)	Growth Phase	Doubling Time (h)
0.5	Lag	~ 4
2	Early Exponential	~ 1
4	Late Exponential	~ 0.65
6	Early Stationary	~ 2
21	Late Stationary	~ 6

After incubation of each of the bacterial samples on the cicada wing and glass control surfaces for 2 hrs, the percentage of dead bacteria was assessed using the live/dead stain assay, with the results presented in Figure 6.3.2.

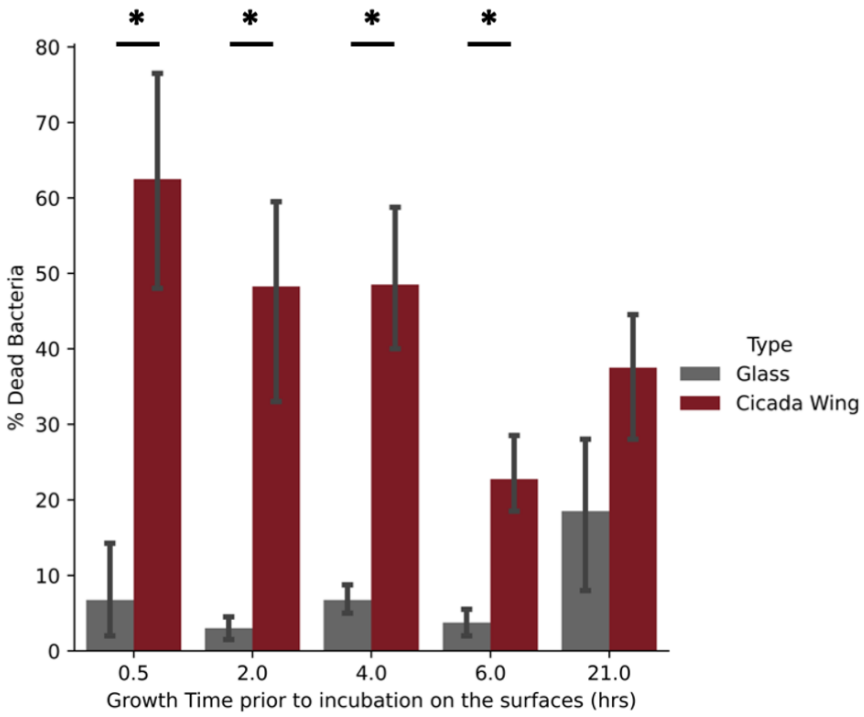


Figure 6.3.2: Percentage of GFP E. coli, taken from different points on the growth curve, killed on the cicada wing surface. Statistical tests were performed by 2-way ANOVA.

There was a significant difference in the percentage of *E. coli* killed between the cicada wing and the control for the 0.5, 2, 4 and 6 hr samples. However, there was no significant differences found between the proportion of cells killed on the cicada wing between the different time-points. Despite this there is a general trend towards a lower percentage of

cells being killed in the samples harvested later in the growth curve compared to those taken from earlier. The 0.5 hr sample (lag phase) was found to be killed the most on the cicada wing, with 63 ± 18% of cells inactivated. For the 6 hr sample (early stationary phase), only 23 ± 6% of cells were found to be killed. This would suggest that there may be some link between the growth rate of the bacteria and how easily they are killed by the NSS.

To explore this effect further and explore whether it is the change in growth rate between the cells at the different points that effects the killing rate, the experiment was repeated with an antibiotic added to arrest the growth of the *E. coli*. The antibiotic Chloramphenicol (cam) was used for this as it is bacteriostatic, therefore preventing the growth of bacteria without killing them. Figure 6.3.3 shows the effect of cam on bacterial growth. When 100 μg/ml cam was added to a growing GFP-expressing *E. coli* culture after 4 hours, no additional growth was observed when compared to a culture that did not have the cam added.

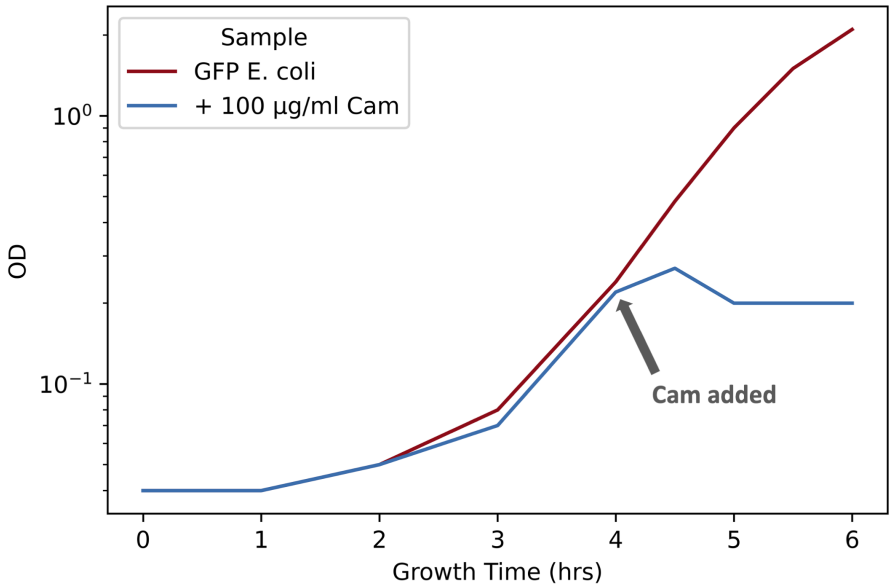


Figure 6.3.3: Growth of GFP-expressing E. coli cells is arrested by 100 µg/ml cam added after 4 h, compared to a culture with no antibiotic added.

When assessing the killing by NSS, 100 μg/ml cam was added to the the bacterial culture just before it was incubated on the surfaces for 2 hrs. This allowed the bacteria to grow to the same point in the cycle that they had for the previous experiment, but allowed no further growth whilst they were on the NSS. Therefore the bacteria will have similar cell wall profiles but will no longer be actively growing. The results from this

experiment are presented in Figure 6.3.4.

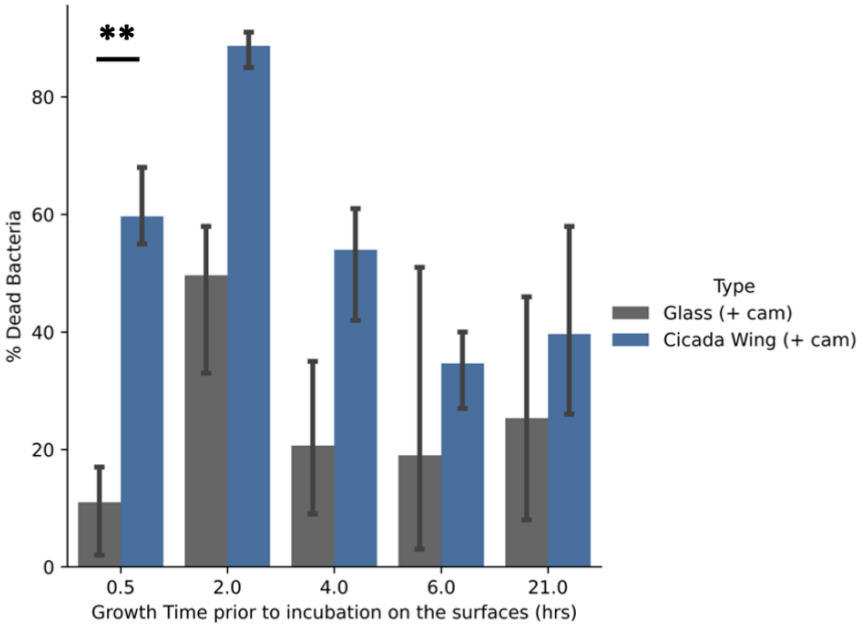


Figure 6.3.4: Percentage of GFP E. coli, taken from different points on the growth curve, killed on the cicada wing surface. Bacteria were treated with 100 μg/ml cam to arrest their growth. Statistical tests were performed by 2-way ANOVA.

Initially is seems that the previous trend observed for the bacteria actively growing on the NSS is not repeated here. For the bacteria incubated with the cam, the greatest proportion of cells were killed in the sample that was grown for 2 hrs before being added to the cicada wing. Only the 0.5 h sample showed a significant increase in killing over the glass control. However, an increased level of killing was seen on both the NSS and glass controls after the cam was added, indicating some bactericidal effect of the antibiotic. Therefore to enable a better comparison between the untreated and antibiotic treated *E. coli*, the fold increase in the percentage of dead bacteria between the control and the cicada wing was taken, using equation 6.3. This yields the results shown in Figure 6.3.5.

$$\text{Fold Increase in Killing} = \frac{\%\ \text{Dead on NSS}}{\%\ \text{Dead on Control}} \tag{6.3}$$

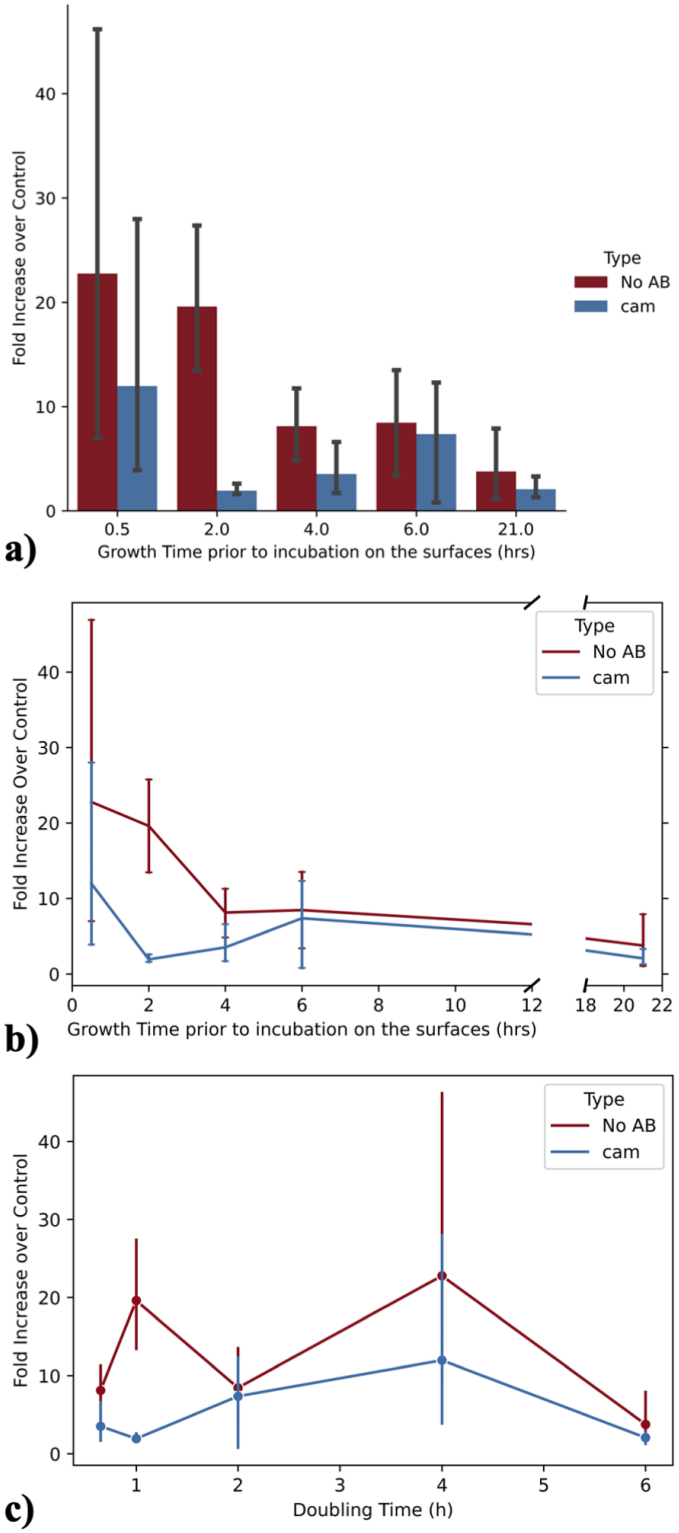


Figure 6.3.5: Fold Increase in the percentage of dead bacteria for the E. coli at different points in the growth curve (both untreated and treated with cam). a) and b) show the fold killing at the different sampling points (time prior to incubation). c) Shows the fold killing relative to the doubling time of the untreated bacteria. Statistical tests were performed with 2-way ANOVA, with no differences found between any of the measurements.

There was no significant difference found between the fold killing of the untreated (no antibiotic) sample and the treated (+cam) sample at each of the growth points, however, there are some trends of interest. For the actively growing bacteria, the killing rate was generally highest for the *E. coli* in the lag phase of growth (0.5 h pre incubation on cicada) and the early exponential phase (2 h). The percentage of dead cells then looked to decrease for the *E. coli* which were grown for longer before incubation on the NSS. The fact that the killing rate remains low for the untreated bacteria as they move into the stationary phase of growth could be due to the fact that the bacterial cell wall generally strengthens and increases in thickness during stationary phase [174]. This would give them an increased resilience to killing by the nanostructures, in the same way that gram-positive bacteria are not killed as effectively as gram-negative bacteria by NSS, due to their thicker cell walls being harder to mechanically rupture [37].

The lack of significant difference between the untreated and treated cells (i.e. the cells which were growing and those whose growth was arrested) may suggest that the growing dynamics of the cell makes no difference to the rate at which they are killed, contrary to what has previously been discussed in the literature [90]. This is supported by the fact that the highest rates of killing are found with the lag-phase bacteria, which are known to have low metabolic activity and little-to-no growth. Additionally, Fig. 6.3.5c shows that there was no correlation found between the fold increase in killing on the NSS and the doubling time of the untreated bacteria. Therefore it would seem unlikely that the growth rate of the bacteria is linked to how easily they are killed by NSS and any differences between the growth phases are more likely a result of differences in cell wall physiology at those points. Interestingly, it has recently been shown that nano-textured silicon surfaces were able to create a bacteriostatic effect for *S. aureus*, without inducing any killing, due to pinning and impedance of the bacteria by the nano-features [91]. This pinning has also recently been suggested to contribute to the bactericidal mechanism of NSS [75]. However, this pinning and impedance may not result in sufficient damage to the bacterial envelope for a cell to register as "dead" with the live/dead stain. Future work would require investigations into alternative methods to assess this effect and find if the NSS have a bacteriostatic as well as bactericidal effect.

6.3.4. Summary of Findings and Conclusions

In this section the effect of the growth rate of *E. coli* on their susceptibility to killing by NSS was evaluated. The key conclusions are as follows:

- The growth of GFP-expressing *E. coli* was determined by performing a growth curve and sampling the OD_{600} every hour.
- Several time points were chosen from this growth curve, to sample a range of growth rates, and incubated on the *M. intermedia* wing to test the bactericidal efficiency.
- Bacterial culture was removed at 0.5, 2, 4, 6, and 21 h and incubated on the cicada wing for a further 2 h.
- The cicada wing killed significantly more *E. coli* than the control at all the time points except the 21 h (stationary phase) sample. This could be due to the cell wall stiffening that occurs during stationary phase.
- Generally, more bacteria were killed for the earlier time-points (lag phase), when the growth rate is lower, compared to later (exponential phase).
- Chloramphenicol was added to the bacterial suspension upon adding to the cicada wing to explore whether this effect is growth-rate related. cam is a bacteriostatic antibiotic which arrests growth.
- There was no significant difference between the amount of untreated and treated cells killed by the cicada wing, indicating that the growth dynamics may not play a role in the bactericidal mechanism. This fits both with the accepted "stretching" mechanism of bacterial death and also the stress mechanism for elastic nanopillars presented in Chapter 5.

6.4. Towards Imaging the Bacteria-Nanopillar Interaction

6.4.1. Introduction

A lot of information about the bactericidal mechanism can be inferred from looking at the effects of changing different parameters, such as surface topography or bacterial characteristics. However, the only way to truly understand this mechanism is to visualise the interactions between the bacterial cell wall and the surface nanopillars. Previously, techniques such as Helium Ion Microscopy (HIM) [41], Transmission Electron Microscopy (TEM) [75] and Scanning Electron Microscopy (SEM) [84] have all been used to visualise the interaction between the bacteria and the nanopillars to gain more insight into the bactericidal mechanism. All of these techniques require cell fixation and sample preparation, typically with some processing that involves heavy-metals. Thus, they are not optimal for investigating the interaction of the bacteria with the NSS as they will only show what the surface looks like after this processing, not what is happening during the interaction. Light-based microscopy is much more suitable for the *in-situ* imaging of the bacteria-nanopillar interaction as it is able to view the surface in real time and does not require extensive sample preparation or fixation. Recently, Bandara *et al.* used 3D Structured Illumination Microscopy (SIM), which is capable of capturing sub-resolution limit images [175, 176], in combination with a cell membrane stain (FM1-43) to image change in the bacteria as a result of interaction with a nanostructured dragonfly wing surface [87]. They reported being able to see damage to the cell membrane on the side that was in contact with the NSS, which resulted in the uptake of a dead cell indicator stain. This is the first report on such fluorescence *in situ* imaging of bacteria on NSS. The key drawback in imaging the interaction with the dragonfly wing is that it is not possible to localise the nanostructures, making it difficult to know exactly where they are interacting with the bacterial envelope.

This section will explore the use of bacterial membrane stains in combination with fluorescent labelling of the nanopillars to visualise their interaction with high-resolution optical microscopy. NSS were formed using the casting method from optically-transparent polystyrene embedded with quantum dots to allow localisation of individual nanopillars. These surfaces were incubated with *E. coli* that were labelled with both SYTO9 and a membrane stain, FM4-64, with the aim of observing any changes in the morphology of

the bacterial cell wall due to the interaction with the nanopillars. This work was carried out in collaboration with Dr. Olivia Hill.

6.4.2. Fluorescently Labelled NSS

In order to identify the points of interaction between the NSS and the bacteria, the nanopillars were embedded with quantum dots (QD). Most materials that have been reported as antibacterial NSS previously are made from inorganic materials such as black silicon or TiO_2. These surfaces are neither optically-transparent nor fabricated in a way that would allow fluorescent labelling of the structures. Here, however, the use of polymeric materials allows fluorescent labelling of the nanopillars in order to localise them and their interaction with the bacterial cell wall. QDs are an ideal choice for this labelling and have previously been used in cell imaging application [177]. Excitation of the quantum dot creates an electron-hole pair (exciton) which later recombines to produce a photon. The confinement size of the exciton, i.e. the size of the quantum dot, defines the wavelength of emission of this photon. This is an attractive characteristic as it allows a QD size to be selected that will give emission at a wavelength distinct from the other fluorescent dyes used in the sample. Additionally, the small size of the QDs (∼10s nm) mean that they can be incorporated into the NSS without disrupting the fabrication.

Methods

The process of casting polymer solutions into the LS mould, described in section 4.2.1, was used again here to create the NSS. Firstly, PS (M_w = 315k) was diluted in toluene to 5 wt%. Next, a 1 wt% solution ZnCdSe/ZnS quantum dots (PlasmaChem) was made in toluene. These QDs have a ZnCdSe core that is ∼ 6 nm in diameter, with a ZnS shell. Their excitation spectra is shown in Figure 6.4.1 and they have an emission peak at 440 ± 5 nm. This QD solution was sonicated for 10 min to ensure good dispersion of the dots throughout the solution. After this, the solution was diluted into the 5 wt% PS solution to achieve a final concentration of 0.1 wt% for the QDs. A final sonication was carried out to fully disperse the QDs throughout the PS solution before it was cast onto the LS mould and cured as previously described. As the high resolution imaging techniques generally have a shallow depth-of-field, the surfaces cast here were made as thin as possible by only depositing a small volume of the PS solution onto the mould. The QD-doped NSS were assessed with AFM, to ensure that the nanostructures were not altered by the QDs, and fluorescence microscopy, to check if the signal was visible in the surface. AFM was carried out with a Veeco Dimension 3100 with a NuNano Scout 350 cantilever (spring constant 42

N/m, resonant frequency 350 kHz). For the microscopy, the NSS were mounted between a slide and a glass coverslip before imaging with the technique described in section 6.4.4.

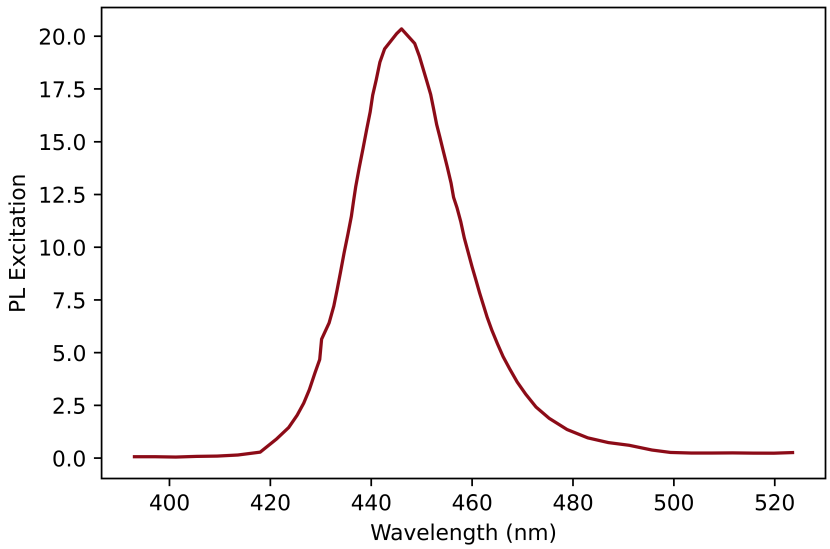


Figure 6.4.1: Excitation spectra of ZnCdSe/ZnS quantum dots used to dope the NSS - adapted from PlasmaChem datasheet.

Results

The example AFM scan in Figure 6.4.2a) shows that the imprinting of the nanostructures in the PS is not significantly effected by the presence of the QDs in the solution. The average feature height was found to be 380 ± 150 nm, which is in line with the previous PS NSS fabricated using this method in chapter 4. It therefore can be concluded that adding the QDs into the polymer solution does not effect the quality of the NSS fabricated by solution casting.

A fluorescence image of the QD-doped PS surface is shown in Figure 6.4.2b. It is possible to see peaks in the intensity (green dots) which correspond to the location of the quantum dots within the surface. These generally appear to be well distributed across the surfaces, although there is large section where they seem to be missing. This indicates the need for better dispersal of the QDs in the PS solution before it is cast onto the moulds. Given that the spacing of the features on the LS moulds is ∼600 nm, it would theoretically be possible to resolve the individual features with standard fluorescence imaging. In the areas in which the fluorescence peaks are the most dense (shown by the arrow in Figure 6.4.2b), it appears that there is a hexagonal arrangement - the same as the packing of the nanopillars. This may indicate that single pillars could be localised,

providing they are separated by a distance greater than the diffraction limit, by doping an optically-transparent polymer with quantum dots.

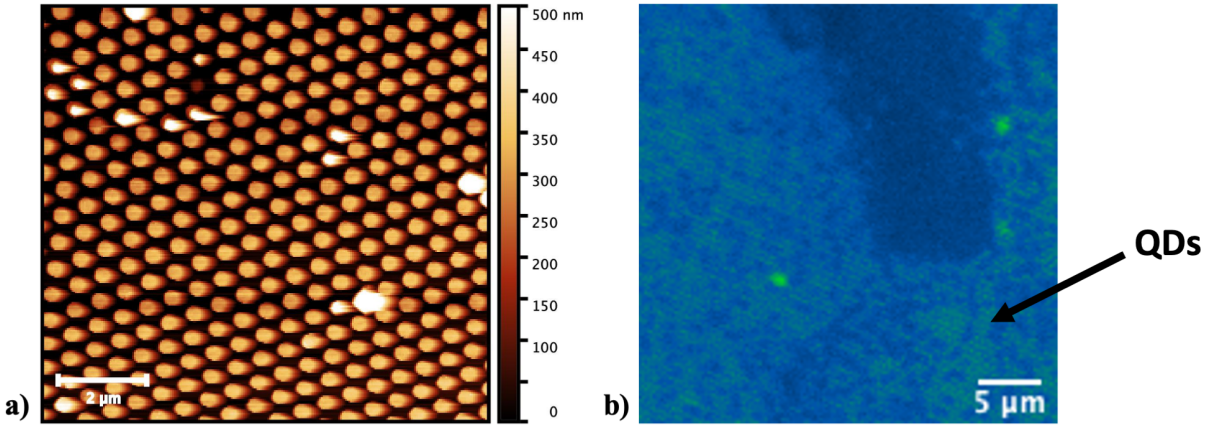


Figure 6.4.2: Characterisation of QD doped PS NSS. a) Tapping-mode AFM showing the similar structures to what is typically produced with standard PS. b) False coloured fluorescence microscopy image of the PS surface, showing small areas of high intensity likely correlating to the QDs.

6.4.3. Visualising the Bacterial Cell Wall

As it is predicted that the bactericidal mechanism stems from disturbances to the cell wall, it is important to be able to see any morphological changes that arise during interaction with the NSS. The aim is to be able to see the bacterial membrane relative to the main body of the cell (as illustrated in Figure 6.4.3). For this, SynaptoRed (or FM4-64) was used as described previously by Pilizota *et al.* [178]. FM4-64 ($\lambda_{ex.}$ = 510 nm/$\lambda_{em.}$ 750 nm) binds to the outer cell membrane of the *E. coli* cells and can be used in combination with a dye that labels the main body of the cell, for example SYTO9 ($\lambda_{ex.}$ = 485 nm/$\lambda_{em.}$ 500 nm) or GFP ($\lambda_{ex.}$ = 488 nm/$\lambda_{em.}$ 510 nm). To test the suitability of these dye combinations, a simple experiment was carried out using GFP-expressing *E. coli* cells on a glass coverslip and a section of cicada wing.

Methods

Firstly, GFP-expressing *E. coli* were grown (at 37°C, shaking at 200 rpm) in an overnight culture in LB media (supplemented with 50 μg/ml kan) before being diluted in fresh media and grown to mid-exponential phase. Once OD_{600} = 0.5 was achieved, the cells were washed three times by centrifugation with 0.9% NaCl buffer. For the cicada sample the FM4-64 dye was then added to a final concentration of 10 μg/ml (as per [178]) and left to incubated for 10 min. The culture was then washed three times again to re-

move any excess dye, before the concentration of the cells was adjusted in buffer to OD_{600} = 0.5. These cells were then added to a section of cicada wing and left to incubate in the dark for 2 h. After this time the cells were aspirated and the surfaces gently washed with buffer, before mounting between a coverslip and a glass slide. For the coverslip sample, the FM4-64 was added to the cells, incubated and washed as before, but then added to a poly-lysine coated coverslip for 10 min before aspirating the cells and rinsing. The bacteria on the surfaces were then imaged with a Nikon Widefield Microscope at 100x magnification. Example images from this are shown in Figure 6.4.4.

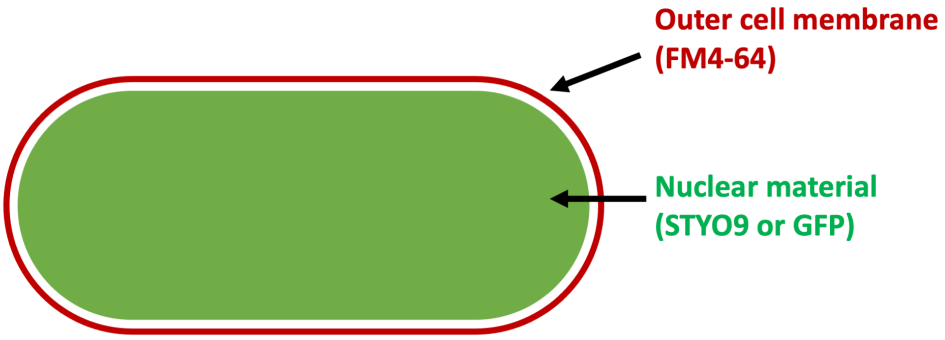


Figure 6.4.3: Visualising the outer bacterial membrane (red) of E. coli with respect to the main body of the cell (green).

Results

The images taken from the coverslip sample clearly show that joint staining of both the main body (cytoplasm) of the *E. coli*, as well as the outer plasma membrane was achieved with this procedure. The line profiles, taken along the length of the cell and showing the normalised intensity of both signals, illustrate that the bulk of the GFP signal is spatially confined within the peaks of the FM4-64 signal. This indicates that the FM4-64 has localised the outer membrane of the cell well, and that it can be distinguished from the body of the bacteria. Whilst the imaging of the *E. coli* on the glass coverslip was used to show the typical morphology of the cells, the bacteria were also incubated on cicada wing surfaces to see if any changes in that morphology could be observed. The example image in Fig. 6.4.4 shows an *E. coli* on the cicada wing with a significantly different shape to that incubated on the coverslip. Firstly, the length of the cell is much longer, $\sim$8 μm (vs. $\sim$2 μm on glass), and more notably, there is a bulge at the end of the cell seen in the GFP signal. The irregular shape of this cell could be due to the interaction with the cicada nanostructures. Unfortunately, the membrane stain for this sample did not appear clearly and it is ambiguous whether the red fluorescence surrounding the cell is membrane

which has been stained but then damaged in some way, or whether it is the more likely scenario that it is just autofluorescence from the cicada wing. One potential issue here is adding the FM4-64 membrane dye to the bacteria before incubating on the surfaces for 2 h, as it seemed to give much worse localisation of the membrane for all cells. In the future the dye would be added after incubation, much like the live/dead stain, and then imaged immediately to prevent any degradation of the dye signal.

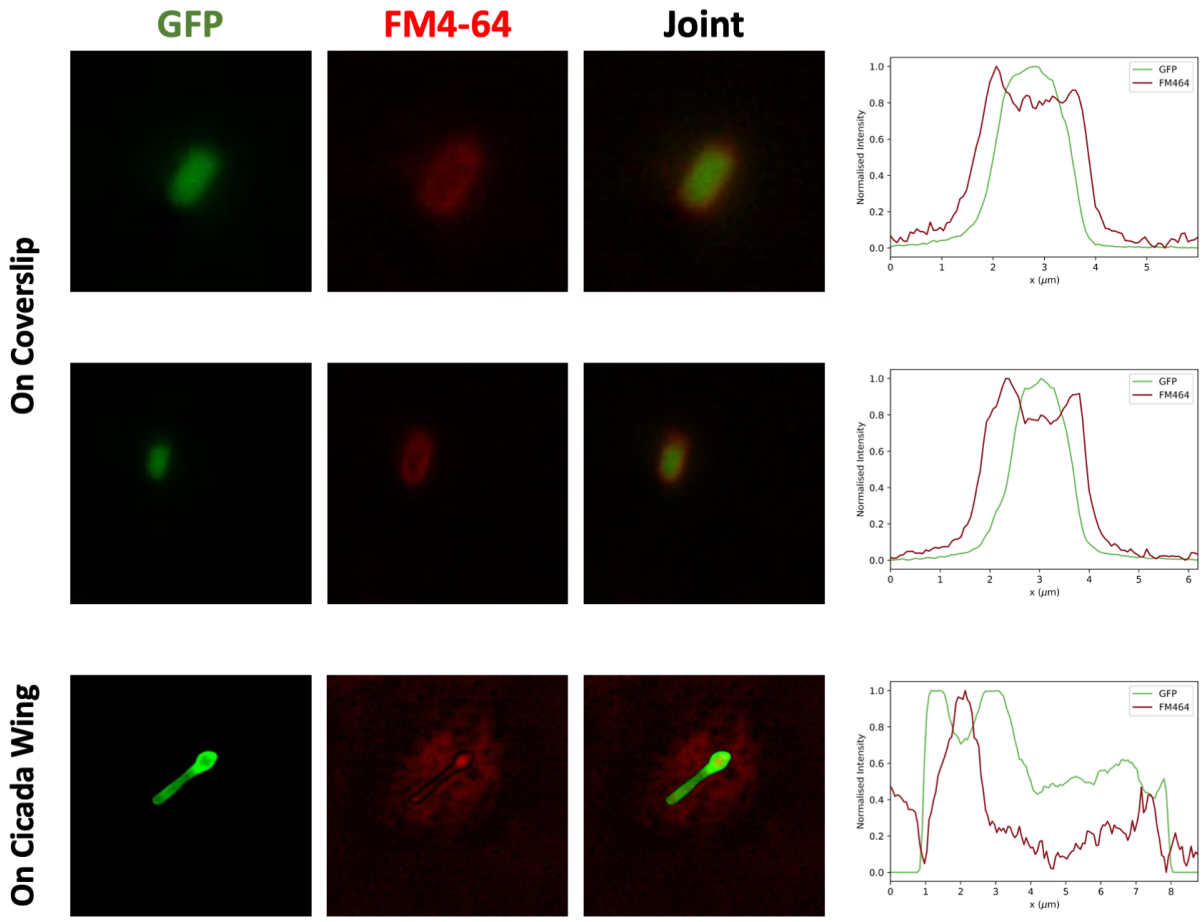


Figure 6.4.4: Joint staining of E. coli cells with GFP and FM4-64 membrane stain, incubated on a glass coverslip or cicada wing surface. Line profiles show the normalised intensity of each fluorescence signal along the length of the cell.

By identifying suitable stains and showing that they can be used to visualise different parts of the cell, a key step in imaging damage to the cell membrane with fluorescence imaging has been achieved here. However, a spatial overlap in the dye signals across the cell length was found throughout, which highlights the issue with using resolution-limited microscopy to image effects on such a small length-scale. Given the resolution of this wide-field fluorescence microscopy can be no better than ∼200 nm, it would not be possible to

resolve any nano-scale perturbations in the cell membrane that occur as a result of the interactions with the NSS. The next section will discuss the preliminary tests into using higher resolution microscopy to image the interaction of the quantum dot-labelled NSS and the stained *E. coli*.

6.4.4. Preliminary Microscopy

It was decided that the best super-resolution microscopy set up to see the bacteria-nanopillar interaction would be Total Internal Reflection Microscopy (TIRFM). TIRFM is a technique which utilises the total internal reflection of the incident light across the sample to achieve high resolution in the z-plane [179]. At a critical angle of incidence, θ_{critical}, incident light will totally internally reflect along the interface between two materials, rather than moving through it. This condition is given by equation 6.4, where n_1 and n_2 are the refractive indexes of the two materials, in this case the sample and the coverslip glass respectively.

$$\theta_{\text{critical}} = \sin^{-1}(\frac{n_1}{n_2}) \tag{6.4}$$

This reflection creates a thin field of evanescence which illuminates the first 100-200 nm of the sample (illustrated in Figure 6.4.5). The narrow band of excitation gives two beneficial properties - firstly the signal-to-noise ratio is greatly increased because a smaller volume of the sample is illuminated and therefore there is less background overall. Additionally, because the evanescent field over extends to ∼200 nm it is possible to achieve that resolution in the z-axis. The depth of this evanescent field is related to the incidence angle of the illumination and it has been shown that by using mutliple angles, it is possible to create a 3D image using TIRFM [180]. Therefore is was hoped that TIRFM would be suitable for imaging the small z-range over which the interaction between the nanopillars and the bacterial membrane occurs. A preliminary trial was set up to image *E. coli* (labelled with SYTO9 and FM4-64) incubated on the PS-QD surfaces.

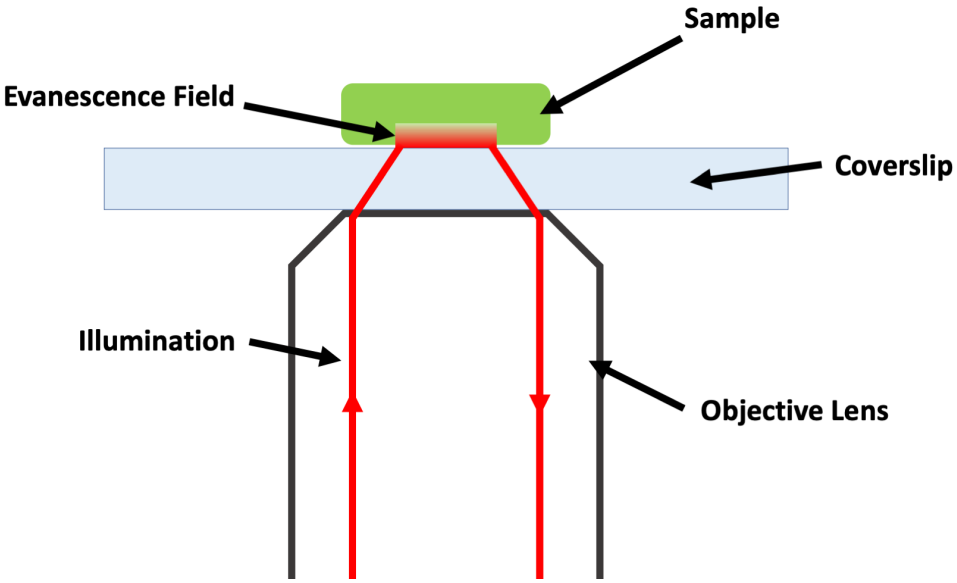


Figure 6.4.5: Illustration of the principal of TIRFM. The illumination which travels up the object lens totally internally reflects at the interface of the coverslip and sample, creating an narrow evanescence field which excites the fluorophores.

Methods

The method for preparing the sample of the fluorescently labelled *E. coli* on the PS-QD NSS is as follows:

A single colony of MG1655 *E. coli* was grown in 5 ml LB media for 16 h at 37°C, shaking at 200 rpm, to produce a stationary phase culture. This is then diluted in fresh media to $OD_{600} = 0.05$ and grown in the same conditions to $OD_{600} = 0.5$ (mid-exponential phase). Then the *E. coli* culture was washed three times in 0.9% NaCl buffer by centrifugation to remove all the media, before resuspending to $OD_{600} = 0.3$. The QD-doped PS NSS were formed as before and secured to a coverslip with a small droplet of PS solution before being left to cure. Then 800 μL of the suspension of bacteria was incubated on the NSS for 2 h in a CoverWell perfusion chamber (Grace Biolabs) to ensure minimal evaporation took place. After this time, the cells were aspirated and the surfaces gently washed to remove non-adhered bacteria. Two separate dye solutions were created - one of SYTO9 (1.5 μL per 1 mL of buffer) and another of FM4-64 (10 μg/mL). The SYTO9 solution was incubated on the surfaces for 30 min followed by the FM4-64 for 10 min. The surfaces were rinsed a final time in buffer to remove excess dye. Next, to ensure that the coverslip was mounted as flat as possible, Mowiol mounting media was placed on the surfaces followed by a glass coverslip. Mowiol sets hard and fixes the coverslip flat but

remains optically clear, which is vital when attempting high-resolution microscopy.

The methods for the preliminary microscopy measurements of the *E. coli* on the labelled NSS are as follows:

Images were collected on a Nikon Ti Eclipse microscope using a 60x ApoTIRF 1.49 NA objective lens, with a motorised TIRF module connected to a laser via a fibre port. The light used for this experiment was filtered to the excitation/emission wavelengths of each dye component (410/440 nm for the QDs, 485/500 nm for the SYTO9 and 510/750 nm for the FM4-64). Images were collected using an iXon EMCCD (Andor) cooled to -70°C, 1024 x 1024 pixel array with a 13 µm pixel size. Image analysis was carried out in FIJI.

Results

Unfortunately, only limited imaging of the *E. coli* on the QD NSS was achieved, and no imaging with TIRFM was obtained. However, some epifluorescence images of the *E. coli* on the QD-NSS were captured, which are demonstrated in Figure 6.4.6. The images show the fluorescence signal from the SYTO9 dye along with the signal from the QDs, which are highlighted by the arrows. Given that this is not a high-resolution technique, it is not possible to resolve the interaction between the bacteria and the nanopillars at this stage. However, what Fig. 6.4.6 does show is that it is possible to distinguish between the cell and the surface, which will be useful in the future when using this technique. Moving forward, the aim is to continue developing this technique in order to achieve high/super-resolution fluorescence imaging of the bacteria interacting with the nanopillars. Bandara *et al.* have previously shown that it is possible to use 3D-SIM to capture perturbations in the bacterial membrane as a result of NSS [87], and it is hoped that by incorporating the use of fluorescently labelled NSS, even more detail of this interaction can be observed.

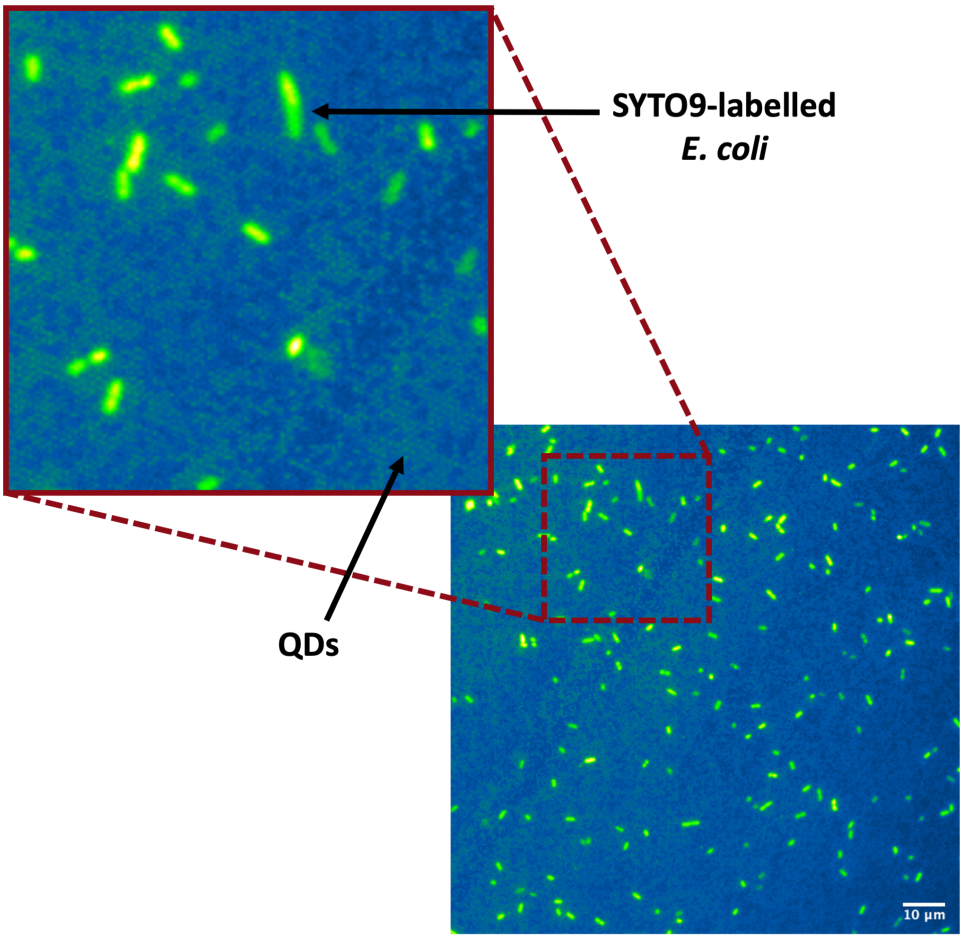


Figure 6.4.6: Epifluorescence image of SYTO9-labelled E. coli on QD-labelled NSS. Inset shows an area where both the SYTO9 labelled E. coli and the QD laden NSS are clearly seen.

6.4.5. Summary of Findings and Conclusions

This section has worked towards developing a technique to image the interaction of the bacteria and nanopillars using fluorescence microscopy. The key conclusions are as follows:

- Fluorescently labelled NSS were fabricated by adding ZnCdSe/ZnS quantum dots to the PS solution to 0.1 wt%.
- This solution was then used to form NSS from the LS using the solution casting method.
- NSS fabricated with QD doped PS were found to be very similar to the normal surfaces.
- SYTO9/GFP and FM4-64 stains were selected to stain the nuclear material and the membrane of the bacteria, respectively.
- Preliminary epifluorescence images show SYTO9 labelled *E. coli* on the QD doped NSS, with good distinction between the two.
- Moving forward it is hoped that high-resolution TIRFM could be used to visualise the interaction between the QD labelled nanopillars and the labelled membrane of the bacteria, in order to learn more about the bactericidal mechanism.

6.5. Overall Conclusions

This chapter has described the work undertaken to learn more about the bactericidal mechanism of NSS. Firstly, a series of different bacterial strains were tested against a PET NSS with ∼120 nm tall features. It was found that both gram-negative strains (MG1655 *E. coli* and UPEC) were killed effectively by the NSS whereas the gram-positive RN4220 *S. aureus* and Je2 strains were not. This fits in with the current theory that the cells are killed through mechanical stretching/breaking of the cell wall, as the gram-positive bacteria have a thicker cell wall [80]. A series of Je2 mutant strains, with knockouts that affect the peptidoglycan machinery, were also investigated in the same way. No significant enhancement in killing of these strains was found for the NSS. This indicated that despite some difference in the cell wall architecture, the thickness of the cell wall still provided enough protection against killing by the nanopillars. Again, this fits into the current bactericidal mechanism theory.

Next, the role of bacterial growth in the killing by NSS (as first proposed by Koller *et al.*) was investigated. The percentage of dead GFP-expressing *E. coli* from different points in their growth cycle (and hence having different growth rates) was assessed after incubation on the cicada wing surface. It was found that more bacteria were killed from the early points in the growth cycle (e.g. lag and early exponential phase) compared to the later times. This trend was found to be the same even after adding the bacteriostatic antibiotic chloramphenicol, which indicates that growth effect are not at play here. Instead, it may be differences in the cell wall structure at the various points which dictates how easily the bacteria are killed - for example the stationary phase cell wall is generally stiffer. This would be indicative of a bactericidal mechanism which mechanically ruptures the cell wall.

Finally, the first steps were taken towards imaging the bacteria-nanopillar interactions directly with fluorescence microscopy. A method of doping the NSS with quantum dots to localise the nanopillar was successfully tested, along with staining the bacterial membrane. More work is required to optimise the methods for use with super-resolution and live imaging techniques, that would hopefully provide much more insight into the bactericidal mechanism of NSS.

Chapter 7

Concluding Remarks and Future Work

The key conclusions from the work presented in this thesis are as follows:

- Analysis of the surface of the *M. intermedia* wing revealed a hexagonal array of nanopillars, $\sim$ 200 nm in height, $\sim$ 140 nm in diameter and with a spacing of $\sim$ 160 nm. The Young's modulus of these nanopillars was measured using quantitative AFM and found to be $\sim 40 \pm 31$ MPa, which is much softer than most of the surfaces currently used to make NSS. FTIR and XPS analysis revealed that, as expected, the wing is composed of mainly chitin and hydrocarbon waxes, neither of which would confer the antibacterial properties. The *M. intermedia* wing was found to kill significantly more *E. coli* than a flat control surface, with $\sim$ 38% of bacteria killed after 20 h of incubation. SEM imaging of the *E. coli* incubated on the wing showed significant changes in the morphology of the cells, with loss or turgor pressure and membrane damage evident.

- Using the cicada wing as inspiration a simple, yet effective, method to produce polymer NSS was developed. For this a master mould (covered in nanoholes 350 nm deep, 165 nm in diameter and 600 nm in spacing) was cleaned with O_2 plasma and then coated with FOTS to allow good release. Polymer solutions were then cast onto the mould, left to cure and then released, leaving the surfaces covered in an array on nanopillars. With glassy polymers such as PS, it was found that residual solvent was often trapped at the base of the mould, resulting in stretched nanopillars upon release. Applying a vacuum during the curing, in addition to reducing the wt% of the solution, helped to overcome this problem. Additionally,

a range of thermoplastic elastomers (Kratons) were also cast and found to provide good replication. The bactericidal ability of the surfaces produced were verified against *E. coli*. An alternative method for producing NSS using NSL was also tested, with the aim of allowing easy alteration of the parameters of the nanopillars. Interface coating was found to be highly effective at depositing a uniform monolayer of colloids onto a polymer film, however, O_2 plasma etching was not sufficient to create nanopillars. Overall, effective nanostructured surfaces were produced for a range of polymers, with different properties, using a low-cost and quick production method.

- Using the solution casting method, NSS were produced from a range of polymer with different stiffnesses. This included the fully glassy PS and a series of Kraton elastomers, with a range of styrene contents. Measurements of the Young's modulus of these polymers found that for the PS, E $\sim$ 3.3 GPa, and for the Kraton polymers, E = 2.7 - 16 MPa. Testing this NSS against exponential-phase *E. coli* found that the polymers with the highest Young's modulus were able to kill the greatest proportion of bacteria - there was also no correlation found between the height of the nanopillars and the killing rate. Whilst no large-scale morphological changes to the *E. coli* incubated on the NSS were seen with SEM, bending of the nanopillars into contact with the bacterial envelope was observed. Measurement of this bending allowed calculation of the forces involved in the interaction and lead to the postulation of the bactericidal mechanism on elastic NSS. It was proposed that the pillar bending and subsequent restoring forces lead to shear stress acting on the bacterial membrane, and that the stiffer nanopillars are able to exert more stress and therefore increased bacterial killing. It is predicted that a combination of pillar stiffness and close spacing contribute to effective killing on the NSS. However, it is thought that on NSS where the pillars are unable to bend, the bactericidal mechanism way be different.

- A high-throughput assay, based on the Live/Dead stain and a microplate reader, was developed to allow the screening of a range of different characteristics much more quickly than the current Live/Dead stain assay using fluorescence microscopy. Using this a range of bacterial strains were tested against a commercially available NSS, g.moth. Both the gram-negative stains, *E. coli* MG1655 and UPEC, were found to be killed significantly more on the NSS compared to the flat control. In contrast, the gram-positive *S. aureus* RN4220, did not display a significant enhancement in killing. Mutant strains of *S. aureus* Je2, which had cell wall defects, were also tested. None of these were found to be killed significantly over the control surfaces. This

shows that the thickness of the gram-positive cell wall is enough to protect them from the bactericidal effect, despite their defects. Additionally, the effect of the growth cycle of bacteria on the bactericidal effect was tested by incubating *E. coli*, which had been grown for different times, on the cicada wing. There was significant killing of the *E. coli* at all time-points apart from stationary phase, and generally more were killed at earlier points. However, adding a bacteriostatic antibiotic to arrest bacterial growth did not change the relative amount of *E. coli* killed at each time-point. This indicates that the growth dynamics of the bacteria do not play a role in the bactericidal mechanism. Finally, preliminary tests of a method to image the bacteria-nanopillar interaction in real time were carried out. This technique used quantum dots embedded into the NSS and a bacterial membrane stain, in order to visualise the nanopillars and the bacteria, respectively. This will be an important tool in understanding more about the bactericidal mechanisms of NSS.

7.1. Plans for Future Work

In order to understand more about the bactericidal mechanisms of nanostructured surfaces, more work is required to both probe the factors which influence the killing efficiency and to visualise the bacteria-nanopillar interaction.

For the former, investigating the link between both feature spacing and stiffness, and the bactericidal efficiency is key when considering the killing mechanism on elastic NSS. To that end, the ability to tune the spacing of the nanopillars would be required. It is envisaged that a method of hot embossing could be used with a series of custom-made moulds (through links with Professor Chris Ober, Cornell University), to create a range of NSS with different spacings. This could then be coupled with polymers which cover a larger range of Young's modulus values, through blending SEBS copolymers with PS or through using SEBS with different copolymer architectures (provided by Kraton polymers). This would result in NSS which cover a wider range of parameter space, in both stiffness and spacing, and allow the effect of both to be investigate even more thoroughly. It may also be possible from this to confirm whether there are different bactericidal mechanisms on different types of NSS.

More experimentation is required in order to visualise the bacteria-nanopillar interaction with fluorescence microscopy. As most techniques currently employed to look at

this interaction rely heavily on sample preparation and are carried out as an "end-point" measurement, fluorescence microscopy provide the only route to imaging the bactericidal mechanism in real-time, *in situ*. Some progress on a method for this has been made here however more time is required in order to fine-tune the process. This will involve improving the sample preparation process, in order to achieve the high resolution imaging that is required to identify the contact points between the bacteria and nanopillars. It is also hoped that this technique could be used for real-time imaging of the samples, helping to identify the timescales over which the killing processes take place.

In order for these nanostructured antibacterial surfaces to be considered as a viable alternative to the current materials used in medical devices, they must be tested to the same rigorous standards. This would involve testing the killing ability of the NSS against a range of clinically-relevant pathogens, through both the current Live/Dead assays and also with standard CFU counting methods. The biocompatibility of the nanostructures with human cell cultures would also have to be tested to ensure that they would be safe for use in indwelling medical devices. Additionally, if these NSS were to be used in tubing-style devices, understanding how they perform under flow conditions is key, as this often how bacteria would be presented to them in a real scenario. This could be performed through stop-flow experiments or using micro-fluidic devices, to vary the flow of bacteria and measure the proportion of dead cells using the Live/Dead stain. Finally, it will be important to begin exploring methods to scale-up the production of the NSS to create larger area surfaces, which can then be implemented into current medical device technology.

Bibliography

1. Tackling Drug-Resistant Infections Globally: Final Report and Recommendations (Chaired by Jim O'Neill) - The Review on Antimicrobial Resistance (2016).
2. De Kraker, M. E. A., Stewardson, A. J. & Harbarth, S. Will 10 Million People Die a Year due to Antimicrobial Resistance by 2050? *PLoS Med* **13,** e1002184 (2016).
3. Murray, C. J. *et al.* Global burden of bacterial antimicrobial resistance in 2019: a systematic analysis. *The Lancet* **399,** 629–655 (2022).
4. Prestinaci, F., Pezzotti, P. & Pantosti, A. Antimicrobial resistance: a global multifaceted phenomenon. *Pathogens and Global Health* **109,** 309–318 (2015).
5. Guest, J. F., Keating, T., Gould, D. & Wigglesworth, N. Modelling the annual NHS costs and outcomes attributable to healthcare-associated infections in England. *BMJ Open* **10,** e033367 (2020).
6. Morones, J. R. *et al.* The bactericidal effect of silver nanoparticles. *Nanotechnology* **16,** 2346–2353 (2005).
7. Radin, S., Campbell, J. T., Ducheyne, P. & Cuckler, J. M. Calcium phosphate ceramic coatings as carriers of vancomycin. *Biomaterials* **18,** 777–782 (1997).
8. Jose, B., Antoci, V., Zeiger, A. R., Wickstrom, E. & Hickok, N. J. Vancomycin covalently bonded to titanium beads kills *Staphylococcus aureus*. *Chemistry and Biology* **12,** 1041–1048 (2005).
9. Feng, Q. L. *et al.* A mechanistic study of the antibacterial effect of silver ions on *Escherichia coli* and *Staphylococcus aureus*. *Journal of Biomedical Materials Research* **52,** 662–668 (2000).
10. Hasan, J., Crawford, R. J. & Ivanova, E. P. Antibacterial surfaces: The quest for a new generation of biomaterials. *Trends in Biotechnology* **31,** 295–304 (2013).
11. Ivanova, E. P. *et al.* Natural Bactericidal Surfaces: Mechanical Rupture of *Pseudomonas aeruginosa* cells by Cicada Wings. *Small* **8,** 2489–2494 (2012).

12. Barthlott, W. & Neinhuis, C. Purity of the sacred lotus, or escape from contamination in biological surfaces. *Planta* **202,** 1–8 (1997).

13. Chung, K. K. *et al.* Impact of engineered surface microtopography on biofilm formation of *Staphylococcus aureus*. *Biointerphases* **2,** 89–94 (2007).

14. Ivanova, E. P. *et al.* Bactericidal activity of black silicon. *Nature Communications* **4,** 1–7 (2013).

15. Silhavy, T. J., Kahne, D. & Walker, S. The Bacterial Cell Envelope. *Cold Spring Harbor Perspectives in Biology* **2,** a000414–a000414 (2010).

16. Salamaga, B. *et al.* Demonstration of the role of cell wall homeostasis in *Staphylococcus aureus* growth and the action of bactericidal antibiotics. *Proc Natl Acad Sci USA* **118,** e2106022118 (2021).

17. Matias, V. R. F., Al-Amoudi, A., Dubochet, J. & Beveridge, T. J. Cryo-Transmission Electron Microscopy of Frozen-Hydrated Sections of *Escherichia coli* and *Pseudomonas aeruginosa*. *J Bacteriol* **185,** 6112–6118 (2003).

18. Pasquina-Lemonche, L. *et al.* The architecture of the Gram-positive bacterial cell wall. *Nature* **582,** 294–297 (2020).

19. Matias, V. R. F. & Beveridge, T. J. Cryo-electron microscopy reveals native polymeric cell wall structure in *Bacillus subtilis* 168 and the existence of a periplasmic space: Gram-positive cell walls and periplasm shown by cryo-TEM. *Molecular Microbiology* **56,** 240–251 (2005).

20. Flemming, H.-C., Neu, T. R. & Wozniak, D. J. The EPS Matrix: The "House of Biofilm Cells". *Journal of Bacteriology* **189,** 7945–7947 (2007).

21. Costerton, J. Introduction to biofilm. *International Journal of Antimicrobial Agents* **11,** 217–221 (1999).

22. Davies, D. Understanding biofilm resistance to antibacterial agents. *Nature Reviews Drug Discovery* **2,** 114–122 (2003).

23. Costerton, J., Stewart, P. & Greenberg, E. Bacterial biofilms: a common cause of persistent infections. *Science* **284,** 1318 (1999).

24. Muhammad, M. H. *et al.* Beyond Risk: Bacterial Biofilms and Their Regulating Approaches. *Front. Microbiol.* **11,** 928 (2020).

25. Hoštacká, A., Čižnár, I. & Štefkovičová, M. Temperature and pH affect the production of bacterial biofilm. *Folia Microbiol* **55,** 75–78 (2010).

26. Zmantar, T., Kouidhi, B., Miladi, H., Mahdouani, K. & Bakhrouf, A. A Microtiter plate assay for *Staphylococcus aureus* biofilm quantification at various pH levels and hydrogen peroxide supplementation. *New Microbiologica* **33,** 10 (2010).

27. Rochex, A. & Lebeault, J.-M. Effects of nutrients on biofilm formation and detachment of a *Pseudomonas putida* strain isolated from a paper machine. *Water Research* **41,** 2885–2892 (2007).

28. Brown, M. R. W., Allison, D. G. & Gilbert, P. Resistance of bacterial biofilms to antibiotics: a growth rate related effect? *Journal of Antimicrobial Chemotherapy* **22,** 777–780 (1988).

29. Cloutier, M., Mantovani, D. & Rosei, F. Antibacterial Coatings: Challenges, Perspectives, and Opportunities. *Trends in Biotechnology* **33,** 637–652 (2015).

30. Young, T. III. An essay on the cohesion of fluids. *Philosophical Transactions of the Royal Society B: Biological Sciences* **95,** 65–87 (1805).

31. Solga, A., Cerman, Z., Striffler, B. F., Spaeth, M. & Barthlott, W. The dream of staying clean: Lotus and biomimetic surfaces. *Bioinspiration and Biomimetics* **2** (2007).

32. Cassie, A. B. D. & Baxter, S. Wettability of Porous Surfaces. *Trans. Faraday Soc* **40,** 546–551 (1944).

33. Youngblood, J. P. & McCarthy, T. J. Ultrahydrophobic Polymer Surfaces Prepared by Simultaneous Ablation of Polypropylene and Sputtering of Poly(tetrafluoroethylene) Using Radio Frequency Plasma. *Macromolecules* **32,** 6800–6806 (1999).

34. Murakami, D., Jinnai, H. & Takahara, A. Wetting transition from the cassie-baxter state to the wenzel state on textured polymer surfaces. *Langmuir* **30,** 2061–2067 (2014).

35. Jaggessar, A., Shahali, H., Mathew, A. & Yarlagadda, P. K. Bio-mimicking nano and micro-structured surface fabrication for antibacterial properties in medical implants. *Journal of Nanobiotechnology* **15,** 1–20 (2017).

36. Ma, J., Sun, Y., Gleichauf, K., Lou, J. & Li, Q. Nanostructure on Taro Leaves Resists Fouling by Colloids and Bacteria under Submerged Conditions. *Langmuir* **27,** 10035–10040 (2011).

37. Hasan, J. *et al.* Selective bactericidal activity of nanopatterned superhydrophobic cicada *Psaltoda claripennis* wing surfaces. *Applied Microbiology and Biotechnology* **97,** 9257–9262 (2013).

38. Kelleher, S. M. *et al.* Cicada Wing Surface Topography: An Investigation into the Bactericidal Properties of Nanostructural Features. *ACS Applied Materials and Interfaces* **8,** 14966–14974 (2016).

39. Nowlin, K., Boseman, A., Covell, A. & Lajeunesse, D. Adhesion-dependent rupturing of *Saccharomyces cerevisiae* on biological antimicrobial nanostructured surfaces. *J. R. Soc. Interface* **12,** 1–12 (2014).

40. Truong, V. K. *et al.* The susceptibility of *Staphylococcus aureus* CIP 65.8 and *Pseudomonas aeruginosa* ATCC 9721 cells to the bactericidal action of nanostructured *Calopteryx haemorrhoidalis* damselfly wing surfaces. *Appl Microbiol Biotechnol* **101,** 4683–4690 (2017).

41. Bandara, C. D. *et al.* Bactericidal Effects of Natural Nanotopography of Dragonfly Wing on *Escherichia coli*. *ACS Applied Materials and Interfaces* **9,** 6746–6760 (2017).

42. Ivanova, E. P. *et al.* Molecular Organization of the Nanoscale Surface Structures of the Dragonfly *Hemianax papuensis* Wing Epicuticle. *PLoS ONE* **8,** 1–8 (2013).

43. Yoshida, A., Motoyama, M., Kosaku, A. & Miyamoto, K. Nanoprotuberance Array in the Transparent Wing of a Hawkmoth, *Cephonodes hylas*. *Zoological Science* **13,** 525–526 (1996).

44. Diu, T. *et al.* Cicada-inspired cell-instructive nanopatterned arrays. *Scientific Reports* **4** (2014).

45. Sengstock, C. *et al.* Structure-related antibacterial activity of a titanium nanostructured surface fabricated by glancing angle sputter deposition. *Nanotechnology* **25.** Publisher: IOP Publishing (2014).

46. Dickson, M. N., Liang, E. I., Rodriguez, L. A., Vollereaux, N. & Yee, A. F. Nanopatterned polymer surfaces with bactericidal properties. *Biointerphases* **10,** 021010 (2015).

47. Hasan, J., Raj, S., Yadav, L. & Chatterjee, K. Engineering a nanostructured "super surface" with superhydrophobic and superkilling properties. *RSC Advances* **5,** 44953–44959 (2015).

48. Bhadra, C. M. *et al.* Antibacterial titanium nano- patterned arrays inspired by dragonfly wings. *Scientific Reports* **5,** 1–12 (2015).

49. Fisher, L. E. *et al.* Bactericidal activity of biomimetic diamond nanocone surfaces. *Biointerphases* **11,** 011014 (2016).

50. May, P. W. *et al.* Diamond-coated 'black silicon' as a promising material for high-surface-area electrochemical electrodes and antibacterial surfaces. *Journal of Materials Chemistry B* **4,** 5737–5746 (2016).

51. Tsimbouri, P. M. *et al.* Osteogenic and bactericidal surfaces from hydrothermal titania nanowires on titanium substrates. *Scientific Reports* **6,** 1–12 (2016).

52. Linklater, D. P., Nguyen, H. K. D., Bhadra, C. M., Juodkazis, S. & Ivanova, E. P. Influence of nanoscale topology on the bactericidal efficiency of black silicon surfaces. *Nanotechnology* **28.** Publisher: IOP Publishing, 1–9 (2017).

53. Tripathy, A. *et al.* Enhancing the Bactericidal Efficacy of Nanostructured Multifunctional Surface Using an Ultrathin Metal Coating. *Langmuir* **33,** 12569–12579 (2017).

54. Hasan, J., Jain, S. & Chatterjee, K. Nanoscale Topography on Black Titanium Imparts Multi-biofunctional Properties for Orthopedic Applications. *Scientific Reports* **7,** 1–13 (2017).

55. Hazell, G. *et al.* Studies of black silicon and black diamond as materials for antibacterial surfaces. *Biomaterials Science* **6,** 1424–1432 (2018).

56. Linklater, D. P. *et al.* High Aspect Ratio Nanostructures Kill Bacteria via Storage and Release of Mechanical Energy. *ACS Nano* **12,** 6657–6667 (2018).

57. Michalska, M. *et al.* Tuning antimicrobial properties of biomimetic nanopatterned surfaces. *Nanoscale* **10,** 6639–6650 (2018).

58. Wu, S., Zuber, F., Weber, K. M., Brugger, J. & Ren, Q. Nanostructured surface topographies have an effect on bactericidal activity. *Journal of Nanobiotechnology,* 1–9 (2018).

59. Hazell, G., Fisher, L. E., Murray, W. A., Nobbs, A. H. & Su, B. Bioinspired bactericidal surfaces with polymer nanocone arrays. *Journal of Colloid and Interface Science* **528,** 389–399 (2018).

60. Viela, F. *et al.* Nano-engineering safer-by-design nanoparticle based moth-eye mimetic bactericidal and cytocompatible polymer surfaces. *RSC Advances* **8,** 22606–22616 (2018).

61. Tripathy, A. *et al.* Fabrication of Low-Cost Flexible Superhydrophobic Antibacterial Surface with Dual-Scale Roughness. *ACS Biomaterials Science and Engineering* **4.** Publisher: American Chemical Society Genre: research-article, 2213–2223 (2018).

62. Cao, Y. *et al.* Nanostructured titanium surfaces exhibit recalcitrance towards *Staphylococcus epidermidis* biofilm formation. *Scientific Reports* **8,** 1–13 (2018).

63. Reed, J. H. *et al.* Ultrascalable Multifunctional Nanoengineered Copper and Aluminum for Antiadhesion and Bactericidal Applications. *ACS Applied Bio Materials* (2019).

64. Dunseath, O. *et al.* Studies of Black Diamond as an antibacterial surface for Gram Negative bacteria: the interplay between chemical and mechanical bactericidal activity. *Scientific Reports* **9.** ISBN: 4159801945280, 8815 (2019).

65. Park, H.-H. *et al.* Cellulose acetate nanoneedle array covered with phosphorylcholine moiety as a biocompatible and sustainable antifouling material. *Cellulose* **26,** 8775–8788 (2019).

66. Elbourne, A. *et al.* Bacterial-nanostructure interactions: the role of cell elasticity and adhesion forces. *Journal of Colloid and Interface Science* **546,** 192–210 (2019).

67. Mo, S. *et al.* Dimensional-dependent antibacterial behavior on bioactive micro/nano polyetheretherketone (PEEK) arrays. *Chemical Engineering Journal* **392.** Publisher: Elsevier, 123736 (2019).

68. Linklater, D. P., Juodkazis, S., Crawford, R. J. & Ivanova, E. P. Mechanical inactivation of *Staphylococcus aureus* and *Pseudomonas aeruginosa* by titanium substrata with hierarchical surface structures. *Materialia* **5,** 100197 (2019).

69. Li, X. *et al.* A nanostructured anti-biofilm surface widens the efficacy against spindle-shaped and chain-forming rod-like bacteria. *Nanoscale* **12,** 18864–18874 (2020).

70. Heckmann, T. S. & Schiffman, J. D. Spatially Organized Nanopillar Arrays Dissimilarly Affect the Antifouling and Antibacterial Activities of Escherichia coli and Staphylococcus aureus. *ACS Applied Nano Materials* **3,** 977–984 (2020).

71. Tan, R., Marzolini, N., Jiang, P. & Jang, Y. Bio-Inspired Polymer Thin Films with Non-Close-Packed Nanopillars for Enhanced Bactericidal and Antireflective Properties. *ACS Applied Polymer Materials* (2020).

72. Cui, Q., Liu, T., Li, X., Song, K. & Ge, D. Nanopillared Polycarbonate Surfaces Having Variable Feature Parameters as Bactericidal Coatings. *ACS Applied Nano Materials* **3,** 4599–4609 (2020).

73. Elbourne, A. *et al.* Significant Enhancement of Antimicrobial Activity in Oxygen-Deficient Zinc Oxide Nanowires. *ACS Applied Bio Materials* **3,** 2997–3004 (2020).

74. Linklater, D. P. *et al.* Nanopillar Polymer Films as Antibacterial Packaging Materials. *ACS Appl. Nano Mater.* **5,** 2578–2591 (Feb. 25, 2022).

75. Jenkins, J. *et al.* Antibacterial effects of nanopillar surfaces are mediated by cell impedance, penetration and induction of oxidative stress. *Nature Communications* **11** (2020).

76. Fujishima, A. & Honda, K. Electrochemical Photolysis of Water at a Semiconductor Electrode. *Nature* **238,** 37–38 (1972).

77. Nowlin, K. & Lajeunesse, D. R. Fabrication of hierarchical biomimetic polymeric nanostructured surfaces. *Molecular Systems Design and Engineering* **2,** 201–213 (2017).

78. Chandran, R., Nowlin, K. & LaJeunesse, D. R. Nanosphere lithography of chitin and chitosan with colloidal and self-masking patterning. *Polymers* **10** (2018).

79. Mo, S. *et al.* Dimensional-dependent antibacterial behavior on bioactive micro/nano polyetheretherketone (PEEK) arrays. *Chemical Engineering Journal* **392,** 123736 (2020).

80. Pogodin, S. *et al.* Biophysical Model of Bacterial Cell Interactions with Nanopatterned Cicada Wing Surfaces. *Biophysical Journal* **104,** 835–840 (2013).

81. Xue, F., Liu, J., Guo, L., Zhang, L. & Li, Q. Theoretical study on the bactericidal nature of nanopatterned surfaces. *Journal of Theoretical Biology* **385,** 1–7 (2015).

82. Li, X. Bactericidal mechanism of nanopatterned surfaces. *Physical Chemistry Chemical Physics* **18,** 1311–1316 (2016).

83. Joens, M. S. *et al.* Helium Ion Microscopy (HIM) for the imaging of biological samples at sub-nanometer resolution. *Sci Rep* **3,** 3514 (2013).

84. Linklater, D. P., Juodkazis, S., Rubanov, S. & Ivanova, E. P. Comment on "Bactericidal Effects of Natural Nanotopography of Dragonfly Wing on *Escherichia coli*". *ACS Applied Materials and Interfaces* **9,** 29387–29393 (2017).

85. Watson, G. S. *et al.* A Simple Model for Binding and Rupture of Bacterial Cells on Nanopillar Surfaces. *Advanced Materials Interfaces* **1801646** (2019).

86. Liu, T. *et al.* Mechanism Study of Bacteria Killed on Nanostructures. *The Journal of Physical Chemistry B* **123,** 8686–8696 (2019).

87. Bandara, C. D. *et al.* Resolving Bio-Nano Interactions of E.coli Bacteria-Dragonfly Wing Interface with Helium Ion and 3D-Structured Illumination Microscopy to Understand Bacterial Death on Nanotopography. *ACS Biomaterials Science & Engineering* **6** (2020).

88. Maleki, E., Mirzaali, M. J., Guagliano, M. & Bagherifard, S. Analyzing the mechano-bactericidal effect of nano-patterned surfaces on different bacteria species. *Surface and Coatings Technology* **408,** 126782 (2021).

89. Velic, A., Hasan, J., Li, Z. & Yarlagadda, P. K. Mechanics of Bacterial Interaction and Death on Nanopatterned Surfaces. *Biophysical Journal* **120,** 1–15 (2021).

90. Köller, M., Ziegler, N., Sengstock, C., Schildhauer, T. A. & Ludwig, A. Bacterial cell division is involved in the damage of gram-negative bacteria on a nano-pillar titanium surface. *Biomedical Physics and Engineering Express* **4** (2018).

91. Sorzabal-Bellido, I. *et al.* Effect of Local Topography on Cell Division of *Staphylococcus* spp. *Nanomaterials* **12,** 683 (2022).

92. Ishak, M. I. *et al.* Insights into complex nanopillar-bacteria interactions : Roles of nanotopography and bacterial surface proteins. *Journal of Colloid and Interface Science* **604,** 91–103 (2021).

93. Jindai, K. *et al.* Adhesion and bactericidal properties of nanostructured surfaces dependent on bacterial motility. *RSC Advances* **10,** 5673–5680 (2020).

94. Binnig, G. K. Atomic force microscope and method for imaging surfaces with atomic resolution. *United States Patent no. 4,724,318* (1988).

95. Binnig, G., Gerber, C., Albrecht, T. R., Quate, C. F. & Stoll, E. Atomic Resolution with Atomic Force Microscope. *Europhysics Letters* **3,** 1281–1286 (1987).

96. Giessibl, F. J. Atomic Resolution of the Silicon (111) - (7x7) Surface by Atomic Force Microscopy. *Science* **267,** 68–71 (1995).

97. Eaton, P. & West, P. *Atomic Force Microscopy* (Oxford University Press, 2010).

98. Liu, S. & Wang, Y. Application of AFM in microbiology: A review. *Scanning* **32,** 61–73 (2010).

99. Nečas, D. & Klapetek, P. Gwyddion: an open-source software for SPM data analysis. *Open Physics* **10** (2012).

100. Hu, S. *et al. High-speed atomic force microscopy and peak force tapping control* in. SPIE Advanced Lithography (ed Starikov, A.) (San Jose, California, Mar. 29, 2012), 83241O.

101. JPK Instruments. *JPK Data Processing Software Manual* 2012.

102. Zhou, W., Apkarian, R. P., Wang, Z. L. & Joy, D. in *Scanning Microscopy for Nanotechnology* (Springer, New York, 2006).

103. Schindelin, J. *et al.* Fiji: An open-source platform for biological-image analysis. *Nature Methods* **9,** 676–682 (2012).

104. Robertson, J., McGoverin, C., Vanholsbeeck, F. & Swift, S. Optimisation of the protocol for the LIVE/DEAD®BacLightTM bacterial viability kit for rapid determination of bacterial load. *Frontiers in Microbiology* **10,** 1–13 (2019).

105. Bachmann, B. in *Neidhardt (ed), Escherichia coli and Salmonella* 2nd, 2460–2488 (ASM Press, 1996).

106. Totsika, M. *et al.* Insights into a Multidrug Resistant Escherichia coli Pathogen of the Globally Disseminated ST131 Lineage: Genome Analysis and Virulence Mechanisms. *PLoS ONE* **6,** e26578 (2011).

107. Fey, P. D. *et al.* A Genetic Resource for Rapid and Comprehensive Phenotype Screening of Nonessential Staphylococcus aureus Genes. *mBio* **4,** e00537–12 (2013).

108. Distant, W. L. V.— *Rhynchotal Notes* .—XXIX. *Annals and Magazine of Natural History* **15,** 58–70 (1905).

109. Bernhard, C. G. & Miller, W. H. A Corneal Nipple Pattern in Insect Compound Eyes. *Acta Physiologica Scandinavica* **56,** 385–386 (1962).

110. JPK Instruments. *QI™ mode - Quantitative Imaging with the NanoWizard® 3 AFM* Technical Note ().

111. Reid, G. *et al.* Biomimetic Polymer Surfaces by High Resolution Molding of the Wings of Different Cicadas. *Materials* **14,** 1910 (2021).

112. Mainwaring, D. E. *et al.* The nature of inherent bactericidal activity: Insights from the nanotopology of three species of dragonfly. *Nanoscale* **8,** 6527–6534 (2016).

113. Wenzel, R. N. Resistance of solid surfaces to wetting by water. *Industrial and Engineering Chemistry* **28,** 988–994 (1936).

114. Cheng, J., Zhang, Y., Pi, P., Lu, L. & Tang, Y. Effect of gradient wetting surface on liquid flow in rectangular microchannels driven by capillary force and gravity: An analytical study. *International Communications in Heat and Mass Transfer* **38,** 1340–1343 (Dec. 2011).

115. Sett, A. *et al.* Capillary driven flow in wettability altered microchannel. *AIChE J.* **63,** 4616–4627 (Oct. 2017).

116. Chaudhury, M. K. & Whitesides, G. M. How to Make Water Run Uphill. *Science* **256,** 1539–1541 (June 12, 1992).

117. Shahali, H. *Assessment of the bactericidal effect of biomimicked nanopillars of cicada wings on titanium implants* PhD thesis (Queensland University of Technology, 2020).

118. Kappl, M. & Butt, H. J. The colloidal probe technique and its application to adhesion force measurements. *Particle and Particle Systems Characterization* **19,** 129–143 (2002).

119. Chang, J., Toga, K. B., Paulsen, J. D., Menon, N. & Russell, T. P. Thickness Dependence of the Young's Modulus of Polymer Thin Films. *Macromolecules* **51,** 6764–6770 (2018).

120. Miyake, K., Satomi, N. & Sasaki, S. Elastic modulus of polystyrene film from near surface to bulk measured by nanoindentation using atomic force microscopy. *Appl. Phys. Lett.* **89,** 031925 (2006).

121. Hopcroft, M. A., Nix, W. D. & Kenny, T. W. What is the Young's Modulus of Silicon? *J. Microelectromech. Syst.* **19,** 229–238 (2010).

122. Luo, Y., Yang, L. & Tian, M. in *Biomaterials and Medical Tribology* 181–216 (2013).

123. Gere, J. M. & Timoshenko, S. P. *Mechanics of Materials* 4th ed. (PWS Publishing Company, 1997).

124. Schoen, I., Hu, W., Klotzsch, E. & Vogel, V. Probing Cellular Traction Forces by Micropillar Arrays: Contribution of Substrate Warping to Pillar Deflection. *Nano Lett.* **10,** 1823–1830 (2010).

125. Sun, M., Watson, G. S., Zheng, Y., Watson, J. A. & Liang, A. Wetting properties on nanostructured surfaces of cicada wings. *Journal of Experimental Biology* **212,** 3148–3155 (2009).

126. Tobin, M. J. *et al.* High-spatial-resolution mapping of superhydrophobic cicada wing surface chemistry using infrared microspectroscopy and infrared imaging at two synchrotron beamlines. *Journal of Synchrotron Radiation* **20,** 482–489 (2013).

127. Derrick, M. R., Stulik, D. & Landry, J. M. *Infrared spectroscopy in conservation science* 235 pp. (Getty Conservation Institute, Los Angeles, 1999).

128. Nguyen, S., Webb, H., Mahon, P., Crawford, R. & Ivanova, E. Natural Insect and Plant Micro-/Nanostructsured Surfaces: An Excellent Selection of Valuable Templates with Superhydrophobic and Self-Cleaning Properties. *Molecules* **19,** 13614–13630 (2014).

129. Stuhr, S. *et al.* Structure and Chemical Organization in Damselfly Calopteryx haemorrhoidalis Wings: A Spatially Resolved FTIR and XRF Analysis with Synchrotron Radiation. *Scientific Reports* **8,** 1–9 (2018).

130. Negrea, P., Caunii, A., Sarac, I. & Butnariu, M. The study of infrared spectrum of chitin and chitosan extract as potential sources of biomass. *Digest Journal of Nanomaterials and Biostructures* **10,** 1129–1138 (2015).

131. Younes, I. & Rinaudo, M. Chitin and Chitosan Preparation from Marine Sources. Structure, Properties and Applications. *Marine Drugs* **13,** 1133–1174 (2015).

132. Yuan, Y., Hays, M. P., Hardwidge, P. R. & Kim, J. Surface characteristics influencing bacterial adhesion to polymeric substrates. *RSC Advances* **7,** 14254–14261 (2017).

133. Thewes, N. *et al.* Hydrophobic interaction governs unspecific adhesion of staphylococci: A single cell force spectroscopy study. *Beilstein Journal of Nanotechnology* **5,** 1501–1512 (2014).

134. Dunnill, C. *et al.* Reactive oxygen species (ROS) and wound healing: the functional role of ROS and emerging ROS-modulating technologies for augmentation of the healing process: Reactive oxygen species and wound healing. *Int Wound J* **14,** 89–96 (2017).

135. Dryden, M. Reactive oxygen species: a novel antimicrobial. *International Journal of Antimicrobial Agents* **51,** 299–303 (2018).

136. Linley, E., Denyer, S. P., McDonnell, G., Simons, C. & Maillard, J.-Y. Use of hydrogen peroxide as a biocide: new consideration of its mechanisms of biocidal action. *Journal of Antimicrobial Chemotherapy* **67,** 1589–1596 (2012).

137. Jiang, L. *et al.* Surface Wettability of Oxygen Plasma Treated Porous Silicon. *Journal of Nanomaterials* **2014,** 1–6 (2014).

138. Langowski, B. A. & Uhrich, K. E. Oxygen Plasma-Treatment Effects on Si Transfer. *Langmuir* **21,** 6366–6372 (2005).

139. Mayer, T. M., de Boer, M. P., Shinn, N. D., Clews, P. J. & Michalske, T. A. Chemical vapor deposition of fluoroalkylsilane monolayer films for adhesion control in microelectromechanical systems. *J. Vac. Sci. Technol. B* **18,** 2433 (2000).

140. Poh, B. & Ong, B. Dependence of viscosity of polystyrene solutions on molecular weight and concentration. *European Polymer Journal* **20,** 975–978 (1984).

141. Saby-Dubreuil, A.-C., Guerrier, B., Allain, C. & Johannsmann, D. Glass transition induced by solvent desorption for statistical MMA/ n BMA copolymers — Influence of copolymer composition. *Polymer* **42,** 1383–1391 (2001).

142. *Polymer Handbook* (eds Brandrup, J., Immergut, E. H. & Grulke, E. A.) 4th (JOHN WlLEY & SONS).

143. Bates, F. S. & Fredrickson, G. H. Block Copolymers—Designer Soft Materials. *Physics Today* **52,** 32–38 (1999).

144. Wu, J., Soucek, M. D. & Cakmak, M. Investigation of Electron Beam Initiated Reactions of Styrenic Block Copolymers. *Progress in Organic Coatings* **100,** 141–152 (2016).

145. Behera, S. *et al.* Photonic integration of uniform GaAs nanowires in hexagonal and honeycomb lattice for broadband optical absorption. *AIP Advances* **10,** 105211 (2020).

146. Liu, H. & Cao, G. Effectiveness of the Young-Laplace equation at nanoscale. *Sci Rep* **6,** 23936 (2016).

147. Suh, K. Y., Jeong, H. E., Kim, D.-H., Singh, R. A. & Yoon, E.-S. Capillarity-assisted fabrication of nanostructures using a less permeable mold for nanotribological applications. *Journal of Applied Physics* **100,** 034303 (2006).

148. Maghsoudi, K., Vazirinasab, E., Momen, G. & Jafari, R. Advances in the Fabrication of Superhydrophobic Polymeric Surfaces by Polymer Molding Processes. *Ind. Eng. Chem. Res.* **59,** 9343–9363 (2020).

149. Cheung, C. L., Nikolić, R. J., Reinhardt, C. E. & Wang, T. F. Fabrication of nanopillars by nanosphere lithography. *Nanotechnology* **17,** 1339–1343 (2006).

150. Xu, X. *et al.* Multiple-Patterning Nanosphere Lithography for Fabricating Periodic Three-Dimensional Hierarchical Nanostructures. *ACS Nano* **11,** 10384–10391 (2017).

151. Zhao, X. *et al.* Architecture design and applications of nanopatterned arrays based on colloidal lithography. *Journal of Applied Physics* **126** (2019).

152. Chen, J. *et al.* Controllable fabrication of 2D colloidal-crystal films with polystyrene nanospheres of various diameters by spin-coating. *Applied Surface Science* **270,** 6–15 (2013).

153. Toolan, D. T., Fujii, S., Ebbens, S. J., Nakamura, Y. & Howse, J. R. On the mechanisms of colloidal self-assembly during spin-coating. *Soft Matter* **10,** 8804–8812 (2014).

154. Shinde, S. S. & Park, S. Oriented colloidal-crystal thin films of polystyrene spheres via spin coating. *Journal of Semiconductors* **36** (2015).

155. Ivanova, E. P. *et al.* The multi-faceted mechano-bactericidal mechanism of nanostructured surfaces. *PNAS,* 1–8 (2020).

156. Lohmann, S. C., Tripathy, A., Milionis, A., Keller, A. & Poulikakos, D. Effect of Flexibility and Size of Nanofabricated Topographies on the Mechanobactericidal Efficacy of Polymeric Surfaces. *ACS Appl. Bio Mater.* **5,** 1564–1575 (Apr. 18, 2022).

157. Huang, J. *et al.* Capillary Wrinkling of Floating Thin Polymer Films. *Science* **317,** 650–653 (2007).

158. ASTM International. *Test Method for Tensile Properties of Thin Plastic Sheeting* (ASTM International, 2018).

159. Torres, J. M., Stafford, C. M. & Vogt, B. D. Impact of molecular mass on the elastic modulus of thin polystyrene films. *Polymer* **51,** 4211–4217 (2010).

160. Michler, G. H. *et al.* Microhardness of styrene/butadiene block copolymer systems: Influence of molecular architecture: Microhardness of Block Copolymer Systems. *J. Appl. Polym. Sci.* **90,** 1670–1677 (2003).

161. Donald, A. M. Environmental scanning electron microscopy for the study of 'wet' systems. *Current Opinion in Colloid and Interface Science* **3,** 143–147 (1998).

162. Uenishi, M. *et al.* Thin dense films from polymer blend of thermoplastic elastomer and polyolefin by uniaxial stretching. *J. Appl. Polym. Sci.* **128,** 2447–2457 (2013).

163. Tuson, H. H. & Weibel, D. B. Bacteria-surface interactions. *Soft Matter* **9,** 4368–4380 (2014).

164. Bien, J., Sokolova, O. & Bozko, P. Role of Uropathogenic *Escherichia coli* Virulence Factors in Development of Urinary Tract Infection and Kidney Damage. *International Journal of Nephrology* **2012,** 1–15 (2012).

165. Wandiyanto, J. V. *et al.* Outsmarting superbugs: Bactericidal activity of nanostructured titanium surfaces against methicillin- and gentamicin-resistant Staphylococcus aureus ATCC 33592. *Journal of Materials Chemistry B* **7,** 4424–4431 (2019).

166. Reichmann, N. T. *et al.* SEDS–bPBP pairs direct lateral and septal peptidoglycan synthesis in Staphylococcus aureus. *Nat Microbiol* **4,** 1368–1377 (2019).

167. Loskill, P. *et al.* Reduction of the peptidoglycan crosslinking causes a decrease in stiffness of the staphylococcus aureus cell envelope. *Biophysical Journal* **107,** 1082–1089 (2014).

168. Wheeler, R. *et al.* Bacterial cell enlargement requires control of cell wall stiffness mediated by peptidoglycan hydrolases. *mBio* **6,** 1–10 (2015).

169. Sutton, J. A. F. *et al.* Staphylococcus aureus cell wall structure and dynamics during host-pathogen interaction. *PLoS Pathog* **17,** e1009468 (2021).

170. Foster, S. J. Molecular characterization and functional analysis of the major autolysin of Staphylococcus aureus 8325/4. *J Bacteriol* **177,** 5723–5725 (1995).

171. Corrigan, R. M., Bellows, L. E., Wood, A. & Gründling, A. ppGpp negatively impacts ribosome assembly affecting growth and antimicrobial tolerance in Gram-positive bacteria. *Proc. Natl. Acad. Sci. U.S.A.* **113** (2016).

172. ThermoFisher Scientific. *LIVE/DEAD™ BacLight™ Bacterial Viability Kit* `https://www.thermofisher.com/order/catalog/product/L7012?SID=srch-srp-L7012`.

173. Truong, V. K. *et al.* The susceptibility of *Staphylococcus aureus* CIP 65.8 and *Pseudomonas aeruginosa* ATCC 9721 cells to the bactericidal action of nanostructured *Calopteryx haemorrhoidalis* damselfly wing surfaces &. *Applied Microbiology and Biotechnology* **101,** 4683–4690 (2017).

174. Pletnev, P., Osterman, I., Sergiev, P., Bogdanov, A. & Dontsova, O. Survival guide: Escherichia coli in the stationary phase. *Acta Naturae* **7,** 22–33 (2015).

175. Kraus, F. *et al.* Quantitative 3D structured illumination microscopy of nuclear structures. *Nat Protoc* **12,** 1011–1028 (2017).

176. Gustafsson, M. Surpassing the lateral resolution limit by a factor of two using structured illumination microscopy. *Journal of Microscopy* **198,** 82–7 (2000).

177. Barroso, M. M. Quantum Dots in Cell Biology. *J Histochem Cytochem.* **59,** 237–251 (2011).

178. Pilizota, T. & Shaevitz, J. W. Fast, multiphase volume adaptation to hyperosmotic shock by escherichia coli. *PLoS ONE* **7,** 1–10 (2012).

179. Fish, K. N. Total Internal Reflection Fluorescence (TIRF) Microscopy. *Current Protocols in Cytometry* **50** (2009).

180. Boulanger, J. *et al.* Fast high-resolution 3D total internal reflection fluorescence microscopy by incidence angle scanning and azimuthal averaging. *Proc. Natl. Acad. Sci. U.S.A.* **111,** 17164–17169 (2014).